Charge-to-spin conversion phenomena in ion implanted Pt and quasi-two dimensional electron gas based heterostructures

著者	Shashank Utkarsh
その他のタイトル	イオン注入したPtおよび擬二次元電子ガスベースのヘテロ構造における電流からスピン流への変換現象
学位授与年度	令和4年度
学位授与番号	17104甲情工第374号
URL	http://doi.org/10.18997/00009163

Charge-to-spin conversion phenomena in ion implanted Pt and quasi-two dimensional electron gas based heterostructures

（イオン注入した Pt および擬二次元電子ガスベースの
ヘテロ構造における電流からスピン流への変換現象）

Shashank Utkarsh

Department of Physics and Information Technology, Faculty of Computer Science and Systems Engineering,
Kyushu Institute of Technology, Japan

Advisory Committee

Prof. Yasuhiro Fukuma, PhD supervisor

Prof. S. Annapoorni

Prof. Edmund Soji Otabe

Prof. Takashi Okamoto

Abstract

Charge-to-spin conversion phenomena in ion implanted Pt and quasi-two dimensional electron gas based heterostructures

Shashank Utkarsh, Doctor of Philosophy

PhD supervisor: Prof. Yasuhiro Fukuma

Kyushu Institute of Technology, Japan

Spin Hall effect (SHE), initially predicted by Dyakonov and Perel in 1971 and later revisited by Hirsch in 1999 [1], is the generation of spin current density $\boldsymbol{j_s}$ from a charge current density $\boldsymbol{j_c}$**.** The conversion of $\boldsymbol{j_c}$ to $\boldsymbol{j_s}$ via SHE, can exert a damping-like spin-orbit torque (SOT) $\boldsymbol{\tau_{DL}}$ on the magnetization of a ferromagnetic (FM) layer attached to the heavy metal (HM). The charge-to-spin conversion is quantified by the damping-like torque efficiency θ_{DL}, which is given by the relation $\boldsymbol{j_s} = (\hbar/2e)\ \theta_{DL}(\boldsymbol{j_c} \times \boldsymbol{\sigma})$, where $\hbar$ is the reduced Planck constant, e is electronic charge and $\boldsymbol{\sigma}$ is polarization of spin current. Typically, 4d and 5d transition metals (such as Pt, Ta and W) are used as the HM, and their corresponding θ_{DL} are found to be ≈0.1. This intrinsic mechanism depends on the Berry curvature of the material, in which an anomalous velocity arises from a momentum-space Berry phase [2]. An increase in θ_{DL} has been found by alloying the HM with Au, Pd and also by incorporating non-metallic elements (with smaller atomic number Z) into the HM. However, in these materials, a complete understanding of the mechanism responsible for the increase in θ_{DL} remains elusive.

Another phenomenon, the Rashba-Edelstein effect (REE), leads to the generation of nonequilibrium spins at the interface of an inversion asymmetry, in a metal oxide heterostructure [3]. The oxygen vacancies created at the interface lead to mobile conduction electrons forming a quasi-two dimensional electron gas (q-2DEG). An electron having momentum $\boldsymbol{p}$, in the presence of an electric field $\boldsymbol{E}$, experiences an effective magnetic field along $(\boldsymbol{p} \times \boldsymbol{E})$. This field leads to spin polarization of the electrons and subsequently a spin current flows from the metal oxide heterostructure to the FM and exerts

a $\boldsymbol{\tau_{DL}}$ on the magnetization of the FM [4]. Similar to SHE, we can define a charge-to-spin conversion efficiency θ_{DL}. So far, a relation between the number of oxygen vacancies and θ_{DL} is yet to be found. Overall, a high θ_{DL} as well as an investigation of its mechanism for the origin of SHE and REE is important in switching the magnetization for writing operation in next generation based magnetic random access memory (MRAM).

In this thesis, we perform ion implantation in Pt, using different nonmetallic elements, namely sulfur (S), oxygen (O), nitrogen (N), and phosphorus (P) and study the θ_{DL} via spin-torque ferromagnetic resonance (ST-FMR) measurements [5]. Additionally, we incorporate O in Pt via sputtering, *i.e.,* PtO_x to compare the sputtering and ion implantation methods. We also compare the q-2DEG created at the interface of $SrTiO_3$/AlN and $SrTiO_3/Al_2O_3$ in terms of θ_{DL} and a detailed investigation of the angular symmetry of spin-orbit torque (SOT) [6], as well as the calculation of θ_{DL} as a function of temperature and implantation dose (oxygen vacancy) is carried out, revealing the mechanism responsible for enhancement of the SHE (REE) .

We use a low energy of 12 keV to implant S in Pt, Pt(S) at a dose of 0×10^{16}-5×10^{16} ions/cm^2. Next, we use an energy of 20 keV to implant O and N in Pt, Pt(O) and Pt(N), respectively at a varying dose of 0×10^{16}-1×10^{17} ions/cm^2. Finally, we move to a moderate energy of 30 keV to implant P in Pt in a wide range of 0×10^{16}-9×10^{16} ions/cm^2. For Pt(S), we achieve a high θ_{DL} ≈0.50 at 10 K, which is 8-times higher than the θ_{DL} or pure Pt at 10 K. We observe a highly monotonic dose dependence in θ_{DL} of Pt(O) from 0.064 to 0.230 at 293 K, with a smaller trade-off in ρ_{xx} from 55.4 to 159.5 $\mu\Omega$ cm, respectively as we increase the dose from 0×10^{16}-1×10^{17} ions/cm^2. For Pt(N), we attain a high $\theta_{\mathrm{DL}} \approx 0.13$ at 293 K for a particular dose of 5×10^{16} ions/cm^2. Finally, for the Pt(P), we obtain a giant $\theta_{\mathrm{DL}} \approx 0.70$ at 293 K , which makes it an ideal candidate of spintronics based MRAM. For PtO_x, we also report a high $\theta_{\mathrm{DL}} \approx$ 0.40 attesting that O in Pt enhances the SHE via both ion implantation and sputtering method. Finally, we explore REE of the q-2DEG created at the interface of $SrTiO_3$/amorphous oxides, namely the $SrTiO_3$/AlN and $SrTiO_3/Al_2O_3$. We observe a very high θ_{DL} ≈2.44 for $SrTiO_3$/AlN than θ_{DL} ≈1.01 for

$SrTiO_3/Al_2O_3$ due to a higher oxygen vacancy enabled REE for the former. The high θ_{DL} is an order higher than the θ_{DL} of 5d transition metal such as Pt.

For the dominant underlying mechanism for the ion implanted samples, we confirm a linear dependence of spin Hall resistivity from impurities, ρ_{imp}^{SH} with the square of resistivity from impurities, ρ_{imp}^{2}, *i.e.,* $\rho_{imp}^{SH} \propto \rho_{imp}^{2}$ [7], implying an extrinsic origin of side-jump scattering as the dominant origin of SHE for the Pt(S), Pt(O), Pt(N) samples studied as a function of implantation and temperature. On the other hand for the PtO_x , we do not get a linear $\rho_{imp}^{SH} \propto \rho_{imp}^{2}$ especially for the lower concentration (n %) of O in Pt, suggesting an intrinsic mechanism while we obtain an extrinsic side-jump for higher n %.

In order to disentangle the dominant extrinsic side-jump from the intrinsic SHE, we express the spin Hall conductivity, σ_{SH}^{xy} as the sum of intrinsic and extrinsic SHE (skew scattering/side-jump) and study it as a function of square of conductivity, σ_{xx}^{2} [8]. We exclude skew scattering as a possible extrinsic mechanism due to the ion-implanted samples not lying in higher of σ_{xx} of super clean metals ($10^6 < \sigma_{xx} < 10^8$ $\Omega^{-1}cm^{-1}$) [2]. Then, we show that a sudden decrease in intrinsic spin Hall conductivity, σ_{SH}^{int} is counterbalanced by the increase in side-jump induced SHE, θ_{SH}^{sj} due to the increase in residual resistivity from impurities, $\rho_{xx,0}$. Hence, for all ion implanted samples, *viz.,* Pt(S), Pt(O), Pt(N), Pt(P), we find that higher the $\rho_{xx,0}$, higher is the θ_{SH}^{sj}, and lower is the σ_{SH}^{int}. We obtain a simple model that θ_{DL} via SHE can be enhanced by simply increasing $\rho_{xx,0}$ in a 5d transition metal. Moreover, we find a crossover of intrinsic to extrinsic side-jump SHE as we increase the dose of S, O, N, P ions in Pt from $\approx 0 \times 10^{16}$-1 $\times 10^{17}$ in a wide energy range of 12-30 KeV. Overall, the contribution of the extrinsic side jump induced SHE to the increase in θ_{DL} is clearly identified through our studies on the ion implanted samples.

To gain insight into the overlooked contribution of oxygen vacancy to the θ_{DL} via REE in q-2DEG, we find that the higher oxygen vacancy created at $SrTiO_3$/AlN in comparison to $SrTiO_3/Al_2O_3$, not only plays a role in enhancing the electronic transport, but may also lead to a higher θ_{DL}. To confirm the high

θ_{DL} in $SrTiO_3$/AlN, we observe a large direct current modulation of resonance linewidth via direct current biased ST-FMR measurements [5] which is ~1-2 order higher than Pt.

For understanding the angular symmetry of SOT, which is crucial in estimation of θ_{DL}, via ST-FMR lineshape analysis, we study the ST-FMR spectrum as a function of ϕ (where ϕ is the angle between microwave current in device and external magnetic field). In our Pt(S), Pt(O), Pt(N), Pt(P), and PtO_x, we observe no breaking of the two-fold and mirror symmetry of SOT due to the 100 % $sin2\phi cos\phi$ dependence of symmetric(S) and antisymmetric (A) component of ST-FMR spectrum leading to simple estimation of θ_{DL}. Whereas for q-2DEG, we observe a broken symmetry of SOT and develop an analysis protocol by filtering out the $sin2\phi cos\phi$ from S and A arising from $\boldsymbol{\tau_{DL}}$ and reliably estimate the θ_{DL}.

In conclusion, we report that θ_{DL} can be enhanced in host Pt by incorporating non-metallic impurity such as S, O, N, and P in Pt due to the extrinsic side-jump scattering induced SHE from impurities. We obtain a high θ_{DL} for Pt(S) at 10 K and Pt(P) at 293 K. For the q-2DEG, we observe a high θ_{DL} ≈2.44 for $SrTiO_3$/AlN than θ_{DL} ≈1.01 for $SrTiO_3/Al_2O_3$, which is an order higher than Pt. We explicitly probe the overlooked contribution of oxygen vacancy to the θ_{DL} enabled by REE. These results suggest that the SHE and REE materials could help us in the development of not only MRAM but also in various spintronic based memory devices utilizing the high charge-to-spin conversion in future.

Reference:

[1] J. E. Hirsch, *Phys. Rev. Lett.* **83**, 1834 (1999).

[2] N. Nagaosa et. al., *Rev. Mod. Phys.* **82**, 1539 (2010).

[3] V. M. Edelstein, *Solid State Commun.* **73**, 233 (1990).

[4] Y. Wang et. al., *Nano Lett.* 17, 7659 (2017).

[5] L. Liu et. al., *Phys. Rev. Lett.* **106**, 036601 (2011).

[6] Y. Ou et. al., *Nano Lett.* **19**, 3663 (2019).

[7] Y. Niimi et. al., Phys. Rev. Lett. 106, 126601 (2011).

[8] Tian et. al., *Phys. Rev. Lett.* **103**, 087206 (2009).

List of Publications

This thesis is based on the results derived from experiments reported in the following papers:

1. U. Shashank, R. Medwal, T. Shibata, R. Nongjai, J. V. Vas, M. Duchamp, K. Asokan, R. S. Rawat, H. Asada, S. Gupta, and Y. Fukuma, "Enhanced spin Hall effect in S-implanted Pt". *Advanced Quantum Technologies* **4** (1), 2000112, (2021).

2. U. Shashank, R. Medwal, Y. Nakamura, J. R. Mohan, R. Nongjai, A. Kandasami, R. S. Rawat, H. Asada, S. Gupta, and Y. Fukuma, "Highly dose dependent damping-like spin-orbit torque in O-implanted Pt", *Applied Physics Letters* **118** (25), 252406, (2021).

3. U. Shashank, Y. Nakamura, Y. Kusaba, T. Tomoda, R. Nongjai, A. Kandasami, R. Medwal, R. S. Rawat, H. Asada, S. Gupta, and Y. Fukuma, "Disentanglement of intrinsic and extrinsic side-jump scattering induced spin Hall effect in N-implanted Pt", Arxive: http://arxiv.org/abs/2211.03355 *(submitted to Phys. Rev. B).*

4. U. Shashank, A. Deka, C. Ye, S. Gupta, R. Medwal, R. S. Rawat, H. Asada, X. Renshaw Wang, and Y. Fukuma, "Room temperature charge-to-spin conversion from quasi-2D electron gas at $SrTiO_3$-based interfaces", *Phys. Status Solidi RRL* **2200377** (2022).

5. U. Shashank, T. Tomoda, Y. Kusaba, Y. Horibe, M. Ishimaru, H. Asada, and Y. Fukuma, "Giant spin Hall effect in P-implanted Pt layers" *(to be submitted).*

Contents

Chapter 1

Introduction and theory

1. Introduction

The use of electronic devices has become an integral part of our day-to-day lives. A few decades ago, it was difficult to collect any piece of information. However, today, everything is available on the internet. To store such large amount of information on the internet or elsewhere, an improvement in the advancement of memory storage and Von Neumann computing is required. The increasing demand for memory storage in large scale computing, machine learning and high performance multicore processors have led to a paradigm shift in the requirement of fast, reliable, energy efficient and non-volatile memory. Moreover, for large scale computing, large on-chip caches are required. Caches are the fast on-chip memories which hold the most used instructions or programs temporarily. Traditional memory technologies for caches have been dominated by the static random access memory (SRAM) which lies in vicinity of the central processing unit (CPU). Slightly farther away from the CPU lies the dynamic RAM (DRAM) and the NAND flash memory chips for the working memory. SRAMs have a fast speed but are limited by the large areal density on a circuit chip, high power density and volatility. Whereas DRAMs, have a considerable speed, but requires complex design of circuits and are volatile too. With the advent of the spin-transfer torque MRAM, and its non-volatile nature, there has been enormous motivation to supplant the SRAM and DRAM, both of which are volatile. The DRAM requires a certain amount of power to retain information once the power is cut-off, thereby requiring a refresh write operation each time. SRAM, on the other hand does not need a refresh operation. However, the very nature of its data being stored in a transistor requires a constant power and large areal density. Therefore, there is a requirement to replace the existing DRAM and SRAM with a non-volatile, low power consuming and reliable memory.

1.1. Evolution of MRAM

Even though there have been substantial improvements in areal density for cell size of memory, all these SRAM, DRAM and NAND flash memory are finding it an uphill task to keep track with the data growth rate. Furthermore, the DRAM and NAND flash utilizes the electrical current to store binary data (0 or 1). While the MRAM uses the collective magnetization state of the ferromagnetic (FM) layer to switch the magnetization and store the data for a parallel and anti-parallel configuration as 0 or 1. MRAMs mainly comprises of the magnetic tunnel junction (MTJ) in which a tunnel barrier is sandwiched between two FM. The top FM is the fixed layer while the bottom FM is the free layer. To this end, the toggle-mode MRAM based on the magnetic field driven switching was developed (see Fig. 1.1 (a)). Here, an external magnetic field generated from a charge current in metal like Cu was used to switch the magnetization and store the data bits as 0 or 1. By passing a charge current density $\boldsymbol{j_c}$ through the Cu wire and Oersted field h_{rf} was generated, but was limited in application due to the high $\boldsymbol{j_c}$ and spatial distribution of the h_{rf}. This led to the bottleneck of its inability to be scaled down to smaller cell size. For reading, the tunnel magnetoresistance (TMR) is measured by passing a current through the junction. Therefore, based on the orientation of the magnetization of top and bottom FM, the data can be stored as parallel or antiparallel, or simply 0 or 1.

Spintronics based MRAM have shown promise as a viable alternative to the ever-existing conventional RAMs. A giant stride to the commercialization of MRAMs arrived with the invention of the spin-transfer torque (STT) MRAM as shown in Fig. 1.1(b) which basically uses the spin polarized current to switch the magnetization state of FM. By passing a $\boldsymbol{j_c}$ through a top fixed FM layer, a spin polarized current density $\boldsymbol{j_s}$ can be generated. Due to the unequal spin up and spin down electrons, the generated $\boldsymbol{j_s}$ is passed to the bottom free FM via tunnel barrier and spin angular momentum can be transferred. This leads to a torque on the magnetization of the free FM, known as the STT, which changes the magnetization state of the FM. However, the common read and write path is the major drawback of the STT-MRAMs,

thereby impairing the read readability. Moreover, the high $\boldsymbol{j_c}$ arising from the write current can lead to damage of the vulnerable oxide layer of the magnetic tunnel junction. This leads to a deterioration of the STT-MRAM with time. Therefore, the quest for a fast, non-volatile, robust and low power consuming memory device is still required.

Recently, a three terminal spin-orbit torque (SOT) MRAM [1, 2] has tremendous capability to circumvent all the current problems. By placing a material with high spin orbit coupling (SOC) below the free layer of the ferromagnet as shown in Fig. 1.1(c), the read and write path can be separated thereby preventing high $\boldsymbol{j_c}$ passing through the tunnel barrier. In a SOT-MRAM, one of the ways by which the spin current can be generated is by the spin Hall effect (SHE) or the Rashba- Edelstein effect (REE will discuss these in detail in next section 1.2. Origin of SOTs. Coming back to SOT-MRAM, the $\boldsymbol{j_s}$ generated from the $\boldsymbol{j_c}$ in SOC material can switch the magnetization of the bottom FM, thereby separating the write path from the read path. This conversion of $\boldsymbol{j_c}$ to $\boldsymbol{j_s}$ is called the charge-to-spin conversion efficiency (θ_{DL}) (also called spin hall angle or damping-like torque efficiency). Another yardstick for the SOT-MRAM is the lower longitudinal resistivity ρ_{xx} of the SOC. Therefore, the combination of high θ_{DL} and low ρ_{xx} are the main ingredients of an energy efficient SOT-MRAM. The low ρ_{xx} can alleviate the damage from the Joule heating of the tunnel barrier by separating the write and read path leading to high endurance and low power consumption. The high θ_{DL} can lead to deterministic switching and eradicate the switching delay which was present in the STT-MRAM. However, the θ_{DL} of most HM is around 0.1. Therefore, an innovation in improving the θ_{DL} with a little trade-off in ρ_{xx} is important to unlock the full potential of SOT-MRAM in order to make it commercially viable. Table 1-I summarizes the memory technology comparison for DRAM, SRAM, NAND flash, STT-MRAM and SOT-MRAM [1]. The separate write and read latency has led to tremendous research for finding a suitable material for SOT-MRAM.

Memory technology comparison

	DRAM	SRAM	Flash	STT-MRAM	SOT-MRAM
Write latency	✓	✓✓✓		✓	✓✓✓
Read latency	✓	✓✓		✓✓	✓✓✓
Cell size	✓✓✓	✓	✓✓✓	✓✓	✓
Endurance	✓✓✓	✓✓✓		✓✓✓	✓✓✓
Non-volatility	No	No	Yes	Yes	Yes

Table 1-I. Comparison of memory technology comparison for DRAM, SRAM, Flash, STT-MRAM and SOT-MRAM[1]. Image is reproduced with permission from https://doi.org/10.1109/VLSICircuits18222.2020.9162774.

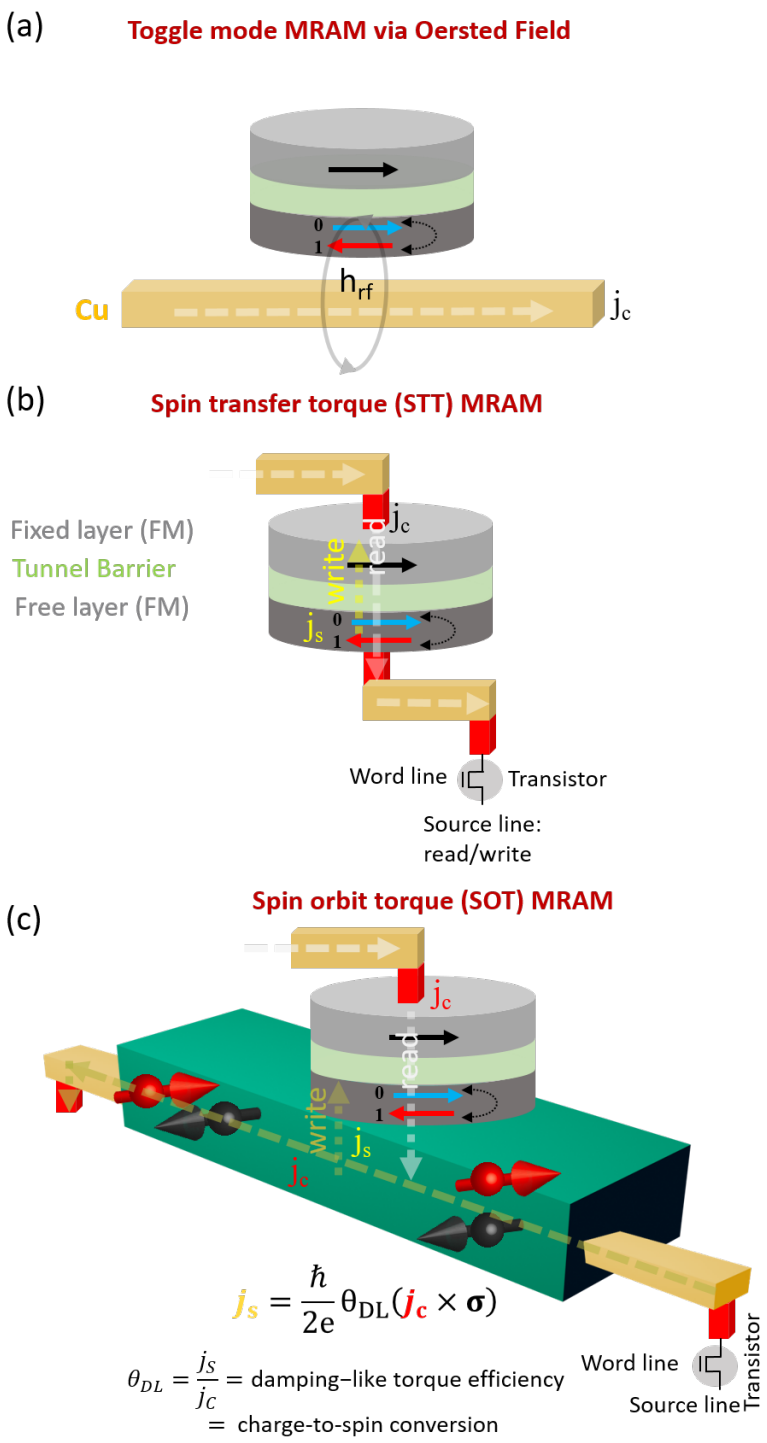

Figure 1.1. Schematic of (a) Toggle MRAM driven by Oersted field, (b) STT-MRAM driven by spin polarized current from top fixed layer, and (c) SOT-MRAM using SOC material placed below the free layer to switch the magnetization.

1.2. What is spintronics?

Spintronics is the field of study which makes use of the additional degree of freedom called spin angular momentum of electron, apart from its charge. The history of spintronics dates back to 1987 when the Giant magnetoresistance was discovered individually by Albert Fert and Peter Grünberg [3, 4], for which they were awarded the Nobel Prize in 2007. GMR led to contribute greatly to hard disk drive but was later replaced with tunneling magnetoresistance (TMR) which later revolutionized the MRAM industry, as we read in the last section.

1.2.1 Generation of charge current, spin-polarized current, and pure spin current

The first question that comes to our mind is: How can we "generate" such a spin? The electrons comprise of not only charge but also an important thing called the spin. First, the charge current is composed of an equal up-spin and down-spin which both cancels each other and leads to charge current as shown in Fig. 1.2 (a). Second, the spin polarized current is the one that has unequal number of up-spin and down-spin as shown in Fig. 1.2 (b), leading to a flow of both spin and charge. Third, if we flow two different electrons in opposite direction, with each having an up-spin and down-spin, respectively, then it leads to a flow of pure spin current as shown in Fig. 1.2 (c). So, let us explore the second type- the spin polarized current and its implications on the STT.

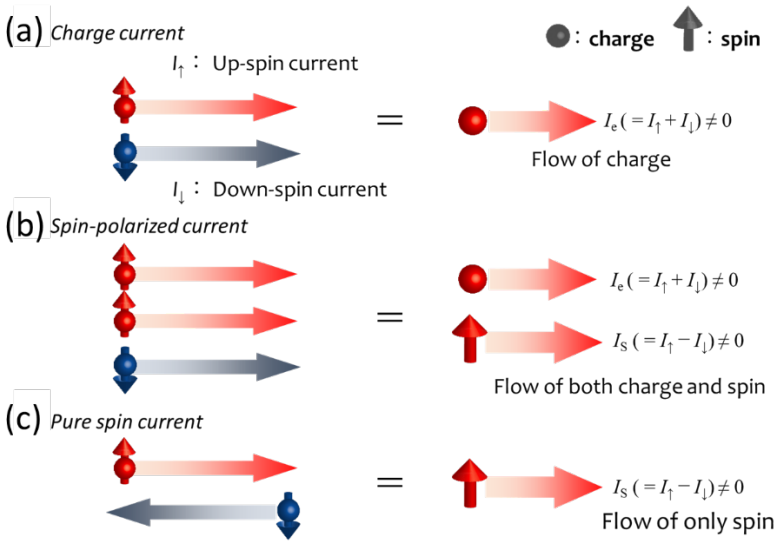

Figure. 1.2. Generation of charge current, spin-polarized current, and pure spin current. Image is reproduced from Y. Fukuma et. al., "Giant spin accumulation and long-distance spin precession in metallic lateral spin valves", *APS March Meeting Abstracts*, **P15-004** (2012).

1.2.2. Spin transfer torque

The spin-transfer torque (STT) was proposed separately by Slonczewski [5] and Berger [6]. In STT via spin filtering effect, upon passing through a ferromagnetic material, the conducting electron spins become partially polarized. This arises due to the unequal up-spin and down-spin electrons, leading to a flow of both charge and spin. If we consider two ferromagnet (FM) attached adjacent to each other as depicted in Fig. 1.3, then the polarized spin current from top FM1 will inject into the bottom FM2 and transfer the angular momentum of the spin. Prior to reaching FM2, the spin becomes non-polarized due to the relaxation of spin. Once the electron flow is reflected or transmitted from FM2, due to the conservation of angular momentum, the loss in the angular momentum is equal to the torque exerted on the magnetization. To put it simply, when incoming unpolarized electrons (e^-) reaches FM1, they become polarized after reaching FM2, and exert a torque to rotate their spin angular momentum. Due to conservation of angular momentum, an equal and opposite torque is exerted on magnetic domain of FM2, which is called the spin transfer torque $\boldsymbol{\tau_{STT}}$.

Therefore, the magnetic moment experiences a force (torque) which can be expressed using the generalized Landau-Lifshitz-Gilbert-Slonczewski Equation (LLGS) equation:

$$\frac{d\boldsymbol{m}}{dt} = -\gamma(\boldsymbol{m} \times \boldsymbol{H_{ext}}) + \alpha\left(\boldsymbol{m} \times \frac{d\boldsymbol{m}}{dt}\right) + \boldsymbol{\tau_{STT}}\left(\boldsymbol{m} \times (\hat{\sigma} \times \boldsymbol{m})\right) + \boldsymbol{\tau_{OFT}}(\boldsymbol{m} \times \boldsymbol{H_F}), \qquad (1.1)$$

where **m** is the magnetization unit vector, $\boldsymbol{H_{ext}}$ is the externally applied magnetic field, $\hat{\sigma}$ is the unit vector along the spin polarization direction of the spin current, γ is the gyromagnetic ratio and α is the Gilbert damping constant. The third term corresponds to the STT term whereas the fourth term arises primarily from the Oersted torque and partially from the field-like (FL) torque, $\boldsymbol{\tau_{OFT}}$. Here, $\boldsymbol{\tau_{STT}}$ from the polarized spin current acts along or opposite to damping torque, τ_α (see Fig. 1.3). Later, we will come back to this STT term and replace it with a damping-like torque term arising from SOC (section 1.3.7). In the fourth term, $\boldsymbol{H_F}$ is the current induced field which arises primarily from the Oersted field from the microwave current in FM.

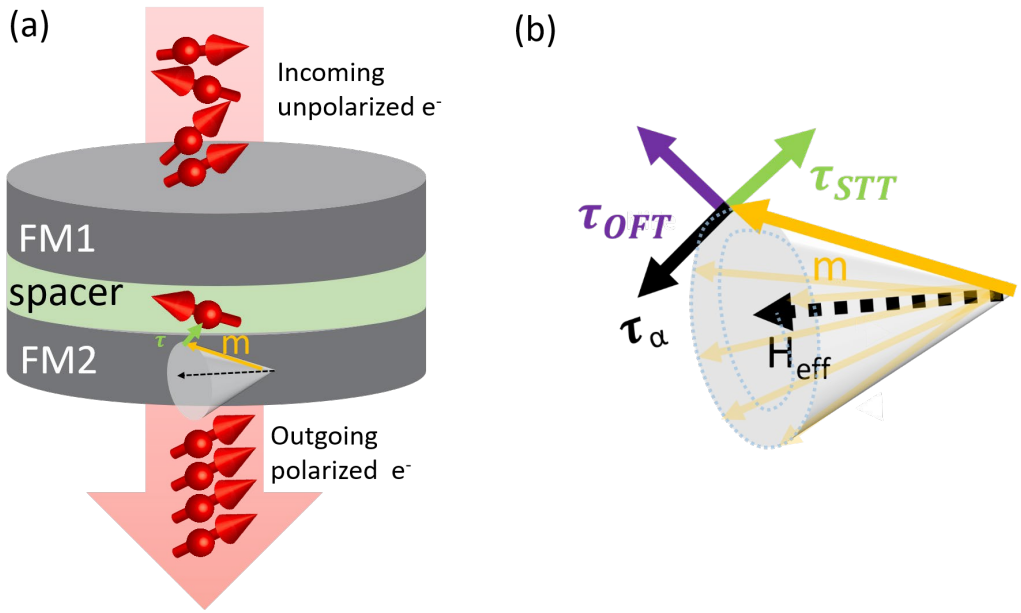

Figure. 1.3. (a) Visualization of spin transfer torque in spacer layer sandwiched between two ferromagnet (FM1 and FM2), and (b) magnetization dynamics in FM2.

As mentioned previously, the use of STT brought an alternative pathway to switch the magnetization instead of using the traditional Oersted field. This revolutionized the magnetic memory towards the development of MRAM. Coming back to STT, there is another method by which spin current can be generated, i.e., from the spin current generated using the spin-orbit coupling (SOC) material.

1.2.3. Spin-orbit coupling

After understanding how can we "generate" a spin current, let us explore how can we "manipulate" this spin current. In classical electromagnetism, when an electron with momentum $\boldsymbol{p}$ moves around a nucleus, it experiences an effective magnetic field $\boldsymbol{B_{eff}}$ given as:

$$\boldsymbol{B_{eff}} = -\frac{\boldsymbol{v}\times\boldsymbol{E}}{c^2}, \tag{1.2}$$

where **v** is the velocity of the electron, **E** is the electric field inside which the electron is moving and c is the speed of light. Using $\boldsymbol{p} = m_e \cdot \boldsymbol{v}$, where m_e is mass of electron, the eqn. 1.2 can be rewritten as:

$$\boldsymbol{B_{eff}} = -\frac{\boldsymbol{p}\times\boldsymbol{E}}{m_e \cdot c^2}, \tag{1.3}$$

By expressing $\boldsymbol{E}$ as a gradient of electric field potential V, and as a result of the experienced B_{eff} on the electron, the magnetic moment μ carried by the spin of electron $\boldsymbol{S}$ leads to a Zeeman energy H_{SO} which is given as:

$$H_{SO} = -\frac{1}{2}\boldsymbol{\mu}\cdot\boldsymbol{B} = \left(-\frac{g\mu_B\boldsymbol{S}}{2\hbar}\right)\cdot\left(-\frac{\boldsymbol{p}\times\boldsymbol{E}}{m_e\cdot c^2}\right) = \frac{g\mu_B}{2m_e c^2\hbar}\boldsymbol{S}\cdot(\nabla V\times\boldsymbol{p}), \tag{1.4}$$

Where g is the electron spin-g factor, μ_B is Bohr magneton, $\hbar$ is reduced Planck constant. If we consider the central field approximation in which we assume all the electrons to coalesce and make up a charge symmetric cloud, then the electric field potential V will be proportional to the distance between electron and nucleus, $\boldsymbol{r}$. Therefore, gradient of electric field potential, ∇V is proportional to r as $\nabla V(r) \propto r$. Further, by expressing orbital angular momentum $\boldsymbol{L}$ as $\boldsymbol{r}\times\boldsymbol{p}$, H_{SO} is written as :

$$H_{SO} \sim \boldsymbol{S} \cdot (\nabla V(\boldsymbol{r}) \times \boldsymbol{p} \sim S \cdot (\boldsymbol{r} \times \boldsymbol{p}) = \boldsymbol{S} \cdot \boldsymbol{L}, \quad (1.5)$$

where, **S** is also referred to as spin angular momentum. Thus, the coupling of the $\boldsymbol{L}$ with $\boldsymbol{S}$ is called the spin orbit coupling (SOC). This is how the SOC is explained for the classical electromagnetism model. Furthermore, the same model can be extended to understand the SOC in electrons in a 5d transition metal with high atomic number Z and structures with broken spatial inversion symmetry. The SOC then generates spin polarization $\boldsymbol{\sigma}$, using two separate effects: spin Hall effect (SHE) and Rashba-Edelstein effect (REE), which will be discussed in detail in section 1.3.

1.2.4. Anisotropic magnetoresistance (AMR)

Apart from the "generation" and "manipulation" of spin current using the STT and SOC respectively lies another important phenomenon, which is the "detection" of spin current. So, for the detection of spin current generated from charge current, a ferromagnet can read the signals based on the orientation of the magnetization $\boldsymbol{M}$ with the direction of electrical current flowing through the sample. In simpler words, the resistance of the sample reduces, when the magnetization of the sample changes from parallel to perpendicular direction with respect to the electric current. Let us understand in terms of the mathematical expressions involved.

When an electric current density $\boldsymbol{j_c}$ flows through a ferromagnet, a current is created magnetically, called as $\boldsymbol{j_M}$. Based on the angle between the resistance and electric current, a parameter is defined, α_{AMR} which is called the AMR coefficient. Therefore, the $\boldsymbol{j_M}$ is defined as:

$$\boldsymbol{j_M} = -\alpha_{AMR} \boldsymbol{M} \cdot (\boldsymbol{M} \cdot \boldsymbol{j_V}), \quad (1.6)$$

The projection of $\boldsymbol{j_M}$ parallel to $\boldsymbol{j_V}$ defines the parallel configuration of AMR effect as $\boldsymbol{j_{M,||}}$:

$$\boldsymbol{j_{M,||}} = -\alpha_{AMR} M^2 \boldsymbol{j_V} cos^2(\phi) = -\frac{1}{2} \alpha_{AMR} M^2 \boldsymbol{j_V} (\cos(2\phi) + 1), \quad (1.7)$$

where ϕ is the angle between $\boldsymbol{M}$ and $\boldsymbol{j_V}$. Similarly, the projection of $\boldsymbol{j_M}$ perpendicular to $\boldsymbol{j_V}$ defines the perpendicular configuration of AMR effect as $\boldsymbol{j_{M,\perp}}$:

$$\boldsymbol{j_{M,\perp}} = -\alpha_{AMR} M^2 \boldsymbol{j_V} \sin(\phi)\cos(\phi) = -\frac{1}{2}\alpha_{AMR} M^2 \boldsymbol{j_V}(\sin(2\phi), \tag{1.8}$$

Therefore, the parallel component of $\boldsymbol{j_M}$ describes AMR, while the perpendicular component describes the planar Hall effect. Further, we can define the net current $\boldsymbol{j}$ flowing through the wire which is the sum of $\boldsymbol{j_V}$ and $\boldsymbol{j_{M,||}}$ given as :

$$\boldsymbol{j} = \boldsymbol{j_{M,||}} + \boldsymbol{j_V} = \boldsymbol{j}_{\perp}\left(\mathbf{1} - \frac{\mathbf{1}}{\mathbf{2}} \cdot \alpha_{AMR} M^2(\cos(2\phi) + 1)\right), \tag{1.9}$$

In above eq. 1.9, $\boldsymbol{j}$ is largest when $\phi = 90°$ or $-90°$ (perpendicular) and smallest when $\phi = 0°$ or $180°$. Additionally, according to Ohm's law, the resistance in the wire can be calculated as:

$$R = \frac{V}{j} \approx R_{\perp}(1 + \frac{1}{2}\alpha_{AMR} M^2(\cos(2\phi) + 1), \tag{1.10}$$

Thus, R becomes largest when **M** is parallel to the wire,

$$R_{//} = R_{\perp}(1 + \alpha_{AMR} M^2), \tag{1.11}$$

Finally, the AMR ratio is defined as the relative change in the resistance upon rotation of the magnetization from the parallel to antiparallel configuration given as:

$$\Delta R_{AMR} = \frac{R_{//} - R_{\perp}}{R_{\perp}} = \alpha_{AMR} M^2, \tag{1.12}$$

We can also rewrite the eq. 1.10, after using $R_{//}$and $R_{\perp}$ and expressing $\frac{1}{2}(cos(2\phi) + 1)$ as $cos^2(\phi)$ given as:

$$R = R_{\perp}\left(1 + \Delta R_{AMR}\cos^2(\phi)\right), \tag{1.13}$$

The AMR follows the $cos^2(\phi)$ angular dependence (eqn. 1.13), which enters the voltage rectification signal in spin torque ferromagnetic resonance (ST-FMR) signal V_{mix} as $\Delta R = sin(2\phi)$. We will explore this

in section 1.3.6 and 1.3.7. After understanding mathematically, we can also understand the same using experimental MR measurements. Figure 1.4. shows the MR measurements of a SOC material (5d transition metal), Pt placed above the ferromagnetic layer NiFe.

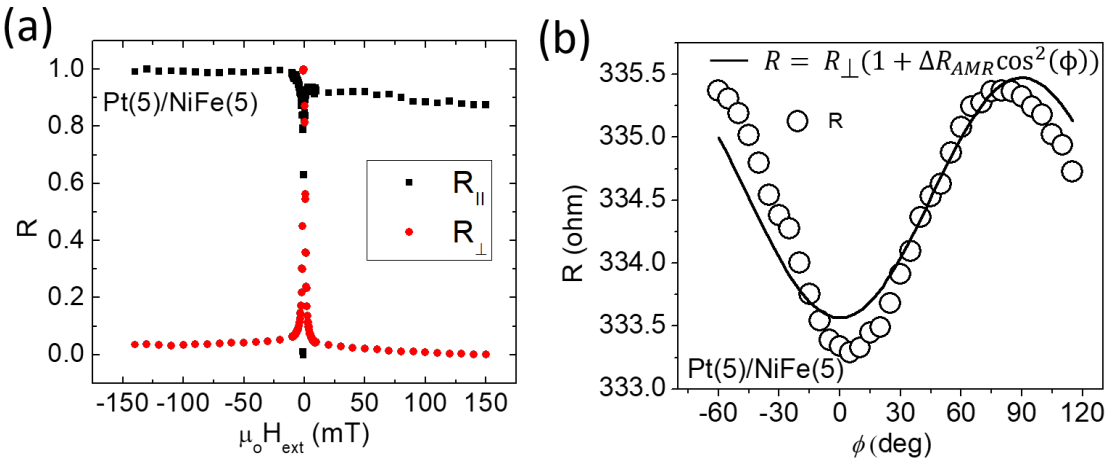

Figure 1.4. (a) Change in resistance ($R_{//}$and $R_{\perp}$) acquired for parallel and antiparallel configuration as a function of applied magnetic field (H_{ext}), and (b) Angular dependent magnetoresistance measurements of R measured as a function of ϕ in the presence of $\mu_o H_{ext}$ = 200 mT.

To sum it up, we have studied the generation, manipulation and detection of spin current. However, despite all these three being critical, the manipulation of spin current is of paramount importance. The high spin current generated can exert a strong spin-orbit torque (SOT) on the magnetization of FM layer, thereby leading to a tremendous potential in SOT-MRAM. Let us study the origin of SOT in next sections.

1.3. Origin of spin-orbit torques

The generation of spin current density $\boldsymbol{j_s}$ from charge current density $\boldsymbol{j_c}$ can be mainly categorized by two SOC phenomena, the spin Hall effect (SHE) and the Rashba-Edelstein effect (REE). We will discuss each in detail in part I and II. Both these effects have the capability of generating $\boldsymbol{j_s}$ from $\boldsymbol{j_c}$ from the SOC which diffuse into the adjacent FM. Then, it can transfer the spin angular momentum to the magnetization of the FM and exert a spin-orbit torque (SOT) on the magnetization of FM.

1.3.1. Part I: Spin Hall effect

The spin Hall effect (SHE) is a bulk SOC phenomenon in which a $\boldsymbol{j_c}$ generates a transverse spin current density $\boldsymbol{j_s}$. To put it simply, if we have a material possessing a strong spin orbit coupling (SOC) in the absence of any external magnetic field, and if we apply $\boldsymbol{j_c}$ along its longitudinal direction, electrons with opposite spins are separated in opposite directions. This is similar to the Hall effect, in which the direction of those spins will be perpendicular to $\boldsymbol{j_c}$ and a transverse $\boldsymbol{j_s}$ is created, which is known as the SHE described by:

$$\boldsymbol{j_s} = \frac{\hbar}{2e}\theta_{DL}(\boldsymbol{j_c} \times \boldsymbol{\sigma}), \tag{1.14}$$

where $\boldsymbol{\sigma}$ is the spin polarization of the spin current. The prerequisite of a conventional SHE is that $\boldsymbol{j_s}$, $\boldsymbol{j_c}$ and $\boldsymbol{\sigma}$ are mutually orthogonal to each other as seen in eqn. 1.14. Furthermore, due to the Onsager reciprocity of this SHE in eqn. 1.14, $\boldsymbol{j_s}$ can also be generated from $\boldsymbol{j_c}$ if $\boldsymbol{\sigma}$ is mutually orthogonal to both $\boldsymbol{j_c}$ and $\boldsymbol{j_s}$. However, we will come back as to how the $\boldsymbol{\sigma}$ in different directions can lead to unconventional SHE in later sections of this chapter. The SHE was predicted initially by Dyakonov and Perel [7] and then later revisited by Hirsch in 1999 [8]. Half a decade later in 2004-2005, the SHE was experimentally demonstrated by Kato et. al., [9] and Wunderlich et. al., [10] in semiconductors and later in metals in 2007 by Kimura et. al., [11]. As an extension to the SHE, the anomalous Hall effect (AHE) was previously observed in magnets to non-magnetic materials by Karplus and Luttinger [12], and Smit [13]. Later, it was realised that with the AHE, the SHE was closely tied to one common factor, which was the SOC and can be intrinsic or extrinsic. In AHE, the intrinsic effect (proposed by Karplus and Luttinger) is dependent on the band structure of the perfect crystal, whereas the extrinsic effect arises from spin-dependent scattering due to impurities. The extrinsic effect in AHE is primarily categorized into skew scattering and side-jump scattering as proposed by Smit [14] and Berger [15], respectively. Recently, it has been experimentally demonstrated that the AHE and the SHE share the same analogy by Moriya et al. [16]. Therefore, we will understand the intrinsic and extrinsic contribution to SHE in detail in analogy with the AHE.

1.3.2. Intrinsic Spin Hall effect

Intrinsic SHE arises in materials with strong SOC, typically in 4d and 5d transition metals with large atomic number Z. So, the intrinsic contribution to SHE is dependent only on the band structure of the perfect crystal. In simpler words, it can be said that the intrinsic SHE is proportional to the integration of the Fermi surface of Berry curvature of each occupied band. The Berry phase means that the system remains unchanged or adiabatic around an evolution of time t. At time t, if we have a Hamiltonian *H(**R**)* depending on a closed path ***R**(t),* we see that the state $|\Psi(t)\rangle$ will evolve according to the Schrödinger's equation as:

$$H(\boldsymbol{R})|\Psi_n(t)\rangle = \boldsymbol{E_n}|\Psi_n(t)\rangle, \tag{1.15}$$

Therefore, assuming that the evolution of the state $|\Psi_n(\boldsymbol{R}(t)\rangle$ is adiabatic, then at every time t, the system will remain in the initial state it was originally prepared apart from a phase factor [17]. Therefore, the intrinsic SHE depends on the berry curvature of the material, in which an anomalous velocity arises from a momentum-space berry phase [18]. It leads to an elastic event in which the wave vector $\vec{k}$ of the up-spin and down-spin electrons generated from charge current is conserved [19]. The path of the up-spin and down-spin electrons are symmetrical to each other as shown in Fig. 1.5 (a), and due to the cancellation of $\vec{k}$ and conservation of momentum, the event is elastic. Due to this elastic event, the spin Hall conductivity, σ_{SH}^{xy} is independent of the momentum relaxation time, τ_{relax}.

1.3.3. Extrinsic side-jump scattering induced spin Hall effect

For side-jump scattering, when high amount of impurities is introduced in the host material (say 4d or 5d transition metal), then a discontinuous side-way displacement is created near the impurities for the up-spin and down-spin electrons generated from charge current. (Fig. 1.5 (b)). The origin of side-jump scattering lies in the time delay in the phase of the component of wave function perpendicular to wave direction. The side-jump scattering, is found in materials with high amount of impurity concentrations in the host, thereby creating a sudden jump near the impurity site while approaching and leaving the impurity. Due to a similar trajectory, the $\vec{k}$ for the up-spin and down-spin electrons are again cancelled and leads to

an elastic event. Similar to intrinsic SHE, σ_{SH}^{xy} is independent of Υ_{relax}. Due to σ_{SH}^{xy} being independent of Υ_{relax} for both intrinsic and side-jump scattering, it has been an experimental challenge to disentangle the intrinsic from the side-jump scattering. We will come back to this disentanglement in chapter 5.

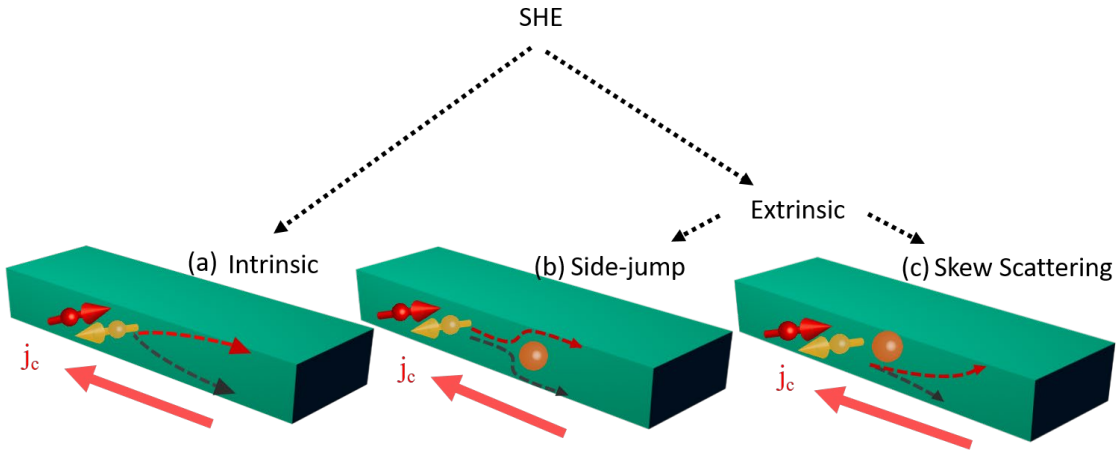

Figure 1.5. Schematic of (a) Intrinsic spin Hall effect (b) Extrinsic side-jump scattering, and (c) Extrinsic skew scattering.

1.3.4. Extrinsic skew scattering induced spin Hall effect

The extrinsic skew scattering arises in materials with low ρ_{xx} or super clean metals with lower amount of impurity concentrations in host. Due to the classical scattering process, it is less trivial to understand as compared to side-jump scattering. An electron with wave vector $\vec{k}$ approaches the impurity and is scattered to a new $\vec{k'}$ which is skewed or bent at an angle with respect to $\vec{k}$. Due to the SOC, the scattering is spin-dependent with up-spin following a slightly skewed trajectory as compared to the down-spin as shown in Fig. 1.5 (c). The difference of the up-spin and down-spin trajectories lead to the $\vec{k}$ not being cancelled and thereby resulting in an inelastic event. Due to the inelastic event, skew scattering shows $\sigma_{SH}^{xy} \propto \Upsilon_{relax}$ scaling.

1.3.5. Part II: Rashba Edelstein effect

Due to lack of crystal inversion symmetry, an electron with momentum $\boldsymbol{p}$, in the presence of an interfacial electric field $\boldsymbol{E}=E_z \cdot z$, may experience a field $\hat{H}_R$ due to REE given as [20]:

$$\hat{H}_R = \frac{\alpha_R}{\hbar}(\boldsymbol{z} \times \boldsymbol{p}) \cdot \boldsymbol{\sigma}, \tag{1.16}$$

where $\boldsymbol{\sigma}$ is the vector of the Pauli spin matrices, $\boldsymbol{z}$ is defined as the direction normal to the plane where the spatial inversion symmetry is broken, and α_R is the Rashba parameter which typically determines the strength of Rashba SOC. An interfacial electric field $\boldsymbol{E} = E_z \cdot \boldsymbol{z}$ applied perpendicular to the plane of broken inversion symmetry leads to an effective Rashba field, $\boldsymbol{B_{Ry}}$, which is experienced by an electron flowing in-plane i.e., along x direction. The schematic diagram of the Inverse Rashba Edelstein effect (IREE) is shown in Fig. 1.6. The Rashba field is mutually orthogonal to symmetry breaking direction and the electron flow direction. Figure 1.6 shows the Rashba interface created between two dissimilar insulating oxides to create a broken inversion symmetry. For eg. a Rashba interface can be created between $SrTiO_3$ and AlN or Al_2O_3. We will come back to this in detail in chapter 7. Figure 1.6 (a) shows how the moving electrons (K_x) experience the Rashba field, $\boldsymbol{B_{Ry}}$ in presence of $\boldsymbol{E_z}$. If the electron is not aligned with $\boldsymbol{B_{Ry}}$, say x, then there is precession of spin depending on the strength of the field. Hence, the spin of the moving electrons precesses around the axis of the Rashba field as shown Fig. 1.6 (b) even in the absence of an applied magnetic field. Consequently, the magnitude of electric field, strength of $\boldsymbol{B_{Ry}}$ can be controlled with an application of gate voltage [21]. One can therefore utilize the Rashba field to polarize the electrons along the direction of field, which is the spin galvanic effect i.e., the inverse of REE. This can be visualized in terms of the Onsager reciprocity of charge-spin interconversion via spin Hall effect (SHE) and Inverse spin Hall effect (ISHE) respectively. We will explore the Onsager reciprocity of SHE in chapter 4.

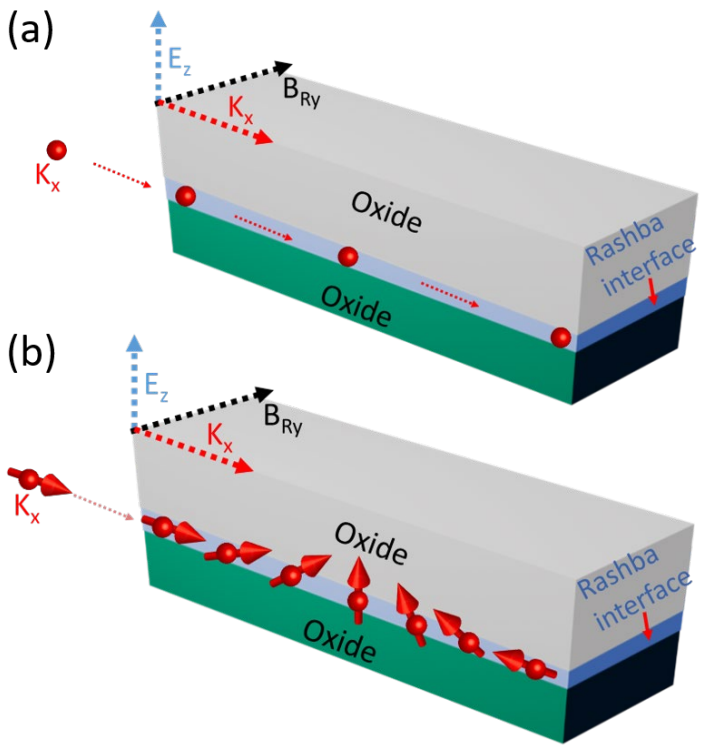

Figure 1.6. Inverse Rashba Edelstein effect and precession of spin in Rashba field. Schematic of (a) moving electrons experiencing the Rashba field in presence of E_z (b) Precession of spin of moving electrons around axis of Rashba field.

1.3.6. Measurement of SOT: spin-torque ferromagnetic resonance

One of the methods to measure the strength of SOTs is the spin-torque ferromagnetic resonance (ST-FMR). In this method, the rectangular device heavy metal/ferromagnet (HM/FM) is excited with a microwave current I_{rf} (See Fig. 1.7). The I_{rf} applied in HM generates, $\boldsymbol{j_s}$ which exerts $\boldsymbol{\tau_{DL}}$. Simultaneously, the I_{rf} generates an Oersted field h_{rf}, which exert an out-of plane Oersted field torque ($\boldsymbol{\tau_{OFT}}$). While at the same time, an in-plane magnetic field H_{ext} is swept at an angle ϕ with I_{rf} direction. Once the Larmor precession frequency from the device matches with the input frequency, a resonance condition is attained. Upon meeting the resonance condition, both $\boldsymbol{\tau_{DL}}$ and $\boldsymbol{\tau_{OFT}}$ drive the magnetization precession, resulting in a periodically varying ΔR due to anisotropic magnetoresistance (AMR) of FM. The mixing of ΔR and I_{rf}

produces a ST-FMR voltage spectrum, expressed as V_{mix} which is used to measure the strength of SOT given as [22],

$$V_{mix} = SF_{sym}(H_{ext}) + AF_{asym}(H_{ext}), \quad (1.17)$$

, where, $F_{sym}(H_{ext}) = \frac{(\Delta H)^2}{(H_{ext}-H_o)^2+(\Delta H)^2}$ is the symmetric component with weight S, and $F_{asym}(H_{ext}) = \frac{\Delta H(H_{ext}-H_o)}{(H_{ext}-H_o)^2+(\Delta H)^2}$ is the antisymmetric component with weight *A* and ΔH and H_o are the half-width-at-half-maximum and resonance field of FMR spectra.

Derivation of the ST-FMR signal V_{mix}

The derivation of ST-FMR signal V_{mix} has been explained in detail by Wang et. al., [23]. The V_{mix} can be expressed as the product of I_{rf} passed in the HM/FM layer and the AMR resistance given as: $V(t) = I(t) \cdot R(t)$. Here, I(t) is the I_{rf} written as eqn. 1.18, and R(t) is change in resistance defined as eqn. 1.19, given as:

$$I(t) = cos(\omega t), \quad (1.18)$$

$$R\ (t) = R_o + \Delta R cos^2\theta(t), \quad (1.19)$$

and $\theta(t) = \theta_o + \theta_c \cos(\omega t + \delta)$, where θ_o is the angle between magnetization ***m*** and I_{rf} (see Fig. 1.7), θ_c is the cone angle, δ is the phase between SOT or Oersted field and ***m***. By using Taylor expansion for $\cos\theta(t)$, we obtain $V(t)$ as:

$$\cos\theta(t) = \cos\theta_o - \sin\theta_o \cdot \theta_c \cos(\omega t + \delta), \quad (1.20)$$

$$R(t) = R_o + \Delta R[cos^2\theta_o - 2\cos\theta_o \cdot \sin\theta_o \cdot \theta_c \cos(\omega t + \delta)], \quad (1.21)$$

$$V(t) = (IR_o + \Delta R cos^2\theta_o)\cos(\omega t) - I\Delta R sin(2\theta_o) \cdot \frac{\theta_c \cos(2\omega t+\delta)}{2} - I\Delta R sin(2\theta_o) \cdot \theta_c cos\frac{\delta}{2}, \quad (1.22)$$

Out of the three terms, the third term which is a time-independent DC term is the V_{mix} voltage, where the $sin(2\theta_o)$ term comes from AMR, while $cos\frac{\delta}{2}$ comes from SOT or Oersted field. This combines to give a $\sin 2\varphi \cos(\varphi)$ dependence, which we will see in next section.

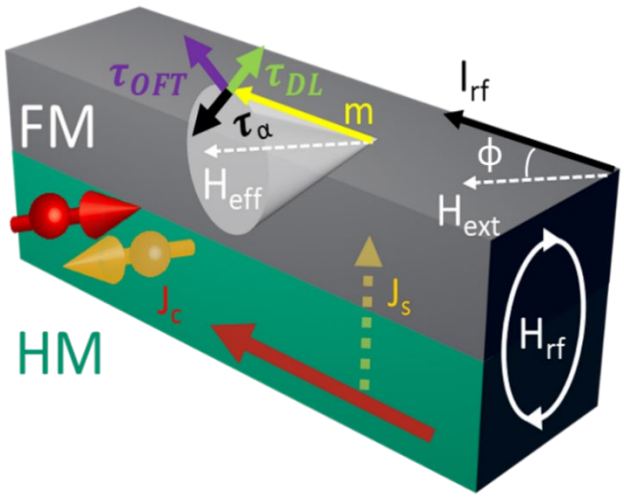

Figure 1.7. Measurement of SOTs: ST-FMR detection principle shown for a HM/FM bilayer system.

1.3.7. Angular dependence of symmetry of torques

We studied about STT in section 1.2.2. Here, we will replace the STT term, τ_{STT} in LLGS eqn. 1.1, with a damping-like torque term, τ_{DL} arising from SOC. The current induced spin-orbit torque arising from the spin-source (HM) is exerted on the adjacent FM layer attached to it. As a consequence, the dynamic response on the magnetization of ferromagnet follows the generalized Landau-Lifshitz-Gilbert-Slonczewski Equation (LLGS) equation 1.1 to be rewritten as:

$$\frac{d\boldsymbol{m}}{dt} = -\gamma(\boldsymbol{m} \times \boldsymbol{H_{ext}}) + \alpha\left(\boldsymbol{m} \times \frac{d\boldsymbol{m}}{dt}\right) + \tau_{DL}\left(\boldsymbol{m} \times (\hat{\sigma} \times \boldsymbol{m})\right) + \tau_{OFT}(\boldsymbol{m} \times \boldsymbol{H_F}), \qquad (1.23)$$

where $\boldsymbol{m}$ is the magnetization unit vector, $\boldsymbol{H_{ext}}$ is the externally applied magnetic field, $\hat{\sigma}$ is the unit vector along the spin polarization direction of the spin current, γ is the gyromagnetic ratio and α is the Gilbert damping constant. The third term corresponds to the damping-like (DL) torque whereas the fourth term arises primarily from the Oersted torque and partially from the field-like (FL) torque. Here, τ_{DL} is the damping-like torque arising from the spin-source i.e., a HM and τ_{OFT} is oersted or the field-like torque term (see figure 1.7). In the fourth term, $\boldsymbol{H_F}$ is the current induced field which arises primarily from the Oersted field from the microwave current in HM and sometimes, partially from any field-like effective field generated from the spin current arising from HM. Hence, for a given HM/FM system in which the FM is

in-plane magnetized (like NiFe), the τ_{DL} and τ_{OFT} can be in-plane (IP) or out-of-plane (OOP) depending on the direction of $\hat{\sigma}$ and $\boldsymbol{H_F}$. Hence, based on the ST-FMR detection efficiency, any IP torque is detected in the symmetric (S) component while the OOP torque is detected in the antisymmetric (A) component.

a. SHE induced SOTs ($\hat{\sigma}_y$ type)

As illustrated in Fig. 1.8, the $\boldsymbol{j_s}$ generated from $\boldsymbol{j_c}$ due to SHE in HM generates an in-plane spin polarization $\hat{\sigma}_y$ which is perpendicular to the $\boldsymbol{j_c}$. This type of SOTs is called the traditional SHE type because $\boldsymbol{j_c}$ (x direction), $\boldsymbol{j_s}$ (z direction) and $\hat{\sigma}_y$ (y direction) are mutually orthogonal to each other. In this case, the angular dependence of the in-plane (IP) damping-like torque is $\boldsymbol{\tau_{DL}}\,(x'\cos(\varphi))$ which is an IP torque detected in the *S* part. In the *A* part, a term $\boldsymbol{\tau_{OFT}}(z'\cos(\varphi))$ arising from the out-of-plane (OOP) torque is seen. Both this torque shows a $\cos(\varphi)$ dependence and combining it with the AMR detection which shows a $\sin(2\varphi)$ dependence, a total term of $\sin(2\varphi)\cos(\varphi)$ is observed in both the *S* and *A* for SHE type torque induced by $\hat{\sigma}_y$.

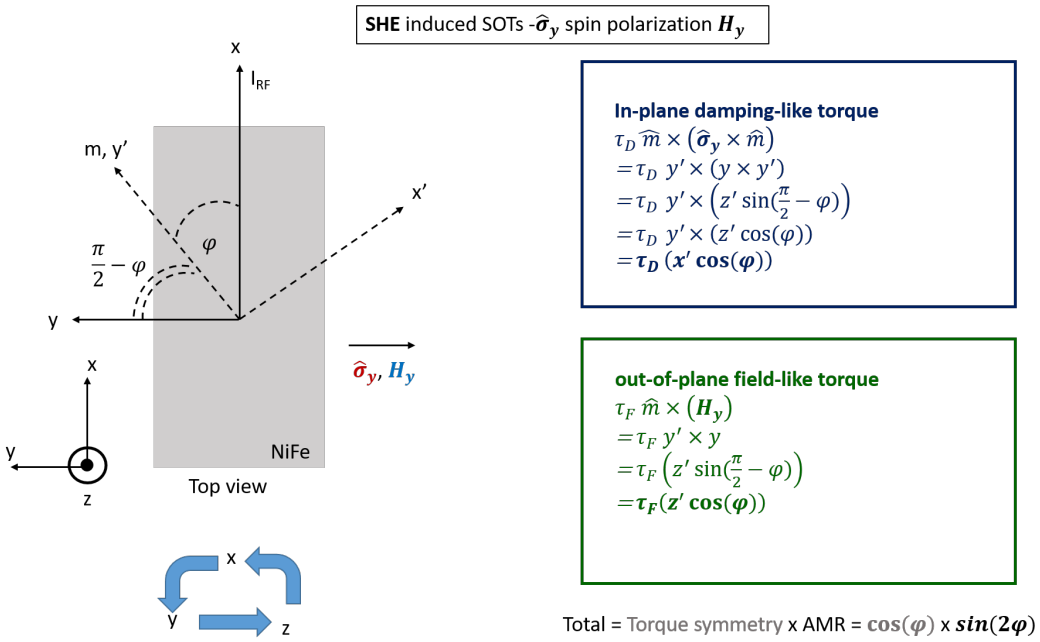

Figure 1.8. Left panel shows the top view of schematic illustration of SHE induced SOTs (**$\hat{\sigma}_y$ type**). Right panel shows the in-plane damping like torque and out-of plane field like torque seen in *S* and *A*, respectively in blue and green box.

b. SOTs arising from $\hat{\sigma}_z$ spin polarization and H_F in z-direction ($\hat{\sigma}_z$ type)

As depicted visually is Fig. 1.9, if there is an OOP spin polarization and effective field then, the overall torques are distinct from the expected $\sin(2\varphi)\cos(\varphi)$ and can be experimentally observed while performing the IP angular ST-FMR measurements. For an IP magnetized FM, if an OOP spin current induced effective field or OOP oersted field due to non-uniform current flow exists, then the generated $\boldsymbol{H_z}$ leads to an IP torque $\boldsymbol{\tau_F(x')}$ in S part and an OOP torque $\boldsymbol{\tau_D(z')}$ detected in A part. Thus, upon being modulated by the AMR detection efficiency, it leads to an overall IP torque $\boldsymbol{\tau_F(x')}\sin(2\varphi)$ in S and OOP torque $\boldsymbol{\tau_D(z')}\sin(2\varphi)$ in A.

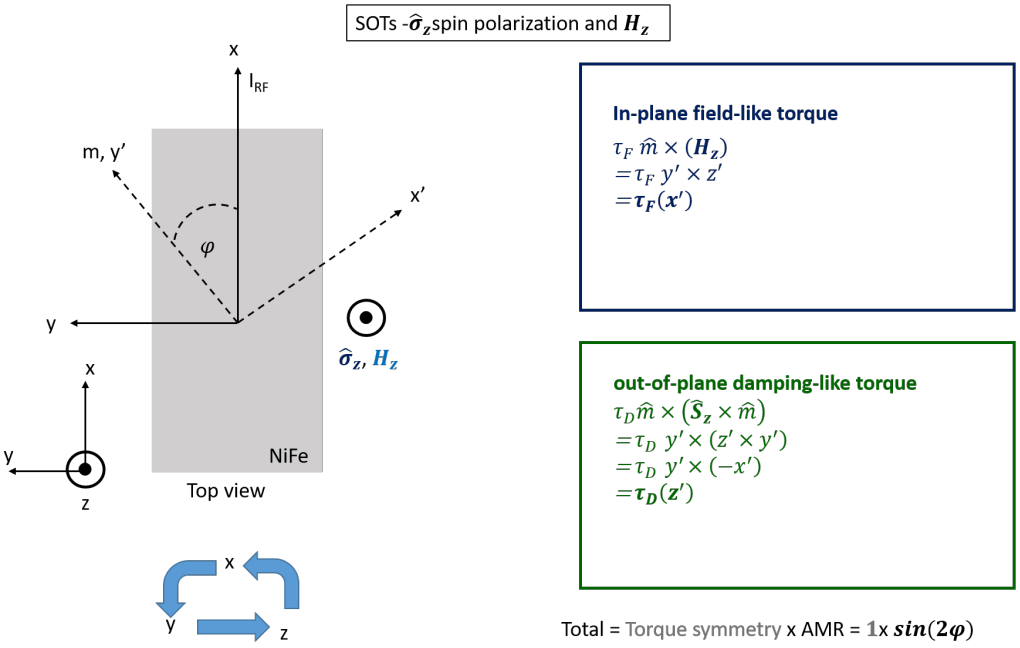

Figure 1.9. Left panel shows the top view of schematic illustration of SHE induced SOTs ($\hat{\sigma}_z$ type). Right panel shows the in-plane field like torque and out-of plane field like torque seen in S and A, respectively in blue and green box.

c. SOTs arising from $\hat{\sigma}_x$ spin polarization and H_F in x-direction ($\hat{\sigma}_x$ type)

Due to phenomena not arising from SHE, there exists effects such as Dresselhaus effect and non-uniform current flow, which may lead to a component parallel to the I_{rf} current in x-direction. If a spin polarization exists parallel to the current flow I_{rf} in x-direction i.e., $\hat{\sigma}_x$ and a relative effective field H_x also parallel to I_{rf}, then it creates an IP DLT $\tau_{DLT}(x' \sin\varphi)$ and OOP field torque $\tau_{OFT}(z' \sin\varphi)$. Please see Fig. 1.10. Hence, by combining with the AMR detection of $\sin(2\varphi)$, it leads to an IP torque $\tau_{DLT}(x' \sin\varphi)\sin(2\varphi)$ in S and OOP torque $\tau_{OFT}(z' \sin\varphi)\sin(2\varphi)$ in A.

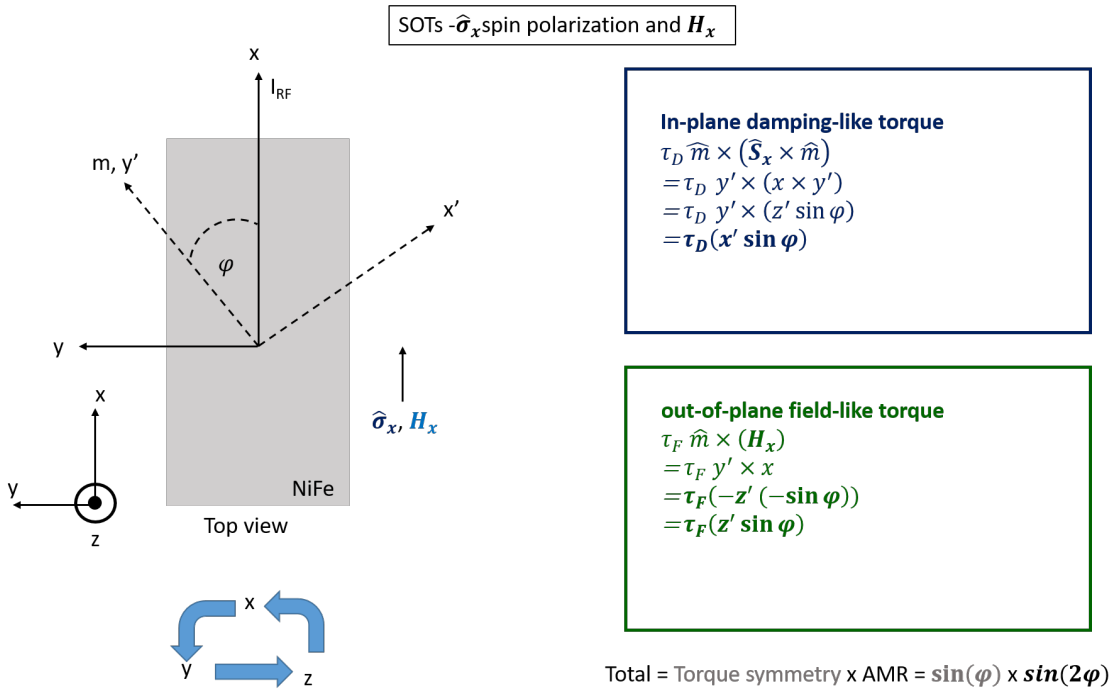

Figure 1.10. Left panel shows the top view of schematic illustration of SHE induced SOTs ($\hat{\sigma}_x$ **type**). Right panel shows the in-plane damping like torque and out-of plane field like torque seen in S and A, respectively in blue and green box.

Hence, the following results of the generated torques have been shown in Table 1-II for SOT and in Table 1-III for Oersted field torque.

Table 1-II. SOT dependence of torques.

	Type	Expression	Direction	Lineshape	ϕ dependence of only torque	ϕ dependence of lineshape (multiplied by AMR detection efficiency)
σ_y	DLT	$m_x \times \sigma_y \times m_x$	IP	Symmetric	cosϕ	cosϕ.sin2ϕ
	FLT	$m_x \times H_y$	OP	Antisymmetric	cosϕ	cosϕ. sin2ϕ
σ_z	DLT	$m_x \times \sigma_z \times m_x$	OP	Antisymmetric	1	sin2ϕ
	FLT	$m_x \times H_z$	IP	Symmetric	1	sin2ϕ
σ_x	DLT	$m_x \times \sigma_x \times m_x$	IP	Symmetric	sinϕ	sinϕ. sin2ϕ
	FLT	$m_x \times H_x$	OP	Antisymmetric	sinϕ	sinϕ. sin2ϕ

Table 1-III. Dependence of torques from Oersted field.

	Expression	Direction	Lineshape	ϕ dependence of only torque	ϕ dependence of lineshape (multiplied by AMR detection efficiency)
$h_{rf,y}$	$m \times h_{rf,y}$	OP	Antisymmetric	cosϕ	cosϕ. sin2ϕ
$h_{rf,z}$	$m \times h_{rf,z}$	OP	Antisymmetric	1	sin2ϕ
$h_{rf,x}$	$m \times h_{rf,x}$	OP	Antisymmetric	sinϕ	sinϕ. sin2ϕ

1.4. Fundamental problems in charge-to-spin conversion material and its implementation in SOT-MRAM

There have been numerous candidates for charge-to-spin conversion material in the SOT-MRAM. The candidates have been divided primarily into SOC materials based on (a) 5d transition metals, (b) alloys, (c) Insertion layers for interface modulation (d) anti-ferromagnets (e) Transition Metal dichalcogenides (TMDs), (f) topological insulators, and (g) Two dimensional electron gases (2DEGs). Let us explore each in detail.

(a) 5d transition metals (TM). The study of charge-to-spin conversion, θ_{DL} has been studied primarily on 5d transition metals such as Pt, Ta, W. Additionally, modifications in deposition conditions due have led to different phase of Ta, W such as β-Ta and β-W, which have shown high θ_{DL}. However,

the longitudinal resistivity, ρ_{xx} has also been found to increase for these TM which is undesirable for being a candidate for SOC material in SOT-MRAM. Moreover, the high θ_{DL} is restricted to few nanometer (nm) depicting an interfacial phenomena rather than bulk.

(b) Alloys. Due to the SOC strength depending on the atomic number Z, alloys of host with large Z have been made with impurity of large Z such AuPt, PdPt, AuW. Alternatively, materials with smaller atomic numbers are found to have a small SOC, and therefore are unsuitable for SOT-MRAM. However, mixing of 5d transition metals (host with large Z) with lighter elements (impurity with small Z) can also lead to an extrinsic SHE and enhance θ_{DL}, due to the difference in Z between the host and impurity. SHE has been found to enhance in CuPt, CuBi. [24-26]. The origin of enhancement of SHE has been a challenge due to the limited variation of θ_{DL}, with ρ_{xx}. Most of these measurements have been performed at room temperature and the underlying mechanism is not clear.

(c) Insertion layers for interface modulation. Hf and Mo have been used as dusting layer to modify the interfacial damping and θ_{DL}, such as in W-Hf, Pt-Hf [27, 28], and in Ta-Mo, W-Mo [29]. Despite tremendous efforts for Pt-Co [30], it has been challenging to disentangle the interfacial from the bulk contribution of SHE/REE.

(d) Anti-ferromagnets (AFM). The AFM plays a pivotal role in pinning the magnetization in a fixed direction for the top FM in STT-MRAM and SOT-MRAM using the exchange bias effect between FM and AFM. Simultaneously, the AFM can also be used to modify the magnetization dynamics via SHE. For example, IrMn (AFM) material when deposited adjacent to NiFe (FM) can be an efficient source of θ_{DL} of 0.12-0.20 as reported in $IrMn_3$/NiFe but with a high ρ_{xx} of 176-204 μΩ cm, it makes them difficult to be incorporated in SOT-MRAM [31]. Moreover, the exchange bias field can also create an angular dependence of torques making the quantization or estimation of θ_{DL} complex as demonstrated in Py/Cu/PtMn tri-layer [32]. We already explored angular dependence of torques in last section.

(e) Transition Metal Dichalcogenides (TMDs). Another family of SOC material that is entwined with the complex angular dependence of torques is the TMDs. Although possessing a broken symmetry of torques, complex analysis can yield a θ_{DL}= 0.029 which is not dramatically high as compared to its out-of plane torque efficiency (3.5) for WTe_2 [33], $NbSe_2$ [34] and $MoTe_2$ [35] also possesses a broken symmetry of torques making the estimation of θ_{DL} complex.

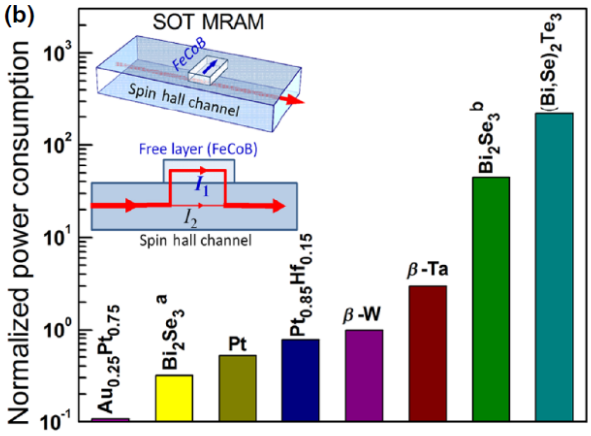

Figure 1.11. Normalized power consumption as calculated for a typical SOT-MRAM device with the different charge-to-spin conversion materials. Figure is reproduced with permission from L. Zhu et. al, Phys. Rev. Appl. **10**, 031001 (2018).

(f) Topological Insulators (TI). Despite being internally insulating; the TI is an intriguing family that have high SOC at the surface. Due to spin momentum locking between spin direction and wave-vector $\vec{k}$, there is a shift in the Fermi surface which leads to spin accumulation. By coupling the spin accumulation to the attached ferromagnet (FM), a flow of spin angular momentum is created which can exert a torque on the magnetization of FM. Although the angular symmetry of torques is usually not broken as seen in Bi_2Se_3 [36] and $(Bi_{1-x}Sb_x)_2Te_3$ [37], the high ρ_{xx} and current shunting into the FM makes it an undesirable candidate for SOT-MRAM, despite its high θ_{DL}.

(g) Two dimensional electron gas (2DEG). Even though its complex, another family that is emerging as a promising candidate for SOC material for SOIT-MRAM is the interfacial two-dimensional

electron gases (2DEGs) created at the interface of two dissimilar insulators. Due to the presence of an inversion asymmetry at the interface, a 2DEG electron with momentum $\boldsymbol{p}$ in the presence of an electric field $\boldsymbol{E}$ can experience a Rashba-like field $\propto \boldsymbol{p} \times \boldsymbol{E}$ in its rest frame due to SOC. Due to this, a spin current is generated in 2DEG from the charge current, and hence a high θ_{DL} is found [38, 39]. However, estimating the ρ_{xx} seems to be a daunting task due to the unknown thickness of the 2DEG. Due to being a low symmetry material, there are additional problems that may arise in correct estimation of θ_{DL} (something which we will explore in detail in chapter 7).

Furthermore, Figure 1.11 summarize the power consumption in SOC material calculated for a typical SOT-MRAM device with the different charge-to-spin conversion materials. As discussed previously, the combination of high θ_{DL} and low ρ_{xx} can lead to a low power consumption in MRAM. The choice of 5d-TM and their alloys along with the other material such as topological insulators are shown. The 5d-TM especially the Pt based alloys seems to be better choice for SOC material in SOT-MRAM. Nevertheless, if one can have a better trade-off in high θ_{DL} and low ρ_{xx}, while at the same time maintaining the bulk charge-to-spin conversion along with an unbroken symmetry of torques, the purpose of finding an apt SOC material seems solved.

To summarize, following are the desirable traits for implementation in SOT-MRAM as shown in Table 1-IV. Out of all the possible choices, the 5d-TM and alloys seems to be better candidate considering the edge that it has over other materials. If the θ_{DL} can be enhanced in 5d-TM with a little trade-off in ρ_{xx}, while at the same time maintaining an unbroken angular symmetry of torques with bulk effect, the SOC material candidate can be quite useful for the next generation of SOT-MRAM low power devices. Hence, in this thesis, we performed series of experiments in the quest of next-generation high charge-to-spin conversion material on non-metallic element incorporated in widely used 5d TM Pt, using ion implantation and sputtering. Further, we go beyond the 5d transition metals and explore the charge-to-spin conversion in a two-dimensional electron gas (2DEG) created at the interface of $SrTiO_3$/amorphous insulators.

Table 1-IV. Summary of the $\theta_{\mathrm{DL}}, \rho_{xx}$, angular symmetry, SHE or REE and origin for various charge-to-spin conversion materials.

SOC material	θ_{DL}	ρ_{xx}	Angular symmetry	SHE or REE	Origin (bulk or interface)
(a) 5d TM	Low	Low	✓	SHE	bulk
(b) Alloys	Moderate	Moderate	---	SHE	bulk
(c) Insertion	Moderate	Moderate	---	SHE + interfacial	interface
(d) AFM	Moderate	High	×	SHE + interfacial	interface
(e) TMDs	Moderate	High	×	SHE + interfacial	interface
(f) TIs	High	Very high	✓	Spin momentum locking	Mostly interface
(g) 2DEG	Very high	Very high/unknown	×	REE	interface

1.5. Overview of this thesis

In this thesis, we present different charge-to-spin conversion materials prepared by incorporating non-metallic element (sulfur, oxygen, nitrogen, phosphorus) using low energy ion implantation in 5d transition metal Pt, non-metallic oxygen in Pt via sputtering, and finally $SrTiO_3$ based quasi-2DEG created by pulse laser deposition towards developing the next generation SOT-MRAM for low power consumption. While at the same time, we develop an understanding the angular symmetry of torques as well as the origin of enhancement of charge-spin interconversion, while studying these samples in detail.

First of all, in chapter 2, we discuss the various experimental methods for sample preparation such as ion implantation, DC sputtering and Pulse laser deposition. Then, we study the various material characterization techniques such as X-ray diffraction (XRD), Transmission Electron Microscopy (TEM),

Scanning Electron Microscopy (SEM), Electron Energy Loss Spectroscopy (EELS), and Atomic Force Microscopy (AFM), We explain the device fabrication and experimental method i.e., spin-torque ferromagnetic resonance (ST-FMR) and spin-pumping inverse spin Hall voltage (SP-ISHV) measurements.

Subsequently in chapter 3, we report a new spin Hall material designed by implanting low energy 12 keV non-metallic Sulfur ions in heavy Metal-Pt, named as Pt(S), which demonstrates 8-times higher conversion efficiency as compared to pristine Pt. In chapter 4, we extend such an approach of utilizing non-metallic element with low atomic number Z i.e., Oxygen in Pt (a host with large Z), to enhance the charge-to-spin conversion and understand the underlying mechanism of enhancement in SHE by using two different methods of doping Oxygen in Pt, via low energy ion implantation and sputtering. Furthermore, in chapter 5, as a trilogy to the low energy ion implantation, we explore another non-metallic element, Nitrogen by incorporating in Pt, and disentangle the intrinsic and extrinsic contribution of SHE.

In chapter 6, we add layers to our existing study of incorporating another non-metallic element phosphorus by 30 keV ion implantation in Pt, i.e., Pt(P). We present the feasibility of these spin Hall materials in terms of a candidate in SOT-MRAM. And finally, in chapter 7, we go beyond the ion-implanted Pt, and explore a new avenue, the quasi-two dimensional electron gases (q-2DEG) created at the interface of $SrTiO_3$/amorphous oxides. We observe a 1-2 times increase in charge-to-spin conversion, an order higher than our engineered HMs but with the additional challenges of unknown thickness of 2DEGs and high sheet resistance, R_s that depict the long road ahead for the oxide spintronics to create a paradigm shift in designing the next-generation SOC material for low power consumption in SOT-MRAM.

References for Chapter 1

1. K. Garello, F. Yasin, S. Couet, L. Souriau, J. Swerts, S. Rao, S. Van Beek, W. Kim, E. Liu, S. Kundu, D. Tsvetanova, N. Jossart, K. Croes, E. Grimaldi, M. Baumgartner, D. Crotti, A. Furnémont , P. Gambardella, G. S. KAr, *2018 IEEE Symposium on VLSI Circuits*, (2018).
2. I. M. Miron, G. Gaudin, S. Auffret, B. Rodmacq, A. Schuhl, S. Pizzini, J. Vogel, P. Gambardella, *Nat. Mater.* **9**, 230 (2010).
3. M. N Baibach, J. M. Broto, A. Fert, F. Nguyen Van Dau, F. Petroff, P. Etiennce, G. Creuzet, A. Friedrich, and J, Chazelas, *Phys. Rev. Lett.* **61**, 2472 (1988).
4. G. Binasch, P. Grünberg, F. Saurenbach, and W. Zinn, *Phys. Rev. B* **39**, 4828(R) (1989).
5. J. C. Slonczewski, *J. Magn. Mater*. **159**, L1 (1996).
6. L. Berger, *Phys. Rev. B* **54**, 9353 (1996).
7. Dynakov and Perel, *Phys. Lett*. **35,** 459 (1971).
8. J. Hirsch, *Phys. Rev. Lett.* **83,** 1834 (1999).
9. Y. K. Kato, R. C. Myers, A. C. Gossard, and D. D. Awschalom, *Science* **306**, 1910 (2004).
10. J. Wunderlich, B. Kaestner, J. Sinova, and T. Jungwirth, *Phys. Rev. Lett.* **94**, 047204 (2005).
11. T. Kimura, Y. Otani, T. Sato, S. Takhashi, and S. Maekawa, *Phys. Rev. Lett*. **98**, 156601 (2007).
12. R. Karplus and J. M. Luttinger, *Phys. Rev*. 95, 1154 (1954).
13. J. Smit, *Physica* 24, 39 (1958).
14. J. Smit, *Physica* 21, 877 (1955).
15. L. Berger, *Phys. Rev. B* **2**, 4559 (1970).
16. H. Moriya, A. Musha, S. Haku, and K. Ando, *Commun. Phys*. **5**, 12 (2022).
17. M. V. Berry, *Proc. R. Soc*. A, **392**, 45 (1984).
18. N. Nagaosa, J. Sinova, S. Onoda, A. H. MacDonald, and N. P. Ong, *Rev. Mod. Phys*. **82,** 1539 (2010).
19. Y. Niimi, and Y. Otani, *Rep. Prog. Phys.* **78**, 124501 (2015).
20. A. Manchon, H. C. Koo, J. Nitta, S. M. Frolov, and R. A. Duine, *Nat. Mater*. **14**, 871 (2015).
21. J. Nitta, T. Akazaki, H. Takayanagi, and T. Enoki, *Phys. Rev. Lett*. **78,** 1335 (1997).
22. L. Liu, T. Moriyama, D. C. Ralph, and R. A. Burhman, *Phys. Rev. Lett*. **106**, 036601 (2011).
23. Y. Wang, R. Ramaswamy, and H. Yang, J. Phys. D: Appl. Phys. **51**, 237002 (2018).
24. Y Niimi, H. Suzuki, Y. Kawanishi, Y. Omori, T. Valet, A. Fert, and Y. Otani, *Phys. Rev B* **89**, 054401 (2014).
25. M. Yamanouchi, L. Chen, J. kim, M. Hayashi, H. Sato, S. Gukami, S. Ikeda, F. Matsukara, and H. Ohno, *Appl. Phys. Lett*, **102**, 212408 (2013).

26. R. Ramaswamy, Y. Wang, M. Elyasi, M. Motapothula, T. Venkatesan, X. Qiu, and H. Yang, *Phys. Rev. Appl.* **8**, 024034 (2017).
27. M. –H Nguyen, C. –F. Pai, K. X. Nguyen, D. A. Muller, D. C. Ralph, and R. A. Burhman, *Appl. Phys. Lett*. **106**, 222402 (2015).
28. H. Mazraati, M. Zahedinejad, and J. Åkerman, *Appl. Phys. Lett*. **113**, 092401 (2018).
29. D. Wu, G. Yu, Q. Shao, X. Li, H. Wu, K. L. Wong, Z. Zhang, X. Han, P. K. Amiri, and K. L. Wang, *Appl. Phys. Lett*. **108**, 212406 (2016).
30. Y. Du, H. Gamou, S. Takahashi, S. Karube, M. Kohda, and J. Nitta, *Phys. Rev. Appl*. **13**, 054014 (2020).
31. W. F. Zhang, S. –H. Yang, Y. Sun, Y. Zhang, B. Yan, and S. S. P. Parkin, *Sci. Adv*. **2**, e1600759 (2016).
32. J. Sklenar, W. Zhang, M. B. Jungfleisch, W. Jiang, H. Saglam, J. E. Pearson, J. B. Ketterson, and A. Hoffmann, *AIP Advances* **6**, 055603 (2016)
33. D. MacNeill, G. M. Stiehl, M. H. D. Guimarães, R. A. Burhman, J. Park, and D. C. Ralph, *Nat. Phys*. **13**, 300 (2017).
34. M. H. D. Guimarães, G. M. Stiehl, D. MacNeill, N. D. Reynolds, and D. C. Ralph, *Nano Lett.***18**, 1311 (2011).
35. G. M. Stiehl, R. Li, V. Gupta, i. E. Baggari, S. Jiang, H. Xie, L. F. Kourkoutis, K. F. Mak, J. Shan, R. A. Burhman, and D. C. Ralph, *Phys. Rev B* **100**, 184402 (2019).
36. A. R. Mellnik, J. S. Lee, A. Richardella, J. L. Grab, P. J. Mintun, M. H. Fischer, A. Vaezi, A. Manchon, E. –A. Kim, N. Samarth, and D. C. Ralph, *Nature* **511**, 449 (2014).
37. K. Kondou, R. Yoshimi, A. Tsukazaki, Y. Fukuma, J, Matsuno, K. S. Takahashi, M. Kawasaki, Y. Tokura, and Y. Otani, *Nat. Phys.* **12**, 1027 (2016).
38. Y. Wang, R. Ramaswamy, M. Motapothula, K. Narayanapillai, D. Zhu, J. Yu, T. Venkatesan, and H. Yang, *Nano Lett.* **17**, 7659 (2017).

Chapter 2

Experimental Methods

The experimental methods and recipes used for the experiments that went into the work behind this thesis are presented in this chapter. We start with the ion implantation method and thin film deposition using DC sputtering method, followed by the characterization methods. Finally, we study the experimental techniques used for studying the charge-to-spin conversion in this thesis.

2.1. Thin Film preparation and Ion implantation

2.1.1. Thin film preparation: DC sputtering

DC sputtering is a method in which the material to be sputtered on the target is placed above the sputtering gun, which acts as a cathode. Whereas the sample holder (area where the sample is to be deposited) is the anode. A creation of potential difference between the anode and cathode allows a plasma to be created as shown in Fig. 2.1, and a strong electric field is applied to ionize the ions of an inert gas (argon etc.). In the onset of the ionization process, secondary electrons are generated which are accelerated with the help of electric field. The positively charged Argon ions with high energy strikes the target and knocks out the target atoms. The energy is transferred from the accelerated ions to the target atom leading to a long mean free path which provides them with enough energy to travel a long distance and reach the anode/substrate and deposit layer-by-layer forming a thin film. It is noteworthy to mention that during this deposition process, the gas ratio of Ar: O_2 can be altered to oxidize or change the deposition conditions of the material (We will explore this in detail in chapter 4).

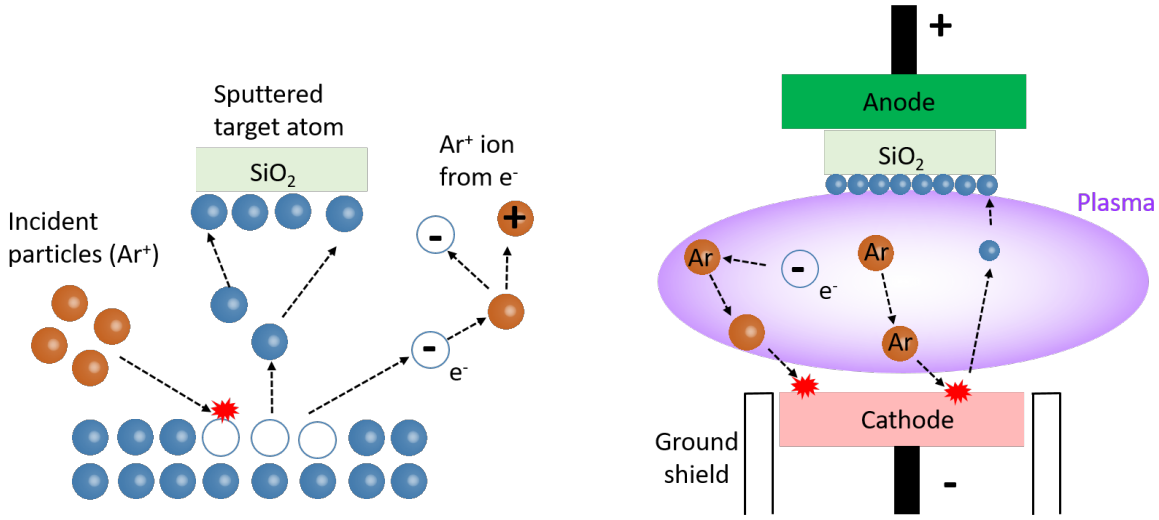

Figure 2.1. (a) Schematic of the DC sputtering process, and visualization of thin film deposition by sputtering method where plasma (purple ellipse) is created between cathode and anode.

2.1.2. Basics of ion implantation

Ion implantation is a process in which ions of a particular desired element are accelerated into a target. The main prerequisites of the ion implantation are the choice of ion, energy, dose and incident angle. The energy, dose, incident angle is pre-simulated using a software such as Stopping of Range of ions in Matter (SRIM 2008) for a particular element to optimize the experimental conditions. Ion Implantation consists of an ion source, in which the choice of ions can be altered, and an accelerator to electrostatically accelerate the ions to a high energy (see Fig. 2.2). The energy in kV is used for plasma to accelerate the ions. By adjusting the magnetic field strength of the bending magnet, the ions are selected and filtered out and focused using a lens. To catch the charged particle in vacuum, an amount of current is needed (in μA) for faraday cup using the current integrator.

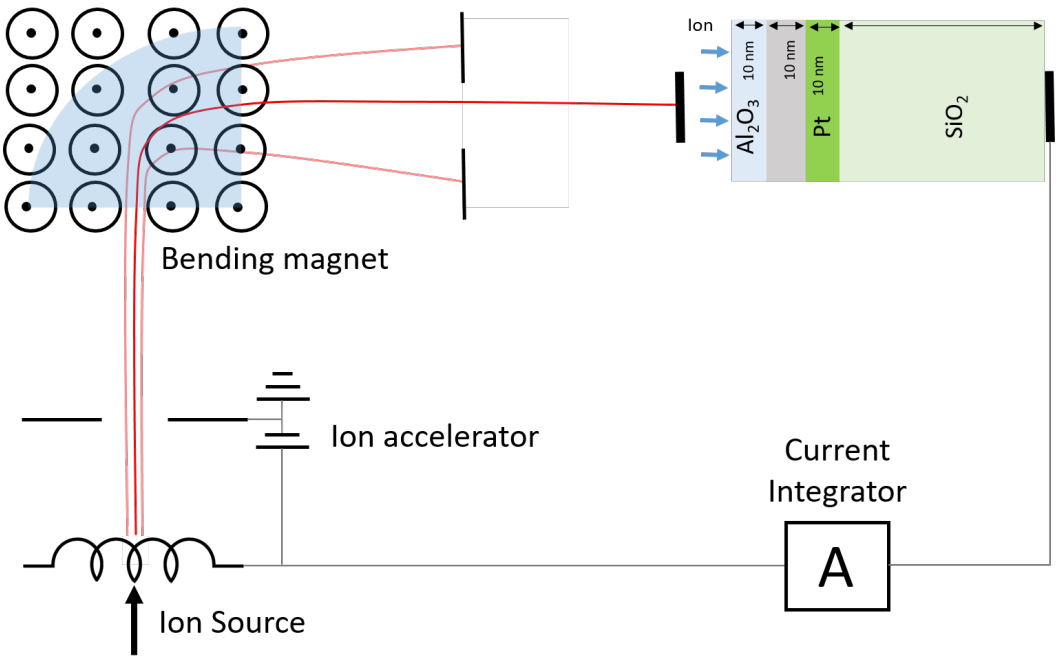

Figure 2.2. Basics of Ion implantation method. The bending magnet allows the ion beam to converge at the sample.

2.1.3. Ion implantation I: 30 kV ion accelerator/implanter

The present ion implantation used in the thesis for chapter 3, 4, 5 was carried out using a 30 kV ion accelerator/ implanter (Fig. 2.3) installed at the Inter-University Accelerator Centre (IUAC), New Delhi. This system comprises of an ion source, a cold plasma-based Penning ion generator, assembled in a nylon housing and connected to a 30 kV power supply which is capable of delivering a stable current of up to 350 µA. An Einzel lens and an electrostatic quadrupole are used for focusing the ion beams. The required ions are selected by adjusting the magnetic field strength of a bending magnet which provides a uniform, variable field of 0.21-0.35 T. The ion beam spot size of 15 × 15 mm^2 can be scanned upon the target in the implantation chamber having a vacuum of 1.3×10^{-4} Pa. The choice of ions can be changed from the tube which is connected to the source chamber. For sulfur ion implantation, carbon disulfide is poured into the tube which separates into carbon and sulfur. Sulfur gets dissolved in the solution while carbon remains undissolved. For oxygen and nitrogen, oxygen and nitrogen gas cylinders are used respectively.

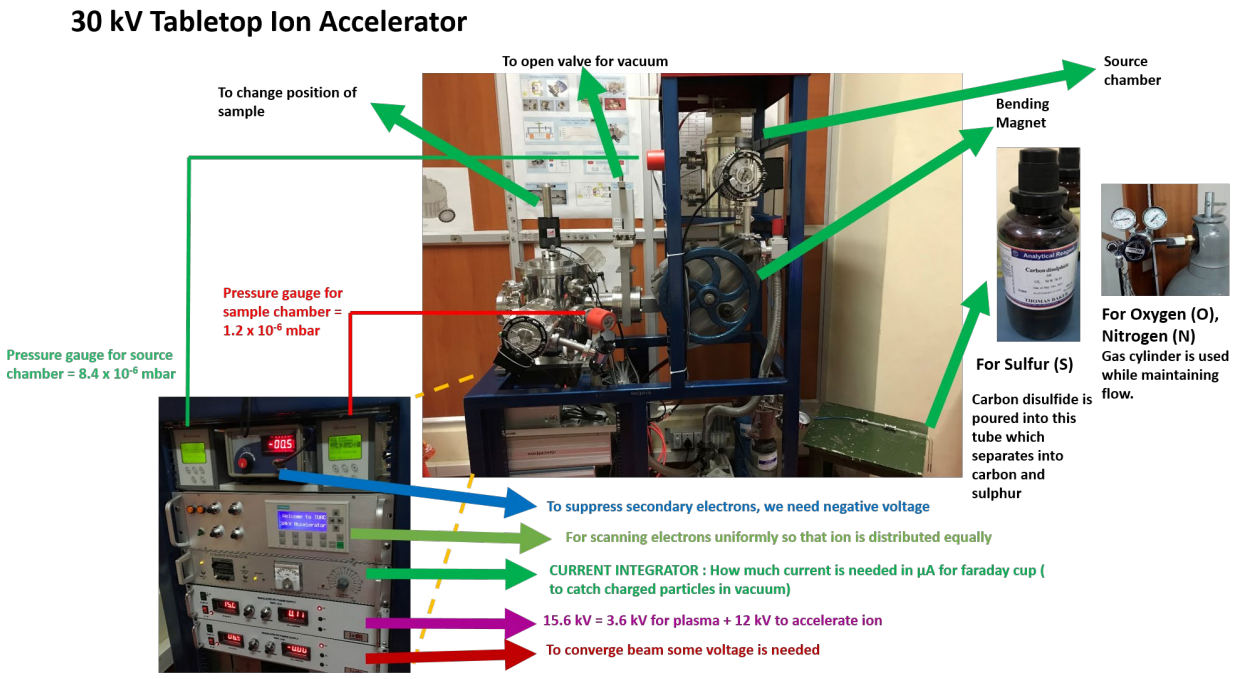

Figure 2.3. 30 kV ion accelerator/implanter at the Inter-University Accelerator Centre (IUAC).

2.1.4. Ion implantation II: IMX -3500

The ion implantation used in chapter 6 is carried out using the IMX-3500 manufactured by ULVAC, which can deliver a wide range of 10-200 kV energy in a target spot beam size of a wafer of diameter 8 inches (~200 mm) allowing a large number of wafers to be loaded at the same time. A picture of the commercial available IMX-3500 is shown in Fig. 2.4.

Figure 2.4. A picture of commercially available IMX-3500 medium Ion Implanter.

2.2. Thin film characterization

The surface morphology and crystallographic properties are studied using X-ray diffraction (XRD), transmission electron microscopy (TEM). The devices are then patterned into rectangular stripes for device fabrication.

2.2.1 X-ray diffraction

In a crystal, the atomic planes cause the incident beam of X-rays to interfere as they are reflected from the crystal. This is known as the X-ray diffraction (XRD). Initially started in the 1950s, the XRD has been extensively used to investigate the crystal orientation, and thereby find the spacing and lattice constant of a crystal solid. One of the most useful take-away from the XRD is its non-destructive nature, which reveals the atomic arrangement in a crystallized material.

When high speed electrons collide with a metal target (usually copper), it leads to production of X-rays. Usually, two different wavelength of X-rays can be generated, 1.54050 Å and 1.54434 Å (Cu Kα-1 and Cu Kα-2). According to the principle of XRD, based on the Bragg's law, the wavelength of the X-rays, λ multiplied with the integer, say β can be expressed as:

$$2d \cdot sin\theta = \beta\lambda, \tag{2.1}$$

Where d is the space between two atomic layers, while θ is the Bragg incidence angle, as depicted in Fig. 2.5. Upon satisfying the Bragg's law condition of constructive interference from planes with space distance d, a diffraction occurs. We can therefore utilize XRD to study the crystallographic properties of the material.

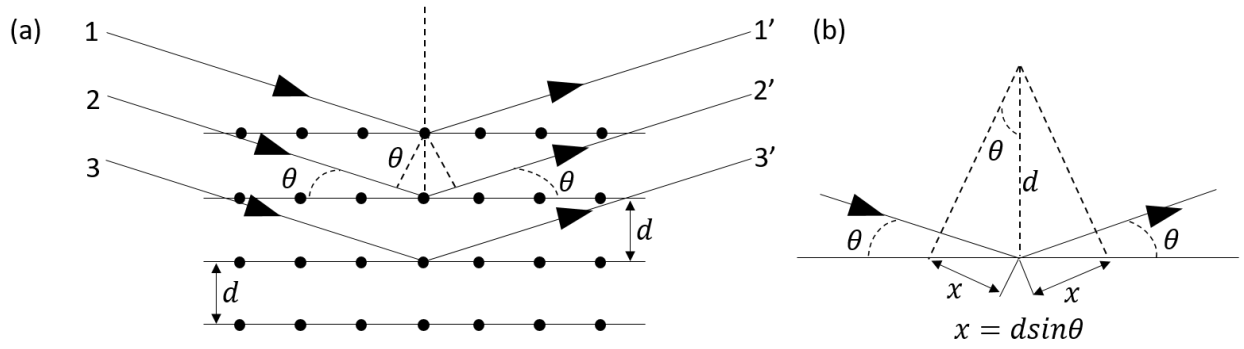

Figure 2.5. (a) X-ray diffraction diagram and its principle based on Bragg's law. Interference of X-rays occur as it gets reflected from different atomic planes with space distance d in a crystal material.

2.2.2. Scanning electron microscope (SEM)

To study the surface morphology and analyze the roughness of the sample, a powerful tool is the Scanning electron microscope (SEM). It is basically an electron microscope that produces image of samples by utilizing the beam of electrons scanned at the surface of sample. The SEM comprises mainly of an electron microscope, a signal collection and processing system, a display for viewing and saving image, and finally a vacuum system. A schematic of SEM is shown in Fig. 2.6. The electron gun has a tungsten filament which emits an electron beam. The beam is accelerated by an electric field, to increase the kinetic energy so that it can pass through the two condenser lens to focus in a small spot. There are deflection coils embedded in the system which can deflect the focused beam in both vertical and horizontal direction to allow a scan of the sample in a rectangular fashion. Upon interaction of the electron beam with the sample, there is an emission of backscattered electrons, secondary electrons, Auger electrons and characteristic X-rays. The secondary electrons having low energy ranging less than 50 eV are generally used to image the morphology of the sample. While the characteristic X-rays are used for determining the elemental composition of the specimen. These emissions are detected by suitable detectors to investigate the morphology and composition of sample.

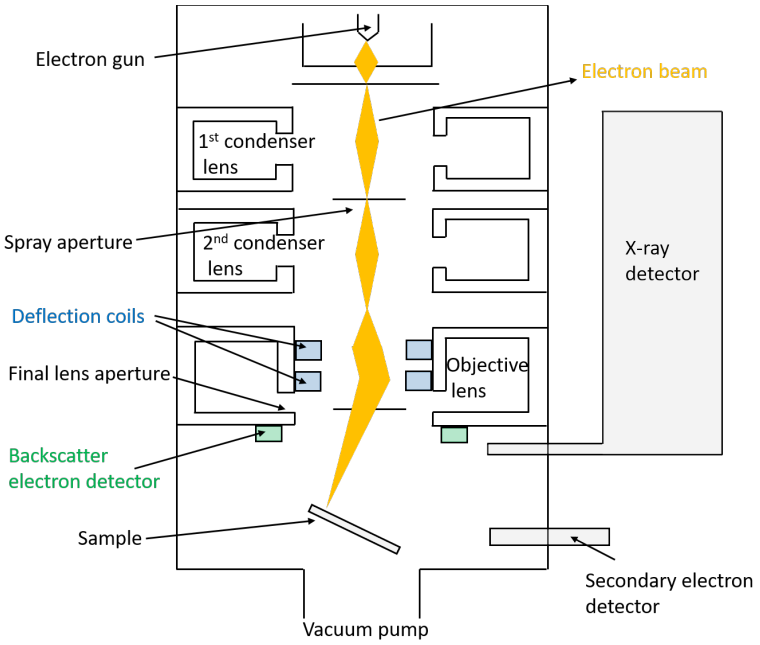

Figure 2.6. Scanning electron microscope (SEM). The electron beam is displayed in orange color emitted from electron gun. Beam is deflected by two condenser lens (1st and 2nd) and focused onto the sample.

2.2.3. Transmission electron microscope (TEM)

Another type of electron microscope that can help in understanding the crystallographic properties is the TEM. A TEM operates by accelerating a beam of electrons to sufficient energy so that electrons get transmitted through the sample when incident on it. The basic components of TEM are: electron gun, gun alignment controller, condenser lenses 1st and 2nd (magnetic lens to collimate beam), objective lens (for magnification and focus), apertures (to control diameter of electron beam), intermediate lens, projective lens, sample holder, view screen, and detectors. Figure 2.7 shows the schematic of the conventional TEM instrument.

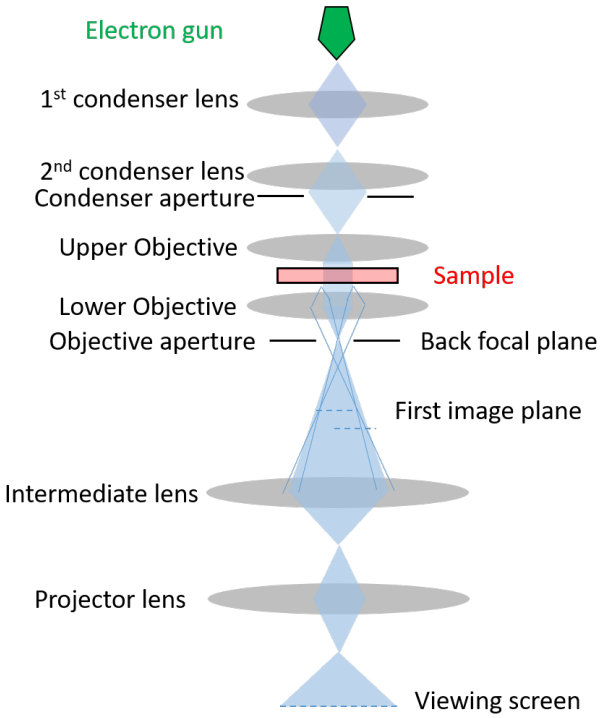

Figure 2.7. Schematic of a conventional TEM. Image is reproduced from J. Sloan, Online Lecture Notes, The University of Warwick (2014).

2.2.4. Atomic force microscopy (AFM)

Atomic force microscopy (AFM) is a powerful tool that can provide micron lateral-scale maps of surface topography with nanometer resolution. A 3D image of the sample surface is created from the reaction of the probe to the forces between probe tip and sample surface. A schematic diagram of the working principle of AFM is shown in Fig. 2.8. An AFM typically consists of a sharp tip (probe), photo-diode and laser to detect the deflection of cantilever, a feedback control system to monitor and control cantilever deflection, a piezoelectric actuator to move the sample, and finally a display system. A sharp tip is mounted on a soft spring like cantilever. The cantilever is held to its position using a rigid support while a piezoelectric element is used to agitate the cantilever at a specific frequency. The sample is mounted on a stage to enable the movement in all the three x, y, z direction.

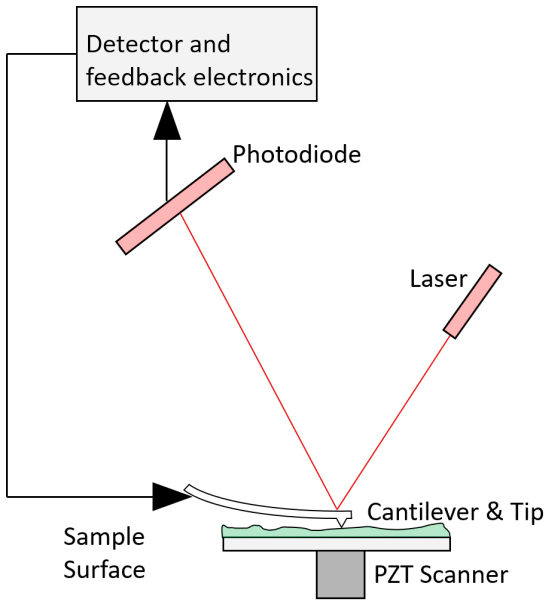

Figure 2.8. Typical block diagram of the set-up of an AFM. The cantilever and tip approaches the sample and forms a 3D surface morphology investigation of sample.

2.2.5. Device fabrication

I. Washing the sample. First the wafer is washed in acetone for 5 minutes, followed by Isopropyl alcohol for 5 minutes and then in water for 1 minute. Then the samples are blown dry using air gun. The entire washing process is performed in an ultrasonicator located in a clean room inside a draft chamber.

II. Spin Coating. This process is performed immediately after washing the samples to prevent any dust particles from adhering to the sample. Spin coating is a process in which the substrate is coated with a photoresist of desired thickness to make patterns using microfabrication. Firstly, a small amount of adhesive promoter or primer i.e., (OAP) is dropped on the substrate using a dropper and then spin coated (using the recipe shown in table 2-I) for 1 minute. Then, the sample is immediately pre-baked at 80°C on a hot plate for 1 minute followed by cooling for 30 seconds. Next, the same sample is coated with a positive photoresist (AZ-1500 38CP) and then spin coated for 1 minute followed by pre-baking on hot plate for 1 minute and then cooling for 30 seconds. The positive resists are those in which the dark part which is covered using a pattern remains while the uncovered bright part is removed/dissolved using developing.

Table 2-I. Spin coating recipe (where rpm is rotation per minute).

No.	Rotation/slope	Time (seconds)
0	300 rpm	5 sec
1	slope	10 sec
2	4000 rpm	20 sec
3	6000 rpm	0.2 sec
4	slope	10 sec

III. Mask less photolithography and electrode deposition

Once the samples are spin coated, the AutoCAD and PALET machine DDB-701 is used to make the pattern for spin-torque ferromagnetic resonance (ST-FMR) devices. We will discuss ST-FMR in next section. The first pattern i.e., rectangular stripes using mask less photolithography. Following this, the samples are developed in NMD for 1 minute and washed immediately in clean running water for 1 minute. After confirming a distinct pattern using optical microscope, the multilayer stack is patterned into a rectangular stripes using Ar^+ ion milling. After milling, the sample is washed and spin coated (as explained earlier in Step I, II) and then the second pattern of coplanar waveguide (CPW) is made using photolithography followed by developing using NMD. Then again, the alignment of CPW and rectangular stripe is checked using optical microscope. Finally, Ti (10 nm)/Al (200 nm) electrode is deposited on either side of the rectangular stripes using DC sputtering of 50 W and 100 W DC power respectively for Ti and Al. The samples are then washed in acetone to get the final device. The entire device fabrication process is shown in Fig. 2.9. pictorially.

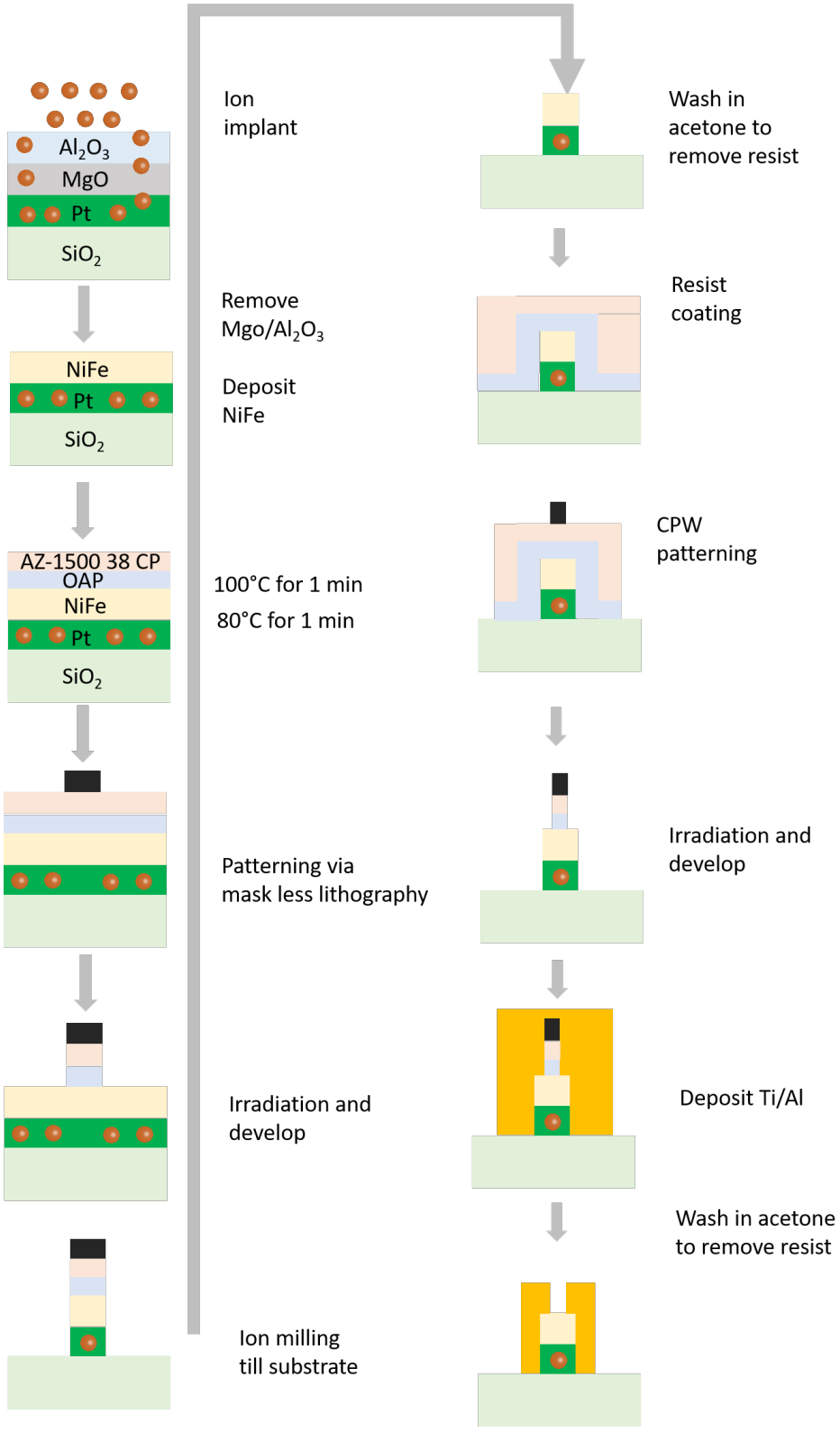

Figure 2.9. Flowchart of the process used to fabricate ST-FMR devices.

2.3. Measurement techniques

2.3.1. Spin torque ferromagnetic resonance (ST-FMR) measurements

For the study of charge-to-spin conversion and its associated properties, the devices prepared using lithography were measured using ST-FMR measurements. The devices used for ST-FMR are typically a heavy metal (HM)/ferromagnet (FM) bilayer. In this method, the rectangular device (HM/FM) is excited with a microwave current I_{rf} along the longitudinal direction of varying frequency with an applied power using a MXG Analog Signal Generator (N5183A) (see Fig. 2.10). The I_{rf} applied in HM through CPW generates a spin current density, $\boldsymbol{j_s}$ which exerts a damping-like torque, $\boldsymbol{\tau_{DL}}$ (we will discuss in detail in chapter 3). Simultaneously, the I_{rf} generates an Oersted field h_{rf}, which exert an out-of plane Oersted field torque (τ_{OFT}). While at the same time, an in-plane magnetic field H_{ext} is swept at an angle ϕ with I_{rf} direction. Once the Larmor precession frequency from the device matches with the input frequency, a resonance condition is attained. Upon meeting the resonance condition, both $\boldsymbol{\tau_{DL}}$ and $\boldsymbol{\tau_{OFT}}$ drive the magnetization precession, resulting in a periodically varying ΔR due to anisotropic magnetoresistance (AMR) of FM (here NiFe). The mixing of ΔR and I_{rf} produces a DC voltage V_{mix}, which is recorded using a LI-5640 Digital Lock-in Amplifier via a bias tee. The amplitude of microwave signals is modulated with a frequency of 79 Hz. Sometimes, an additional DC, I_{DC} is also applied along with I_{rf} to measure V_{mix} using R6161 Advantest DC current source as shown in Fig. 2.10. An analysis of such a spectrum will be discussed first in chapter 3. For low temperature ST-FMR measurements, the sample is placed inside a cryogenic probe station that uses a He compressor for reaching temperatures down from room temperature to 10 K.

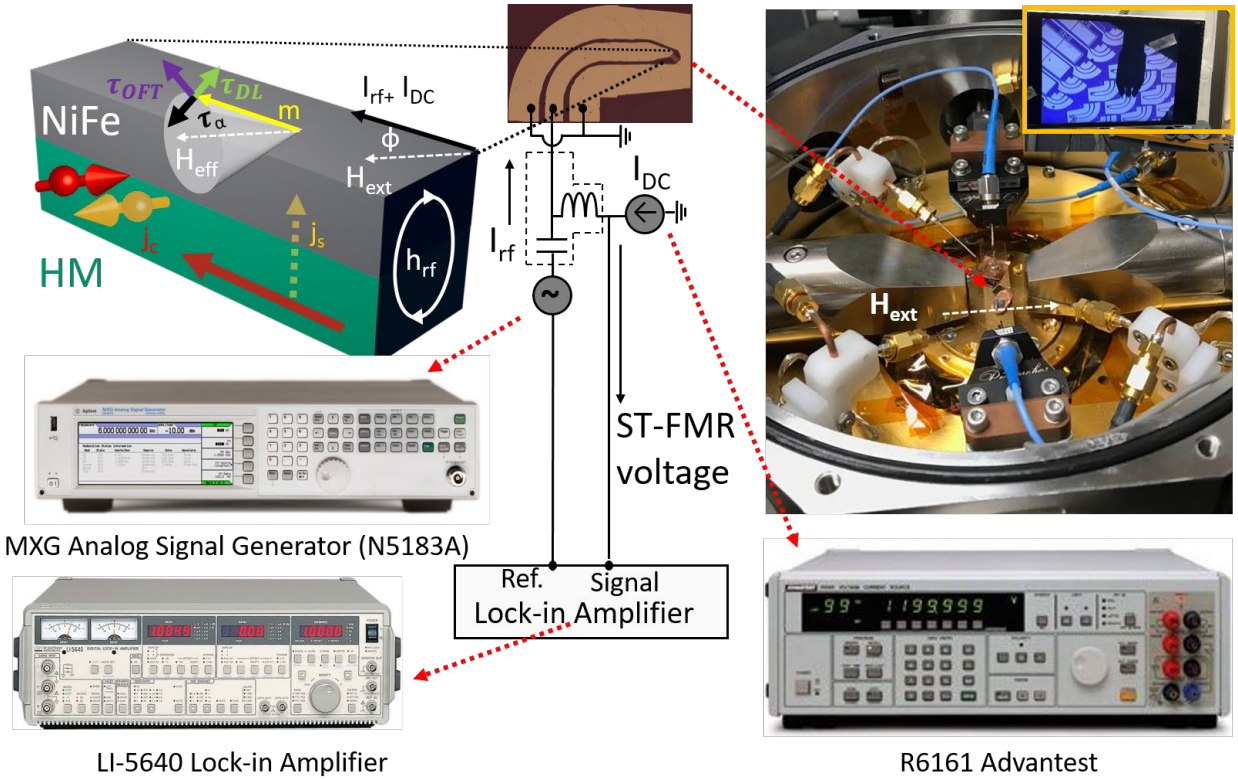

Figure 2.10. Experimental set-up of ST-FMR measurements. Left panel shows the detection principle of the ST-FMR. Right panel shows the cryogenic probe station where the sample is placed in vacuum and a static magnetic field H_{ext} is applied. The inset in top right panel shows the microwave tip connected to device for applying I_{rf}.

2.3.2. Spin-pumping Inverse Spin Hall voltage measurements (SP-ISHV)

For the study of spin-to-charge conversion (see chapter 3 for details), the SP-ISHV measurements were performed using an out-of plane h_{rf} excited device as shown in Fig. 2.11. In this, an I_{rf} is applied close to the length of the device through CPW using a MXG Analog Signal Generator (N5183A) while a careful alignment of H_{ext} at ϕ = 90° or 270° respect to I_{rf} to I_{rf} is made to minimize the unwanted contribution from AMR. The h_{rf} starts the magnetization precession in FM (here NiFe) and passes the $\boldsymbol{j_s}$ to HM which gets converted to $\boldsymbol{j_c}$ via inverse spin Hall effect. The $\boldsymbol{j_c}$ is detected in the form of an ISHE voltage through the device via LI-5640 Lock-in Amplifier across the ends of rectangular pads. A typical SP-ISHV measurement set-up is shown in Fig. 2.11.

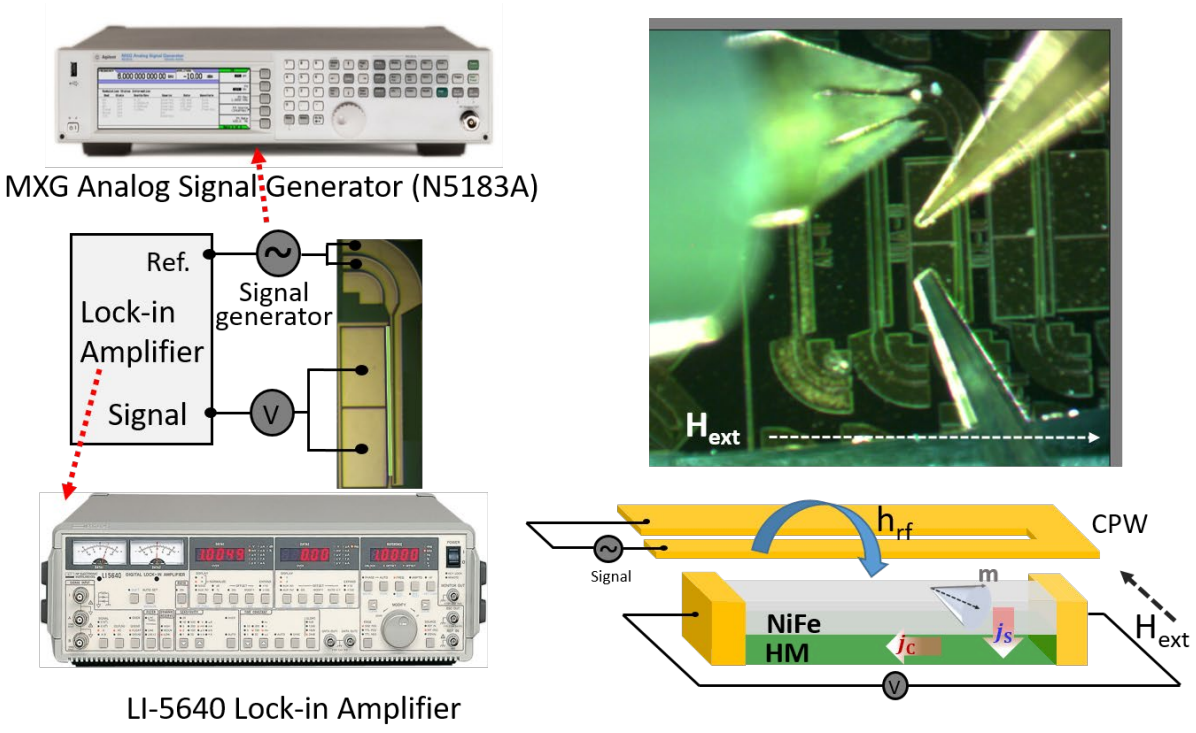

Figure 2.11. Experimental set-up of SP-ISHV measurements. Left panel shows the detection principle of the ISHE. Top right panel shows the I_{rf} applied along the length of device with an external magnetic field at an angle of 90°.

Chapter 3

Enhanced spin Hall effect in S-implanted Pt

(This chapter is based on the results published in Adv. Quantum Technol. Paper 1 [Ref. 40], and it appears here as a modified version)

In chapter 1, we discussed about the various candidates for the SOC material in SOT-MRAM. Due to the combination of high θ_{DL} and considerable conductivity σ_{xx}, we extend the approach of incorporating non-metallic element in Pt, but with less explored approach of ion implantation.

3.1. Introduction

The recent development in the spin-orbit torque magnetic random-access memory (SOT-MRAM) by utilizing the spin Hall effect (SHE) [1-4] arising from spin-orbit coupling (SOC) has been attracting much attention due to its low power consumption and efficient magnetization switching [4]. The modification of SHE to switch the magnetization has led to tremendous development in the low power consumption of SOT-MRAM [5]. Typically, in a heavy metal (HM)/ ferromagnet (FM) system, a charge current density $\boldsymbol{j_c}$ in HM is converted to $\boldsymbol{js}$ via SHE, which then exerts an in-plane damping-like torque on the magnetization of the adjacent FM [6]. This conversion of charge to spin current density is given as $\boldsymbol{j_s} = \frac{\hbar}{2e}\theta_{DL}(\boldsymbol{j_c} \times \boldsymbol{\sigma})$, where θ_{DL} is the spin Hall angle (or charge-to-spin conversion or the damping-like torque efficiency) and $\hbar$ is reduced Planck constant, e is the elementary charge and $\boldsymbol{\sigma}$ is the spin polarization vector. There have been tremendous efforts to find a suitable HM exhibiting high θ_{DL}. With the strength of SOC depending on Z^4 (Z is the atomic number) [6], 5d transition metals (HM) have been explored to maximize the SHE. However, the value of θ_{DL} for the HM has been around 0.1 only (see Fig. 3.1). The control of resistivity (ρ_{xx}) or conductivity (σ_{xx}), along with high θ_{DL} is also important in the overall high spin Hall conductivity, σ_{SH}^{xy} ,

which becomes useful to circumvent the issues of separating the write path from the read path in SOT-MRAM [5] as explained in Chapter 1.

Maximizing θ_{DL} requires a combined effort of first picking an amenable HM such as Pt, with a large intrinsic SHE and then increasing its SHE via interface modification, alloying, defects, oxidation and varying deposition . The interface modification can arise in HM with low thickness or in non-equilibrium state. To date, Pt is the more explored HM based spin Hall material (SHM) due to its large spin-orbit interaction and high conductivity [8-12] and has been previously engineered by oxidation [13], varying deposition conditions [14], and alloying with other metals [15-22]. For example, θ_{DL} is shown to be improved marginally from 0.044 $\rightarrow$ 0.059 by oxygen incorporation in Pt [13] and by varying deposition conditions. Rigorously studied 5d transition metal Pt-based alloys in combination to a variety of FM showed wide distribution in θ_{DL} values (in parentheses) like $Pt_{53}Au_{47}$/NiFe (0.33 ± 0.09) [15], $Pt_{75}Au_{25}$/Co (0.35) [16], $Pt_{75}Pd_{25}/Fe_{0.6}Co_{0.2}B_{0.2}$ (0.26 ± 0.02) [17], $Pt_{45}Pd_{55}$/NiFe (0.06) [18], $Pt_{90}Pd_{10}/Y_3Fe_5O_{12}$ (0.17) [19], $Pt_{85}Hf_{15}$/Co (0.16 ± 0.01) [20], $Pt_{92}Bi_8/Y_3Fe_5O_{12}$ (0.106 ± 0.005) [21] and $Pt_{28}Cu_{72}$/NiFe (0.07 ± 0.002) [22].

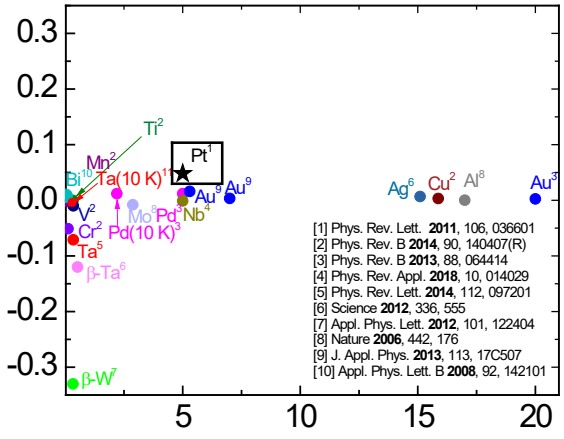

Figure 3.1. Room temperature θ_{DL} as a function of σ_{xx} for various 5d transition metals. The value of Pd is reported at both room temperature and 10 K.

Alternatively, non-metallic elements (impurities with smaller Z) have been incorporated into 5d transition metals (host with larger Z). The difference in Z between the host and the impurity has been found

to result in an enhancement of SHE [23]. However, in this respect, ion-implantation or irradiation-based engineering is not studied to tune the conversion efficiency of Pt despite being capable of molding spin-based properties such as local control of magnetization dynamics in NiFe/Pt [24], and reduced critical current for switching in Pt/Co/Ta [25]. So, in this work, we utilized the novel approach of ion implantation to tune the θ_{DL} by using a low energy 12 keV S ion implantation.

3.2. Experimental details

Multilayer stack of Pt (10 nm)/MgO (10 nm)/Al_2O_3(10 nm) was deposited on Si/SiO_2 substrates at room temperature using ultra high vacuum magnetron sputtering with base pressure ~ 5 $\times 10^{-7}$ Pa. Polycrystalline Pt layer was deposited at DC power of 50 W and Ar gas pressure of 1 Pa. Then the sample was transferred to an oxide deposition chamber for preparing MgO and Al_2O_3 capping layers under partial pressure of Ar and O_2 gas. Secondly, the samples were implanted with 12 keV S-ion beam at a fluence of 5×10^{16} ion/cm^2. The selected 12 keV energy of S-ions was pre-simulated using the Stopping of Range of ions in Matter (SRIM 2008). Note that the two capping layers of Al_2O_3 and MgO were purposefully deposited for two-fold benefits (1) least perturbation of target-Pt layer while attaining throughout S-distribution and (2) precise ion-milling in follow-up step as MgO provides good end-point-detector signal whereas Al_2O_3 protects hygroscopic MgO from self-sputtering in S-implantation process. Then deposited Pt/MgO/Al_2O_3 stacks were implanted with 12 keV-S ion-beam using 30 kV Tabletop Accelerator system. The optimized beam spot size of 15 × 15 mm^2 was used for the implantation in the samples with size of 10 mm × 10 mm.

The deposited multilayer stack of Pt (10 nm)/ MgO (10 nm)/ Al_2O_3 (10 nm) were implanted with 12 keV S ion beam, as shown in Fig. 5 (a). The two protective layers (MgO and Al_2O_3) were deposited above Pt for the following two reasons: First, the protective layers allowed the least disturbance to the target Pt layer while ensuring the uniform distribution of S ions in Pt. Second, the MgO provides a good end-point detector signal during the Ar^+ ion milling whereas Al_2O_3 protects the hygroscopic MgO from self-sputtering

in the implantation process. Then, oxide capping layers of MgO and Al_2O_3 were removed by ion milling and top FM layer of NiFe (5nm) was then sputtered on these samples (See Fig. 3.2).

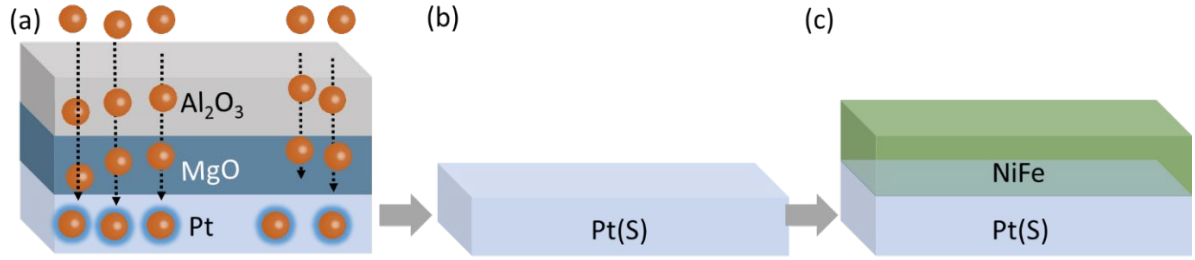

Figure 3.2. Ion implantation method: (a) Visualization of ion implantation followed by removal of protective layers (b) and (c) after the deposition of NiFe on top of Pt.

3.2.1. Material characterization

Cross-section transmission electron microscopy (TEM) image of pristine (Fig. 3.3 (a)) and implanted sample (Fig. 3.3 (b)) clearly shows no significant change in interface quality and total thickness of target Pt layer. Further, high-resolution images in Fig. 3.3 (c) and Fig. 3.3 (d) indicate no visible loss in the polycrystallinity of Pt(S) as compared to pristine Pt deposited in fcc structure (see Fast Fourier Transform analysis in respective insets). Further, energy filtered electron energy loss spectra (EELS) maps of host Pt ($O_{2,3}$ edge, 51.7 -63.7 eV) and Implanted-S ($L_{2,3}$ edge, 165-182.1 eV) are shown in 3.3 (e) and 3.3 (f) respectively. Referring to Fig. 3.3 (f), we can see that the majority of S-ions are stopped at capping MgO/Al_2O_3 layer and the remaining ions are well dispersed throughout the target Pt layer, in agreement with TRIM simulations. The cross section of S and Pt were converted into atomic percentage based on the standard EELS spectra of the corresponding elements using the Gatan Microscopy Suite Software. The ratio of the S/Pt cross section with depth profile is given in the Fig. 1(g) and the percentage of implanted S in Pt(S) layer is estimated to be ~10%.

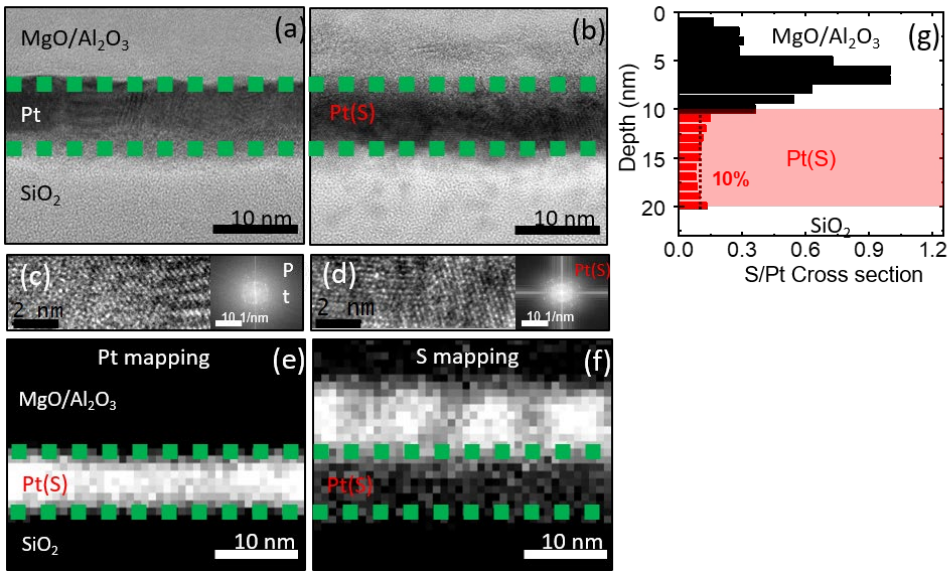

Figure 3.3. Cross-sectional TEM image of (a) pristine $Si/SiO_2/Pt/MgO/Al_2O_3$ stack and (b) implanted $Si/SiO_2/Pt(S)/MgO/Al_2O_3$ stack unveil relatively no change in interface quality and thickness of target layer. High-resolution TEM shows polycrystalline nature of (c) Pt and (d) Pt(S)-layer. Inset shows respective Fast Fourier transform analysis. EELS elemental-mapping of (e) target-Pt and (f) implanted-S distribution in $Si/SiO_2/Pt(S)/MgO/Al_2O_3$ stack. (g) Histogram showing average atomic percentage of sulfur in platinum quantified by depth dependent S/Pt cross section.

3.3. Room temperature ST-FMR measurements

To study the charge-to-spin conversion in Pt(S), ST-FMR measurements (see Fig. 3.4(a)) were performed by applying microwave signal (f = 5 to 11 GHz) at 15 dBm in the presence of varying in-plane magnetic field (H_{ext} = -200 to +200 mT) at ϕ = 45°. The applied microwave signal generates oscillating H_{rf} and simultaneously converted oscillating spin current exerts respective Oersted field torque and SOT on local magnetization of the NiFe layer which collectively drive the magnetization dynamics, as depicted in 3.4(b)). Upon satisfying a resonance condition, magnetization precession leads to a time-dependent change in resistance due to the anisotropic magnetoresistance (AMR) of NiFe. The mixing of microwave current and oscillating resistance produces rectified DC voltage signal. Typical frequency dependent-rectified voltage spectra (V_{mix}) are plotted in Fig. 3.4 (c), for both Pt/NiFe and Pt(S)/NiFe samples. The V_{mix} can be

expressed as $V_{mix} = SF_{sym}(H_{ext}) + AF_{asym}(H_{ext})$ where $F_{sym} = \frac{\Delta H^2}{\Delta H^2 + (H_{ext} - H_o)^2}$ defines an symmetric Lorentzian component and $F_{asym} = \frac{\Delta H\,(H_{ext} - H_o)}{\Delta H^2 + (H_{ext} - H_o)^2}$ is an antisymmetric Lorentzian component, where S and A to be their weight factors, respectively, ΔH is the half width half maxima (HWHM) and the H_o is the resonance field [13, 28]. As shown in Fig. 2 (c), reversing the H_{ext} direction changes the sign of the V_{mix} signal as expected for spin-Hall voltage. A decrease in the amplitude of the V_{mix} signal for Pt(S)/NiFe as compared to Pt/NiFe is observed, as reported for Pt(O) [13] and Cu(O) [29]. The values of ΔH as a function of applied microwave frequency f are plotted in Fig. 3.4(d). The effective Gilbert damping parameter α is estimated, using $\Delta H = \Delta H_o + \frac{2\pi}{\gamma}\alpha f$, from the slope of the linear frequency dependence. Here, ΔH_o is the inhomogeneous line broadening. The estimated value of α, for Pt(S)/NiFe (0.0280 ± 0.0003) is larger than that for Pt/NiFe (0.0118 ± 0.0003), which indicates an enhanced spin injection into the Pt(S) layer. The variation of H_o as a function of f for Pt/NiFe and Pt(S)/NiFe is plotted in Fig. 2(e) and the effective magnetization ($\mu_o M_{eff}$) is estimated using Kittel equation, $f = \gamma/2\pi \sqrt{H_o(H_o + M_{eff})}$. The value of $\mu_o M_{eff}$ is reduced from 965 mT (for Pt/NiFe) to 778 mT (for Pt(S)/NiFe). This reduction in $\mu_o M_{eff}$ can be understood in terms of an interface-perpendicular magnetic anisotropy [30].

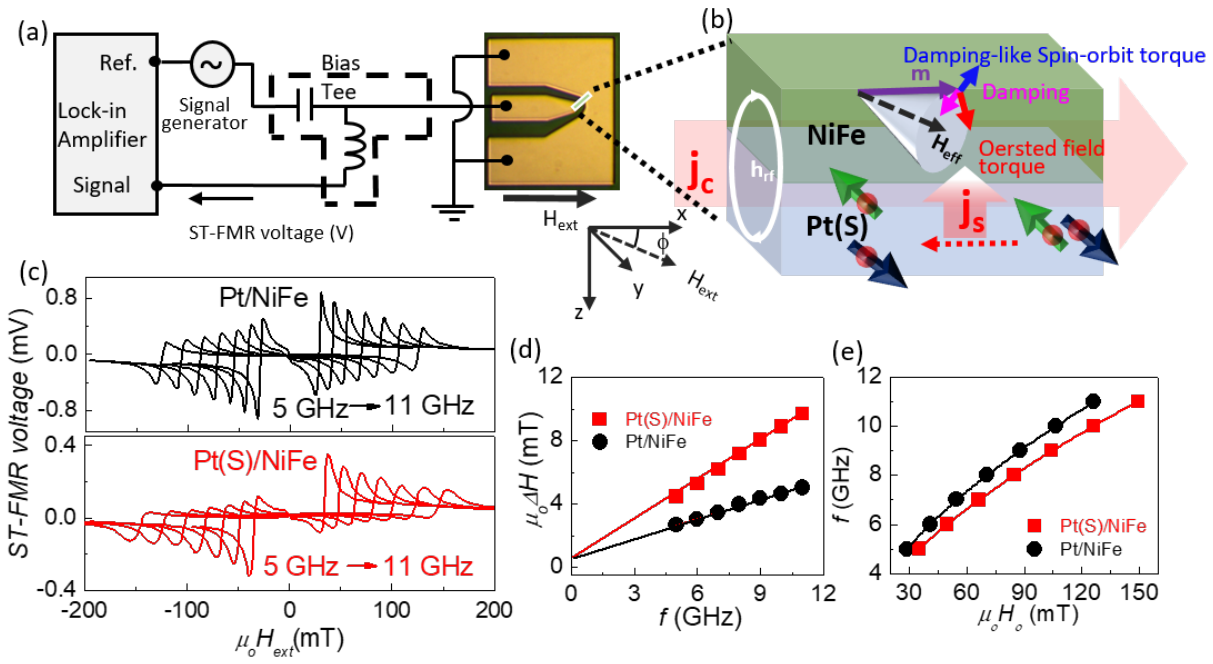

Figure 3.4. Schematic illustration of a) ST-FMR detection with optical image of micro-device and b) SHE induced spin-torque effect. c) Frequency-dependent V_{mix} spectra for Pt/NiFe and Pt(S)/NiFe. d) ΔH versus *f* with linear fit (solid lines). e) *f* versus H_o with Kittel equation fit (solid lines).

The symmetric and anti-symmetric components of the V_{mix} signal obtained at $f = 9$ GHz for Pt/NiFe and Pt(S)/NiFe are plotted in Fig. 3.5 (a) and 3.5 (b), respectively. The weight factor $S = \frac{\hbar J_S}{2e\mu_o M_S t}$ is proportional to the damping-like SOT, which is exerting an in-phase component with the magnetization precession, and the weight factor $A \approx \frac{J_C d}{2}\sqrt{1+\left(\frac{4\pi M_{eff}}{H_o}\right)}$ is attributed to the Oersted field torque exerting an out-of-phase component with it. Here e is electron charge, μ_o is permeability of the free space, t is thickness of the NiFe layer and d is thickness of the Pt or Pt(S) layer. A sharp increase in the relative amplitude of symmetric component for Pt(S) compared to Pt implies an increase of damping-like torque due to larger ***JS***. Furthermore, the ratio of injected ***JS*** to applied ***JC*** which effectively determines the conversion efficiency of SHM is given as $\theta_{DL}^{LS} = \frac{S}{A}\frac{e\mu_o M_S t d}{\hbar}\sqrt{1+\left(\frac{4\pi M_{eff}}{H_o}\right)}$ [13,28,29]. Figure 3.5 (c) shows the

estimated values of frequency invariant θ_{SH}^{LS} with average 3 times increase from 0.092 ± 0.008 (Pt) to 0.276 ± 0.011 (Pt(S)) after S implantation.

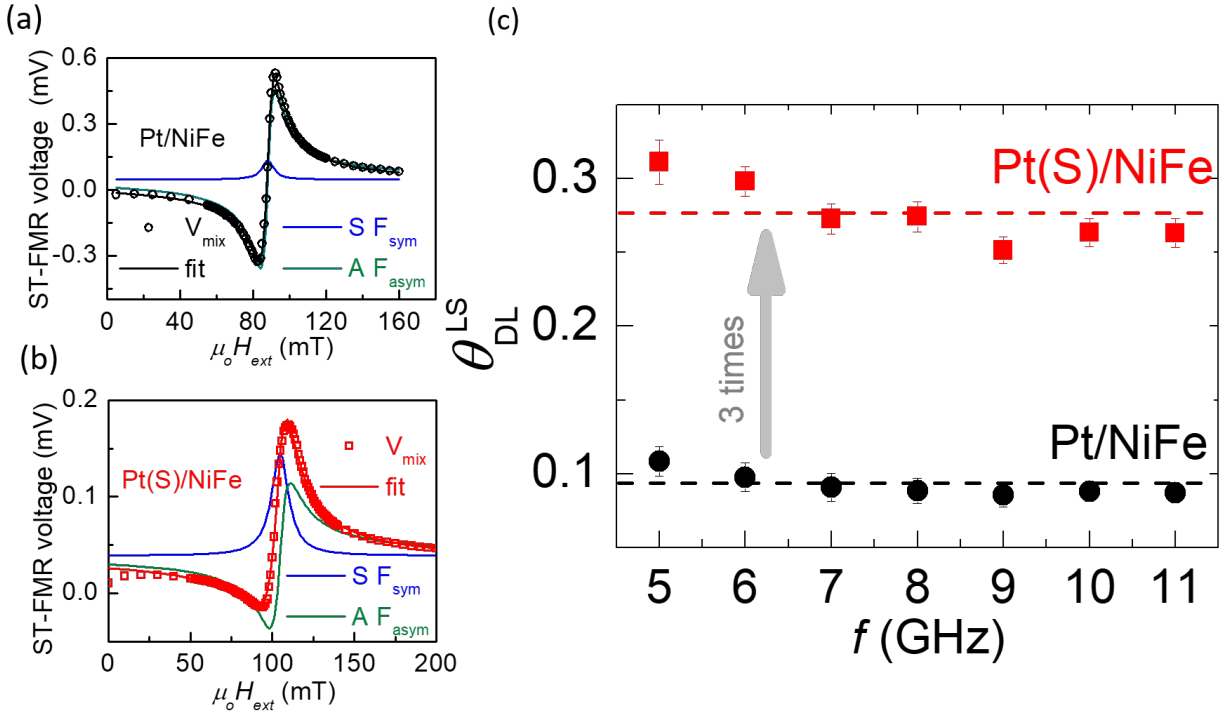

Figure 3.5. Lorentzian fitting of ST-FMR spectra for a) Pt/NiFe and b) Pt(S)/NiFe into symmetric (blue) and antisymmetric (green) components. c) Frequency invariant θ_{SH}^{LS} for Pt/NiFe and Pt(S)/NiFe.

3.3.1. Separation of spin pumping contribution from ST-FMR signal

The symmetric component in ST-FMR spectra might arise not only from the damping-like SOT but SP effect in which a precessing magnet (here NiFe) pumps a spin current back into the SHM (here Pt or Pt(S)) where it is converted to a symmetric voltage output by spin-to-charge conversion. The influence of spin pumping contribution can be expressed as $V_{ISHE} = \frac{\theta_{DL} l \lambda_{sd}}{d\sigma_{SHM} + t\sigma_{NiFe}} tanh\left(\frac{d}{2\lambda_{sd}}\right) j_S \, sin\phi$ where, θ_{DL} is the charge-to-spin conversion of Pt and Pt(S), l is the length of the device, λ_{sd} is the spin diffusion length of SHE (Here either Pt or Pt(S)), d and σ_{SHM} are the thickness and conductivity of SHM layer, t and σ_{NiFe} are the thickness and conductivity of top ferromagnetic NiFe layer, e is the electronic charge, $\hbar$ is the

reduced Planck constant, ϕ is the angle between external magnetic field and microwave current (45° in our case), J_S is the spin pumping current into the Pt(S) layer due to precessing NiFe given as $j_s = \frac{2e}{\hbar} \times \frac{\hbar\omega}{4\pi} g^{\uparrow\downarrow} sin^2\,\theta_C \left[2\omega \frac{\left(\gamma M_S + \sqrt{(\gamma M_S)^2 + (2\omega)^2}\right)}{(\gamma M_S)^2 + (2\omega)^2}\right]$ where, $\omega = 2\pi f$ is the applied microwave frequency and $g^{\uparrow\downarrow}$ is the spin mixing conductance. While θ_C is the precession cone angle, estimated using $\theta_C = \frac{1}{dR/d\phi}\frac{2}{I_{rf}}\sqrt{S^2 + A^2}$ in which S and A are the voltage weight factors of symmetric and antisymmetric component, $dR/d\phi$ is obtained from angular magnetoresistance measurements, and I_{rf} is the microwave current in the device. The estimated spin pumping contribution V_{ISHE} is found to be 1.82 μV at 9 GHz which is much less compared to S = 95.72 μV for Pt(S)/NiFe while for control sample Pt/NiFe, V_{SP} is found to be 7.97 μV at 9 GHz which is also less compared to S = 101.88 μV. Therefore, SP contribution does not affect our estimation of θ_{DL}^{LS} using line-shape analysis. We found the SP contribution (V_{SP}) to be very less compared to symmetric weight factor S in Pt and Pt(S) respectively.

3.3.2. DC-bias ST-FMR measurements

The antisymmetric component in the ST-FMR spectra from lineshape analysis is assumed here to be purely arising from Oersted field torque, which may not be valid in general. Therefore, we also performed modulation of damping (MOD) measurements to further confirm the conversion efficiency of Pt(S), defined as θ_{DL}^{LW}. The SOT being collinear to the damping either increase or decrease the linewidth depending upon the injected spin polarization $\hat{\sigma}$ and the polarity of applied dc current I_{dc} [28]. To probe change in ΔH of ST-FMR spectra under additional DC current with microwave signal for Pt(S)/NiFe and Pt/NiFe, we performed DC biased ST-FMR measurements keeping ϕ at 45° as shown in the set-up image. Figure 3.6 (a) shows selected spectra for Pt(S)/NiFe to highlight ΔH increase as I_{dc} is sequentially changed from -0.25 to 0.25 mA for negative H_{ext} direction (here, full range is not shown for brevity). Consequently, ΔH gets narrower for positive H_{ext} as seen in Figure 3.6 (b). Noticeably, ΔH shows a linear variation with I_{dc} and slope gets reverse with slight swing when H_{ext} direction is 180° shifted to ϕ = 225°. The θ_{DL}^{LW} is

determined to be 0.354 ± 0.089 using $\theta_{DL}^{LW} = \frac{\frac{2e}{\hbar}\left(H_o + \frac{M_{eff}}{2}\right)\mu_o M_S t \left|\frac{\Delta\alpha_{eff}}{\Delta J_C}\right|}{sin\phi}$ where $\Delta\alpha_{eff}$ implies to I_{dc} dependent change in effective damping [28]. In case of Pt/NiFe sample, signal to noise ratio did not decrease significantly and we were able to apply higher DC current up to ± 0.8 mA. However, only small change in ΔH (around 0.15 mT) was observed (Refer Figure 3.6 (c)) and correspondingly smaller $\theta_{DL} = 0.102 \pm 0.040$ is estimated. While we obtained a large change in ΔH (around 0.40 mT) for Pt(S)/NiFe under lower applied dc current range due to its large SHE.

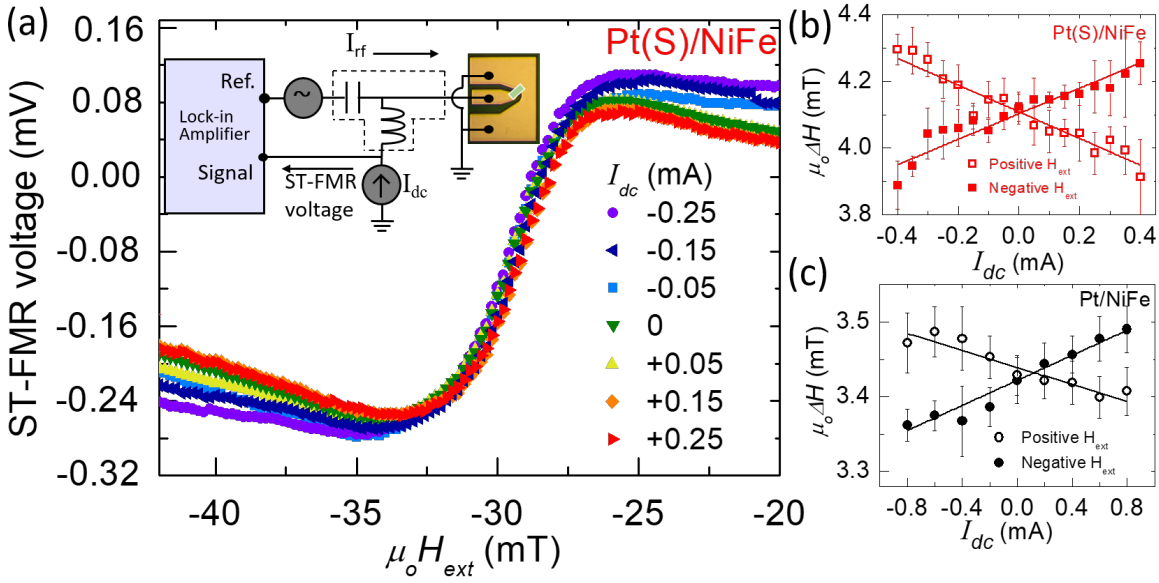

Figure 3.6. (a) Varying HWHM of ST-FMR spectra under I_{dc} range of ± 0.25 mA applied to Pt(S)/NiFe and obtained at f = 5 GHz. Inset shows MOD measurement set-up. Change in $\mu_o\Delta H$ as a function of I_{dc} for (b) Pt(S)/NiFe and c) Pt/NiFe.

3.3.3. Angular dependent ST-FMR measurements

The angular dependent studies must be carefully analyzed before accurately assessing the torques in ST-FMR line-shape analysis as it requires careful attention from possible artefacts such as spin torque with different symmetries. In V_{mix} signal, the contributions to expected angular dependence partially arise from AMR with sin (2ϕ) dependence, while the current-induced torque exhibit cos(ϕ) dependence. We performed angular dependent measurement of ST-FMR signal for Pt/NiFe sample from ϕ=0° to ϕ=360° by

changing the direction of applied external DC magnetic field with respect to I_{rf} current of fixed frequency ~ 9 GHz at 15 dBm. The symmetric and antisymmetric components weight factors are extracted as a function of ϕ and plotted in Fig. 3.7. Both symmetric and antisymmetric components yield the same angular dependence behavior, match well with in-plane excitation and fitted by sin(2ϕ)cos(ϕ) function.

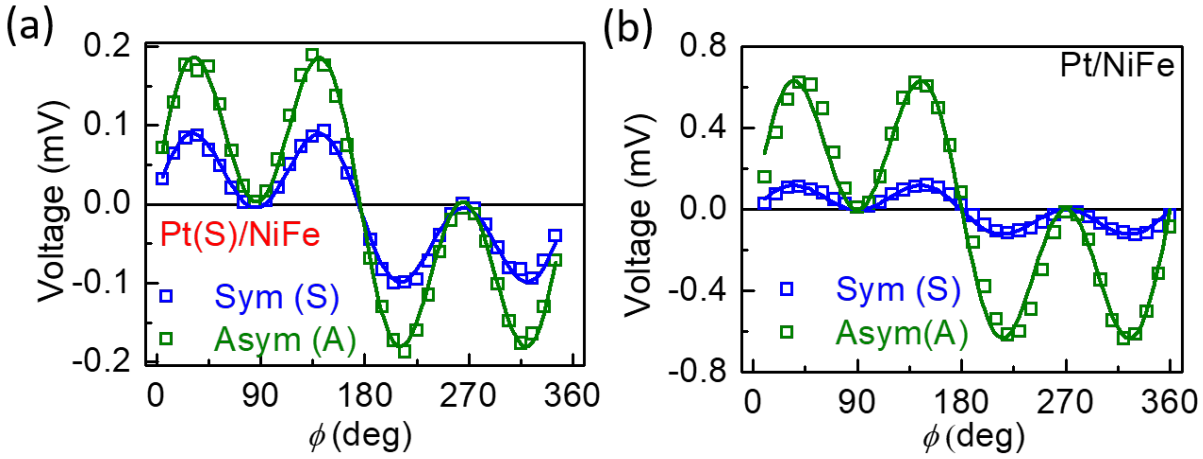

Figure 3.7. Angular dependence of symmetric and antisymmetric component of the ST-FMR voltage in (a) Pt(S)/NiFe and (b) Pt/NiFe.

3.4. Temperature dependent ST-FMR measurements

To gain a better understanding of underlying mechanism behind enhanced SHE in Pt(S) we carried out temperature (T) dependent ST-FMR measurements. Figure 3.8 (a) shows θ_{DL} as a function of T ranging from 300 to 10 K for Pt and Pt(S), respectively. The θ_{DL}^{Pt} shows a weak temperature dependence with slight decrease from 0.092 at 300 K to 0.064 at 10 K, is found to be consistent with earlier reports [33-35]. Figure 3.8 (b) shows nearly invariant behavior of σ_{SH}^{Pt} with σ_{xx}^{Pt} that suggest an intrinsic origin of SHE in Pt in a metal conduction regime [7,14,26,34]. On the other hand, $\theta_{DL}^{Pt(S)}$ monotonically ramps up to 0.502 ± 0.016 with decreasing T suggesting and intrinsic and/or side-jump scattering and noticeably $\theta_{DL}^{Pt(S)}$ at 10 K becomes 8-times-higher than that for Pt (see Fig. 3.8 (a)). Also, continuous increase in $\sigma_{xx}^{Pt(S)}$ with decreasing T

conjointly results in 2.5-times enhanced $\sigma_{SH}^{Pt(S)}$ i.e. from 3.13 × 10^5 ($\frac{\hbar}{2e}$) $\Omega^{-1}m^{-1}$ at 300 K to 8.32 × 10^5 ($\frac{\hbar}{2e}$) $\Omega^{-1}m^{-1}$ at 10 K.

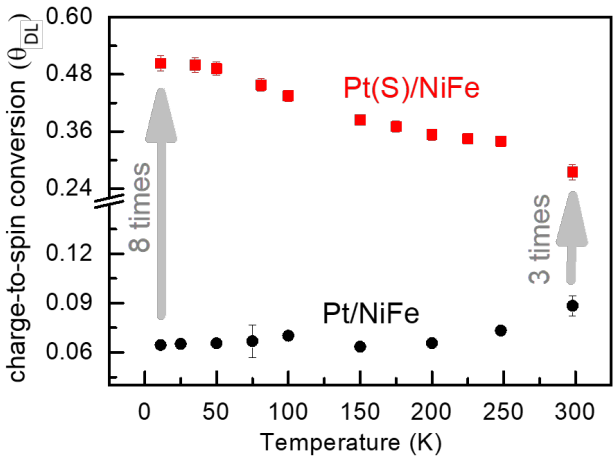

Figure 3.8. Temperature dependent θ_{SH} variation for e) Pt/NiFe and f) Pt(S)/NiFe. First inset shows temperature invariant σ_{SH}^{Pt} behavior and second inset shows $\sigma_{SH}^{Pt(S)}$ versus $\sigma_{xx}^{Pt(S)}$ plot and corresponding non-linear fitting.

3.5. Spin-pumping Inverse spin Hall voltage (SP-ISHV) measurements

We performed SP-ISHV measurements using coplanar waveguide based micro device as shown in Fig. 3.9 (a). SP is defined as the injection of pure spin current into adjacent HM metallic layer (say Pt or Pt(S) in present case) due to magnetization precession in magnetic (NiFe) layer. The spin current injected into HM layer then gets converted into transverse charge current (DC voltage) by means of inverse-SHE. To minimize unwanted spin rectification signals, we employed out-of-plane excitation geometry as described in the schematic (Fig. 3.9 (b)). Here careful alignment of H_{ext} at $\phi = 90^o$ or 270^o with respect to micro-strip leads to zero rectification-voltage contribution as it exhibits sin(2ϕ) dependency while V_{ISHE} reaches to maximum amplitude, due to $sin(\phi)$ dependence of SHE. As compared to measured V_{ISHE} signal across Pt/NiFe bilayer, Pt(S)/NiFe sample showed anticipated increase in V_{ISHE} amplitude for all rf frequencies (5-11 GHz, 15dBm), which are plotted respectively in Fig. 3.9 (c) and 3.9 (d) as a function of

H_{ext}. The symmetric Lorentz line shape of V_{ISHE} spectrum along with sign reversal with equal magnitude under H_{ext} inversion implies its ISHE origin. In addition, the linear scaling of V_{ISHE} with microwave power with intercept at origin (0,0) is consistent with the theory, implying the measurements were performed in linear excitation regime (see inset of Fig. 3.9 (c)). One may notice that *f* dependent V_{ISHE} amplitude behavior, common in both pristine and implanted Pt seems to differ from spin pumping theory that amplitude of voltage signal to be proportional to *f*. However, the trend observed here is attributed to trajectory dependent $\boldsymbol{j_s}$, as given by $\boldsymbol{j_s} = \frac{2e}{\hbar} \times \frac{\hbar\omega}{4\pi} g^{\uparrow\downarrow} sin^2\,\theta_C \left[2\omega \frac{\left(\gamma M_S + \sqrt{(\gamma M_S)^2 + (2\omega)^2}\right)}{(\gamma M_S)^2 + (2\omega)^2}\right]$ and we previously confirmed by independent determination of precession cone angle θ_C for wide $\omega = 2\pi f$ range that disclosed same trend in $\boldsymbol{j_s}$ values as well [32]. We then calculate spin mixing conductance $g^{\uparrow\downarrow}$, which is an important parameter that determines the spin pumping efficiency, using $g^{\uparrow\downarrow} = \frac{4\pi M_S t \alpha}{g\mu_o\mu_B}$, where α accounts for increase in Gilbert damping due to loss in angular spin momentum during spin pumping. The $g^{\uparrow\downarrow}$ value approximately doubled from 26.2 nm^2 for Pt/NiFe to 49.8 nm^2 for Pt(S)/NiFe indicates increase in injected $\boldsymbol{j_s}$ for same resonance conditions. This increase of $g^{\uparrow\downarrow}$ value is ascribed to large spin relaxation and high spin-orbit-interaction in Pt(S)/NiFe system. Therefore, from V_{ISHE} values, estimated from Lorentzian fitting (shown in inset of Fig. 3.9 (d)) and θ_{DL}^{LS}, we deduced 43% reduction in λ_{sd} in Pt(S), well-suited with the fundamental fact that spin diffusion length must decrease with higher resistivity in specimen.

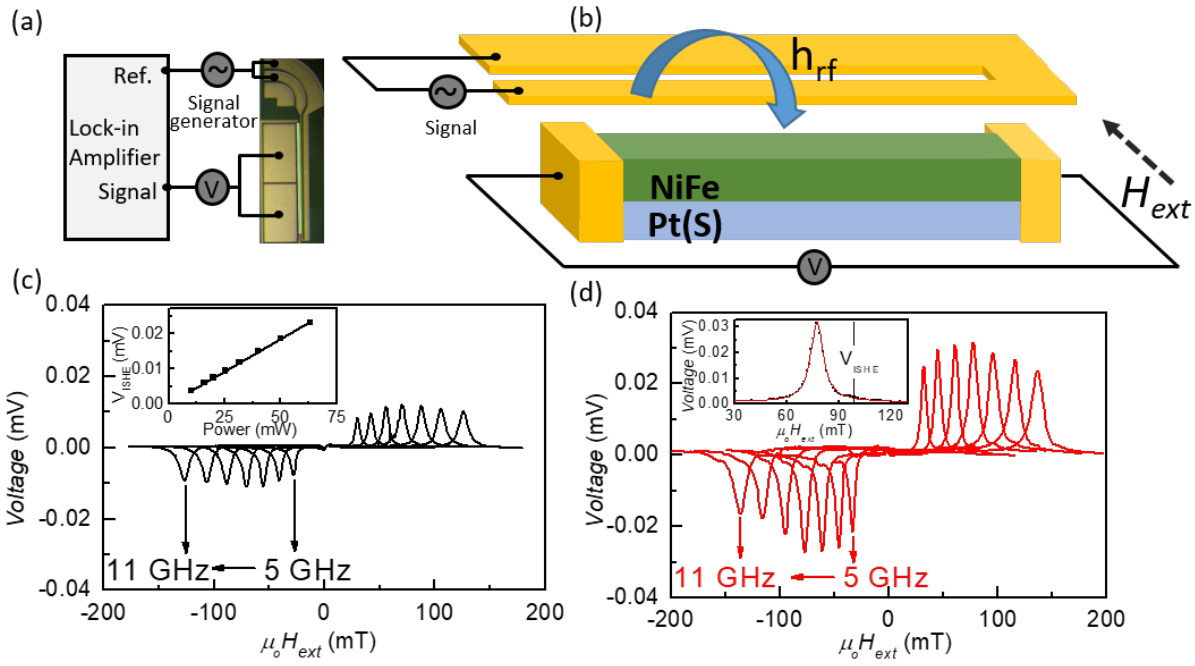

Figure 3.9. (a) Optical image of micro device with measurement setup. (b) Schematic illustration of out of plane excitation, opted to minimize unwanted spin rectification signals. Symmetric voltage spectra obtained for (c) Pt/NiFe and (d) Pt(S)/NiFe for frequency range (5-11 GHz) show approx. 3 times increase in signal amplitude. First inset shows V_{ISHE} as a linear function of rf power determined by Lorentzian fitting (second inset) of voltage signal at $f = 8$ GHz.

3.6. θ_{DL} of Pt and Pt(S) in this study and other Pt derivative alloys as a function of σ_{xx})

Figure 4 summarizes θ_{SH} of Pt and Pt(S) in this study and other Pt derivative alloys as a function of σ_{xx} to provide bird-eye view. Pt shows highest SHE in pure metallic form, but the value of θ_{SH} is around 0.1 for its intrinsic mechanism [7,11,12,28,33]. By alloying or impurity doping in Pt, we modified SHE and thus the enhancement of θ_{DL} is observed. In comparison to Pt-Au alloys such as $Pt_{53}Au_{47}$ (0.33) [15] and $Pt_{75}Au_{25}$ (0.35) [16] the room temperature θ_{DL} for Pt(S) is slightly less, but at 10 K $\theta_{DL}^{Pt(S)}$ of 0.502 and $\sigma_{SH}^{Pt(S)}$ of 8.32 $\times 10^5 (\frac{\hbar}{2e})$ $\Omega^{-1}m^{-1}$ is so far superior among Pt based SHMs including recent discoveries of $Pt_{92}Bi_8$ (0.106) [21], $Pt_{0.5}(MgO)_{0.5}$ (0.31) [36] and $PtTe_2$ (0.15) [37]. Moreover, the fabrication process for Pt(S) on Si/SiO_2 substrates

such as sputtering and ion-implantation is compatible with CMOS technology, which is preferred for memory and logic applications, if compared to topological insulators like Bi_2Se_3 or $(Bi,Sb)_2Te_3$ on GaAs or/and sapphire substrates showing high conversion efficiency but also requiring molecular beam epitaxy systems [38, 39].

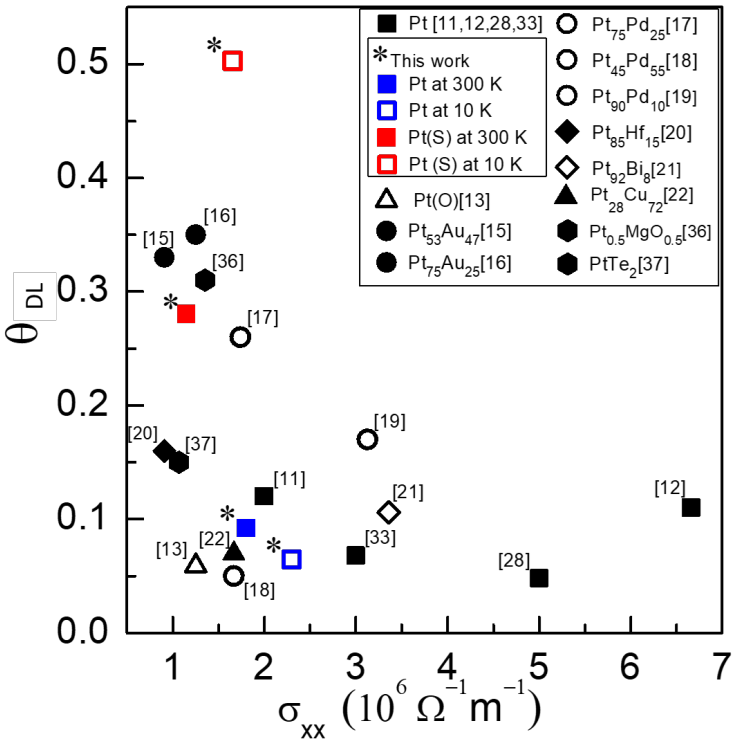

Figure 3.10. Bird-eye view showing reported θ_{DL} values for pure-Pt and its derivative alloys together with Pt(S) as a function of electrical conductivity σ_{xx}.

3.7. Conclusion

To summarize, we studied spin Hall effect in S-implanted Pt with 5×10^{16} ions per cm^{-2} dosage at low energy of 12 keV. The large $\theta_{DL}^{Pt(S)}$ of 0.502 along with high $\sigma_{SH}^{Pt(S)}$ of 8.32×10^5 $(\frac{\hbar}{2e})$ $\Omega^{-1}m^{-1}$ at reasonable conductivity $\sigma_{xx}^{Pt(S)}$ of 1.65×10^6 $\Omega^{-1}m^{-1}$ is explained as a consequence of effectively increased charge scattering as well as spin-orbit coupling after introducing S ions in Pt. Importantly, the enhancement of spin Hall effect is confirmed by multiple means i.e. line shape analysis and modulation of damping in spin-torque ferromagnetic measurements, and spin pumping-inverse spin Hall voltage measurements. Not only the large spin conductivity but also the good spin transparency at the Pt(S)/NiFe interface are a crucial

factor to design new spintronic devices using spin-orbit-torque. We believe that these results encourage implantation-engineering as an effective tool to design custom-made spin Hall materials that can exert enhanced spin-orbit-torque by virtue of efficient charge-spin interconversion, indispensable in modern spintronics field. The results presented in this chapter has been published in Advanced Quantum Technologies [40].

References for Chapter 3

1. J. E. Hirsch, *Phys. Rev. Lett.*, **83**, 1834 (1999)
2. S. O. Valenzuela, M. Tinkham, *Nature*, **442**, 176 **(2006)**.
3. Y. K. Kato, R. C. Myers, A. C. Gossard, D. D. Awschalom, *Science*, **306**, 1910 (2004).
4. J. Ryu, S. Lee, K. J. Lee, B. G. Park, *Adv. Mater.*, **32,** 1907148 (2020).
5. L. Zhu, L. Zhu, S. Shi, D. C. Ralph, and R. A. Burhman, *Adv. Electron. Mater.* **6**, 1901131 (2020).
6. H. L. Wang, C. H. Du, Y. Pu, R. Adur, P. C. Hammel, and F. Y. Yang, *Phys. Rev. Lett.* **112**, 197201 (2014).
7. L. Zhu, D. C. Ralph, and R. A. Burhman, *Appl. Phys. Rev.* **8**, 031308 (2021).
8. L. Zhu, R. A. Buhrman, *Phys. Rev. Appl.*, **12**, 051002 (2019).
9. E. Saitoh, M. Ueda, H. Miyajima, G. Tatara, *Appl. Phys. Lett.*, **88,** 182509 (2006).
10. T. Kimura, Y. Otani, T. Sato, S. Takahashi, S. Maekawa, *Phys. Rev. Lett.* **98***,* 156601 (2007).
11. M. H. Nguyen, D. C. Ralph, R. A. Buhrman, *Phys. Rev. Lett.* **116**, 126601 (2016).
12. W. Zhang, W. Han, X. Jiang, S. H. Yang, S. S. Parkin, *Nat. Phys.* **11***,* 496 (2015).
13. H. An, T. Ohno, Y. Kanno, Y. Kageyama, Y. Monnai, H. Maki, J. Shi, K. Ando, *Sci. Adv.* **4***,* eaar2250 (2018).
14. E. Sagasta, Y. Omori, M. Isasa, M. Gradhand, L. E. Hueso, Y. Niimi, Y. Otani, F. Casanova, *Phys. Rev. B* **94**, 060412 (2016).
15. M. Obstbaum, M. Decker, A. K. Greitner, M. Haertinger, T. N. G. Meier, M. Kronseder, K. Chadova, S. Wimmer, D. Ködderitzsch, H. Ebert, C. H. Back, *Phys. Rev. Lett.* **117**, 167204 (2016).
16. L. Zhu, D. C. Ralph, R. A. Buhrman, *Phys. Rev. Appl.* **10**, 031001 (2018).
17. L. Zhu, K. Sobotkiewich, X. Ma, X. Li, D. C. Ralph, R. A. Buhrman, *Adv. Funct. Mater.* **29**, 1805822 (2019).
18. X. Zhou, M. Tang, X. L. Fan, X. P. Qiu, S. M. Zhou, *Phys. Rev. B*. **94**, 144427 (2016).
19. L. Ma, H. A. Zhou, L. Wang, X. L. Fan, W. J. Fan, D. S. Xue, K. Xia, Z. Wang, R. Q. Wu, G. Y. Guo, L. Sun, X. Wang, X. M. Cheng, S. M. Zhou, *Adv. Elec. Mater. **2***, 1600112 (2016).
20. M. H. Nguyen, M. Zhao, D. C. Ralph, R. A. Buhrman, *Appl. Phys. Lett.* **108**, 242407 (2016).
21. C. Hong, L. Jin, H. Zhang, M. Li, Y. Rao, B. Ma, J. Li, Z. Zhong, Q. Yang, *Adv. Electron. Mater.* **4**, 1700632 (2018).
22. R. Ramaswamy, Y. Wang, M. Elyasi, M. Motapothula, T. Venkatesan, X. Qiu, H. Yang, *Phys. Rev. Appl.* **8**, 024034 (2017).
23. Y. Niimi, Y. kawanishi, D. H.Wei. C. Deranlot, H. X. Yang, M. Chshiev, T. Valet, A. Fert, Y. Otani, *Phys. Rev. Lett.* **109**, 156602 (2012).

24. A. Ganguly, S. Azzawi, S. Saha, J. A. King, R. M. Rowan-Robinson, A. T. Hindmarch, J. Sinha, D. Atkinson, A. Barman, *Sci. Rep.* **5***,* 17596 (2015).
25. J. Yun, Y. Zuo, J. Mao, M. Chang, S. Zhang, J. Liu, L. Xi, *Appl. Phys. Lett.* **115**, 032404 (2019).
26. N. Nagaosa, J. Sinova, S. Onoda, A. H. MacDonald, N. P. Ong, *Rev. Mod. Phys. 82*, 1539 (2010).
27. A. Romanchenko, M. Likhatski, Y. Mikhlin, *Minerals* **8**, 578 (2018).
28. L. Liu, T. Moriyama, D. C. Ralph, R. A. Buhrman, *Phys. Rev. Lett.* **106**, 036601 (2011).
29. Y. Kageyama, Y. Tazaki, H. An, T. Harumoto, T. Gao, J. Shi, K. Ando, *Sci. Adv.* **5**, eaax4278 (2019).
30. R. Medwal, S. Gupta, R. S. Rawat, A. Subramanian, Y. Fukuma, *Physica Status Solidi (RRL)–Rapid Research Lett.* **13**, 1900267 (2019).
31. J. Sklenar, W. Zhang, M. B. Jungfleisch, H. Saglam, S. Grudichak, W. Jiang, J. E. Pearson, J. B. Ketterson, A. Hoffmann, *Phys. Rev. B* **95**, 224431 (2017).
32. S. Gupta, R. Medwal, D. Kodama, K. Kondou, Y. Otani, Y. Fukuma. *Appl. Phys. Lett.* **110**, 022404 (2017).
33. Y. Wang, P. Deorani, X. Qiu, J. H. Kwon, H. Yang, *Appl. Phys. Lett.* **105**, 152412 (2014).
34. W. Zhang, M. B. Jungfleisch, W. Jiang, Y. Liu, J. E. Pearson, S. G. Te Velthuis, A. Hoffmann, F. Freimuth, Y. Mokrousov, *Phys. Rev. B* **91**, 115316 (2015).
35. M. Isasa, E. Villamor, L. E. Hueso, M. Gradhand, F. Casanova, *Phys. Rev. B* **91**, 024402 (2015).
36. L. Zhu, L. Zhu, M. Sui, D. C. Ralph, R. A. Buhrman, *Sci. Adv.* **5**, eaav8025 (2019).
37. H. Xu, J. Wei, H. Zhou, J. Feng, T. Xu, H. Du, C. He, Y. Huang, J. Zhang, Y. Liu, H. C. Wu, C. Guo, X. Wang, Y. Guang, H. Wei, Y. Peng, W. Jiang, G. Yu, X. Han, *Adv. Mater.* **32**, 2000513 (2020).
38. A. R. Mellnik, J. S. Lee, A. Richardella, J. L. Grab, P. J. Mintun, M. H. Fischer, A. Vaezi, A. Manchon, E. –A. Kim, N. Samarth, D. C. Ralph, *Nature* **511***,* 449 (2014).
39. K. Kondou, R. Yoshimi, A. Tsukazaki, Y. Fukuma, J. Matsuno, K. S. Takahashi, M. Kawasaki, Y. Tokura, Y. Otani, *Nat. Phys.* **12***,* 1027 (2016).
40. U. Shashank, R. Medwal, T. Shibata, R. Nongjai, J. V. Vas, M. Duchamp, K. Asokan, R. S. Rawat, H. Asada, S. Gupta, and Y. Fukuma, *Adv. Quantum Technol.* **4**, 2000112 (2021).

Chapter 4

Dose dependent spin Hall effect in O-implanted Pt and O_x sputtered Pt

(This chapter is based on the results published in Appl. Phys. Lett. [Ref. 44] and room temperature ST-FMR measurements from O_x sputtered Pt, whose manuscript is under preparation)

In chapter 3, we enhanced the spin Hall effect (SHE) in S-implanted Pt. Extending our approach to incorporate another non-metallic element oxygen (O) in Pt, we employed two different methods, ion implantation and DC sputtering, to incorporate O in Pt and to study the dependence of oxygen concentration on the SHE in Pt using room temperature ST-FMR measurements.

4.1. Preface: choice of non-metallic impurity in 5d transition metal

The spin-orbit coupling (SOC) is theoretically determined by the product of spin S and orbital L moment. This is associated with a spin orbit coupling constant λ_{SOC}. The Hamiltonian H_{SO}, which is the energy for spin with opposite spin polarization, is given as: $H_{SO} = \lambda_{SOC} S.L$. As discussed in last chapter, SOC is generally dependent on the fourth power of Z, written as Z^4. 5d transition metals, which are heavy metals having a large Z, have a higher SOC as compared to lighter elements such as 3d and 4d transition metals [1] (see Fig. 4.1). Due to the general acceptance that SOC is proportional to Z^4, 5d transition metals such as Pt, Ta, W were widely studied until the combination of low Z combined with a large Z was recently explored in the last decade by Niimi et. al., [2] and Shu et. al., [3].

As discussed in the previous chapter, the SHE can be enhanced by incorporating non-metallic impurities with small Z such as sulfur (S) to the 5d transition metals (host with large Z) such as Pt, Ta, W etc. Previously, spin Hall effect has been enhanced by the natural oxidation of a lighter metal, Cu [4]. Recently, Haku et. al., [5] oxidized Pd, another transition metal and enhanced the SHE. Thus, the wide commercial availability and affordability of Oxygen makes it a popular choice for impurity with low Z. Next, for the

host, Pt is a HM with a lower resistivity as compared to Ta, W. Typically, addition of a non-metallic element to HM leads to an increase of resistivity, ρ_{xx} [4]. Thus, as discussed in chapter 1, a higher ρ_{xx} is undesirable for implementation in SOT-MRAM. Hence, Pt is our choice of host while we explore how the ρ_{xx} can be controlled while increasing the SHE at the same time. So, after enhancing the SHE via S-implanted Pt, we were quite interested in the possibility of utilizing the reactive non-metals (impurity with low Z) to 5d transition metal Pt (host with large Z). Out of all the possible choices, due to the unavailability of all the reactive non-metals, we restricted our study to sulfur (chapter 3), oxygen (chapter 4), nitrogen (chapter 5), and phosphorus (chapter 6). Please see Fig. 4.2 to see the choice of non-metals. We will study each in detail. Therefore, first, we explored the possibility of an enhancement in SHE by incorporating a widely used non-metallic element Oxygen (O) in Pt. Oxygen is a non-metallic element with low Z= 8 and can be easily incorporated in 5d transition metal.

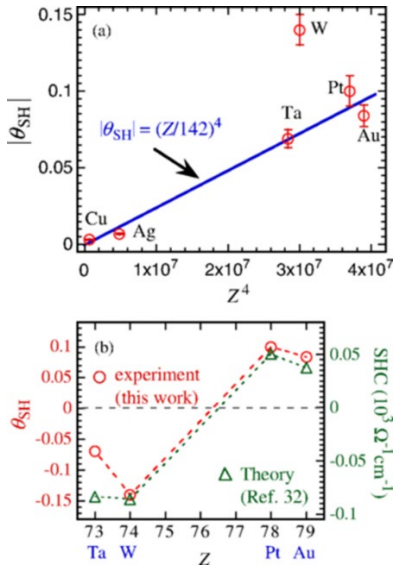

Figure 4.1. (a) Spin Hall angle as a function of Z^4 for various light and heavy metal. The blue line is the least square fit to the equation $\theta_{SH} = (Z/142)^4$. (b) spin Hall angle for 5d transition metals such Ta, W, Pt, Au. Image is reproduced with permission from https://doi.org/10.1103/PhysRevLett.112.197201 [Ref. 1].

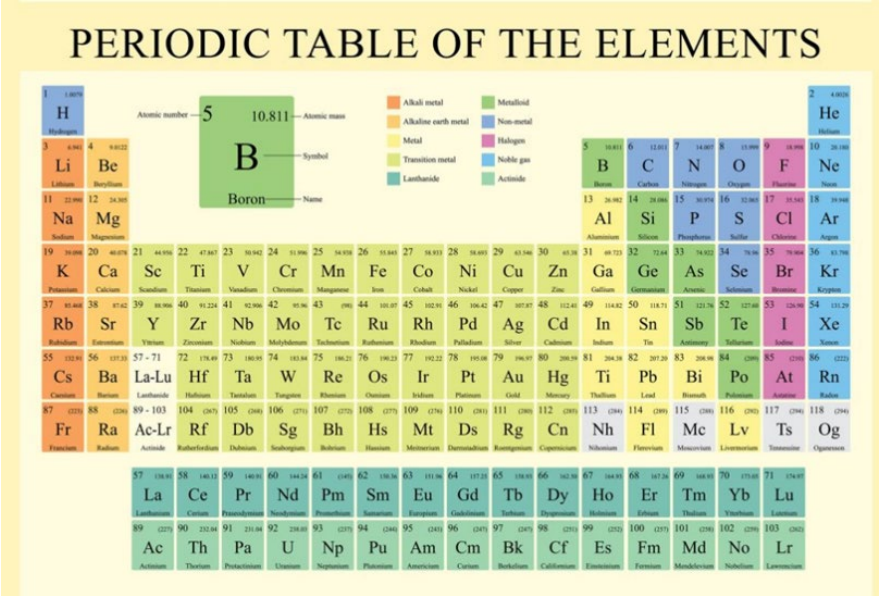

Figure 4.2. Periodic table of elements. Image is reproduced from https://ptable.com/image/periodic-table.svg.

4.2. Introduction

The existence of a strong spin-orbit coupling (SOC) in heavy metal (HM) has been instrumental in the research based on spin-based memory and logic devices [6-8]. The high SOC is utilized to generate large spin current density (J_S) converted from charge current density (J_C) in HM by means of phenomenological spin Hall effect (SHE) [9]. This spin current exerts a spin-orbit torque (SOT) on the magnetization of the adjacent ferromagnet (FM) layer attached to HM, which is one of the most important features of SHE [10, 11]. There are two basic components of SOT, first being the damping-like torque (DLT) $\boldsymbol{\tau_{DL}} \propto \boldsymbol{m} \times (\boldsymbol{\sigma} \times \boldsymbol{m})$, and second is the field-like torque (FLT) $\boldsymbol{\tau_{FL}} \propto -(\boldsymbol{\sigma} \times \boldsymbol{m})$ [12, 13], where $\boldsymbol{\sigma}$ is the unit vector along the spin polarization direction of the spin current, and $\hat{\mathrm{m}}$ is the magnetization unit vector. In fact, the former is more critical than the latter considering the intriguing applications that it provides in SOT-MRAM, logic operations, auto-oscillations, spin waves transmission and domain wall motion[7, 14-17].

The possibility of a strong DLT from the pre-existing heavy metals has attracted various groups to enhance it even further by alloying with metals such as PtSn alloy [18], Zn and Ni-doped Pt [19], Cu-Pt alloy [20],

Pt-Pd Alloy [21] Pt-Au alloy [22], Pt-Hf dusting [23, 24] and also by the inclusion of lighter elements like oxidation of Pt [25], Ta [26], W [27] and even recently adding nitrogen in Pt [28] have been shown as successful approaches to improve the charge-spin interconversion efficiency. However, for oxidation, most of the incorporation in these materials is attained from the natural process of sputtering which, if not controlled artificially such as alloying or other methods, may not be monotonic in DLT with varying concentrations [26, 28]. Hence, in this respect, ion implantation, being an established artificial material engineering technique in the semiconductor industry is much more useful to incorporate non-metallic elements in heavy metals to enhance the DLT further. As a matter of fact, ion implantation or ion irradiation is already taking huge strides in the design of future generation spintronic devices such as in spin-torque nano-oscillator using He^+ irradiation [29], interfacial hydrogen and oxygen ion manipulation at CoFeB/MgO based magnetic tunneling junction structures [30], SOT driven multi-level switching in He^+ irradiated W/CoFeB/MgO hall bars [31] etc. To add, we had previously designed a new spin Hall material (SHM) by implanting low energy 12 keV sulfur ions in prototype Pt which demonstrated eight-times enhanced charge-to-spin interconversion efficiency and a very large spin Hall conductivity of ~ 8.32×10^5 $(\frac{\hbar}{2e})$ $\Omega^{-1}m^{-1}$ at 10 K, highest among reported Pt and its derivatives [32].

4.3. Sample preparation and characterization I: O-ion implantation in Pt

I. Sample preparation

The deposited multilayer stack of Pt (10 nm)/ MgO (10 nm)/ Al_2O_3 (10 nm) were implanted with 20 keV O ion beam and the same procedure was followed as discussed in previous chapter.

II. Surface morphology: SEM

The multilayer stack of Pt (10 nm)/MgO (10 nm)/Al_2O_3 (10 nm) on Si/SiO_2 substrates were deposited at room temperature using an ultrahigh vacuum sputtering. Then, samples were implanted with 20 keV O ion beam at a dose/fluence of 2×10^{16} ions cm^{-2}, 5×10^{16} ions cm^{-2}, and 1×10^{17} ions cm^{-2}

respectively. Then, oxide capping layers of MgO and Al_2O_3 were removed by Ar^+ ion milling. One batch of samples was used for microstructure and surface morphology investigations. Figure 4.3 (a-c) depicts the microstructure images of respective O-implanted Pt surfaces using the scanning electron microscope (SEM) and affirm no substantial surface damage on any of the samples exposed to respective ion fluences of 2×10^{16} ions cm^{-2}, 5×10^{16} ions cm^{-2}, and 1×10^{17} ions cm^{-2}. The average root-mean-square roughness was determined to be varying only from (0.76 - 0.96) ± 0.01 nm from respective topography image analysis. So, these results indicate that the optimized oxide capping layer provided the necessary protection and led to minimal surface agitation of 10 nm thick Pt films.

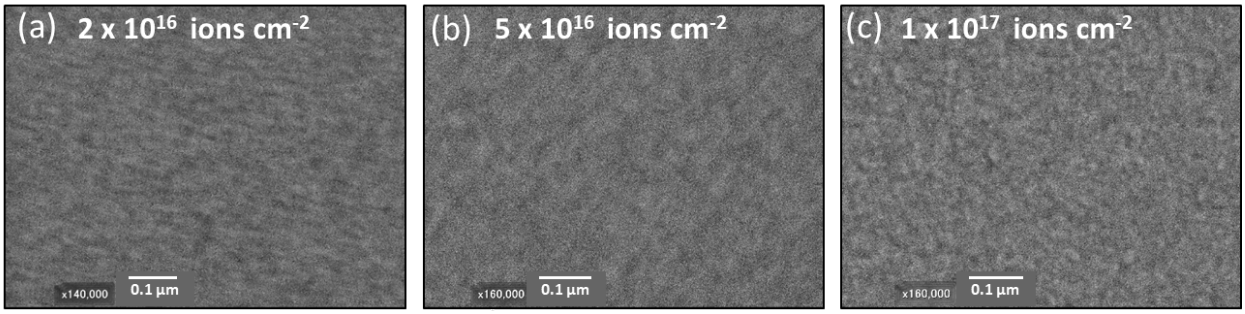

Figure 4.3: Microstructure for different doses of O-implanted Pt, (a) 2×10^{16} ions cm^{-2}, (b) 5×10^{16} ions cm^{-2}, and (c) 1×10^{17} ions cm^{-2} respectively, after removal of capping layers (MgO/Al_2O_3).

III. Device fabrication

We used the second batch to deposit the top NiFe (5 nm) layer using an ultrahigh vacuum sputtering immediately after the Ar^+-milling process. Using photolithography, all the three bilayer samples (named as Pt(O) 2×10^{16}, Pt(O) 5×10^{16}, and Pt(O) 1×10^{17} with implanted doses of 2×10^{16} ions cm^{-2}, 5×10^{16} ions cm^{-2}, and 1×10^{17} ions cm^{-2}, respectively) were then patterned into micro strips. Finally, Ti (10nm)/Al (200 nm) electrodes were deposited using a lift-off process to design the co-planar waveguide structure for ST-FMR measurements. Similarly, Hall bars were also fabricated to determine the longitudinal resistivity $\rho_{Pt-oxide}$ of different O-dose implanted Pt without the top NiFe layer.

4.4. Sample preparation and characterization II: O_x sputtered Pt

I. Sample preparation

First, the SiO_2 substrates were ultrasonically cleaned in acetone and rinsed with ethanol, and then PtO_x was deposited on the SiO_2 substrate using an ultrahigh vacuum sputtering system. The sputtering rate and other parameters are shown in Table 4-I. Prior to sputtering, reverse sputtering for 30 seconds and pre-sputtering for 1 minute were performed immediately before sputtering on each substrate. For the O_x sputtered Pt, ST-FMR and Hall bars were made on the samples after deposition of 5 nm NiFe on top of O_x sputtered Pt.

Table 4-I. Deposition conditions. O_2 ratio, Gas ratio, Voltage, current, deposition rate and deposition time for the various O_x sputtered Pt samples.

O_2 ratio	Gas ratio ($Ar:O_2$)	Voltage (V)	Electric Current (A)	Deposition rate (nm/s)	time (s)
0 %	10:0	373	0.13	16.70	36
1 %	19.8:0.2	393	0.13	16.85	36
2.5 %	19.5:0.5	420	0.12	16.87	36
5 %	19:1	440	0.11	15.86	38
10 %	18:2	454	0.11	20.51	29
20 %	16:4	473	0.11	22.72	26

II. Surface morphology: AFM measurements

To carry out the surface morphology investigations for the prepared samples, AFM measurements were performed. The average roughness (R_a) values are all less than 1 nm and did not follow any specific trend with the oxygen concentration. The R_a for each of the prepared samples are shown in Fig. 4.4.

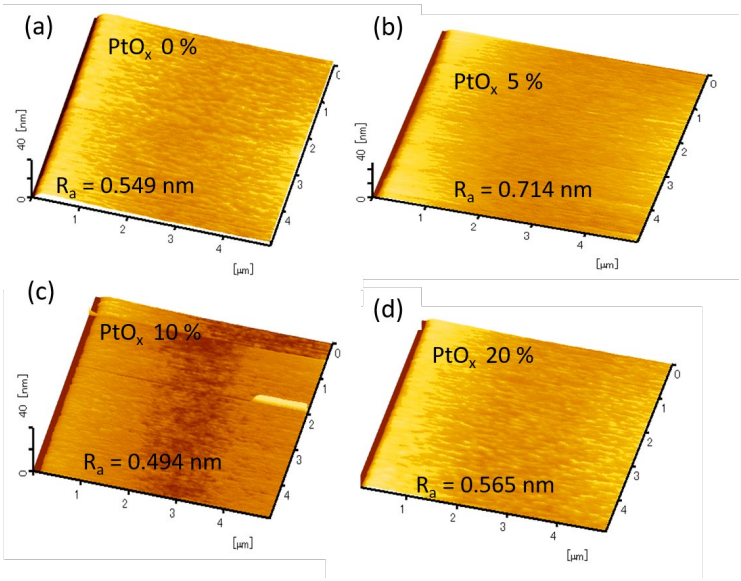

Figure 4.4. Surface morphology investigations using AFM for the PtO_x samples prepared on SiO_2 substrates.

III. X-ray diffraction measurement

To understand the change in the crystallographic properties with the oxygen concentration, the XRD measurements were carried out. For the pure samples i.e., PtO_x 0%, a strong Pt (111) peak was observed and a weak peak of Pt (100) were observed in addition to the Si peak. This indicated that the Pt is oriented along (111). However, with the increase of oxygen concentration, the Pt (111) peak diminished for PtO_x 5 % and shifted slightly to left. Furthermore, for the higher oxygen concentration, of 10 and 20 %, i.e., PtO_x 10% and PtO_x 20%, no Pt peaks were observed.

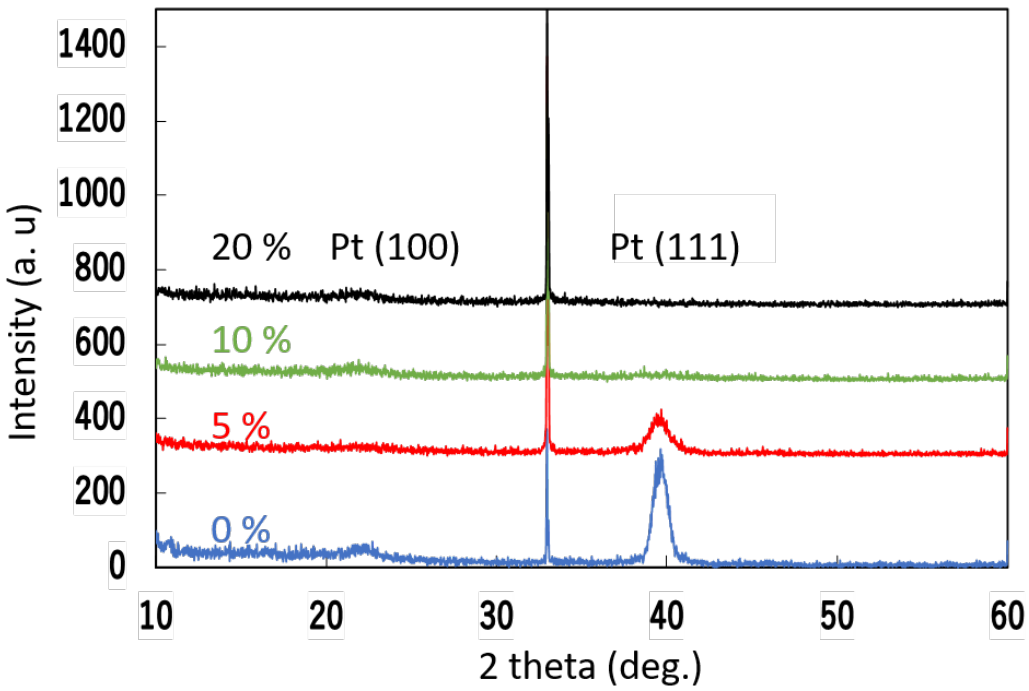

Figure 4.5. Crystallographic investigations using XRD for PtO_x.

4.5. Room temperature ST-FMR measurements: O-implanted Pt

4.5.1 Lineshape analysis: O-implanted Pt

First, to determine the DLT efficiency θ_{DL}, we perform the lineshape analysis which uses the ratio of symmetric and antisymmetric components of ST-FMR spectra. The schematic of the ST-FMR measurement set-up is shown in Fig. 4.6 (a). The device is excited with a microwave current I_{rf} of varying frequency f (5-11 GHz) with an applied power of P_{app} =10 dBm (10 mW). Simultaneously, an in-plane magnetic field H_{ext}, is swept from –200 mT to +200 mT at an angle of $\phi = 45^{o}$ with respect to the device length. Thereby, j_c flowing in the O-implanted Pt layer gets converted into J_S due to SHE and exerts a DLT on the magnetization of the adjacent FM layer. Meanwhile, the h_{rf} arising from I_{rf} exerts an Oersted field torque (OFT) (Ampere's Law) and both the torques together drive magnetization precession in the NiFe layer. At FMR conditions, the mixing of periodic change in the magnetoresistance ΔR of NiFe and I_{rf} produces a rectified DC voltage V_{mix} which is detected using a lockin amplifier. Next, figure 4.5 (b-d) shows the ST-FMR spectrum obtained at f = 5GHz, respectively for Pt(O) 2×10^{16}, Pt(O) 5×10^{16}, and Pt(O) 1×10^{17} sample which are then subsequently fitted using the Lorentzian function

$$V_{mix} = SF_{sym}(H_{ext}) + AF_{asym}(H_{ext}), \quad (4.1)$$

where, $F_{sym}(H_{ext}) = \frac{(\Delta H)^2}{(H_{ext}-H_o)^2+(\Delta H)^2}$ is the symmetric component with weight S, and $F_{asym}(H_{ext}) = \frac{\Delta H(H_{ext}-H_o)}{(H_{ext}-H_o)^2+(\Delta H)^2}$ is the antisymmetric component with weight A and ΔH and H_o are the half-width-at-half-maximum and resonance field of FMR spectra. While the symmetric component is proportional to DLT, the antisymmetric component is proportional to OFT. The V_{mix} spectrum is de-convoluted into symmetric and antisymmetric components for Pt(O) 2×10^{16}, Pt(O) 5×10^{16}, and Pt(O) 1×10^{17} samples. It can be noticed that there is an increase in the symmetric component as the dosage of the oxygen ions increases 5 times.

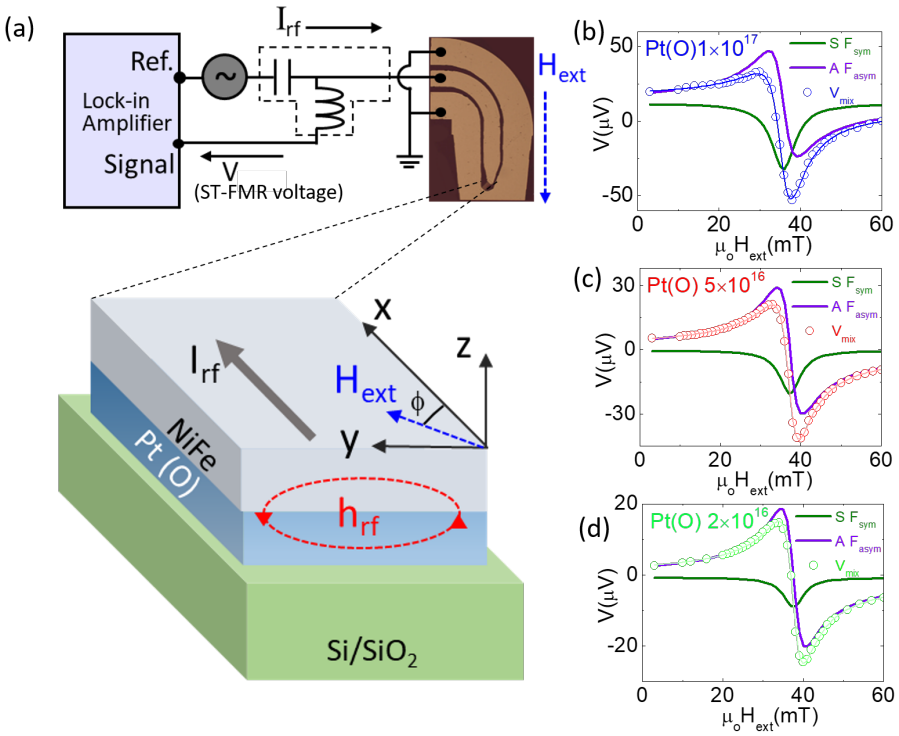

Figure 4.6. (a) Schematic showing ST-FMR measurement technique with optical image of micro-device and detection principle in bilayer thin film. De-convolution fitting of V_{mix} measured at f = 5 GHz into symmetric and antisymmetric components displayed by green and violet solid line respectively for (b) Pt(O) 2×10^{16}, (c) Pt(O) 5×10^{16}, and (d) Pt(O) 1×10^{17} sample shows continuous increase in DLT.

4.5.2. Frequency dependent ST-FMR: its associated properties and damping-like torque efficiency

Figure 4.7. (a-c) shows the typical ST-FMR spectra for Pt(O) 2×10^{16}, Pt(O) 5×10^{16}, and Pt(O) 1×10^{17}, respectively. Note that, there is a reversal of symmetric component with the reverse in polarity of external magnetic field (H_{ext}) which agrees with SHE symmetry and it also rules out the possibility of non-controlled relative phase between I_{rf} and h_{rf} that we retained in present measurements for a wide frequency range[29].

Furthermore, ΔH is plotted as a function of the applied frequency f in Fig. 4.7(d), Pt(O) 2×10^{16}, Pt(O) 5×10^{16}, and Pt(O) 1×10^{17}. The Gilbert damping parameter α is estimated using:

$$\Delta H = \Delta H_o + \frac{2\pi\alpha}{\gamma} f, \tag{4.2}$$

where the first term ΔH_o is the inhomogeneous linewidth broadening and γ is the gyromagnetic ratio. Here, α is found to be increasing with dose for O-implanted Pt, Pt(O) 2×10^{16}, (0.0137), Pt(O) 5×10^{16} (0.0153) and Pt(O) 1×10^{17} (0.0164), unlike to Ta(O)/Py [26] which showed a small deviation around average ~0.01 for different oxygen flow rates in Ta. Important to notice, that the inhomogeneous linewidth $\mu_o\Delta H_o$ ~0.5 mT in all cases was found to very small which further confirmed the smooth and high quality of O-implanted Pt/NiFe interface fabrication. Dose dependent increase in α clearly indicates the effect of enhanced DLT from O-implanted Pt. However, the additional spin relaxation due to the presence of spin pumping cannot be ruled out here. Further, the spin pumping also contributes to the symmetric component of the rectified V_{mix} signal in ST-FMR measurements [35]. Therefore, to confirm that the symmetric part is dominantly proportional to DLT here, the spin pumping contribution, V_{sp} (see section 4.5.3) was estimated and found it to be ~1 % only. It showed that the spin current pumping back into the O-implanted Pt layer from precessing NiFe was negligible.

The effective magnetization $\mu_o M_{eff}$ values were then extracted by fitting the resonance frequency f as a function of H_o using the Kittel formula (See Fig. 4.7 (e)) due to the negligibly small in-plane magnetic anisotropy for Pt(O) 2×10^{16}, Pt(O) 5×10^{16}, and Pt(O) 1×10^{17} sample using:

$$f = \frac{\gamma}{2\pi}\sqrt{H_o(H_o + M_{eff})}, \tag{4.3}$$

The effective magnetization $\mu_o M_{eff}$ was calculated to be 799 mT, 800 mT and 811 mT for Pt(O) 2×10^{16}, Pt(O) 5×10^{16}, and Pt(O) 1×10^{17}, respectively. We also evaluated the spin mixing conductance $g_{eff}^{\uparrow\downarrow}$ [30,31] which is an important parameter describing the absorption of transverse spin current which is influenced by HM/FM interface. The $g_{eff}^{\uparrow\downarrow}$ was estimated using the difference in linewidth δ from the ST-FMR spectra ($\delta = \Delta H_{Pt-Oxide/NiFe} - \Delta H_{NiFe}$) using $g_{eff}^{\uparrow\downarrow} = (\frac{\gamma}{2\pi f})(\frac{4\pi M_s t \delta}{g\mu_o\mu_B})$ where, g is the Landé g factor, μ_o is the permeability of free space, t is thickness of NiFe layer , M_S is the saturation magnetization of NiFe and μ_B is the Bohr magneton. There is an enhancement of $g_{eff}^{\uparrow\downarrow}$ with dose from 1.53×10^{19} m^{-2} (Pt(O) 2×10^{16}) to 2.05×10^{19} m^{-2} (Pt(O) 1×10^{17}). So, after confirming the insignificant contribution of spin pumping in

symmetric component of the spectra and the enhancement of $g_{eff}^{\uparrow\downarrow}$ with dose, we proceeded to quantify DLT efficiency θ_{DL}, given as [33]:

$$\theta_{DL}^{LS} = \frac{S}{A}\frac{e\mu_o M_s t d}{\hbar}\sqrt{1+\frac{4\pi M_{eff}}{H_o}}, \tag{4.4}$$

where, e is the electron charge, d is thickness of Pt-Oxide layer. Figure 4.7(f) shows the calculated value of θ_{DL}^{LS} of 0.075± 0.002, 0.107± 0.002 and 0.230± 0.003 for Pt(O) 2×10^{16}, Pt(O) 5×10^{16}, and Pt(O) 1×10^{17}, respectively. This monotonic increase of θ_{DL}^{LS} with O-dose shows that ion implantation could be a better alternative to incorporate nonmetallic elements in transition metals when compared to incorporating oxides/nitrides via sputtering [26, 28].

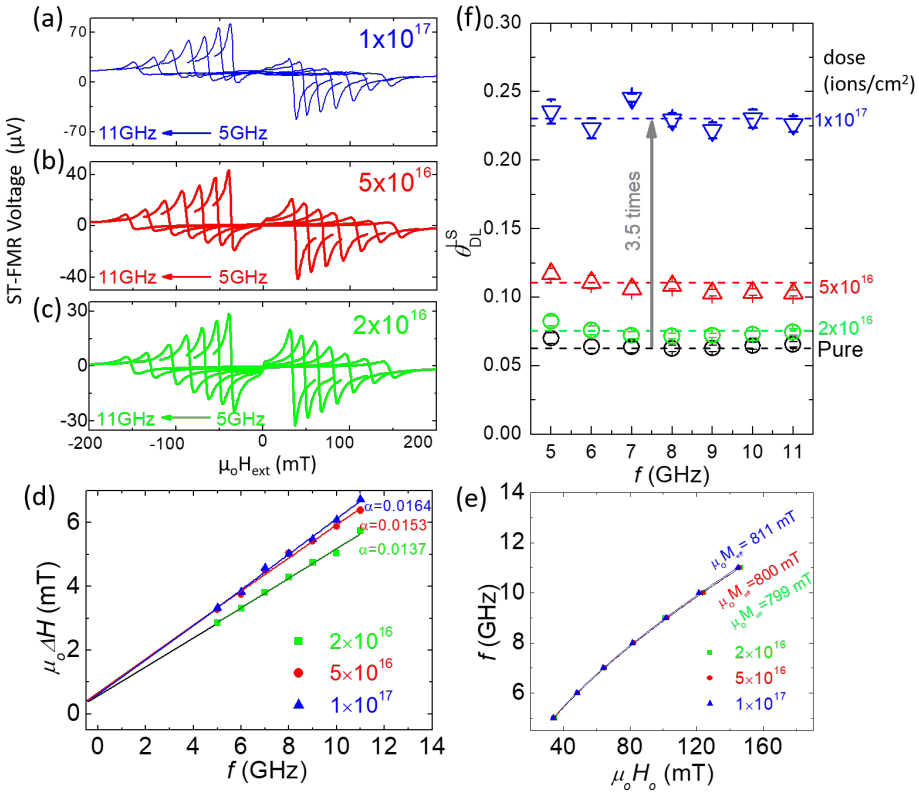

Figure 4.7. STFMR spectra plotted for f = 5 to 11 GHz range obtained from different O-implanted samples in (a)-(c). (d) ΔH vs f (with solid lines as linear fit), (e) f vs H_o (with solid lines as Kittel equation fit) for different O-implanted Pt samples. (f) Frequency invariant θ_{DL}^{LS} obtained for Pt(O) 2×10^{16}, Pt(O) 5×10^{16}, and Pt(O) 1×10^{17}, respectively along with pure Pt as a function of f.

4.5.3. Role of Spin pumping contribution in the symmetric component of ST-FMR signal

The symmetric component in ST-FMR spectra must be analyzed precisely for weak resonance signal since it might originate not only from DLT but also by spin pumping in which a precessing ferromagnet (here NiFe) pumps a spin current back into the Pt-Oxide. This spin current might get converted back to voltage output by inverse spin-to-charge conversion. Moreover, the spin pumping contribution has the same $\sin 2\phi \cos \phi$ dependence (see next section 3.3.4) and so angular dependent ST-FMR cannot be used to differentiate these two effects.

Hence, the role of spin pumping can be assessed by calculating the spin pumping contribution which can be expressed as $V_{SP} = \frac{\theta_{DL} l \lambda_{sd}}{d\sigma_{Pt(O)} + t\sigma_{NiFe}} tanh\left(\frac{d}{2\lambda_{sd}}\right)\left(\frac{2e}{\hbar}\right) j_s \sin\phi$ where, θ_{DL} is DLT efficiency of Pt-Oxide, l is the length of device, λ_{sd} is the spin diffusion length in the Pt-Oxide, d and $\sigma_{Pt(O)}$ are thickness and conductivity of Pt-Oxide, t and σ_{NiFe} are the thickness and conductivity of NiFe, e is the electronic charge, $\hbar$ is the reduced Planck constant, φ is the angle between external magnetic field and microwave current (45° for this case), ***Js*** is the spin pumping current into Pt-Oxide due to precessing NiFe given as $j_S = \frac{h}{2} f \sin^2\theta_c \, g_{eff}^{\uparrow\downarrow}$ where, f is frequency, $g_{eff}^{\uparrow\downarrow}$ is the spin mixing conductance and $\theta_c = \frac{1}{dR/d\phi}\frac{2}{I_{rf}}\sqrt{S^2 + A^2}$ in which S and A are the weight factors for symmetric and antisymmetric components respectively, $dR/d\phi$ is obtained from AMR, I_{rf} is the amount of current in device. For e.g., V_{SP} is found to be 0.05 μV as compared to S = 8.15 μV which is less than 1% (~0.65 %) at 5 GHz for Pt(O) 2×10^{16}, V_{SP} is found to be 0.11 μV as compared to S = 20.2 μV for Pt(O) 5×10^{16} (~0.56 %) and V_{SP} is found to be 0.23 μV as compared to S = 43.67 μV for Pt(O) 1×10^{17} (~0.53 %). Therefore, spin pumping contribution does not play a significant role in the symmetric component of present ST-FMR signal.

4.5.4. Angular dependent ST-FMR measurements

The careful analysis of ST-FMR lineshape is a prerequisite to quantify the DLT as there may be latent effects such as effective field with different spin polarization, ambiguous effective field orientation,

apart from the conventional spin Hall effect [38]. This may overlap with Symmetric and Antisymmetric signal of ST-FMR spectra. Hence, we performed angular dependent ST-FMR measurements to rule out these possibilities in our system by varying the direction of H_{ext} with respect to device length (I_{rf}) from 0^o to 360^o. The symmetric (S) and antisymmetric(A) components can be fitted with $\sin 2\phi \cos\phi$ where, $\sin 2\phi$ is from AMR, whereas $\cos\phi$ is from DLT and OFT for S and A respectively.

In particular, the lineshape analysis performed here only at an angle of $\phi = 45^o$ may not reveal the complete visualization of the generated spin-orbit torques [37] and therefore, angular ST-FMR measurements by varying the H_{ext} from $\phi = 0^o$ to 360^o is also crucial to analyze. Figure 4.8 shows that both S and A component are well fitted with the expected $\sin 2\phi \cos\phi$ behavior for highest dose of 1×10^{17} ions cm^{-2} implanted Pt samples with no breaking of the mirror and the two-fold symmetries [38]. It implies that lineshape analysis can be used for O-implanted Pt system which could give it an edge over other transition-metal dichalcogenides [38], where due to the broken symmetries, complex analysis are required to quantify the torques.

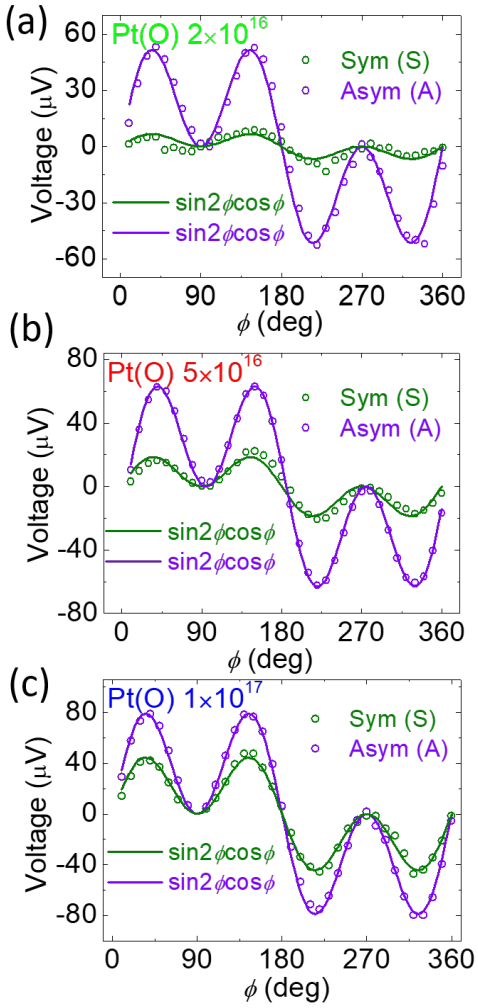

Figure 4.8. Angular dependence of symmetric and antisymmetric component measured at $f = 5$ GHz for mT for Pt(O) 2×10^{16}, Pt(O) 5×10^{16}, and Pt(O) 1×10^{17}, respectively in (a)-(c). The solid lines are fit by sin2ϕ cosϕ.

4.5.5. Power dependent ST-FMR: O-implanted Pt

We used a nominal power of P_{app} =10 dBm (10 mW) in our ST-FMR measurements. To understand if this power is not large enough to induce a nonlinear FMR in NiFe, we focused on the power dependent ST-FMR measurements [33] by measuring V_{mix} at f = 5 GHz in a wide range of P_{app} (1-12.58 mW). Figure 4.9 shows V_{mix} for one of the O-implanted Pt samples exhibiting no change in ΔH and H_o with an increase in P_{app}. Further, the extracted weight S and A (green and violet symbols) are plotted as a function of power in Fig. 4.9 (b) with a linear fit (solid line). We can infer that the precessing magnetization is in the linear regime at P_{app} =10 dBm (10mW) (red box). Additionally, we plot the ratio of weights S/A as a function of power and find it to be invariant in this applied power range as shown in Fig. 4.9 (c).

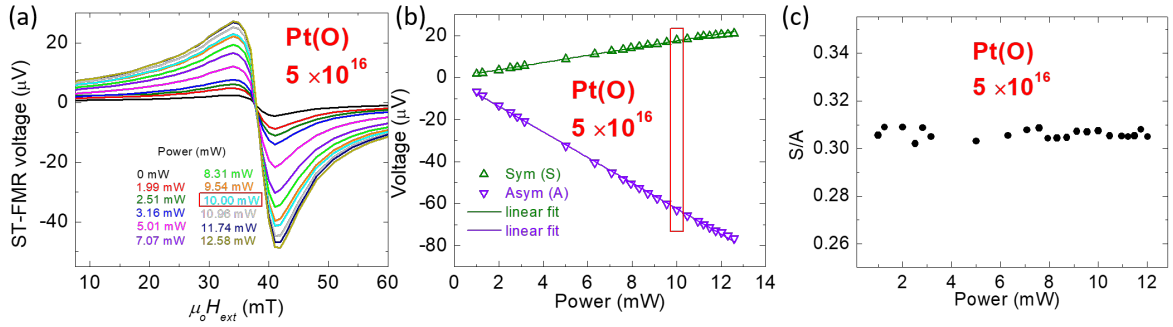

Figure 4.9. (a) Obtained rectified voltage spectra V_{mix} at f = 5 GHz for power 1-12.58 mW for one of the O-implanted Pt sample. (b) Extracted S and A (with solid lines as linear fit) and (c) invariant S/A as a function of power.

4.5.6. Linewidth analysis (DC-biased ST-FMR) : O-implanted Pt

Second, to make the estimation of DLT efficiency, θ_{DL}, more comprehensive, we employed an alternative approach of linewidth modulation as well since this method is free from spin pumping [39]. We used DC-biased ST-FMR technique [33] in which an additional direct current I_{dc} (+/-0.8mA) is also applied along with I_{rf} to modulate the linewidth ΔH which either gets increased or decreased based on the polarity of applied H_{ext}. The change in $\mu_o \Delta H$ can be seen in Fig. 3.10 (a-c) for N1, N2 and N3 respectively which

explicitly increased from ~0.1 mT (and Pt(O) 2×10^{16}) to ~0.17 mT (Pt(O) 5×10^{16}) and finally to ~0.3 mT (Pt(O) 1×10^{17}). Further, using this change in ΔH, we evaluated θ_{DL} using the equation [40]:

$$\theta_{DL}^{LW} = \frac{\frac{2e}{\hbar}\left(H_o+\frac{M_{eff}}{2}\right)\mu_o M_s t\left|\frac{\Delta\alpha_{eff}}{\Delta J_C}\right|}{sin\phi}, \tag{4.5}$$

where, $\Delta\alpha_{eff}$ is the effective change in damping due to I_{dc}. In accordance with the lineshape analysis, we observe a similar trend where θ_{DL}^{LW} increases monotonically from 0.074± 0.006 for N1 to 0.106± 0.009 for N2 and then finally to 0.231± 0.012 for N3.

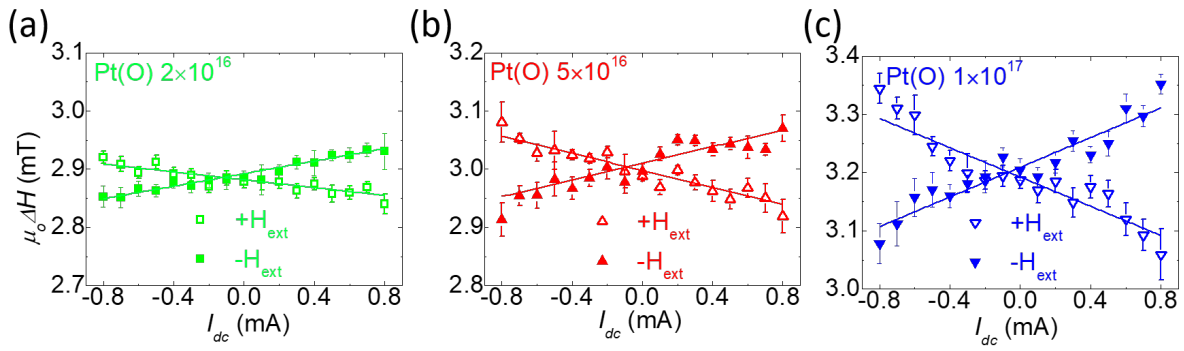

Figure 4.10. (a)-(c) Varying $\mu_o\Delta H$ plotted as a function of I_{dc} (+/- 0.8 mA) for f = 5 GHz with slope determined from linear fit (solid lines) for Pt(O) 2×10^{16}, Pt(O) 5×10^{16}, and Pt(O) 1×10^{17}, respectively.

4.5.7. Inverse spin Hall effect: O-implanted Pt

To confirm the Onsager reciprocity of charge-to-spin, we perform the spin-pumping inverse spin Hall effect (SP-ISHE) measurements. The details of SP-ISHE measurement is discussed in Chapter 2. First, to carefully minimize the unwanted spin rectification signal, we employ an out-of-plane excitation geometry in which the out-of-plane generated $h_{rf,z}$ at an angle of ϕ = 90° or 270° with respect to the length of device leads to a pure V_{ISHE} voltage [32, 34]. We measured the V_{ISHE} for a wide frequency range of 5-11 GHz for Pt(O) 5 × 10^{16}, and Pt(O)1 × 10^{17}, respectively. In comparison to pure Pt/NiFe, we observe an increase in V_{ISHE} for Pt(O) 5×10^{16}, and Pt(O) 1×10^{17}, respectively.

Furthermore, we measure the angular dependent SP-ISHE to rule out other artifacts in our measurements by varying the angle ϕ from 0° to 360°. Due to the fact that V_{ISHE} reaches its maximum value at 90°, we also found a perfect sinϕ dependence confirming that the V_{ISHE} we measure is purely from SHE. We observed an increase in V_{ISHE} with increase in the implantation dose. This concludes that there is no contribution of anomalous Hall effect or AMR in our V_{ISHE} and the voltage purely originates due to SHE [34].

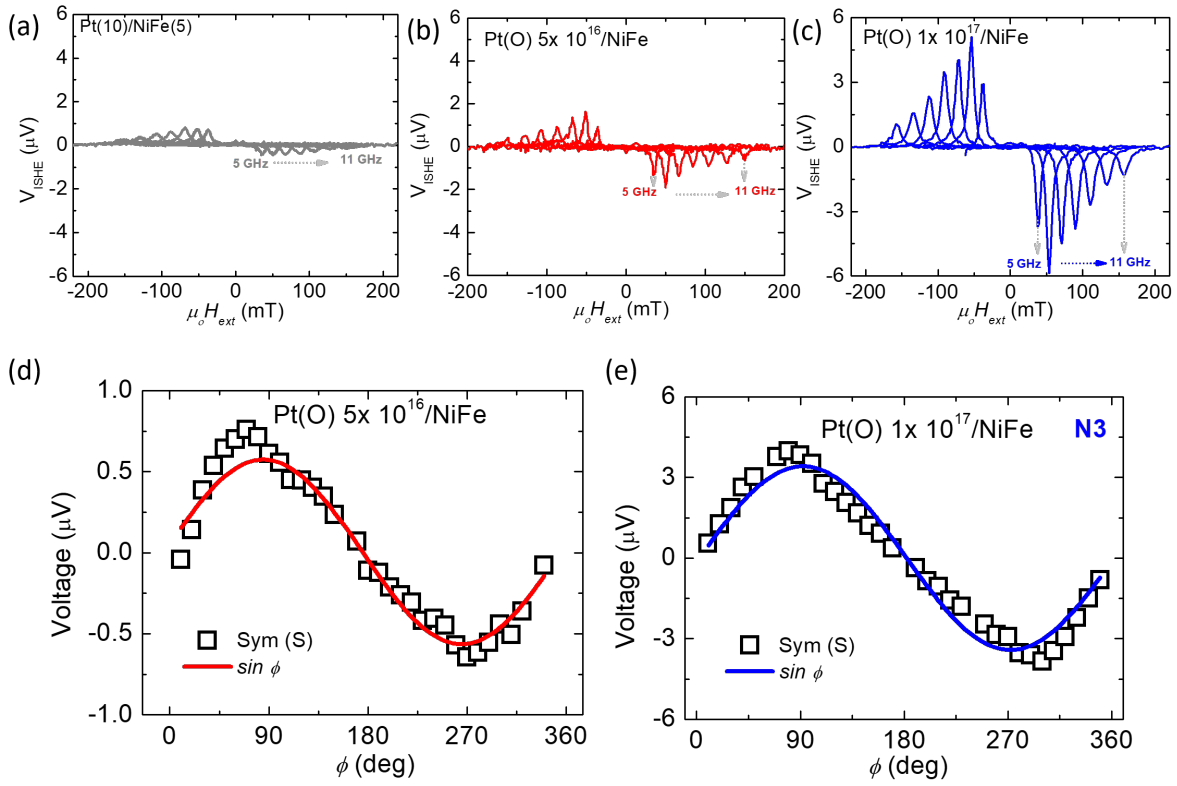

Figure 4.11. Symmetric voltage spectra obtained for (a) pure Pt (b) Pt(O) 5×10^{16} and (c) Pt(O) 1×10^{17} for frequency range (5-11 GHz). Angular dependent SP-ISHE of output voltage V_{ISHE}. for (d) Pt(O) 5×10^{16} and (e) Pt(O) 1×10^{17}. The solid lines are fit by sinϕ.

4.5.8. Dominant mechanism of enhanced SHE: O-implanted Pt

Essentially by changing the impurity concentration i.e. different O-implantation dose in much wider range, we can obtain a highly dose dependent DLT efficiency and therefore, it is more likely to be

caused by an extrinsic mechanism. There are two types of mechanism of extrinsic SHE namely, the skew scattering governed by explicit behavior of SH resistivity (ρ_{SH}^{imp}) proportional to impurity induced resistivity (ρ_{imp}), while, the side jumping scattering is associated with $\rho_{SH}^{imp} \propto \rho_{imp}^{2}$ relationship when impurities are the only source of resistivity [41]. We find a monotonic dependence of θ_{DL} with the increase in longitudinal resistivity $\rho_{Pt-Oxide}$ as the concentration of O^{+} implantation increased as shown in Fig. 4.12, it hints towards the intrinsic and/or side-jump mechanism as the dominant origin of the enhanced SHE. To further probe the explicit contribution of impurities, we next focus on $\rho_{SH}^{imp} = \rho_{SH}^{Pt-Oxide} - \rho_{SH}^{Pt}$ where $\rho_{SH}^{Pt-Oxide}$ and ρ_{SH}^{Pt} are the SH resistivity of Pt-Oxide and pristine Pt which were estimated from respective charge-spin interconversion efficiency. Here, the longitudinal resistivity from impurities ρ_{imp}, is identified using $\rho_{imp} = \rho_{Pt-Oxide} - \rho_{Pt}$ and prominent signature of linear trend in ρ_{SH}^{imp} *vs* ρ_{imp}^{2}, plot (see Fig. 4.12 (b)) establishes the extrinsic side-jump as the dominant origin of (3.5 times) 250% enhanced SHE in O-implanted Pt for a smaller trade-off in longitudinal resistivity from 55.4 to 159.5 μΩ-cm. For comparison, Yang et. al., obtained comparative θ_{DL} of ~ -0.30 with $\rho_{Ta(O)}$ of ~200 μΩ-cm [26] and Chen et. al., obtained a θ_{DL} of ~ -0.15 with a $\rho_{Ta(N)}$ of ~3000 μΩ-cm [42], which highlights the present O-implanted Pt as a more promising material for spintronic applications using DLT.

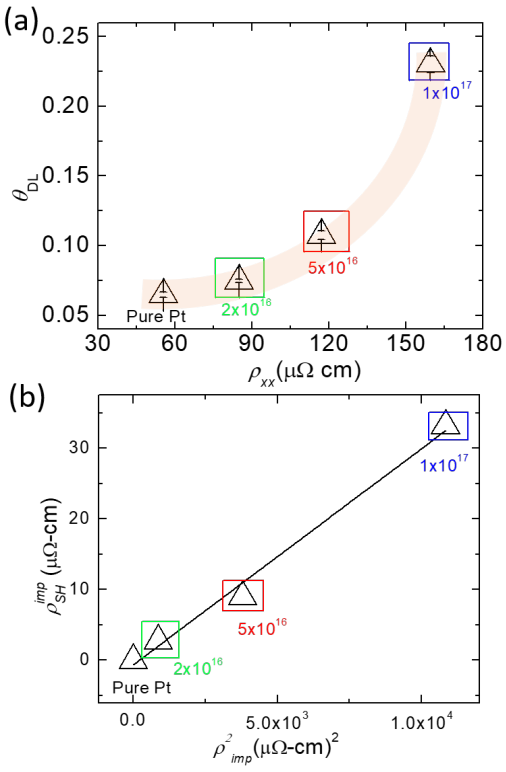

Figure 4.12. (a) θ_{DL} as a function of $\rho_{Pt-oxide}$ obtained for N0 (Pure Pt/NiFe), Pt(O) 2×10^{16}, Pt(O) 5×10^{16}, and Pt(O) 1×10^{17} (b) ρ_{SH}^{imp} vs ρ_{imp}^{2} behavior with solid black line as a linear fit.

4.6. Room temperature ST-FMR measurements: O_x sputtered Pt

In the beginning of this chapter, we discussed about the two methods used for incorporating Oxygen (O) in Pt. So, after discussing the first method, ion implantation, we will discuss the second method, which is DC sputtering to incorporate O in Pt.

4.6.1. Lineshape analysis: O_x sputtered Pt

To understand if the Oxygen incorporated via sputtering have a different concentration dependence on the SHE or not, we perform the lineshape analysis (using eqn. 4.4). By separating the V_{mix} spectra into S and A components using Eqn. 4.1, we plot the ratio of the weight factors S/A. The S/A for different concentration of PtO_x/NiFe is given in Fig. 4.13 (a)-(e). Using the ratio S/A averaged over a wide range of f = 5-11 GHz (Fig. 4.13 (b)), the θ_{DL}^{LS} is found to be monotonically increasing with the oxygen concentration dose as shown in Fig. 4.13 (c). We report a 2 times increase in θ_{DL}^{LS} from 0.08 to 0.16 as the oxygen concentration dose increases from 0 to 10 %.

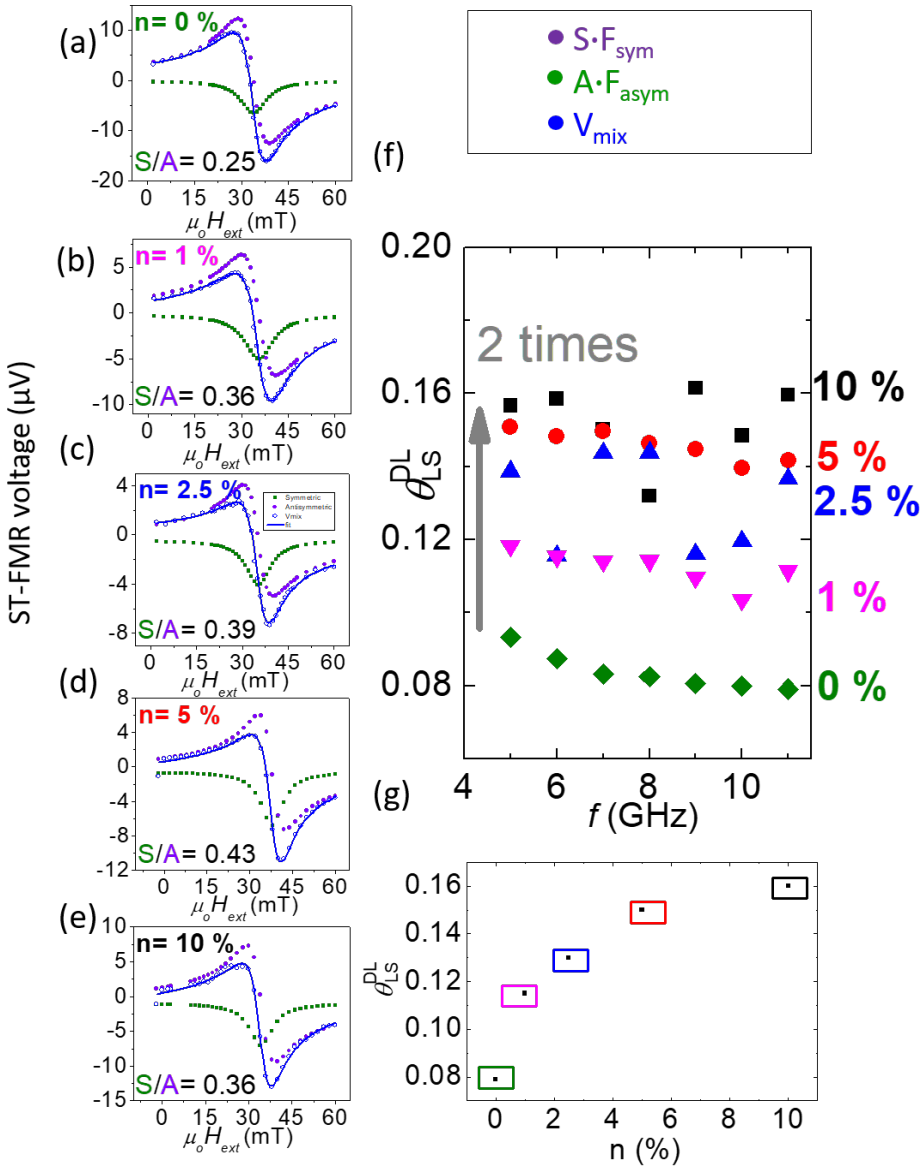

Figure 4.13. De-convolution fitting of V_{mix} measured at f = 5 GHz into symmetric and antisymmetric components displayed by green and violet solid line for Symmetric and Antisymmetric spectra for n= 0, 1, 2.5, 5, 10 % in (a)-(e), respectively. (f) θ_{DL}^{LS} as a function of f = 5-11 GHz and (g) θ_{DL}^{LS} averaged over 5-11 GHz as function of n (%).

4.6.2. Linewidth analysis: O_x sputtered Pt

To make the estimation of damping-like torque efficiency more comprehensive, we employed an alternative approach of linewidth modulation since this method is free from spin pumping [39]. Figure 4.13 shows the modulation in linewidth of ST-FMR spectra for three DC -4, 0, +4 mA. A clear change in $\mu_o\Delta H$ is seen. Additionally, the lineshape analysis assumes that the antisymmetric component (A) comprises purely of the Oersted torque, but it might arise from the field-like torque as well [40]. The inset of Fig. 4.14 (a) shows no change in resonance magnetic field, H_o which implies no presence of field like torque in the samples [40] .We find that the change in linewidth ($\mu_o\Delta H$) becomes more dominant for higher oxygen concentration. In Eqn. 4.5, $\theta_{DL}^{LW} = \frac{\frac{2e}{\hbar}\left(H_o+\frac{M_{eff}}{2}\right)\mu_o M_s t\left|\frac{\Delta\alpha_{eff}}{\Delta j_C}\right|}{sin\phi}$, is calculated from the slope of the $\left|\frac{\Delta\alpha_{eff}}{\Delta j_C}\right|$, deduced from the change in $\mu_o\Delta H$ as a function of I_{dc} as shown in Fig. 4.14 (b)-(e). Here, $\boldsymbol{j_c}$ is estimated from the resistivity, ρ_{xx} as shown in Fig. 4.14 (f). By measuring the change in linewidth as a function of applied DC, i.e., I_{dc} , (see we find that θ_{DL}^{LW} shows a similar trend of monotonic increase with O_x concentration as shown in Fig. 4.14 (g)).

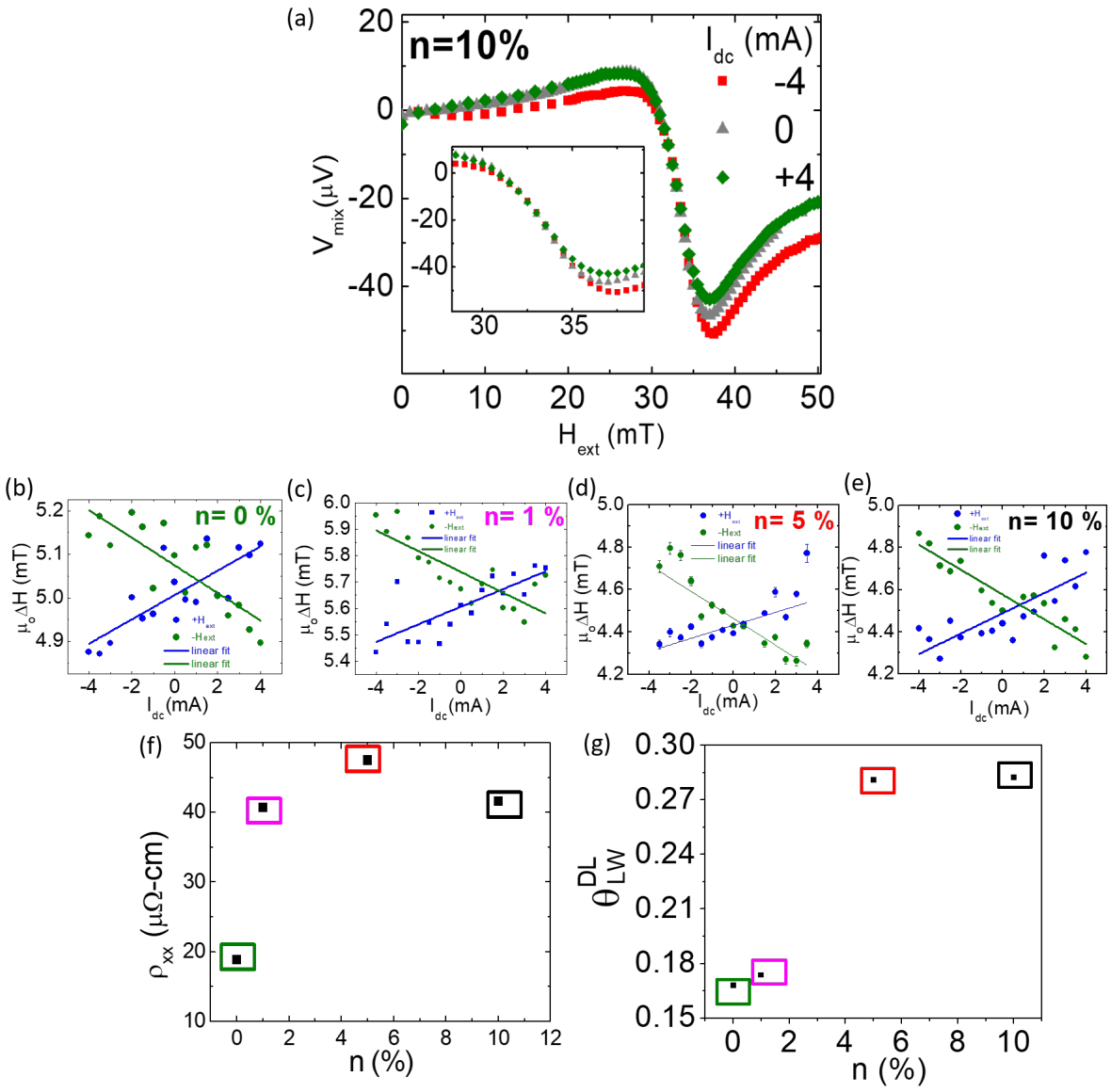

Figure 4.14. (a) DC-biased ST-FMR spectra for PtOx (n=10 %). Inset shows zoomed spectra. Varying ΔH plotted as a function of I_{dc} (+/- 4 mA) for f = 5 GHz with slope determined from linear fit (solid lines) for n= 0, 1, 5, 10 % in (b)-(e), respectively. (f) ρ_{xx} as a function of oxygen dose concentration (n %) and (g) θ_{DL}^{LW} as a function of n (%).

4.6.3. Angular dependent ST-FMR: O-implanted Pt and O_x sputtered Pt

Furthermore, to see if the O_x sputtered Pt follows the same trend of the expected $sin2\phi cos\phi$ in S and A, we performed the angular dependent ST-FMR measurements. Similar to O-implanted Pt, we see that both the S and A can be well fitted with the expected $sin2\phi cos\phi$ for both S and A as shown in Fig. 4.15.

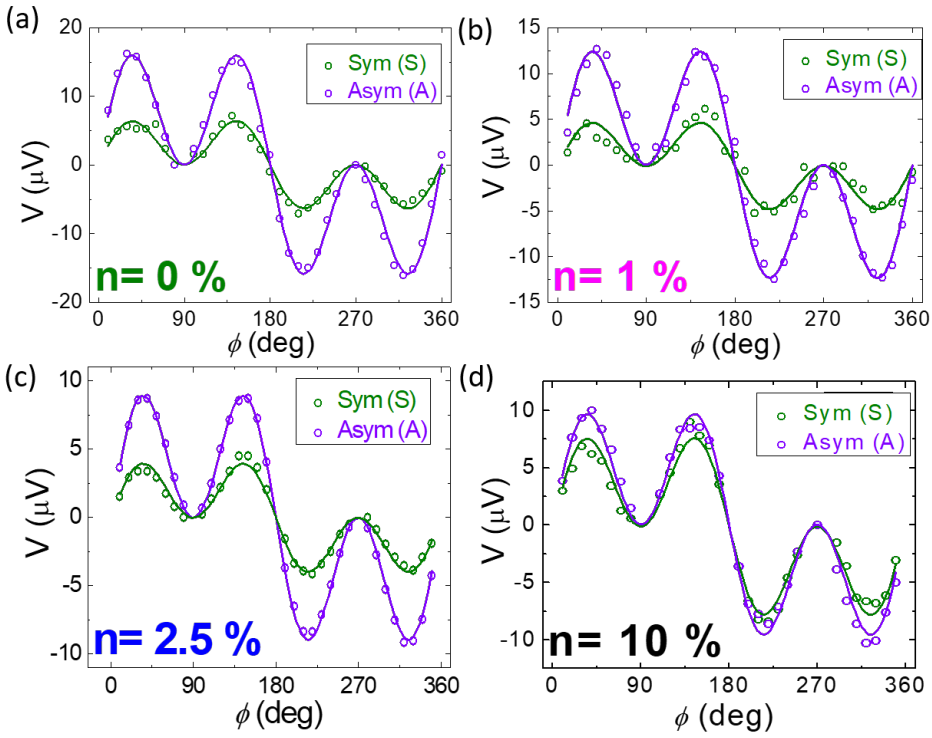

Figure 4.15. Angular dependence of symmetric and antisymmetric component measured at f = 5 GHz for PtO_x 0, 1, 2.5, and 10 % respectively.

4.6.4. Inverse spin Hall effect: O_x sputtered Pt

To understand if the Onsager reciprocity of the charge-to-spin interconversion holds for the O_x sputtered as well, we perform the SP-ISHE measurements at ϕ= 90°. By normalizing V_{ISHE} with the resistance of the device, we obtained an equivalent of charge current obtained from spin current via SP-

ISHE. We obtained a monotonic increase in the V_{ISHE}/R with the oxygen concentration from 0 to 10% (See Fig. 4.16). This is basically the spin-to-charge estimation assuming the other parameters such as spin diffusion length and cone angle are not drastically changed. Noticeably, we observed a similar trend for the charge-to-spin conversion where the θ_{DL}^{LS} and θ_{DL}^{LW} increased monotonically from 0 to 10%. Therefore, by using the ST-FMR and SP-ISHE measurements, we confirmed the Onsager reciprocity of SHE in both O-implanted Pt and O_x sputtered Pt.

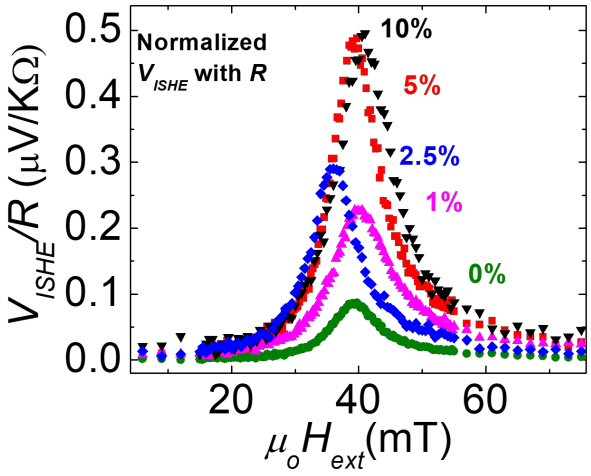

Figure 4.16. Output ISHE voltage V_{ISHE} normalized with device resistance (R) for different O_x sputtered Pt samples, n = 0, 1, 2.5, 5, 10 % as a function of H_{ext}.

4.6.5. Dominant mechanism of the enhanced SHE: O_x sputtered Pt

As discussed previously, the θ_{DL}^{LS} and θ_{DL}^{LW} as shown in Fig. 4.12 (g) and 4.13 (f) respectively seems to be widely tuned by controlling the concentration of oxygen. θ_{DL} seems to be proportional to longitudinal resistivity, ρ_{xx}, i.e., $\theta_{DL} \propto \rho_{xx}$. According to the theory of SHE, if the phenomenon is driven by the intrinsic and/or side-jump scattering [42, 43], then the resulting charge-to-spin conversion, θ_{DL} follows a monotonic dependence with ρ_{xx}. However, it has been challenging to disentangle the intrinsic from the side-jump scattering. We will come back to this problem later in Chapter 5. We also prepared two different batches of O_x sputtered Pt. In the batch 2, we modified the Ar:O_2 gas ratio to enhance the θ_{DL} even further.

Fig. 4.17 (a) shows the θ_{DL} as a function of ρ_{xx}. Therefore, we can see that both the O-implanted Pt and O_x sputtered Pt shows a $\theta_{DL} \propto \rho_{xx}$, dependence hinting that the dominant mechanism is intrinsic and/or side-jump scattering.

Furthermore, as discussed previously in this chapter, we study the dominant mechanism behind the enhancement of charge-to-spin conversion in O_x sputtered Pt. By fitting $\rho_{SH}^{imp} vs\ \rho_{imp}^{2}$, we did not obtain a linear fitting as shown in Fig. 4.17 (b). This shows that the dominant mechanism for the enhancement of SHE is not extrinsic side-jump scattering. Therefore, from the room temperature ST-FMR measurements, a possible dominant mechanism for enhancement of SHE is the intrinsic SHE. Later, in chapter 5, we will revisit the contribution to SHE via Temperature dependent ST-FMR measurements to explicitly find out the contribution of intrinsic and extrinsic side-jump scattering.

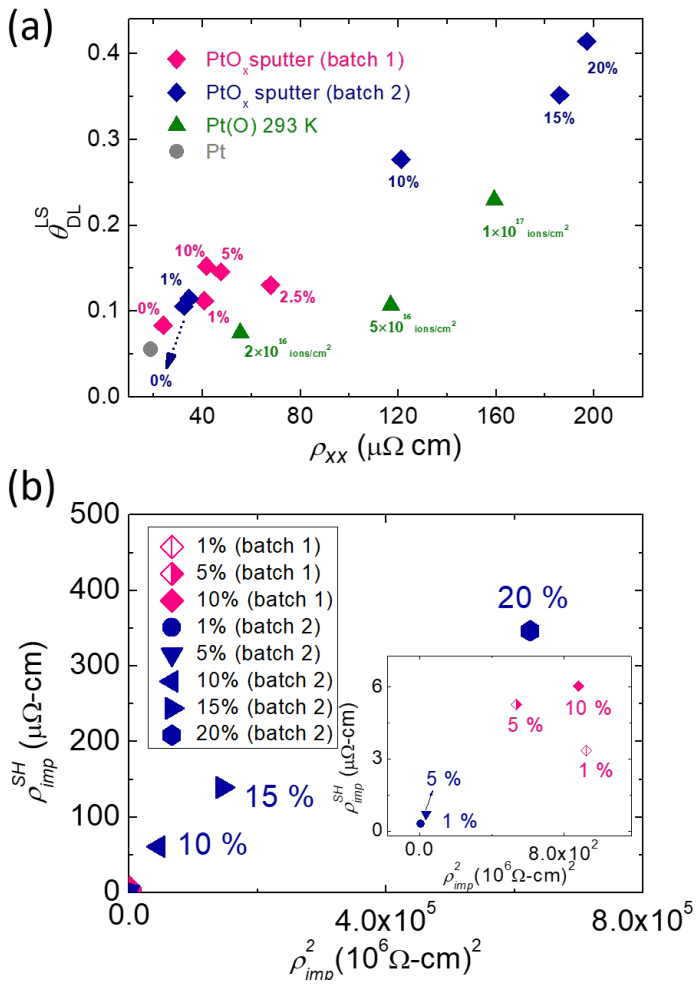

Figure 4.17. (a) θ_{DL} as a function of ρ_{xx} for O-implanted Pt, Pt(O) and O_x sputtered Pt, PtO_x along with Pure Pt, and (b) ρ_{SH}^{imp} *vs* ρ_{imp}^2 for PtO_x.

4.7. Conclusion

In conclusion, we demonstrated a simple and effective implantation method that promotes the extrinsic spin Hall effect in a Pt layer to significantly enhance the room temperature damping-like-torque efficiency by more than 250%. The highest O^+ ion implantation of 1×10^{17} ions cm^{-2} fluence at an optimized energy of 20 keV in Pt led to a very high damping-like-torque θ_{DL} = 0.230, which is 3.5 times larger than the control sample of pristine Pt (θ_{DL} = 0.064). Both spectral line shape and modulation of damping in ST-FMR measurements unveiled the highly dose dependent increase in θ_{DL} with improved spin transmission. Furthermore, linear fit of ρ_{SH}^{imp} *vs* ρ_{imp}^2 plot, highlights the side-jump scattering as the dominant mechanism of the enhanced SHE in our samples. Furthermore, we extend such an approach of incorporating Oxygen by the method of sputtering and obtain an $\theta_{DL} \propto \rho_{xx}$, dependence hinting that the dominant mechanism is intrinsic and/or side-jump scattering. Additionally, we observe an non-linear ρ_{SH}^{imp} *vs* ρ_{imp}^2 behavior depicting that the dominant mechanism is not side-jump scattering but an intrinsic SHE for the O_x sputtered Pt. Our results emphasize on the ability to efficiently interconvert spin into electrical currents via custom engineered ion implantation. The results presented in this chapter pertaining to O-implanted Pt have been published in Applied Physics Letters [44].

References for Chapter 4

1. H. L. Wang, C. H. Du, Y. Pu, R. Adur, P. C. Hammel, and F. Y. Yang, *Phys. Rev. Lett.* **112**, 197201 (2014).
2. Y. Niimi, Y. Kawanishi, D. H.Wei. C. Deranlot, H. X. Yang, M. Chshiev, T. Valet, A. Fert, Y. Otani, *Phys. Rev. Lett.* **109**, 156602 (2012).
3. X. Shu, J. Shou, J. Deng, W. Lin, J. Yu, L. Liu, C. Zhou, P. Yang, J. Chen, *Phys. Rev. Mater.* **3**, 114410 (2019).
4. H. An, Y. Kageyama, Y. kanno, N. Enishi, and K. Ando, *Nat. Commun.* **7**, 13069 (2016).
5. S. Haku, H. Moriya, H. An, A. Musha, and K. Ando, *Phys. Rev. B* **104**, 174403 (2021).
6. L. Liu, O.J Lee, T. J. Gudmundsen, D. C. Ralph, and R. A. Burhman, *Phys. Rev. Lett.* **109**, 096602 (2012).
7. A. Manchon, J. Železný, I. M. Miron, T. Jungwirth, J. Sinova, A. Thiaville, K. Garello, and P. Gambardella, *Rev. Mod. Phys.* **91**, 035004 (2019).
8. A. Soumyanarayanan, N. Reyren, A. Fert, and C. Panagopoulos, *Nature,* **539**, 509 (2016).
9. J. E. Hirsch, Phys. Rev. Lett. **83**, 1834 (1999).
10. L. Liu, C.-F. Pai, Y. Li, H. W. Tseng, D.C. Ralph, and R.A. Burhman, *Science* **336**, 555 (2012).
11. S. Emori, U. Bauer, S. M. Ahn, E. Martinez, and G. S. D. Beach, *Nat. Mater*. **12**, 611 (2013).
12. W. Zhang, W. Han, X. Jiang, S. –H. Yang, and S. S. P. Parkin, *Nat. Phys*. **11**, 496 (2015).
13. H. Kurebayashi, J. Sinova, D. Fang, A. C. Irvine, T. D. Skinner, J. Wunderlich, V. Novák, R. P. Campion, B. L. Gallagher, E. K. Vehstedt, L. P. Zârbo, K. Výborný, A. J. Ferguson, and T. Jungwirth, *Nat. Nanotechnol*. **9**, 211 (2014).
14. J.Ryu. S. Lee, K. J. Lee, and B. G. Park, *Adv. Mater.* **32**, 1907148 (2020).
15. B. Divinsky, V. E. Demidov, S. Urazdin, R. Freeman, A. N. Rinkevich, and S.O Demokritov, *Adv. Mater.* **30**, 1802837 (2018).
16. Q. Shao, P. Li, L. Liu, H. Yang, S. Fukami, A. Razavi, H. Wu, F. Freimuth, Y. Mokrousov, M. D. Stiles, S. Emori. A. Hoffman, J. Åkerman, K. Roy, J. -P. Wang, S. -H. Yang, K. Garellob, and W. Zhang, *IEEE Trans. Magn*. (2021).
17. T. Chen, R. K. Dumas, A. Eklund, P. K. Muduli, A. Houshang, A. A. Awad, P. Dürrenfeld, B. G. Malm, A. Rusu, and J. Åkerman, *Proceedings of the IEEE*, **104,** 1919 (2016).
18. M. Li, L. Jin, Y. H. Rao, Z. Zhong, X. Tang, B. Liu, H. Meng, Q. Yang, Y. Lin, and H. Zhang, *Journal of Mag. and Magn. Mater.* **507**, 166860 (2020).
19. W. Iwamoto, T. Yamamoto, K. Tsuchii, Y. Tazaki, A. Asami, H. Hayashi, Y. Einaga, and K. Ando, *ACS Appl. Electron. Mater.* **2**, 2098 (2020).

20. G. D. H. Wong, W. C. Law, F. N. Tan, W. L. Gan, C. C. I. Ang, Z. Xu, C. S. Seet, and W. S. Lew, *Sci. Rep*. **10**, 9631 (2020).
21. X. Zhou, M. Tang, X. L. Fan, X. P. Qiu, and S. M. Zhou, *Phys. Rev. B* **94**, 144427 (2016).
22. L. Zhu, D. C. Ralph, and R. A. Burhman, *Phys. Rev. Appl.* **10**, 031001 (2018). 1
23. M. -H. Nguyen, C. -F. Pai, K. X. Nguyen, D. A. Muller, D. C. Ralph, and R. A. Burhman, *Appl. Phys. Lett.* **106**, 222402 (2015).
24. H. Mazraati, M. Zahedinejad, and J. Åkerman, *Appl. Phys. Lett.* **113**, 092401 (2018).
25. H. An. Y. Kanno, A. Asami, and K. Ando, Phys. Rev. B **98**, 014401 (2018).
26. L. Yang, Y. Fei, K. Zhou, L. Chen, Q. Fu, L. Li, C. Yan, H. Li, Y. Du, and R. Liu, *Appl. Phys, Lett.* **118**, 032405, (2021).
27. K. U. Demasius, T. Phung, W. Zhang, B. P. Hughes, S. H. Yang, A. Kellock, W. Han, A. Pushp, and S. S. P. Parkin, Nat. Commun. **7**, 10644 (2016).
28. Z. Xu, G. D. H. Wong, J. Tang, E. Liu, W. Gan, F. Xu, and W. S. Lew, *Appl. Phys. Lett.* **118**, 062406 (2021).
29. S. Jiang, R. Khymyn, S. Chung, T. Q. Le, L. H. Diez, A. Houshang, M. Zahedinejad, D. Ravelosona, and J. Åkerman, *Appl. Phys. Lett*. **116**, 072403 (2020).
30. W. L. Peng, J. Y. Zhang, G. N. Feng, X. L. Xu, C. Yang, Y. L. Jia, and G. H. Yu, *Appl. Phys. Lett.* **115**, 092402 (2019).
31. X. Zhao, Y. Liu, D. Zhu, M. Sall, X. Zhang, H. Ma, J. Langer, B. Ocker, S. Jaiswal, G. Jakob, M. Kläui, W. Zhao, and D. Ravelosona, *Appl. Phys. Lett.* **116**, 242401 (2020).
32. U. Shashank, R. Medwal, T. Shibata, R. Nongjai, J. V. Vas, M. Duchamp, K. Asokan, R. S. Rawat, H. Asada, S. Gupta, and Y. Fukuma, Adv. Quantum Technol. **4**, 2000112 (2021).
33. L. Liu, T. Moriyama, D. C. Ralph, and R. A. Burhman, *Phys. Rev. Lett.* **106**, 036601 (2011).
34. M. Harder, Y. Gui, and C.-M. Hu, *Phys. Rep.* **661**, 1 (2016).
35. S. Gupta, R. Medwal, D. Kodama, K. Kondou, Y. Otani, and Y. Fukuma, *Appl. Phys. Lett.* **110**, 022404 (2017).
36. R. Medwal, S. Gupta, R. S. Rawat, A. Subramanian, and Y. Fukuma, *Phys. Status Solidi RRL* **13**, 1900267 (2019).
37. J. Sklenar, W. Zhang, M. B. Jungfleisch, H. Saglam, S. Grudichak, W. Jiang, J. E. Pearson, J. B. Ketterson, and A. Hoffman, *Phys. Rev. B* **95**, 224431 (2017).
38. D. MacNeill, G. M. Steihl, M. H. D. Guimaraes, R. A. Burhman, J. Park, and D. C. Ralph, *Nat. Phys.* **13**, 300 (2017).
39. A. Okada, Y. Takeuchi, K. Furuya, C. Zhang, H. Sato, S. Fukami, and H. Ohno, *Phys. Rev. Appl*. **12**, 014040 (2019).

40. T. Nan, S. Emori, C. T. Boone, X. Wang, T. X. Oxholm, J. G. Jones, B. M. Howe, G. J. Brown, and N. X. Sun, *Phys. Rev. B* **91**, 214416 (2015).
41. Y. Niimi, M. Morota, D. H. Wei, C. Deranlot, M. Basletic, A. Hamzic, A. Fert, and Y. Otani, *Phys. Rev. Lett.* **106**, 126601 (2011).
42. T.-Y. Chen, C.-T. Wu, H.-W. Yen, and C.-F. Pai, *Phys. Rev. B* **96**, 104434 (2017).
43. L. Qian, K, Wang, Y. Zheng, and G. Xiao, *Phys. Rev. B* **102**. 094438 (2020).
44. U. Shashank, R. Medwal, Y. Nakamura, J. R. Mohan, R. Nongjai, A. Kandasami, R. S. Rawat, H. Asada, S. Gupta, and Y. Fukuma, *Appl. Phys. Lett.* **118** 252406 (2021).

Chapter 5

Disentanglement of intrinsic and extrinsic side-jump scattering induced spin Hall effect in O and N-implanted Pt

(This chapter is based on the results submitted to Physical Review B [Ref. 53] and unpublished temperature dependent ST-FMR measurements/analysis from S and O-implanted Pt and O_x sputtered Pt)

In the last chapter, we studied the two methods to incorporate a non-metallic element oxygen in Pt. Motivated by the enhancement of damping-like torque (DLT) in Pt by incorporating S, O in Pt, via ion implantation, we implanted another, yet less explored non-metallic element Nitrogen in Pt, and studied the dose and temperature dependent ST-FMR studies by comparing with S and O-implanted Pt. But, as seen in the last chapter, we were also interested in finding the origin of enhancement in DLT. So, in this chapter, we will explore how temperature dependent studies becomes so important in unraveling the underlying origin of enhancement of SHE.

5.1. Introduction

As discussed in chapter 1, the enhancement in DLT can arise from various origin, one of which is the Spin Hall effect (SHE). The SHE [1-4] has been garnering much attention in the development of spin-orbit torque magnetic random access memory (SOT-MRAM) [5-8] due to its low power consumption and efficient magnetization switching. As explained in previous chapters, a charge current density $\boldsymbol{j_c}$ in a heavy metal (HM) is converted into a spin current density $\boldsymbol{js}$ via SHE, which then exerts an in-plane damping-like SOT $\boldsymbol{\tau_{DL}}$ on the magnetization of the adjacent ferromagnet (FM) [9, 10]. The ratio of $\boldsymbol{j_s}$ to $\boldsymbol{j_c}$ is called the damping-like torque (DLT) efficiency θ_{DL} (also termed as charge-to-spin conversion efficiency or spin Hall angle). With the strength of spin-orbit coupling (SOC) depending on the atomic number Z, 5d transition metals such as Pt, Ta, W [9, 11-15] have been improved by alloying with other heavy metals with large Z such

as Au, Pd [16-18]. Alternatively, non-metallic elements (impurities with smaller Z) have been incorporated into 5d transition metals (host with larger Z). Recently, as experimentally demonstrated by The difference in Z between the host and the impurity has been found to result in an enhancement of SHE [19]. θ_{DL} has been enhanced by incorporating non-metallic elements into 5d transition metals such as sulfur (S) in Pt [20], oxygen (O) in Pt [21-24], Ta [25], and W [26], and nitrogen (N) in Pt [27], Ta [28] and W [29]. However, the effects of nitrogen (N) incorporation are still underexplored, especially in controlling the longitudinal resistivity ρ_{xx}, which is an important yardstick to be considered for SOT-MRAM applications. Incorporation of nitrogen has led to an undesirable increase in ρ_{xx} of Ta(N) and W(N) [28, 29]. Furthermore, the origin responsible for the enhancement in SHE in non-metallic doped Pt, Ta, and W has not yet been confirmed explicitly [25, 27, 28, 29]. Studies on the temperature dependence of the SHE in 5d transitions metal having non-metallic impurities, are scarce. Most room temperature studies have reported a limited variation of θ_{DL} with resistivity ρ_{xx}.

We had discussed briefly in chapter 1 about the mechanism responsible for the enhancement of SHE. Let us recapitulate one more time. There have been extensive efforts to enhance the SHE, mainly via two mechanisms: intrinsic and extrinsic SHE [30-34]. The intrinsic SHE depends on the berry curvature of the material, in which an anomalous velocity arises from a momentum-space berry phase [31]. It leads to an elastic event in which the wave-vector $\vec{k}$ of the up-spin and down-spin electrons generated from charge current is conserved [32, 33], and is typically seen in 4d and 5d transition metals. The extrinsic SHE arises when impurities are introduced in the HM, and can be further classified into side-jump and skew-scattering [34]. For side-jump scattering, a discontinuous side-ways displacement is created near the impurities for the up-spin and down-spin electrons generated from charge current, leading to an elastic event due to the cancellation of $\vec{k}$, and is found in materials with high amount of impurity concentrations in host. The skew scattering, however, is different from the intrinsic and side-jump mechanism as scattering bends or skews the trajectories of up-spin and down-spin electrons in different directions, and is found in super-clean or low resistivity materials [32]. This leads to a condition where $\vec{k}$ is not conserved, resulting in an inelastic event. Given the separation of SHE based on elastic and inelastic events, a strong correlation between spin Hall

conductivity, σ_{SH}^{xy} and momentum relaxation time τ_{relax} can be obtained. Intrinsic SHE and side-jump scattering share the same scaling, with σ_{SH}^{xy} being independent of τ_{relax}. Skew scattering shows $\sigma_{SH}^{xy} \propto \tau_{relax}$ scaling. Therefore, it is hard to disentangle the contribution of the intrinsic from the side-jump scattering. Despite tremendous efforts [18, 27, 28, 29], a clear separation between the contributions of intrinsic and side-jump scattering to the SHE in non-metallic element doped HM has eluded us so far. The limited variation of θ_{DL} with resistivity ρ_{xx} at room temperature and the choice of host/impurity combinations, especially for incorporation of non-metallic elements in the HM, need to be addressed.

In this chapter, we present a successful disentanglement of intrinsic and extrinsic side-jump scattering by studying the SHE using a non-metallic Nitrogen (N) implanted in Pt, at 100-293 K using spin-torque ferromagnetic resonance (ST-FMR) lineshape (spectral) analysis. We observe a crossover from intrinsic to extrinsic side-jump scattering mechanism as the N-ion dose increases from 2×10^{16} to 1×10^{17} ions/cm^2. We also compare the disentanglement of intrinsic and side-jump scattering for previous samples discussed in chapter 3 and 4, i.e., the Pt(S) and Pt(O), respectively.

5.2. Experimental details

Thin films of Pt (10 nm)/ MgO (10 nm)/ Al_2O_3 (10 nm) layers were deposited on a Si/SiO_2 substrate at room temperature using an ultrahigh vacuum sputtering. The thin film stacks were implanted sequentially with doses of 2×10^{16} ions/cm^2, 5×10^{16} ions/cm^2 and 1×10^{17} ions/cm^2 by an N-ion source beam having an energy of 20 keV. After ion implantation, the capping layers of MgO and Al_2O_3 were removed by Ar^+ ion milling and then a FM layer of NiFe (5nm) was sputtered on these samples (See Appendix A). Hereafter, they will be referred to as Pt(N) 2×10^{16}, Pt(N) 5×10^{16}, and Pt(N) 1×10^{17}. All the three bilayer samples were then patterned into rectangular micro strips using photolithography. Thereafter, Ti (10 nm)/Al (200 nm) electrodes were deposited. The design of the co-planar waveguides for ST-FMR measurements is shown in Fig. 1(a). The temperature dependent ST-FMR measurements were performed in the range of 100-293 K. To compare the mechanism for other implanted samples viz. the Pt(S) and Pt(O), temperature dependent ST-FMR measurements were also performed in the same range of 100-293 K.

5.3. Results and discussion

5.3.1. Dose-dependent ST-FMR measurements at room temperature (293 K)

To study the influence of dose on SHE in Pt(N), we first performed the ST-FMR based lineshape analysis to determine θ_{DL}. Figure 1(a) shows the schematic of the ST-FMR measurement set-up. In this technique, when a microwave current I_{rf} flows in the longitudinal direction of HM/FM bilayer, a transverse spin current density $\boldsymbol{j_s}$ is generated, which exerts a DLT, on the local magnetization of FM. So, an I_{rf} was passed in the longitudinal direction of the device with an applied power of 10 dBm. The I_{rf} generates an rf Oersted field h_{rf} (according to Ampère's Law), which simultaneously exerts an Oersted field torque τ_{OFT}. An external magnetic field $\mu_o H_{ext}$ was swept in the range of ±240 mT at an angle of ϕ = 45° with respect to the longitudinal direction of the device. At resonance condition, both $\boldsymbol{\tau_{DL}}$ and $\boldsymbol{\tau_{OFT}}$ drive the magnetization precession in the FM, which results in a periodically varying resistance ΔR due to the anisotropic magnetoresistance (AMR) of NiFe. The mixing of the oscillating ΔR and I_{rf} produces a ST-FMR voltage, which is detected using a lock-in amplifier via a bias tee, and is expressed as [9, 20, 25, 26]:

$$V_{mix} = SF_{sym}(H_{ext}) + AF_{asym}(H_{ext}), \tag{5.1}$$

where, $F_{sym}(H_{ext}) = \frac{(\Delta H)^2}{(H_{ext}-H_o)^2+(\Delta H)^2}$, is the symmetric part of the V_{mix} spectrum, $F_{asym}(H_{ext}) = \frac{\Delta H(H_{ext}-H_o)}{(H_{ext}-H_o)^2+(\Delta H)^2}$, is the antisymmetric part, ΔH and H_0 are the half-width-at-half-maximum (linewidth) and the resonance field, and S and A are the weight factors of the symmetric and antisymmetric spectra respectively. For the observed spectra, while the symmetric component is dominated by the τ_{DL} contribution (from $\boldsymbol{j_s}$), the antisymmetric component is primarily dominated by τ_{OFT} (from $\boldsymbol{jc}$). Figure 1(b) shows the de-convoluted ST-FMR spectra of V_{mix} measured at 5 GHz for Pt(N) 5×10^{16}.

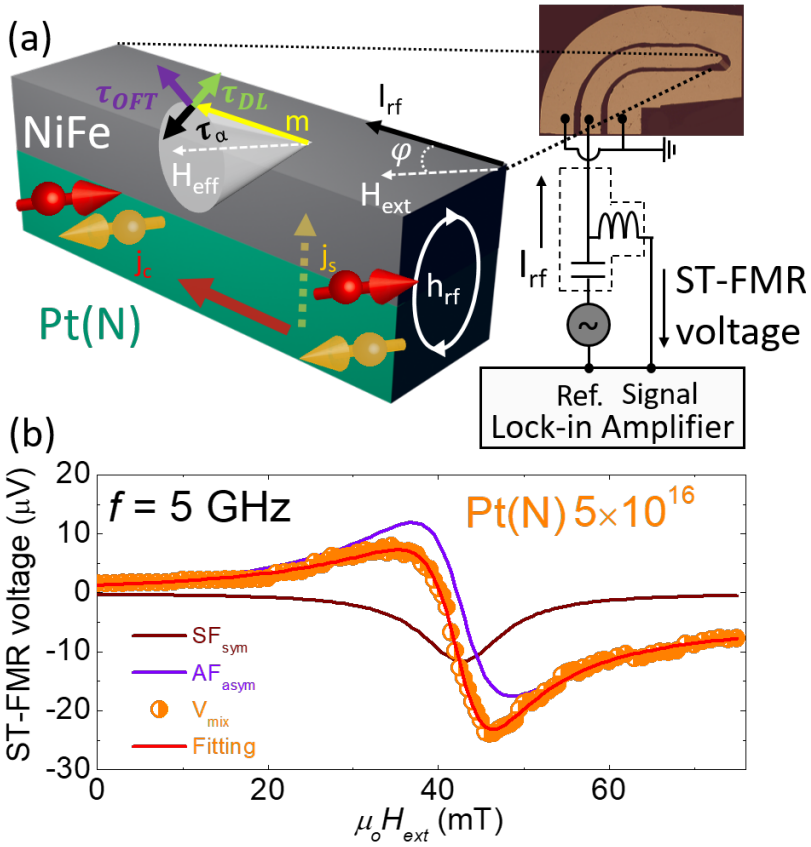

Figure 5.1. a) Schematic showing ST-FMR measurement technique and detection principle for a bilayer thin film, along with an optical image of the micro-device. (b) ST-FMR spectra (V_{mix}) for f = 5 GHz obtained for Pt(N) 5×10^{16}, fitted using Eq. (1). De-convolution fitting of V_{mix} into symmetric and antisymmetric components displayed by brown and violet solid lines respectively.

Next, to understand the contribution of the symmetric and antisymmetric component for the other dose of Pt(N), we also checked the de-convolution fitting of V_{mix} for Pt(N) 2×10^{16} and Pt(N) 2×10^{17} as shown in Fig. 5.2 (a), (b). Next, to extract the f-dependent properties, we performed the ST-FMR measurements for a wide range of f = 5-11 GHz. The broad range of ST-FMR spectra obtained for applied frequency f = 5-11 GHz is shown for all the samples in 5.2 (c)-(e). From the f-dependent ST-FMR, the Gilbert damping parameter α which depends on linewidth ΔH, is estimated using [21]:

$$\Delta H = \Delta H_o + \frac{2\pi f}{\gamma}\alpha, \tag{5.2}$$

where, γ is the gyromagnetic ratio and ΔH_o is the inhomogeneous linewidth broadening which is independent of f. Referring to (Fig. 5.2 (f)), α is estimated from the slope of ΔH plotted as a function of f. The value of α is higher for Pt(N) 5×10^{16} as compared to that of Pt(N) 2×10^{16} and Pt(N) 1×10^{17} . To quantify θ_{DL}, we performed the lineshape analysis of the ST-FMR spectrum, using Eq. (3) [9]:

$$\theta_{DL} = \frac{S}{A}\frac{e\mu_o M_s t d}{\hbar}\sqrt{1+\frac{M_{eff}}{H_o}}, \tag{5.3}$$

where e is the elementary charge, ħ is the reduced Planck constant, t is the thickness of the NiFe layer, d is the thickness of the heavy metal layer and the effective magnetization M_{eff} is obtained from Kittel fitting. The figures in Appendix B show the obtained values of θ_{DL} for the studied frequency range of 5-11 GHz. θ_{DL} is found to be invariant with frequency, implying a negligible role of thermal effect and non-controlled relative phase between I_{rf} and h_{rf} that arises from sample design [21, 35, 36.] The average θ_{DL} values obtained are 0.119 ± 0.002 for Pt(N) 2×10^{16}, 0.132 ± 0.008 for Pt(N) 5×10^{16} and 0.098 ± 0.008 for Pt(N) 1×10^{17}. Noticeably, the θ_{DL} of pure sample (Pt/NiFe) is found to be 0.062± 0.004. It demonstrates that ion implantation provides a better alternative to incorporate nitrogen in Pt when compared to the sputtering method, as even a small dose of 2×10^{16} ions/cm^2 in Pt leads to ~1.9 times enhancement in θ_{DL} from 0.062 to 0.119. We find a ~2.2 times enhancement in θ_{DL} from 0.062 (Pt) to 0.132 (Pt(N) 5×10^{16}). However, we

observe a non-monotonic dependence of θ_{DL} on implantation dose, similar to Xu et. al. [27] where nitrogen was incorporated in Pt via sputtering. On the contrary, we observed a monotonic dependence of θ_{DL} on oxygen (O) implantation dose [21] in chapter 4 and also in sputtered Pt.

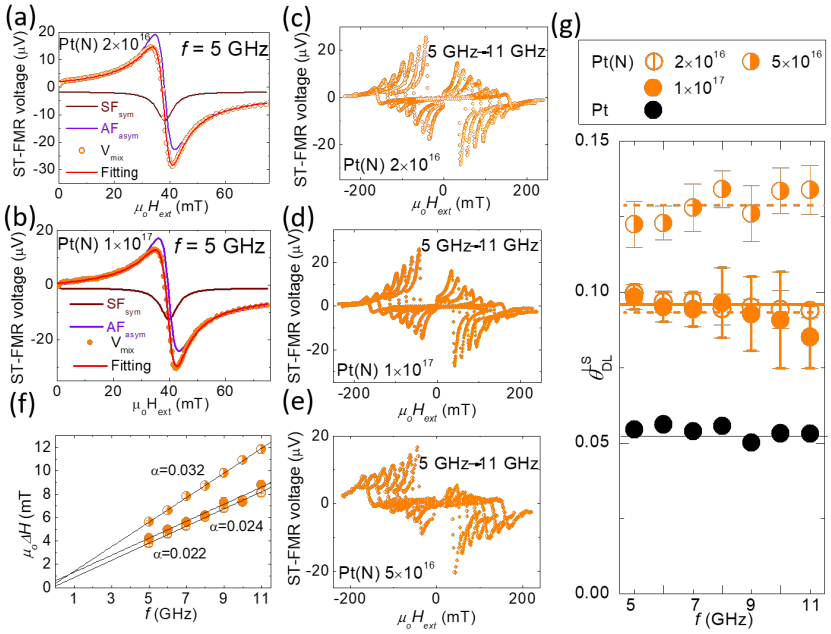

Figure 5.2. De-convolution fitting of ST-FMR voltage (spectrum) measured at f = 5 GHz into symmetric and antisymmetric components displayed by brown and violet solid lines respectively for (a) Pt(N) 2×10^{16}, and (b) Pt(N) 1×10^{17}, ST-FMR spectra V_{mix} obtained for (c) Pt(N) 2×10^{16}, (d) Pt(N) 1×10^{17}, (e) Pt(N) 5×10^{16}. (f) $\mu_o\Delta H$ vs f (with solid lines as linear fit), and (g) Frequency invariant θ_{DL} obtained for Pt(N) 2×10^{16}, Pt(N) 5×10^{16}, Pt(N) 1×10^{17} and Pure Pt. The lines represent the average value.

5.3.2. Angular dependent ST-FMR measurements

The lineshape analysis which uses the ratio of symmetric (S) to antisymmetric (A) component at one fixed angle of $\phi = 45°$, could be a hindrance in revealing the complete picture of exerted spin-orbit torques [21, 36]. There may be hidden effects apart from SHE, such as effective field with different spin polarization, poor device designs, Nernst heating, etc. which may serve as an artifact and lead to an unreliable assessment of spin-orbit torque. So, we performed the angular ST-FMR measurements by varying the angle between applied H_{ext} and length of device axis from $\phi = 0^o$ to 360^o. By deconvolution of V_{mix} using Eq. (1) into S and A, we fitted the data with the anticipated $\sin2\phi\cos\phi$ for the implanted sample

Pt(N) 2×10^{16}, Pt(N) 5×10^{16} and Pt(N) 1×10^{17} (Fig. 5.3 (a), (b), (c)). It shows that the SOT traces similar lineshape when the magnetization is rotated by 180° which implies that there is no breaking of the twofold (180° +ϕ) and mirror (180° -ϕ) symmetries of torques, affirming SHE as the only origin of the rectified voltage [21] obtained by ST-FMR. The $\cos\phi$ arises from τ_{DL} and τ_{OFT} in S and A, respectively, while $\sin2\phi$ arises from AMR.

5.3.3. Spin Pumping Contribution

Spin pumping contribution V_{sp} in the symmetric component of the ST-FMR spectrum may have a role to play in the high values of α, $g_{eff}^{\uparrow\downarrow}$ and θ_{DL} for Pt(N) 5×10^{16}, and therefore it might be naive to not identify this contribution. To confirm that the enhanced α, $g_{eff}^{\uparrow\downarrow}$ and θ_{DL} in N-implanted sample may be attributed to the enhanced DLT, and is not due to the contribution of spin pumping voltage in the symmetric component of ST-FMR spectrum, we investigated the spin pumping contribution V_{sp} using the derived values of $g_{eff}^{\uparrow\downarrow}$ and θ_{DL}^{LS} by [11]:

$$V_{SP} = \frac{\theta_{DL} l \lambda_{sd}}{d\sigma_{Pt(N)} + t\sigma_{NiFe}} tanh\left(\frac{d}{2\lambda_{sd}}\right)\left(\frac{2e}{h}\right) j_S \sin(\phi)\,, \tag{5.4}$$

where, l is the length of the device, λ_{sd} is the spin diffusion length of Pt(N) layer, d and $\sigma_{Pt(N)}$ are the thickness and conductivity of Pt(N), t and σ_{NiFe} are the thickness and conductivity of NiFe, and ϕ is the angle between H_{ext} and I_{rf} applied in the longitudinal direction of device (45°), j_S is the spin current density from the precessing NiFe into the Pt(N), given as $j_S = \frac{h}{2} f \sin^2(\theta_C) g_{eff}^{\uparrow\downarrow}$, where the precession cone angle θ_C is given by $\theta_C = \frac{1}{dR/d\phi}\frac{2}{I_{rf}}\sqrt{S^2 + A^2}$, $dR/d\phi$ is obtained from anisotropic magnetoresistance, and I_{rf} is the current in the device. The ratio of the spin pumping voltage V_{sp} to the symmetric component S is found to be 0.39% for Pt(N) 2×10^{16}, 0.49% for Pt(N) 5×10^{16} and 0.25% for Pt(N) 1×10^{17}, which are all less than 1%. Figure 5.3 (d) shows S and V_{sp} plotted for Pt(N) 5×10^{16} as a function of frequency, confirming the negligible contribution of V_{sp} as compared to S.

5.3.4. Spin mixing conductance

Spin mixing conductance $g_{eff}^{\uparrow\downarrow}$ is an important parameter that provides a better picture of transversely generated ***js*** created at the FM/HM interface. Based on the theory of spin pumping, assuming that there is no significant spin memory loss, the $g_{eff}^{\uparrow\downarrow}$ [21] can be estimated from the linewidth difference δ of ST-FMR spectra ($\delta = \Delta H_{Pt(N)/NiFe} - \Delta H_{NiFe}$), and is given by:

$$g_{eff}^{\uparrow\downarrow} = \left(\frac{\gamma}{2\pi f}\right)\left(\frac{4\pi M_s t\delta}{g\mu_o\mu_B}\right), \tag{5.5}$$

where, g is the Landé g factor, μ_o is the permeability of free space, M_S is the saturation magnetization of NiFe and μ_B is the Bohr magneton constant. The average value of $g_{eff}^{\uparrow\downarrow}$ is found to be 2.08×10^{19} m^{-2} for Pt(N) 2×10^{16}, 3.10×10^{19} m^{-2} for Pt(N) 5×10^{16} and 2.57×10^{19} m^{-2} for Pt(N) 1×10^{17} as shown by the dashed lines in Fig. 5.3 (e). Most importantly, Pt(N) 5×10^{16} was found to have a higher $g_{eff}^{\uparrow\downarrow}$ value in comparison to Pt(N) 2×10^{16} and Pt(N) 1×10^{17}. For a HM layer much thicker than its spin diffusion length, θ_{DL} is found to be proportional to $g_{eff}^{\uparrow\downarrow}$ [37]. This is linked to the fact that the Gilbert damping parameter $g_{eff}^{\uparrow\downarrow}$ and θ_{DL} of Pt(N) 5×10^{16} is found to be larger than that of Pt(N) 2×10^{16} and Pt(N) 1×10^{17}.

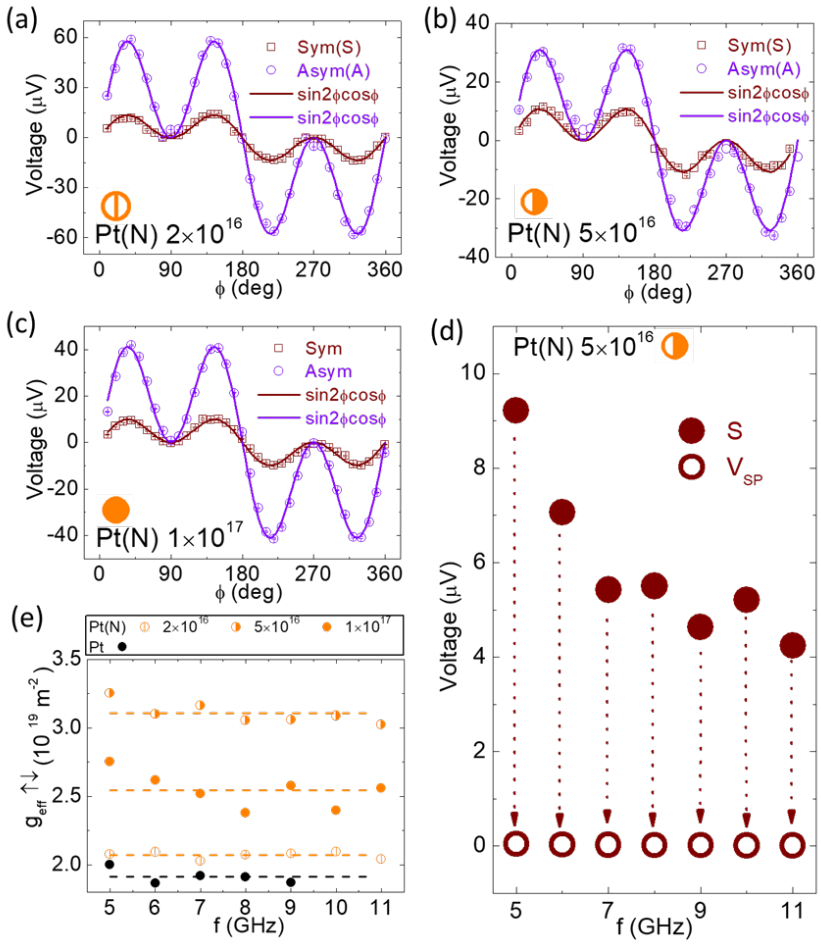

Figure 5.3. (a), (b), (c) Angular dependence of symmetric (S) and antisymmetric (A) components in ST-FMR spectra for Pt(N) 2×10^{16}, Pt(N) 5×10^{16}, and Pt(N) 1×10^{17} (f = 5 GHz) with solid lines fitted by $\sin 2\phi \cos \phi$. (d) Symmetric component (S) and spin pumping contribution (V_{sp}) plotted as a function of frequency for Pt(N) 5×10^{16}. (e) $g_{eff}^{\uparrow\downarrow}$ obtained as a function of f for Pt(N) 2×10^{16}, Pt(N) 5×10^{16}, Pt(N) 1×10^{17} along with pure Pt. The dashed lines represent the average value.

5.3.5. Correlation of associated properties with dose

After confirming the unbroken symmetry of torques, negligible spin pumping contribution and spin mixing conductance, we proceed to picturize these associated properties as a function of implantation dose. To picturize the correlation among ρ_{xx}, α, $\mu_o M_{eff}$, spin mixing conductance $g_{eff}^{\uparrow\downarrow}$ and θ_{DL} for Pt(N), we plot these parameters as a function of implantation dose as shown in Fig. 5.4. First, ρ_{xx} is found to be monotonically increasing in Fig. 5.4(a), which is similar to previous report [27]. Second, α shows a non-monotonic dependence with an increase of N-ion dose, where a maximum value of 0.032 is obtained for the dose of 5×10^{16} (Fig. 5.3(b)). Third, M_{eff} decreases with increasing N-ion dose (Fig. 5.3(c)). Noticeably, a minimum $\mu_o M_{eff}$ = 610 mT is seen for Pt(N) 5×10^{16} as compared to 711 mT for Pt(N) 2×10^{16} and 686 mT for Pt(N) 1×10^{17}, indicating a change in the perpendicular magnetic anisotropy field H_p. The $\mu_o M_{eff}$ of pure Pt is found to be 765 mT, indicating less H_p. Fourth, the $g_{eff}^{\uparrow\downarrow}$ shows a similar trend as obtained for α (Fig. 5.3(d)), indicating an enhanced ***js*** at the HM/FM interface. Fifth, θ_{DL} in Fig. 5.3(e) shows a similar trend as obtained for α and $g_{eff}^{\uparrow\downarrow}$. Summarizing the dose dependent results, both α and θ_{DL} increase monotonically from 0 to 5×10^{16} ions/cm^2 and then suddenly decrease for 1×10^{17} ions/cm^2, similar to the results obtained by Xu et. al. [27]. In agreement with the highest α and $g_{eff}^{\uparrow\downarrow}$ for Pt(N) 5×10^{16}, θ_{DL} is found to be maximum for Pt(N) 5×10^{16} [37]. However, due to the limited variation of θ_{DL} with ρ_{xx}, studying the θ_{DL} for different doses of impurities at room temperature alone may be insufficient in understanding the underlying mechanism. Hence, it is also important to investigate the dependence of θ_{DL} and associated properties on temperature.

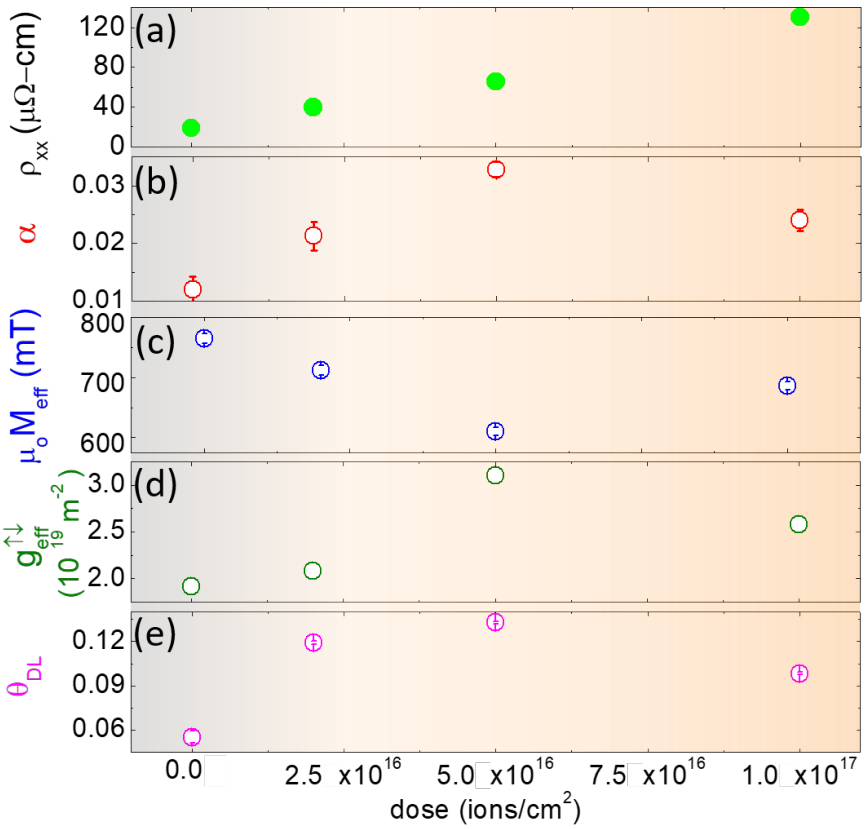

Figure 5.4. (a) ρ_{xx}, (b) α, (c) $\mu_o M_{eff}$, (d) $g_{eff}^{\uparrow\downarrow}$, and (e) θ_{DL} for different doses of nitrogen in Pt, at room temperature (293 K).

5.3.6. Temperature-dependent ST-FMR measurements: N-implanted Pt

In order to gain a deeper understanding of the enhancement in SHE of Pt(N), we performed temperature (T) dependent ST-FMR measurements in the range of 100-293 K. A linear increase of ρ_{xx} as a function of T (for T = 10-293 K) is observed in Fig. 5.5(a), which confirms a metallic behavior [31]. Fitting a straight line to the data and extrapolating to T = 0 K allowed us to deduce the residual resistivity $\rho_{xx,0}$, which is summarized in Table 5-I. Second, the linewidth ΔH and gilbert damping parameter α increase at lower *T* as shown in Fig. 3 (b. i, ii). This enhancement in α may be due to two reasons: an increase of ***js*** at lower *T*, and the increase of magnetic damping at the surface contribution. We consider the latter to be unlikely as it arises in a ferromagnet at a very low temperature range and with low thickness [38]. Third,

$\mu_o M_{eff}$ increases at lower T, as seen in Fig. 5.5(c). This is in accordance with $M_s \propto \frac{1}{T}$, assuming that H_p remains invariant with temperature [39]. Fourth, to confirm the high ***js*** created at FM/HM interface [37], $g_{eff}^{\uparrow\downarrow}$ is found to increase with decreasing T, as shown in Fig. 5.5(d), especially for the higher doses of Pt(N) 5×10^{16} and Pt(N) 1×10^{17}. Lastly, θ_{DL} is plotted as a function of T in Fig. 5.5(e), and is found to increase with decreasing T for Pt(N) 5×10^{16} and Pt(N) 1×10^{17}. Consequently, a high θ_{DL} of 0.18-0.19 is obtained for Pt(N) 5×10^{16} and Pt(N) 1×10^{17}. The θ_{DL} is found to be invariant with T for Pt(N) 2×10^{16} and Pt. Such a kind of increase/decrease of θ_{DL} with T hints at the possibility of an intrinsic and/or extrinsic side-jump contribution [33, 40, 41].

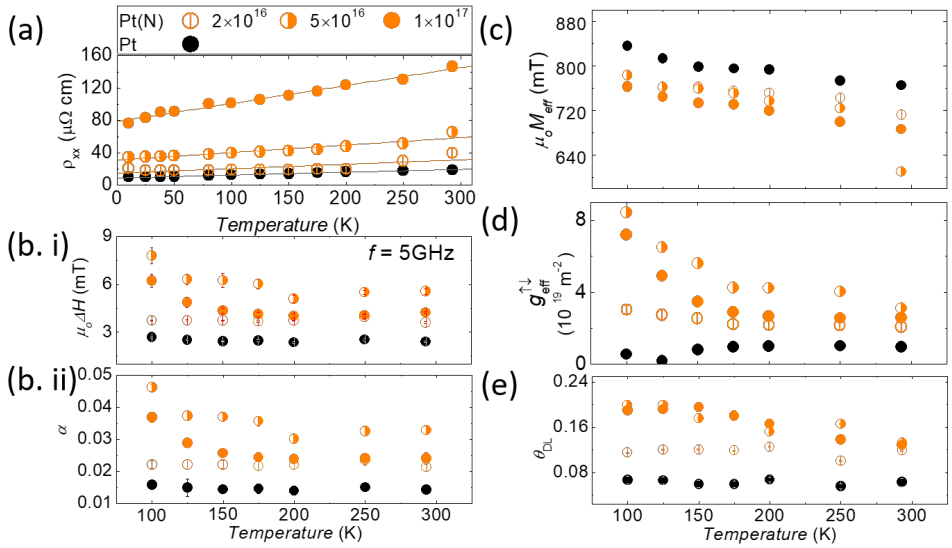

Figure 5.5. (a) ρ_{xx}, (b. i) ΔH, (b. ii) α, (c) $\mu_o M_{eff}$, (d) $g_{eff}^{\uparrow\downarrow}$, and (e) θ_{DL} for different doses of nitrogen in Pt plotted as a function of temperature. The solid line in Fig. 3 (a) represents the linear fitting.

Table 5-I. $\boldsymbol{\rho_{xx,0}}$, $\boldsymbol{\sigma_{SH}^{int}}$, and $\boldsymbol{\theta_{SH}^{sj}}$ for different N-ion dose

Sample	$\boldsymbol{\rho_{xx,0}}$ **(μΩ cm)**	$\boldsymbol{\sigma_{SH}^{int}}$ $(\frac{\hbar}{\mathbf{2e}}\mathbf{\Omega^{-1}cm^{-1}})$	$\boldsymbol{\theta_{SH}^{sj}}$
Pure Pt	9.01	1303.29	0.069
Pt(N) 2×10^{16} ions/cm^2	14.8	1283.55	0.251
Pt(N) 5×10^{16} ions/cm^2	31.1	1146.01	0.315
Pt(N) 1×10^{17} ions/cm^2	78.8	422.72	0.262

5.3.7. Contribution to SHE: N-implanted Pt

In anomalous Hall effect (AHE), the side-jump term, ρ_{sj} or σ_{sj} (proposed by Berger) [42] arising from extrinsic effect was confusingly viewed as an intrinsic term, ρ_{int} or σ_{int} (proposed by Karplus and Luttinger) [43]. This happened due to both the ρ_{int} and ρ_{sj} being proportional to ρ_{xx}^2 (or, simply $\sigma_{int} \propto \sigma_{xx}^2$ and $\sigma_{sj} \propto \sigma_{xx}^2$), where ρ_{xx}^2 is square of resistivity and σ_{xx}^2 is square of conductivity. This was accepted until the concept of residual resistivity arising from impurities, $\rho_{xx,0}$ was introduced by Tian et al., [44]. They proposed that the proper scaling for the AHE should involve not only the ρ_{xx} (or σ_{xx}), but also an important term, the residual resistivity $\rho_{xx,0}$. The AHE and SHE share the same analogy as demonstrated experimentally by Moriya et. al. [45]. Therefore, the total spin Hall conductivity σ_{SH}^{xy} can be expressed as a sum of intrinsic and extrinsic SHE (side-jump and skew scattering) [30, 33, 44, 46]:

$$\left|\sigma_{SH}^{xy}\right| = \sigma_{SH}^{int} + \left|\sigma_{SH}^{sj} + \sigma_{SH}^{ss}\right|, \tag{5.6}$$

$$= \sigma_{SH}^{int} + \left|\left(\theta_{SH}^{sj}\,\rho_{xx,0} + \theta_{SH}^{ss}\,\rho_{xx,0}\right)\sigma_{xx}^2\right|, \tag{5.7}$$

where, σ_{SH}^{int} is intrinsic spin Hall conductivity, σ_{SH}^{sj} is spin Hall conductivity due to side-jump scattering, σ_{SH}^{ss} is spin Hall conductivity due to skew scattering, θ_{SH}^{sj} is side-jump induced SHE efficiency, θ_{SH}^{ss} is skew scattering induced SHE efficiency, and σ_{xx} is conductivity.

To elucidate the explicit contribution from intrinsic and side-jump to the SHE, and to understand if skew scattering has any significant role to play, σ_{SH}^{xy} is plotted as a function of σ_{xx} in the inset of Fig. 5.6(a). σ_{xx} is in the range of 10^4 Ω^{-1}cm^{-1}. In the analogy to AHE, skew scattering arises in the higher conductivity range of super clean metals ($10^6 < \sigma_{xx} < 10^8$ Ω^{-1}cm^{-1}) [47]. Additionally, impurity induced skew scattering shows a *T*-independent θ_{DL} which was not observed for the higher doses in our samples [34, 40, 41]. Hence, skew scattering is not a possible mechanism in our samples. After excluding skew scattering, Eq. (5.7) can be expressed as:

$$\left|\sigma_{SH}^{xy}\right| = \sigma_{SH}^{int} + \left|(\theta_{SH}^{sj}\,\rho_{xx,0})\sigma_{xx}^{2}\right|, \tag{5.8}$$

To probe the exact contributions from intrinsic and side-jump scattering, σ_{SH}^{xy} is plotted as a function of σ_{xx}^2 in Fig. 5.6(a). Using the value of $\rho_{xx,0}$, σ_{SH}^{int} of 1303.29 $(\frac{\hbar}{2e})\Omega^{-1}$cm^{-1} is obtained for Pt, which is found to be very close to the theoretical value of 1300 $(\frac{\hbar}{2e})$ Ω^{-1}cm^{-1} reported by Tanaka et. al., [48]. Further, for Pt(N), σ_{SH}^{xy} is fitted to Eq. (5.8) and a σ_{SH}^{int} of 1283.55 $(\frac{\hbar}{2e})\Omega^{-1}$cm^{-1} is obtained for lower dose Pt(N) 2×10^{16} as shown in Fig. 5.6(b) . This is close to σ_{SH}^{int} of Pt, hinting at the dominant intrinsic SHE mechanism. However, the surprising result is the lower σ_{SH}^{int} of 1146.01 $(\frac{\hbar}{2e})\Omega^{-1}$cm^{-1} and 422.72 $(\frac{\hbar}{2e})\Omega^{-1}$cm^{-1} for Pt(N) 5×10^{16} and Pt(N) 1×10^{17}, respectively. A sudden decrease in σ_{SH}^{int} is counterbalanced by an increase of θ_{SH}^{sj}. The θ_{SH}^{sj} is found to be 0.31 and 0.26 for Pt(N) 5×10^{16} and Pt(N) 1×10^{17}, respectively (Fig. 5.6 (c)). Pt is a spin Hall material having a positive SHE sign [9, 11, 48, 49] and so, the positive sign of σ_{SH}^{int} indicates that intrinsic SHE still has some contribution to the SHE [30, 33, 47, 49]. Please see table 5.1 for details. Hence, the increase in θ_{DL} in Pt (N) is also influenced by extrinsic side-jump scattering, especially for the high implanted dose samples Pt(N) 5×10^{16} and Pt(N) 1×10^{17}. Therefore, with the increase in dose, we observe an increase in extrinsic side-jump contribution to SHE, which could play a significant role in the enhancement of SHE. This also leads to a reduction in the intrinsic SHE. Therefore, a crossover of intrinsic to extrinsic side-jump induced SHE is observed as the implantation of N-dose from 2×10^{16} ions/cm^2 to 1×10^{17} ions/cm^2 is

increased in the Pt layer. The successful disentanglement of intrinsic and extrinsic side jump induced by SHE could be a promising approach to understand the mechanism for enhancement in SHE.

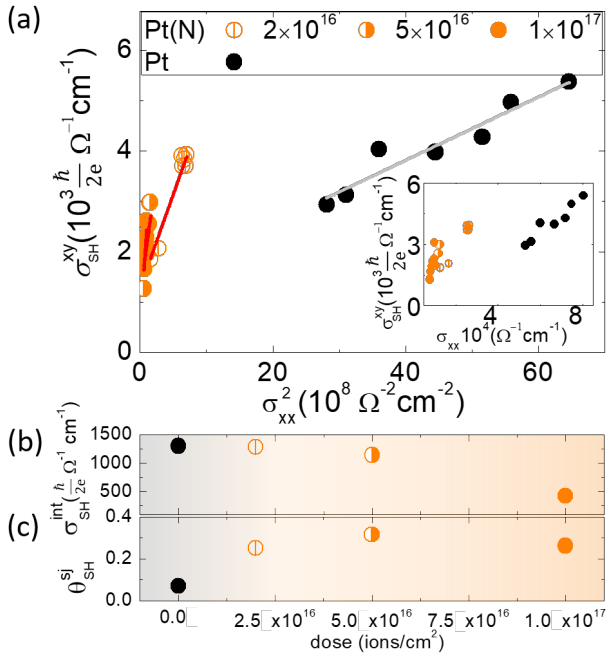

Figure 5.6. (a) σ_{SH}^{xy} plotted as a function of σ_{xx}^2 for implantation (orange data points) and Pure Pt (black data points). The solid lines represent the fitting using Eq. (5.8). Inset shows σ_{SH}^{xy} plotted as a function of σ_{xx}. (b) σ_{SH}^{int}, and (c) θ_{SH}^{sj} plotted as a function of N-ion dose.

5.3.8. Temperature dependent ST-FMR: Comparison of Pt(N) with S and O-implanted Pt

Extending our approach to understand the mechanism for enhancement of SHE in Pt(S) and Pt(O), we performed temperature dependent ST-FMR measurements. For the S-implanted Pt, Pt(S), we observe that the θ_{DL} increases at lower T, while for the O-implanted Pt, the higher doses of O-implanted Pt, θ_{DL} increases at lower T for the higher doses of 5×10^{16} and 1×10^{17}. For the lower dose of Pt(O) 2×10^{16}, θ_{DL} is found to be invariant with T. As discussed in previous section 5.3.6, such a kind of increase/decrease of θ_{DL} with T hints at the possibility of an intrinsic and/or extrinsic side-jump contribution [33, 40, 41]. We also measure the ρ_{xx} as a function of T (for T = 10-293 K) is observed in Fig. 3(a) (while the comparing the results with Pt(N)), which confirms a metallic behavior of ion-implanted Pt [31]. Extrapolating the ρ_{xx} at $T = 0$ K allows us to deduce the residual resistivity arising from impurities, $\rho_{xx,0}$. We find the $\rho_{xx,0}$ to be increasing with the implantation dose. The $\rho_{xx,0}$ influences the contribution of extrinsic SHE. This is in corroboration with the fact that the $\rho_{xx,0}$ is found to be minimum for pure Pt, hinting at the least contribution of extrinsic SHE in Pure Pt.

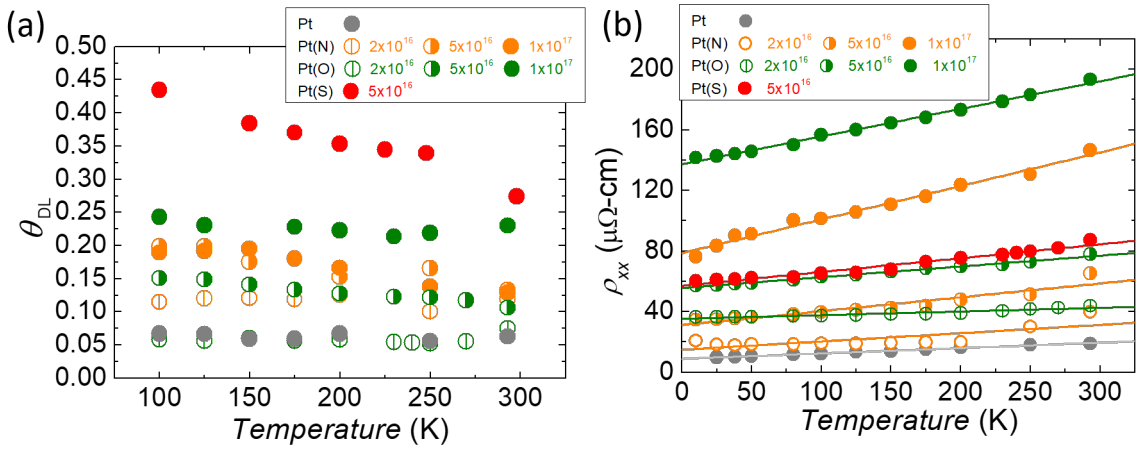

Figure 5.7. (a) θ_{DL} and (b) ρ_{xx} for different doses of S, O, N in Pt plotted as a function of temperature along with Pt.

5.3.9. Contribution to SHE: Comparison of Pt(N) with S and O-implanted Pt

The explicit contribution of intrinsic and extrinsic side-jump scattering has to be disentangled to understand the SHE enhancement. Additionally, it is also important to understand if skew scattering has any explicit role to play in enhancement or not. It is noteworthy to mention that θ_{DL} should be invariant with T for all the doses if the dominant mechanism for enhancement in SHE is extrinsic skew scattering. We did not obtain a *T*-independent θ_{DL} for the higher doses of ion-implanted Pt. So, skew scattering seems unlikely to contribute to SHE in all the implanted samples. Furthermore, σ_{SH}^{xy} is plotted as a function of σ_{xx} as shown in Fig. 5.8. σ_{xx} is in the range of 10^4 Ω^{-1}cm^{-1}. In the analogy to AHE, skew scattering arises in the higher conductivity range of super clean metals ($10^6 < \sigma_{xx} < 10^8$ Ω^{-1}cm^{-1}) [47]. So, we can safely exclude skew scattering as a possible mechanism for Pt(S) and Pt(O). Next using the same eqn. 5.8, $\left|\sigma_{SH}^{xy}\right| = \sigma_{SH}^{int} + \left|(\theta_{SH}^{sj}\,\rho_{xx,0})\sigma_{xx}^{2}\right|$, we find that the dominant contribution is extrinsic side-jump as shown in Fig. 5.7(b) as the implantation dose increases. The extracted contribution of σ_{SH}^{int} and θ_{SH}^{sj} along with θ_{DL} (100 K) is summarized in Table 5-II. This brings us to the assertion that higher the $\rho_{xx,0}$, higher is the θ_{SH}^{sj} , and therefore lower is the σ_{SH}^{int}. This gives us a model that by simply increasing the ρ_{xx} and hence the $\rho_{xx,0}$, the SHE can be enhanced. The values of σ_{SH}^{int}, θ_{SH}^{sj} and θ_{DL} (at 100 K) have been summarized for all the implantation samples in Table 5.2.

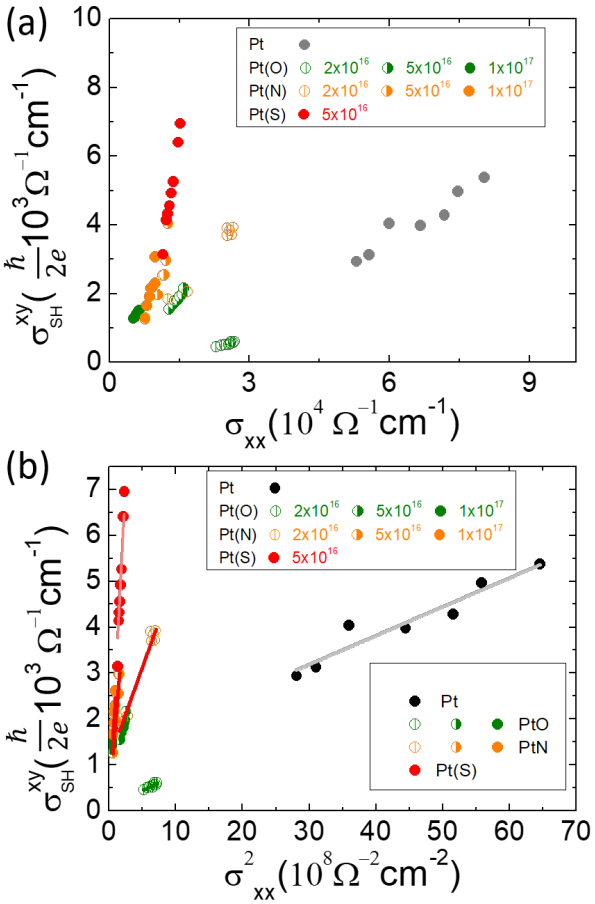

Figure 5.8. (a) σ_{SH}^{xy} plotted as a function of σ_{xx} for Pt(S), Pt(O), Pt(N) along with pure Pt. (b) σ_{SH}^{xy} plotted as a function of σ_{xx}^{2} for implantation and Pure Pt (black data points). The solid lines represent the fitting using Eq. (5.8).

Table 5-II. $\boldsymbol{\rho_{xx,0}}$, $\boldsymbol{\sigma_{SH}^{int}}$, and $\boldsymbol{\theta_{SH}^{sj}}$ and $\boldsymbol{\theta_{DL}}$ (at 100 K) for all the implantation samples, Pt(S), Pt(O), and Pt(N).

Sample	$\boldsymbol{\sigma_{SH}^{int}(\Omega^{-1}cm^{-1})}$	$\boldsymbol{\theta_{SH}^{sj}}$	$\boldsymbol{\theta_{DL}}$ **(100K)**
Pt	1303.29	0.069	0.066
Pt(S) 5×10^{16}	182.34	0.462	0.434
Pt(O) 2×10^{16}	421.43	0.005	0.058
Pt(O) 5×10^{16}	400.36	0.121	0.150
Pt(O) 1×10^{17}	376.31	0.214	0.243
Pt(N) 2×10^{16}	1283.55	0.251	0.115
Pt(N) 5×10^{16}	1146.01	0.315	0.198
Pt(N) 1×10^{17}	422.72	0.262	0.189

To confirm the influence of impurities on extrinsic side-jump induced SHE, we next focus on $\rho_{SH}^{imp} = \rho_{SH}^{Pt(S\ or\ O\ or\ N)} - \rho_{SH}^{Pt}$ where $\rho_{SH}^{Pt(S\ or\ O\ orN)}$ and ρ_{SH}^{Pt} are the SH resistivity of Pt(S), Pt(O) and Pt(N), respectively and pure Pt which are estimated from respective charge-spin interconversion efficiency. Here, the longitudinal resistivity from impurities ρ_{imp}, is identified using $\rho_{imp} = \rho_{Pt(S\ or\ O\ or\ N)} - \rho_{Pt}$ and prominent signature of linear trend in ρ_{SH}^{imp} *vs* ρ_{imp}^2, as seen in figure R4 using the linear fit of all the Pt(S), Pt(O), Pt(N) samples. This confirms the influence of side-jump induced SHE for non-metallic impurity O and N implanted in host Pt [50, 51, 52].

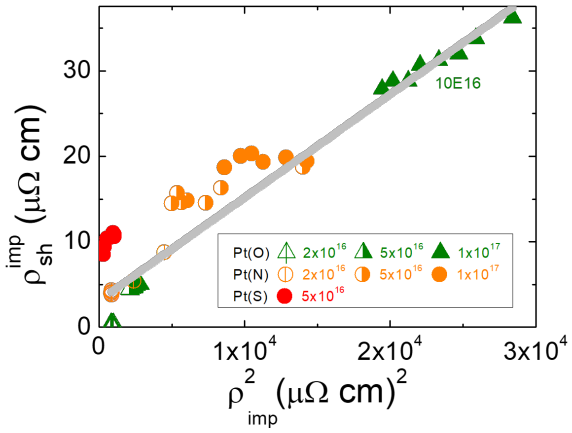

Figure 5.9. ρ_{SH}^{imp} vs ρ_{imp}^{2} behavior for Pt(O) and Pt(N). Solid grey line shows the concatenated linear fit.

5.4. Conclusion

In conclusion, we utilized a novel approach of ion-implantation to incorporate Nitrogen in Pt by varying dose from 2×10^{16} to 1×10^{17} ions/cm^2. We studied the dependence of θ_{DL} on both S, O, N-ion dose and temperature, to disentangle the intrinsic and extrinsic side-jump scattering mechanism in spin Hall effect. We found a crossover of intrinsic to extrinsic side-jump induced SHE as N and O-ion dose increased from 2×10^{16} ions/cm^2 to 1×10^{17} ions/cm^2. A sudden decrease in σ_{SH}^{int} is counterbalanced by the increase in θ_{SH}^{sj}. These results give us a model that by simply increasing the ρ_{xx} and hence the $\rho_{xx,0}$, the SHE can be enhanced. The results indicate that studying the θ_{DL} as a function of implantation dose, as well as a function of temperature, is important to understand the underlying physical phenomenon contributing to SHE. We believe that such a deep comprehension of enhancement in SHE may help us in revealing the host and impurity combination to unlock the full potential of SHE in 5d transition metals for SOT-MRAM application. The results presented in this chapter pertaining to N-implanted Pt have been submitted to Physical Review B [53].

References for chapter 5

1. J. E. Hirsch, *Phys. Rev. Lett.* **83**, 1834 (1999).
2. Y. K. Kato, R. C. Myers, A. C. Gossard, D. D. Awschalom, *Science* **306**, 1910 (2004).
3. J. Wunderlich, B. Kaestner, J. Sinova, and T. Jungwirth, *Phys. Rev. Lett.* **94,** 047204 (2005).
4. S. O. Valenzuela and M. Tinkham, *Nature* **442** 176 (2006).
5. X. Han, X. Wang, C. Wan, G. Yu, and Xiaorong Lv, *Appl. Phys. Lett.* **118**, 120502 (2021).
6. L. Zhu, D. C. Ralph, and R. A. Burhman, *Appl. Phys. Rev.* **8**, 031308 (2021).
7. L. Zhu, L. Zhu, S. Shi, D. C. Ralph, and R. A. Burhman, *Adv. Elec. Mater.* **6**, 1901131 (2020).
8. L. Liu L, C. –F. Pai, Y. Li, H. W. Tseng, D. C. Ralph and R. A. Buhrman, *Science* **336** 555 (2012).
9. L. Liu, T. Moriyama, D. C. Ralph, and R. A. Buhrman, *Phys. Rev. Lett.* **106** 036601 (2011).
10. D. Fang, H. Kurebayashi, J. Wunderlich, K. Výborný, L. P. Zârbo, R. P. Campion, A. Casiraghi, B. L. Gallagher, T. Jungwirth, and A. J. Ferguson, *Nature Nanotechnol.* 6, 413 (2011).
11. Y. Wang, P. Deorani, X. Qiu , J. H. Kwon and H. Yang *Appl. Phys. Lett.* **105** 152412 (2014).
12. M. Morota, Y. Niimi, K. Ohnishi, D. H. Wei, T. Tanaka, H. Kontani, T. Kimura and Y. Otani *Phys. Rev. B* **83** 174405 (2011).
13. H. L. Wang, C. H. Du, Y. Pu, R. Adur, P. C. Hammel, and F. Y. Yang, *Phys. Rev. Lett.* **112** 197201 (2014).
14. E. Sagasta, Y. Omori, S. Vélez, R. Llopis, C. Tollan, A. Chuvilin, L. E. Hueso, M. Gradhand, Y. Otani, and F. Casanova, *Phys. Rev. B* **98** 060410 (R) (2018).
15. S. Gupta, R. Medwal, D. Kodama, K. Kondou, Y. Otani, and Y. Fukuma, *Appl. Phys. Lett.* **110**, 022404 (2017).
16. L. Zhu, K. Sobotkiewich, X. Ma, X. Li, D. C. Ralph, and R. A. Buhrman, *Adv. Funct. Mater*. **29** 1805822 (2019).
17. P. Laczkowski, Y. Fu, H. Yang, J. -C. Rojas-Sánchez, P. Noel, V. T. Pham, G. Zahnd, C. Deranlot, S. Collin, C. Bouard, P. Warin, V. Maurel, M. Chshiev, A. Marty, J. –P. Attané, A. Fert, H. Jaffrès, L. Vila, and J. –M. George, *Phys. Rev. B* **96** 140405 (R) (2017).
18. L. Qian, K, Wang, Y. Zheng, and G. Xiao, *Phys. Rev. B* **102**. 094438 (2020).
19. P. Wang, A. Migliorini, S. -H. Yang, J. -C. Jeon, I. Kostanovskiy, H. Meyerheim, H. Han, H. Deniz, and S. S. P. Parkin, *Adv. Mater.* **34**, 2109406 (2022).
20. U. Shashank, R. Medwal, T. Shibata, R. Nongjai, J. V. Vas, M. Duchamp, K. Asokan, R. S. Rawat, H. Asada, S. Gupta, Y. Fukuma, *Adv. Quantum Technol.* **4** 2000112 (2021).
21. U. Shashank, R. Medwal, Y. Nakamura, J. R. Mohan, R. Nongjai, A. Kandasami, R. S. Rawat, H. Asada, S. Gupta, and Y. Fukuma, *Appl. Phys. Lett.* **118** 252406 (2021).
22. A. Asami, H. An, A. Musha, T. Gao, M. Kuroda, and K. Ando, *Phys. Rev. B* **99** 024432 (2019).

23. H. An, T. Ohno, Y. Kanno, Y. Kageyama, Y. Monnai, H. Maki, J. Shi, and K. Ando, *Sci. Adv*. **4**, eaar2250 (2018).
24. H. Xie, J. Yuan, Z. Luo, Y. Yang, and Y. Wu, *Sci. Rep.* **9** 17251 (2019).
25. L. Yang, Y. Fei, K. Zhou, L. Chen, Q. Fu, L. Li, C. Yan, H. Li, Y. Du, and R. Liu, *Appl. Phys. Lett.* **118** 032405 (2021).
26. K. -U. Demasius, T. Phung, W. Zhang, B. P. Hughes, S. -H. Yang, A. Kellock, W. Han, A. Pushp, and S. S. P. Parkin, *Nat. Commun.* **7** 10644 (2016).
27. Z. Xu, G. D. H. Wong, J. Tang, E. Liu, W. Gan, F. Xu, and W. S. Lew, *Appl. Phys. Lett.* **118** 062406 (2021).
28. T. -Y. Chen, C –T. Wu, H. -W. Yen, and C. -F. Pai, *Phys. Rev. B* **96** 104434 (2017).
29. Y. J. Kim, M. H. Lee, G. W. Kim, T. Kim, I. H. Cha, Q. A. T. Nguyen, S. H. Rhim, and Y. K. Kim, *Acta Mater.* **200** (2020).
30. J. Sinova, S. O. Valenzuela, J. Wunderlich, C. H. Back, and T. Jungwirth, *Rev. Mod. Phys*. **87**, 1213 (2015).
31. N. Nagaosa, J. Sinova, S. Onoda, A. H. MacDonald, and N. P. Ong, *Rev. Mod. Phys*. **82,** 1539 (2010).
32. Y. Niimi, and Y. Otani, *Rep. Prog. Phys*. **78**, 124501 (2015).
33. M. Isasa, E. Villamor, L. E. Hueso, M. Gradhand, and F. Casanova, *Phys. Rev. B* **91**, 024402 (2015).
34. Y. Niimi, M. Morota, D. H. Wei, C. Deranlot, M. Basletic, A. Hamzic, A. Fert, and Y. Otani, *Phys. Rev. Lett*. **106**, 126601 (2011).
35. M. Harder, Z. X. Cao. Y. S. Gui, X. L. Fan, and C. –M. Hu, *Phys. Rev. B* **84**, 054423 (2011).
36. M. Harder, Y. Gui, and C.-M. Hu, *Phys. Rep*. **661**, 1 (2016).
37. T. Nan, S. Emori, C. T. Boone, X. Wang, T. X. Oxholm, J. G. Jones, B. M. Howe, G. J. Brown, and N. X. Sun, *Phys. Rev. B* **91**, 214416 (2015).
38. Y. Zhao, Q. Song, S. -H. Yang, T. Su, W. Yuan, S. S. P. Parkin, J. Shi, and W. Han, *Sci. Rep.* **6**, 22890 (2016).
39. A. Deka, B. Rana, R. Anami, K. Miura, H. Takahashi, Y. Otani, and Y. Fukuma, *Phys. Rev. B* **101**, 174405 (2020).
40. L. Vila, T. Kimura, and Y. Otani, *Phys. Rev, Lett.* **99**, 226604 (2007).
41. Y. Niimi, H. Suzuki, Y. Kawanishi, Y. Omori, T. Valet, A. Fert, and Y. Otani, *Phys. Rev. B* **89**, 054401 (2014).
42. L. Berger, *Phys. Rev. B* **2**, 4559 (1970).
43. R. Karplus and J. M. Luttinger, *Phys. Rev*. **95**, 1154 (1954)].
44. Y. Tian, L. Ye, and X. Jin, *Phys. Rev. Lett.* **103**, 087206 (2009).

45. H. Moriya, A. Musha, S. Haku, and K. Ando, *Commun. Phys*. **5**, 12 (2022).
46. A. Kumar, R. Bansal, S. Chaudhary, and P. K. Muduli, *Phys. Rev. B* **98**, 104403 (2018).
47. A. Hoffmann, *IEEE Trans. Magn*. **49**, 5172 (2013).
48. T. Tanaka, H. Kontani, M. Naito, T. Naito, D. S. Hirashima, K. Yamada, and J. Inoue, *Phys. Rev. B* **77**, 165117 (2008).
49. E. Sagasta, Y. Omori, M. Isasa, M. Gradhand, L. E. Hueso, Y. Niimi, Y. Otani, and F. Casanova, *Phys. Rev. B* **94**, 060412(R) (2016).
50. R. Asomoza, A. Fert, R. Reich, J. Less-Common Met. **90**, 177 (1983).
51. R. Ramaswamy, Y. Wang, M. Elyasi, M. Motapothula, T. Venkatesan, X. P. Qiu, H. Yang, *Phys. Rev. Appl.* **8**, 024034 (2017).
52. X. Xu, D. Zhang, B. Liu, H. Meng, J. Xu, Z. Zhong, X/ Tang, H. Zhang, and L. Jin, *Adv. Sci.* **9**, 2105729 (2022).
53. U. Shashank, Y. Nakamura, Y. Kusaba, T. Tomoda, R. Nongjai, A. Kandasami, R. Medwal, R. S. Rawat, H. Asada, S. Gupta, and Y. Fukuma, *submitted to Physical Review B.*

Chapter 6

Giant spin Hall effect in P-implanted Pt layers

(This chapter is based on the unpublished results on Phosphorus implanted Pt, whose manuscript is under preparation)

In chapters 3, 4, 5, we employed the 30 kV ion accelerator/ implanter to perform low energy 12-20 keV ion implantation of S, O, N ions. So, after confirming that non-metallic lighter impurity with low Z increases the spin Hall effect in Pt, we extend our approach to implant another non-metallic element Phosphorus in Pt. However, we employ a moderate energy of 30 KeV using an ULVAC IMX-3500 ion implanter (see chapter 2 for details of implanter) to study the SHE in phosphorus implanted Pt, *i.e.,* Pt(P) in this chapter.

6.1. Introduction

The evolution of spintronics has led to a paradigm shift in designing the materials with high spin-orbit torque (SOT) in magnetic random-access memory (MRAM) [1-3]. The SOT is generated from the damping-like torque efficiency, θ_{DL} via spin Hall effect (SHE) [4, 5], and maintains a focal point in writing memory bits in MRAM. 5d transition metals (5d TM) with high atomic number Z are found to have a high SHE, due to their high spin-orbit coupling (SOC) strength [6]. Apart from 5d transition metals, there have been tremendous efforts to find a suitable SOT material like metal-alloys [7, 8], insertion layers [9, 10], antiferromagnetic materials [11], transition metal dichalcogenides [12], and topological insulators [13] to name a few. Despite being endowed with a very-high SOT, the practical use of these materials in SOT-MRAM, seems to be a long road ahead due to effects being restricted to interface rather than bulk [14], broken angular symmetry of SOT [12, 15], and high resistivity, ρ_{xx} [13], thereby limiting its application in SOT-MRAM [2, 14]. Out of all these possibilities, the 5d TM such as Pt seems to be an archetypal choice due to the three-fold benefits of low ρ_{xx}, bulk SHE and unbroken symmetry of SOT. Pt is a SHE material having all the three traits, but, the θ_{DL} of Pt is ~0.06 only [16]. Therefore, if the θ_{DL} can be enhanced in Pt with a little trade-off in ρ_{xx},

while at the same time, maintain an unbroken angular symmetry of SOT with bulk SHE, the long road to reach a compatible SHE material for SOT-MRAM, seems not far.

The bulk SHE can primarily be enhanced by two mechanisms: intrinsic and extrinsic SHE [17-19]. Intrinsic SHE originates from the band structure or the berry curvature of the material [17, 18] while the extrinsic SHE is catalyzed by localized impurity scattering [17-19]. The extrinsic SHE can be enhanced by doping non-metallic impurity (low Z) in 5d TM host (high Z) due to difference in Z of host and impurity [20]. Recently, Lau et. al., have demonstrated a high θ_{DL} of 0.20 in $Pt_{78}Al_{22}$ alloy [21] while Wang et. al., have demonstrated a high θ_{DL} of ≈0.3 in $Pt_{30}Al_{70}$, [20] in which the impurity is Al (Z=13) and host is Pt (Z=78). Concomitantly, we obtained a high θ_{DL} of 0.27 in sulfur implanted Pt, Pt(S), where impurity is S (Z=16) [22], and a θ_{DL} of 0.23 in oxygen implanted Pt, Pt(O), where impurity is O (Z=8) [23]. Furthermore, the extrinsic SHE is found to be enhanced at the amorphous-crystalline boundary of the SHE material [20, 21]. In fact, a clear correlation between the SHE and structural phases of early 5d transition metals such as Ta, W etc. have already been demonstrated by Liu et. al. [24]. It has been shown that largest θ_{DL} of 0.23 and 0.07 for Ta, W, respectively is found when the dominant phase is amorphous-like. The SHE has also been enhanced by simply depositing amorphous materials such as Au-Ta [25] and recently, by gradually changing Pt films to amorphous structure by oxidation [26]. In this respect, phosphorus (P), also a non-metallic element with low Z has been unexplored as an impurity in Pt via amorphization of Pt.

In this chapter, we report a giant θ_{DL} in P (Z=15) implanted Pt, Pt(P) fabricated by incorporating non-metallic P impurity in host Pt by a moderate energy of 30 keV studied by varying fluence/dose from 2.5×10^{16} - 9×10^{16} ions/cm^2. We perform the X-ray diffraction (XRD) to understand the change in crystallographic properties of Pt with amount of P dose. We observe a peak broadening and peak shift from Pure Pt to Pt(P), suggesting the transition of polycrystalline to amorphous Pt. By using the difference in periodicity of the oscillations from X-ray reflectivity (XRR), we observe an increase in the thickness of Pt layer due to the intermixing with protective layers of MgO and Al_2O_3 after implantation of P ions. Moreover, we observe an increase in the thickness of Pt layer after implantation of P ions using cross-sectional high

resolution transmission electron microscopy (HR-TEM). Furthermore, by electron diffraction from Pt, we observe transition of polycrystalline to amorphous Pt for pure Pt and Pt(P) respectively. We find a giant $\theta_{DL} \approx 0.75$ for the highest Pt(P) dose of 9×10^{16} in corroboration with amorphization of Pt using three different spin-torque ferromagnetic resonance ST-FMR techniques viz., lineshape, and angular, and DC-bias ST-FMR (linewidth) measurements. Also, we observe an unbroken symmetry of SOT using angular ST-FMR measurements to rule out parasitic effects in our measurements. We demonstrate a simpler method of ion implantation to enhance the SHE in the archetypal Pt by incorporation of non-metallic phosphorus ions to make strides in the development of high SHE material for low power consumption in SOT-MRAM.

6.2. Experimental methods

The multilayer stack of Pt (10 nm)/MgO (10 nm)/Al_2O_3 (10 nm) on Si/SiO_2 were deposited at room temperature using an ultrahigh vacuum sputtering. Then, samples were implanted with 30 KeV P ion beam using ULVAC IMX-3500 medium current implanter at a dose/fluence of 2.5×10^{16} - 9×10^{16} ions/cm^2 (hereafter, Pt(P) 2.5×10^{16} and Pt(P) 9×10^{16}). The first batch of samples were studied with XRD, XRR and HR-TEM to study the crystalline and amorphous nature of Pt after ion implantation of P ions. The XRD patterns were recorded on PANalytical X'Pert Pro MPD diffractometer with Cu Kα irradiation. Simultaneously, the HR-TEM images were recorded on a JEM-ARM200CF at an acceleration voltage of 120 kV. The second batch of samples was used for the ST-FMR measurements. In the second batch, the remaining protective layers (MgO/Al_2O_3) were removed by Ar^+ ion milling and monitored using an end point detector. Then, NiFe (5 nm) was deposited on top of these samples by using an ultrahigh vacuum sputtering after the Ar^+ ion milling process. Micron-sized Hall bar and ST-FMR devices were patterned using standard mask less photolithography and Ar^+ ion milling. Then, coplanar waveguides (CPW) were formed by DC sputtering of Ti (10 nm) and Al (200 nm) using 50 W and 100 W power respectively. ST-FMR measurements were performed by applying a microwave signal using MXG Analog Signal Generator (N5183A) and direct current (DC) using R6161 Advantest DC source or Keithley 6221 AC/DC current source. The generated DC voltage signal were recorded using a LI-5640 Digital Lock-in Amplifier via a

bias tee after a signal modulation with a frequency of 79 Hz. All measurements were performed at room temperature.

6.3. Experimental results

6.3.1. Surface Morphology and structural phase study

To study the surface morphology and compare structural change on the impact of P ions implanted in Pt/MgO/Al_2O_3, we performed the dose dependence of XRD profiles as shown in Fig. 6.1. For the pure Pt/MgO/Al_2O_3, we observe a clear Pt (111) peak indicating a preferred (111)- growth implying the high polycrystallinity of the Pt film with sharp interfaces [21, 27]. With the increase in the implantation dose from 2.5×10^{16} - 9×10^{16}, we notice a clear reduction in the intensity of the Pt (111) peak, indicating a transformation of the polycrystalline to amorphous Pt [21, 26]. The Pt (111) shows a marked broadening and weakening with increasing P dose in Pt from 2.5×10^{16} - 9×10^{16} due to the presence of P, and possibly MgO impurities along with the reduction in volume of Pt [28]. Furthermore, the peak broadening and peak shift between pure Pt and Pt(P) 2.5×10^{16} is seen, which is ascribed to the amorphization of Pt similar to the results obtained from the amorphous state of Au-Ta alloy [21, 25, 28]. The broadening of the Pt (111) peak could be ascribed to Scherrer broadening similar to the results obtained by Chi et. al., in $Pt_{1-x}Bi_x$ alloy [29]. Moreover, the peak broadening and peak shift from Pt(P) 2.5×10^{16} to Pt(P) 9×10^{16} may result from some reaction between Pt and P, leading to a drastic change in the lattice parameters. We also observe additional Pt (200) and Pt (220) peaks for pure Pt. Noticeably, we see a reduction in intensity of Pt (200) peak of Pt(P) 2.5×10^{16} and Pt(P) 9×10^{16} which may ascribe to amorphization of Pt. A complete loss of Pt (220) peak is observed for Pt(P) 9×10^{16}. Furthermore, to comprehend the change in thickness of the Pt layer after ion implantation, we utilize the periodicity of the oscillations using X-ray reflectivity (XRR). Therefore, we estimate the thickness from the periodicities of the oscillation to be 11.5 nm, 20.5 nm, and 36.7 nm for the Pure Pt, Pt(P) 2.5×10^{16} and Pt(P) 9×10^{16}. The intermixing of protective MgO and Al_2O_3 with Pt could lead to increase in the overall thickness of implanted Pt layers.

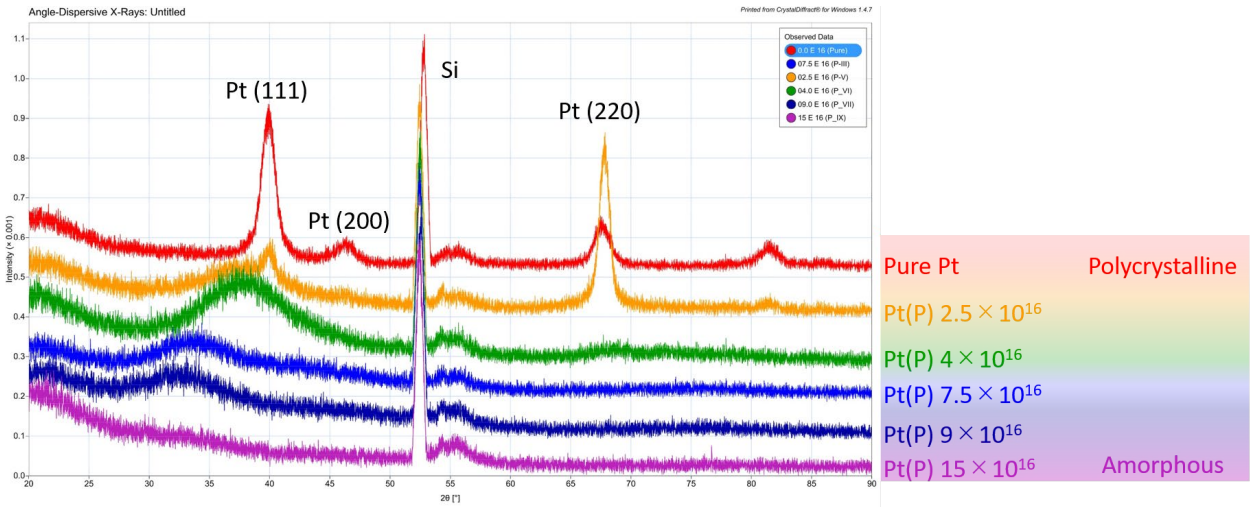

Figure 6.1. X-ray diffraction (XRD) spectra of Pure Pt, Pt(P) 2.5 $\times 10^{16}$, Pt(P) 4.0 $\times 10^{16}$, Pt(P) 7.5 $\times 10^{16}$, Pt(P) 9.0 $\times 10^{16}$ and Pt(P) 9.0 $\times 10^{16}$. Data is shifted vertically for clarity.

To gain a direct insight into the observation of increased thickness and change in crystallographic properties, we performed the cross sectional HR-TEM and electron diffraction measurements. Figure 6.2 (a, b) shows the HR-TEM image of the Pure Pt/MgO/Al_2O_3 for 300 K and 400 K magnification, respectively. Here, for the pure Pt, lattice fringes are largely observed depicting the polycrystalline nature of as-deposited Pt [22, 28]. However, we observe a visible loss of lattice fringes/streaks depicting the amorphous nature of Pt(P) 9.0×10^{16}/MgO/Al_2O_3 as seen in Fig. 6.2 (c, d) at 100 K and 400 K magnification, respectively. Noticeably, we observe bubbles (voids) with a brighter contrast. The presence of brighter voids could correspond to lighter total mass accumulated throughout the dark contrasted Pt leading to reduction in volume of Pt [28]. However, it is unclear if the voids clearly correspond to lighter phosphorus or other elements such as Mg, Al. Nevertheless, a clear transition of polycrystalline to amorphous nature of Pt is seen. To confirm the polycrystalline Pt, we observe annular dark rings performed using the fast Fourier transform (FFT) analysis using the electron diffraction as shown in Fig. 6.2 (e). In contrary to this, we observe a loss of annular dark rings depicting the loss of crystallinity of Pt using FFT as shown in Fig. 6.2 (f). Moreover, to confirm the presence of bubbles/voids, we also employ the High Annular Angle Dark field imaging (HAADF-STEM) and observe clear voids due to lighter atoms in Pt(P) 9.0×10^{16}/MgO/Al_2O_3 (Fig. 6.2 (h)) as compared to Pure Pt/ MgO/Al_2O_3(Fig. 6.2 (g)). Therefore, with XRD, HR-TEM, and HAADF-STEM, we confirm the change in crystallographic properties of Pt after implantation of P ions.

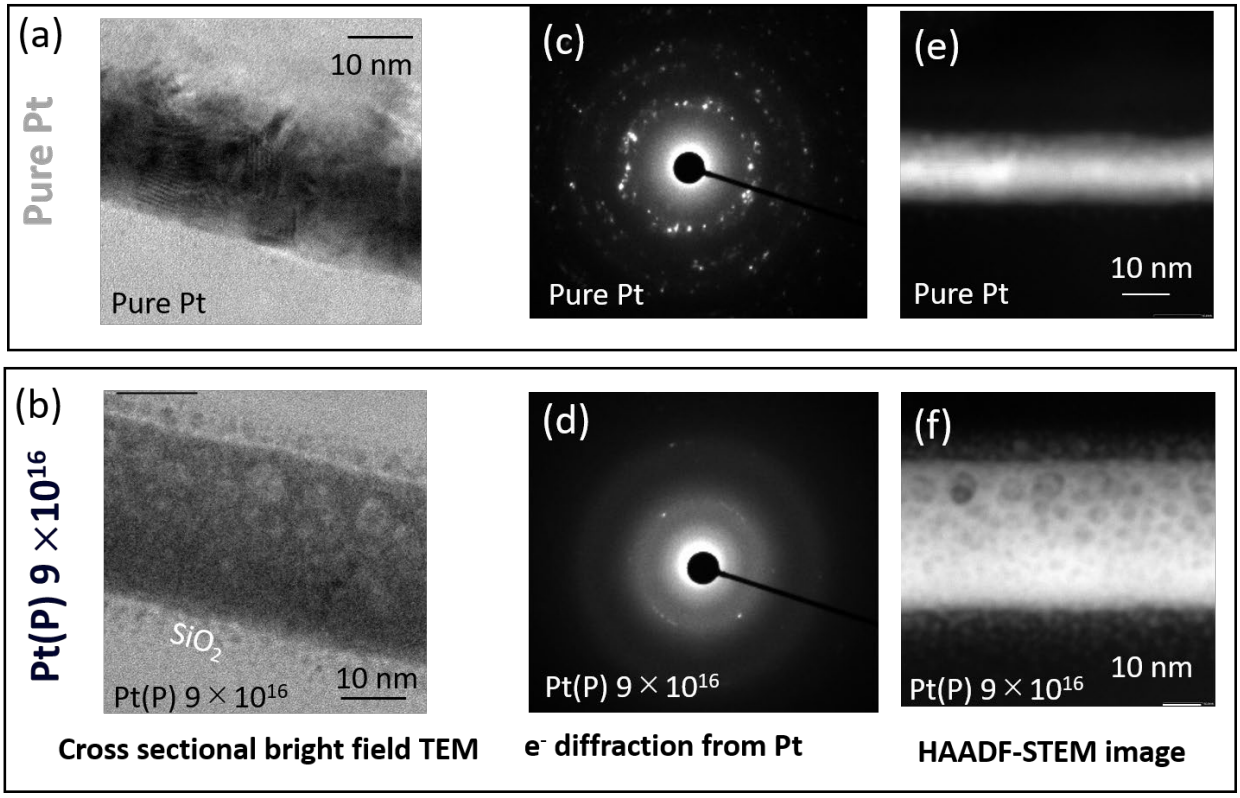

Figure 6.2. Cross sectional bright field high resolution TEM for (a) Pure Pt/MgO/Al_2O_3, and (b) Pt(P) 9×10^{16}/MgO/Al_2O_3. Electron diffraction patterns of respective selected area for (c) Pure Pt/MgO/Al_2O_3 and (d) Pt(P) 9×10^{16}/MgO/Al_2O_3. Clear rings in (c) depict the polycrystalline structure whereas the halo ring-like structure in (d) confirms the amorphous structure of Pt(P). High Annular Angle Dark field imaging (HAADF-STEM) for (e) Pure Pt and (f) for Pt(P) 9×10^{16}.

6.3.2. ST-FMR measurements

I. Lineshape analysis

Next, we measure the damping-like torque efficiency for pure Pt and Pt(P) using the various methods of spin-torque ferromagnetic resonance (ST-FMR) measurements [16] i.e., lineshape analysis, angular ST-FMR and linewidth analysis (DC-bias ST-FMR). The schematic of the ST-FMR measurement set-up is shown in Fig. 3(a). In this measurement technique, a microwave current, I_{rf} is passed along the length of the device with an applied power of 5 dBm in the Pt(P)/NiFe. Additionally, an in-plane magnetic field $\mu_o H_{ext}$, is applied from −200 mT to +200 mT Oe at an angle of ϕ = 45° with respect to the device length. Due to SHE, non-equilibrium spins are generated in the Pt(P) layers, which travels upwards to the NiFe and exerts an-in plane damping-like torque, τ_{DL} on the magnetization of NiFe. Simultaneously, the Oersted field (h_{rf}) generated from the I_{rf} exerts an Oersted field torque, τ_{OFT} according to Ampere's Law. Upon satisfying the ferromagnetic resonance (FMR) condition, the periodic mixing of the change in magnetoresistance ΔR of NiFe and I_{rf} produces an output DC voltage V_{mix} which is detected using a lock-in technique via a bias tee. Since the obtained V_{mix} is of the order of $\sim\mu V$, a sinusoidal signal of 79 Hz is used to modulate the I_{rf}, thereby providing a better signal-to-noise ratio. Figure 3(b) shows the ST-FMR voltage V_{mix} obtained at f = 5 GHz at I_{dc} = 0 mA for pure Pt/NiFe and Pt(P)/NiFe expressed as: $V_{mix} = SF_{sym}(H_{ext}) + AF_{asym}(H_{ext})$, where, $F_{sym}(H_{ext}) = \frac{(\Delta H)^2}{(H_{ext}-H_o)^2+(\Delta H)^2}$ is the symmetric part, and $F_{asym}(H_{ext}) = \frac{\Delta H(H_{ext}-H_o)}{(H_{ext}-H_o)^2+(\Delta H)^2}$ is the antisymmetric part, A and ΔH and H_o are the linewidth and resonance field of FMR spectra, while S and A are the weight factors of the symmetric and antisymmetric part, respectively. For the ST-FMR spectra, the symmetric (S) component arises from the τ_{DL} while the antisymmetric (A) component is mainly dominated by the τ_{OFT}. Importantly, the odd parity of the symmetric component with the direction of H_{ext} with I_{rf} indicates that it originates from damping-like spin-orbit torque *i.e.,* τ_{DL} in Pt and Pt(P) layers.

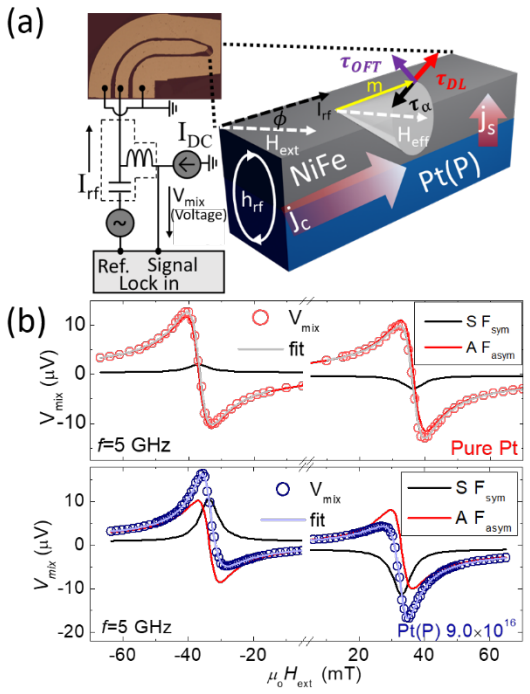

Figure 6.3. Schematic showing ST-FMR measurement technique, and detection principle for the Pt(P) layers/NiFe, along with an optical image of the micro-device. (b) ST-FMR voltage V_{mix} obtained at f = 5 GHz with the de-convoluted symmetric ($S F_{sym}(H_{ext})$) and antisymmetric component ($AF_{asym}(H_{ext})$) fitted using eq. (1) for Pure Pt and Pt(P) 9×10^{16}.

We found this odd parity for a wide range of f = 5-11 GHz (See left panel of Fig. 6.4). Noticeably, a giant symmetric component ($S F_{sym}(H_{ext})$) is observed for the Pt(P) 9×10^{16}/NiFe in comparison to Pure Pt/NiFe. To quantify the τ_{DL} in terms of damping-like torque efficiency using the lineshape analysis, θ_{DL}^{LS} we utilize the ratio of S/A given by: $\theta_{DL}^{LS} = \frac{S}{A}\frac{e\mu_o M_s t d}{\hbar}\sqrt{1+\frac{M_{eff}}{H_o}}$, where e is the electronic charge, μ_o is the permeability of free space, M_s is the saturation magnetization of NiFe, t is NiFe thickness, d is pure Pt or Pt(P) layers thickness measured from XRR, and M_{eff} is effective magnetization obtained from Kittel fitting. The invariant θ_{DL}^{LS} (see right panel of Fig. 6.4) implies a negligible role of thermal effect and uncontrolled relative phase between I_{rf} and h_{rf} that arises from sample design [30].

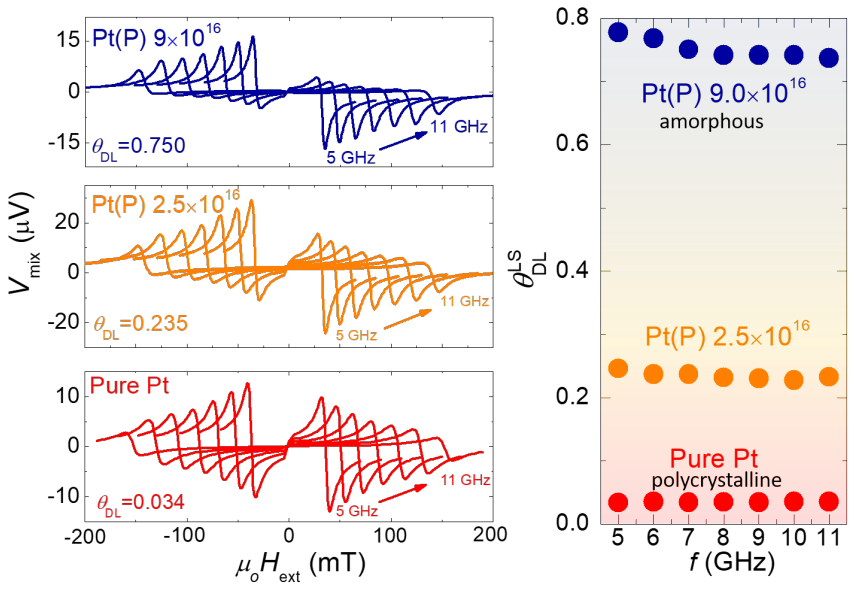

Figure 6.4. Left panel shows the ST-FMR DC voltage V_{mix} spectra obtained as a function of H_{ext} for f= 5-11 GHz for pure Pt, Pt(P) 2.5×10^{16} and Pt(P) 9×10^{16}. Right panel shows θ_{DL}^{LS} as a function of f =5-11 GHz for pure Pt, Pt(P) 2.5×10^{16} and Pt(P) 9×10^{16}.

II. Angular ST-FMR analysis and DC-bias ST-FMR

The lineshape analysis at a limited angular range of ϕ = 45^{o} that relies on the assumption of S/A being invariant with ϕ may not reveal the complete picture of spin-orbit torques. Therefore, it is imperative to perform the in-plane angular dependence of the ST-FMR lineshape to rule out the artifacts and unconventional torques present in a system as independently demonstrated by Skinner and later revisited by Sklenar et. al., [31, 32]. Figure 6.5 (a- c) shows the symmetric (S) and antisymmetric (A) component well fitted with the dominant $\sin 2\phi \cos\phi$ behavior for pure Pt and highest dose i.e., sample with no breaking of the mirror and the two-fold symmetry [33]. Please see chapter 7 for the additional details of angular dependent ST-FMR measurements measured for other samples and at other f and the method devised to calculate the damping-like torque efficiency by filtering out the $\sin 2\phi \cos\phi$ component obtained from angular ST-FMR measurements, i.e., θ_{DL}^{ang}.

The modulation of linewidth (or effective damping, α_{eff}) using DC-bias ST-FMR is an additional tool to circumvent the issues such as spin pumping contribution in the symmetric component of V_{mix} obtained via lineshape analysis [34] , broken two-fold and mirror symmetry of torques, and unconventional SOT [33]. In modulation of linewidth (ΔH), a DC (I_{dc}) is applied along with I_{rf} in the same set-up as shown in Fig. 6.3 (a). Upon changing the polarity of I_{dc}, we observe a reversed slope of α_{eff}, defined as $\alpha_{eff} = \gamma/2\pi\ (\mu_o \Delta H - \mu_o \Delta H_o)$ [34]. By reversing the direction of external magnetic field H_{ext} (from ϕ = 45° to -135°), the NiFe present above the Pt(P) layers magnetizes the sample in the opposite direction thereby leading to a reverse polarity of τ_{DL} as shown in Fig. 3 (d-f) for Pure Pt, Pt(P) 2.5×10^{16} and Pt(P) 9.0×10^{16}, respectively. Therefore, the damping-like torque efficiency evaluated from modulation of linewidth, $\theta_{\mathrm{DL}}^{\mathrm{LW}}$ is given as [35]: $\theta_{\mathrm{DL}}^{\mathrm{LW}} = \frac{\frac{2e}{\hbar}(H_o + \frac{M_{eff}}{2})\mu_o M_s t \left|\frac{\Delta\alpha_{eff}}{\Delta j_{dc}}\right|}{sin\phi}$, where $\frac{\Delta\alpha_{eff}}{\Delta j_{dc}}$ is the slope obtained from the linear fit of Fig. 6.5 (d-f). Noticeably, a higher slope is observed for Pt(P) 9.0×10^{16} depicting a higher $\theta_{\mathrm{DL}}^{\mathrm{LW}}$ compared to pure Pt. A slightly different but comparable value of $\theta_{\mathrm{DL}}^{\mathrm{LW}}$ is obtained for the $+H_{ext}$ and $-H_{ext}$ *i.e.,* 0.582 and 0.745, respectively (see Fig. 6.5 (f)). To avoid the discrepancy in the values, we use the average of the $\theta_{\mathrm{DL}}^{\mathrm{LW}}$ values obtained from $+H_{ext}$ and $-H_{ext}$, respectively. This affirms that the τ_{DL} obtained in our samples is from the conventional τ_{DL} acting on the magnetization of NiFe due to the j_s generated from SHE. Additionally, a high $\theta_{\mathrm{DL}}^{\mathrm{LW}}$ of 0.297 and 0.230 for $+H_{ext}$ and $-H_{ext}$, respectively is also seen for Pt(P) 2.5×10^{16} as seen in Fig. 6.5 (e) confirming that P ions in Pt can catalyze the extrinsic scattering sites and lead to enhancement of SHE. Noticeably, a lower $\theta_{\mathrm{DL}}^{\mathrm{LW}}$ is seen for pure Pt (Fig. 6.5 (d)).

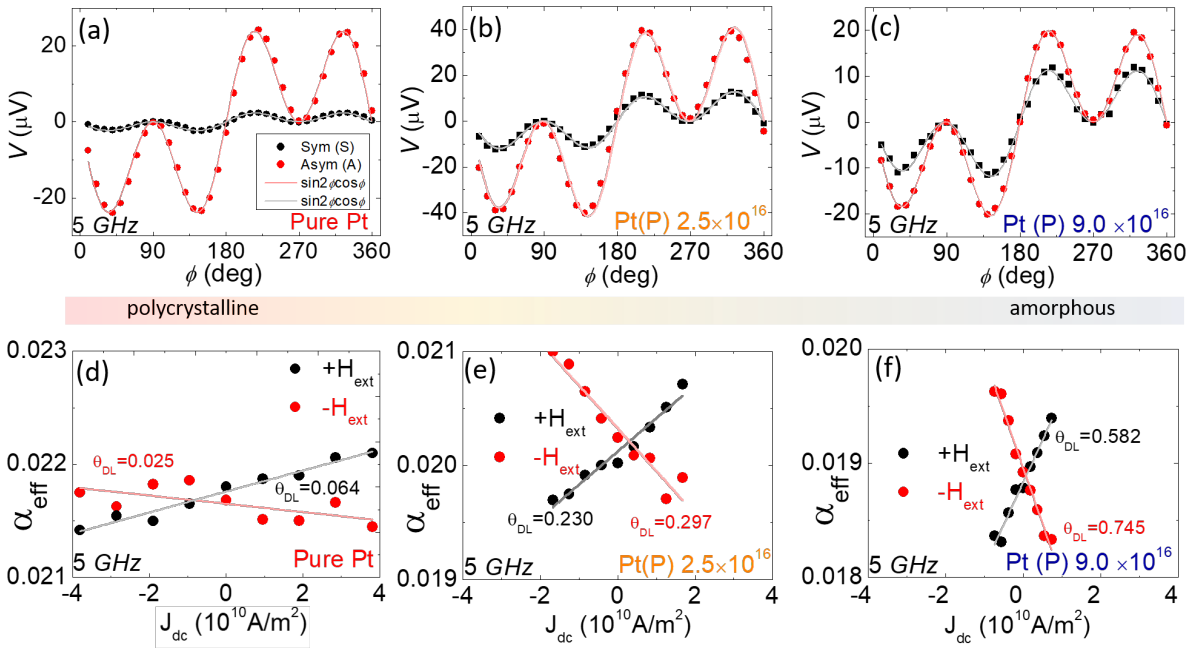

Figure 6.5. Angular dependence of symmetric (S) and antisymmetric (A) weight factors in V_{mix} at $f = 5$ GHz for (a) Pure Pt, (b) Pt(P) 2.5×10^{16} and (c) Pt(P) 9×10^{16}. Modulation in effective damping (or linewidth), α_{eff} as a function of charge current density j_{dc} in pure Pt and Pt(P) layers for (d) Pure Pt, (e) Pt(P) 2.5×10^{16} and (f) Pt(P) 9×10^{16}.

III. Effective demagnetizing field, gilbert damping and longitudinal resistivity

To picturize the correlation among effective demagnetizing field ($\mu_o M_{eff}$) , gilbert damping (α) and longitudinal resistivity (ρ_{xx}), we plot these parameters as a function of implantation dose as shown in Fig. 6.6. First, a minimum $\mu_o M_{eff}$ = 747 mT is seen for pure Pt as compared to higher $\mu_o M_{eff}$ of 826 and 816 mT for Pt(P) 2.5×10^{16} and Pt(P) 9×10^{16}, respectively indicating a change in the perpendicular magnetic anisotropy field H_p. Second, gilbert damping (α) shows a monotonic dependence with an increase of P-ion dose, where a maximum value of 0.018 is obtained for the dose of 9×10^{16} (Fig. 6.6 (b)). Third, ρ_{xx} is found to be monotonically increasing in Fig. 6.6 (c), similar to our previous result of implanting non-metallic impurity in Pt.

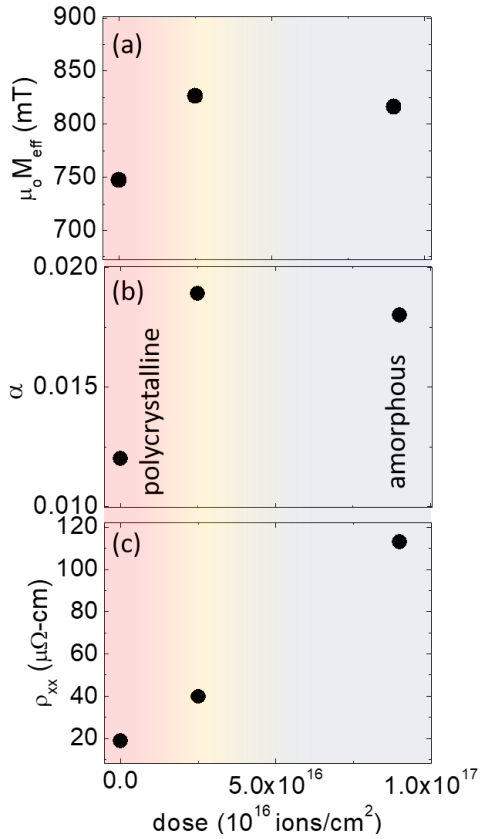

Figure 6.6. Effective demagnetizing field, $\mu_o M_{eff}$, gilbert damping α, and resistivity, ρ_{xx} as a function of P ion dose for Pure Pt, Pt(P) 2.5×10^{16} and Pt(P) 9×10^{16}.

6.3.3. θ_{DL} and σ_{xx}

Finally, to compare the damping-like torque efficiency calculated from three methods, the lineshape, angular and linewidth ST-FMR measurements, i.e., $\theta_{\mathrm{DL}}^{\mathrm{LS}}$, $\theta_{\mathrm{DL}}^{\mathrm{ang}}$ and $\theta_{\mathrm{DL}}^{\mathrm{LW}}$, respectively as a function of longitudinal conductivity, σ_{xx} (See Fig. 6.7). We observe that the θ_{DL}can be enhanced in a Pt based material by simply reducing the σ_{xx}. Also, ρ_{xx} is found to increase with dose in relation with amorphization of Pt similar to results obtained by Li et. al., [26]. This is in corroboration with simply making a 5d transition metal amorphous by reducing its σ_{xx} [20, 21, 24]. The values of thickness obtained from XRR, σ_{xx}, and different θ_{DL} obtained from three different ST-FMR methods, *i.e.,* $\theta_{\mathrm{DL}}^{\mathrm{LS}}$, $\theta_{\mathrm{DL}}^{\mathrm{ang}}$ and $\theta_{\mathrm{DL}}^{\mathrm{LW}}$, have been summarized in Table 6-I. Previously, Chen et. al., succeeded in improving the θ_{DL} in Ta-N [36] but with the additional challenges of high longitudinal resistivity of $\sim$3000 $\mu\Omega$-cm. Furthermore, the SHE in amorphous Au-Ta alloy by Qu et. al., has also provided an alternative path to enhance the SHE in amorphous Au-Ta alloy [25]. Therefore, our findings of a giant SHE in Pt(P) layers ascribed to extrinsic SHE along with a clear observation of crystalline to amorphous transition via ion implantation may provide an alternate path to enhance the SHE in by incorporating non-metallic impurity in host 5d TM such as Pt. Such a finding may pave path for implementation in finding a SHE material for writing memory bits in SOT-MRAM.

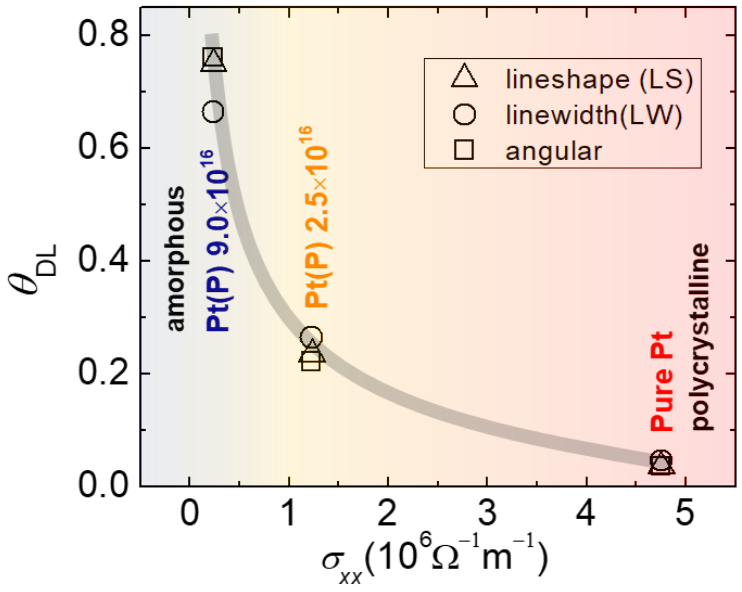

Figure 6.7. θ_{DL} as a function of σ_{xx}, calculated by three ST-FMR methods i.e., lineshape, angular, and linewidth.

Table 6-I. Thickness from XRR, σ_{xx} θ_{DL}^{LS}, θ_{DL}^{ang} , and θ_{DL}^{LW} and σ_{xx} for different dose of P-ion implantation.

Dose	Thickness from XRR (nm)	σ_{xx} $(10^6\Omega^{-1}m^{-1})$	θ_{DL}^{LS}	θ_{DL}^{ang}	θ_{DL}^{LW}
Pure Pt	11.5	4.75	0.034	0.034	0.045
Pt(P) 2.5 $\times 10^{16}$	20.5	1.22	0.264	0.220	0.264
Pt(P) 9.0 $\times 10^{16}$	36.7	0.23	0.750	0.662	0.761

Table 6-II. σ_{SH}^{int}, θ_{SH}^{sj} for P-implanted Pt.

	$\sigma_{SH}^{int}(\Omega^{-1}\mathrm{cm}^{-1})$	θ_{SH}^{sj}
Pt(P) 0.0 $\times 10^{16}$	1303.29	0.19
Pt(P) 2.5 $\times 10^{16}$	1447.62	0.047
Pt(P) 7.5 $\times 10^{16}$	811.20	0.40
Pt(P) 9.0 $\times 10^{16}$	801.26	0.19

6.3.4. Extrinsic side-jump induced SHE

Following the similar model as discussed previously in chapter 5, by using the same eqn. 5.8, $\left|\sigma_{SH}^{xy}\right| = \sigma_{SH}^{int} + \left|(\theta_{SH}^{sj}\,\rho_{xx,0})\sigma_{xx}^{2}\right|$, we find that the dominant contribution is extrinsic side-jump as shown in Fig. 6.8 even for the Pt(P) samples, as the implantation dose increases. The extracted contribution of σ_{SH}^{int} and θ_{SH}^{sj} is summarized in Table 6-II. This brings us to the assertion that higher the $\rho_{xx,0}$, higher is the θ_{SH}^{sj}, and therefore lower is the σ_{SH}^{int}. This gives us a model that by simply increasing the ρ_{xx} and hence the $\rho_{xx,0}$, the SHE can be enhanced for all the ion implanted samples.

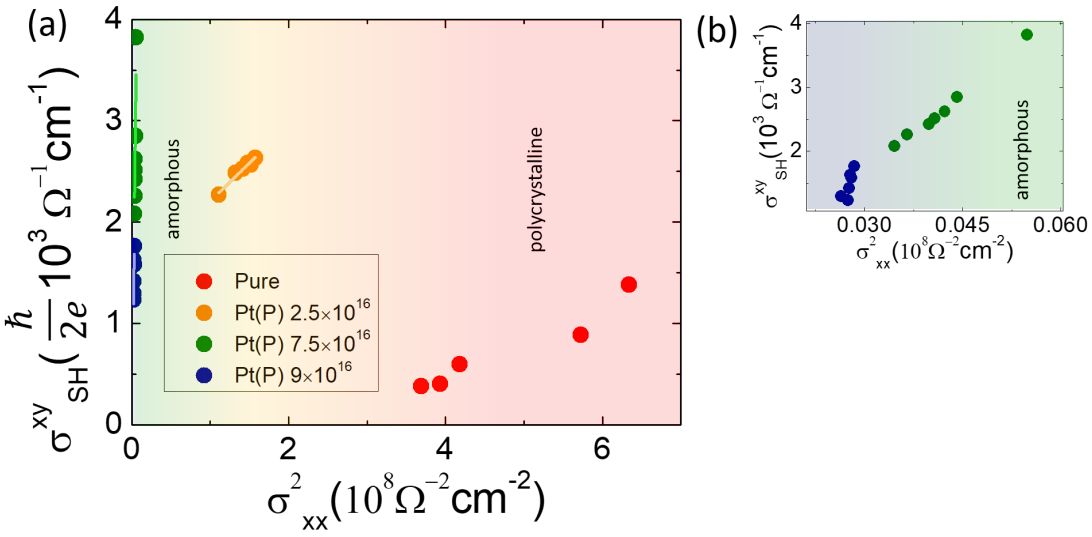

Figure 6.8. (a) σ_{SH}^{xy} plotted as a function of σ_{xx}^{2} for P-ion implantation and Pure Pt (The solid lines represent the fitting using Eq. (5.8). (b) Zoomed plot of σ_{SH}^{xy} plotted as a function of σ_{xx}^{2} for Pt(P) 7.5-9 $\times 10^{16}$.

6.4. Conclusion: benchmark of charge-to-spin conversion

Figure 6.9 summarizes the θ_{DL} as a function of σ_{xx} for ion-implanted Pt along with Pt-based alloys. Therefore, as discussed in the first chapter of this thesis for the better candidates for the replacing the SHE material in SOT-MRAM, The Pt(P) seems to be the best at room temperature due to its giant θ_{DL} and considerable σ_{xx} (or low ρ_{xx}). The Pt(S) may be a suitable SOT-MRAM candidate at cryogenic temperatures. Therefore, we can conclude that ion implantation is a better technique to enhance the charge-to-spin conversion in the archetypal Pt. While at the same time, the dominant extrinsic side-jump induced SHE mechanism is the reason for catalyzing the scattering near these non-metallic impurity sites in Pt.

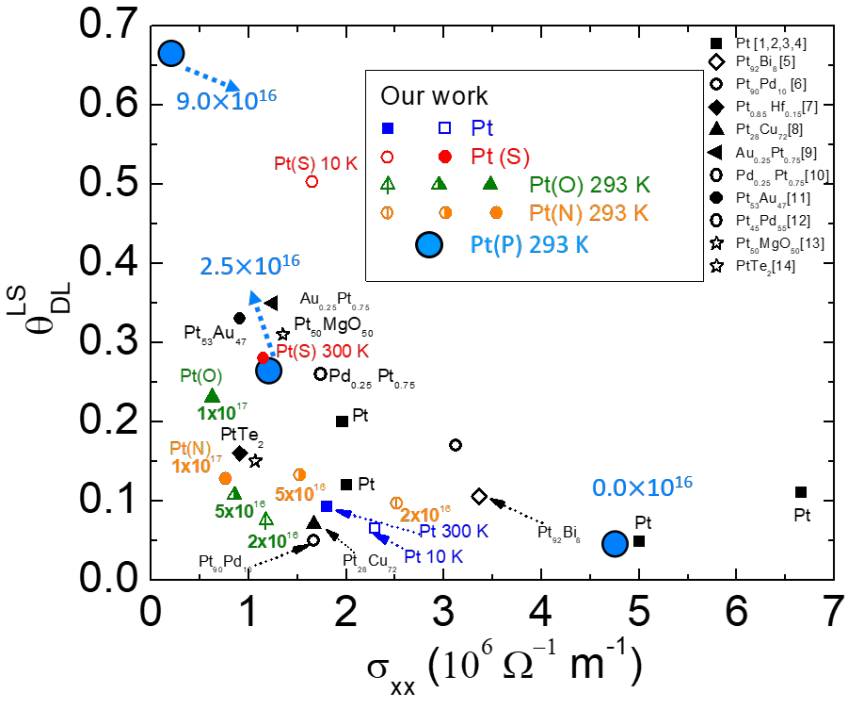

Figure 6.9. Bird-eye view showing reported θ_{DL} values for pure-Pt and its derivative alloys together with Pt (S, O, N, P) as a function of electrical conductivity σ_{xx}.

References for chapter 6

1. L. Liu L, C. –F. Pai, Y. Li, H. W. Tseng, D. C. Ralph and R. A. Buhrman, *Science* **336** 555 (2012).
2. L. Zhu, L. Zhu, S. Shi, D. C. Ralph, and R. A. Burhman, *Adv. Electron Mater*. **6**, 1901131 (2020).
3. X. Han, X. Wang, C. Wan, G. Yu, and X. Lv, *Appl. Phys. Lett.* 118, 120502 (2021).
4. J. E. Hirsch, Phys. Rev. Lett. **83**, 1834 (1999).
5. J. Wunderlich, B. Kaestner, J. Sinova, and T. Jungwirth, *Phys. Rev. Lett.* **94,** 047204 (2005).
6. H. L. Wang, C. H. Du, Y. Pu, R. Adur, P. C. Hammel, and F. Y. Yang, *Phys. Rev. Lett.* **112**, 197201 (2014).
7. L. Zhu, K. Sobotkiewich, X. Ma, X. Li, D. C. Ralph, and R. A. Buhrman, *Adv. Funct. Mater.* **29** 1805822 (2019).
8. L. Qian, K, Wang, Y. Zheng, and G. Xiao, *Phys. Rev. B* **102**. 094438 (2020).
9. M. –H Nguyen, C. –F. Pai, K. X. Nguyen, D.A. Muller, D. C. Ralph, and R. A. Burhman, *Appl. Phys. Lett.* 106, 222402 (2015).
10. H. Mazraati, M. Zahedinejad, and J. Åkerman, *Appl. Phys. Lett.* 113, 092401 (2018).
11. W. F. Zhang, S. –H. Yang, Y. Sun, Y. Zhang, B. Yan, and S. S. P. Parkin, *Sci Adv*. **2**, e1600759 (2016).
12. D. MacNeill, G. M. Stiehl, M. H. D. Guimarães, R. A. Burhman, J. Park, and D. C. Ralph, *Nat. Phys.* **13**, 300 (2017).
13. A. R. Mellnik, J. S. Lee, A. Richardella, J. L. Grab, P. J. Mintun, M. H. Fischer, A. Vaezi, A. Manchon, E. –A. Kim, N. Samarth, and D. C. Ralph, *Nature* **511**, 449 (2014).
14. L. Zhu, D. C. Ralph, and R. A. Burhman, *Phys. Rev. Appl.* **10**, 031001 (2018).
15. J. Sklenar, W. Zhang, M. B. Jungfleisch, H. Saglam, S. Grudichak, W. Jiang, J. E. Pearson, J. B. Ketterson, and A. Hoffmann, *Phys. Rev. B.* **95**, 224431 (2017).
16. L. Liu, T. Moriyama, D. C. Ralph, and R. A. Burhman, *Phys. Rev. Lett.* **106**, 036601 (2011).
17. J. Sinova, S. O. Valenzuela, J. Wunderlich, C. H. Back, and T. Jungwirth, *Rev. Mod. Phys.* **87**, 1213 (2015).
18. N. Nagaosa, J. Sinova, S. Onoda, A. H. MacDonald, and N. P. Ong, *Rev. Mod. Phys.* **82,** 1539 (2010).
19. Y. Niimi, and Y. Otani, *Rep. Prog. Phys.* **78**, 124501 (2015).
20. P. Wang, A. Migliorini, S. -H. Yang, J. -C. Jeon, I. Kostanovskiy, H. Meyerheim, H. Han, H. Deniz, and S. S. P. Parkin, *Adv. Mater.* **34**, 2109406 (2022).
21. Y. –C. Lau, T. Seki, and K. Takanashi, *APL Mater.* **9**, 081113 (2021).
22. U. Shashank, R. Medwal, T. Shibata, R. Nongjai, J. V. Vas, M. Duchamp, K. Asokan, R. S. Rawat,

H. Asada, S. Gupta, Y. Fukuma, *Adv. Quantum Technol.* **4** 2000112 (2021).

23. U. Shashank, R. Medwal, Y. Nakamura, J. R. Mohan, R. Nongjai, A. Kandasami, R. S. Rawat, H. Asada, S. Gupta, and Y. Fukuma, *Appl. Phys. Lett.* **118** 252406 (2021).
24. J. Liu, T. Ohkubo, S. Mitani, K. Hono, and M. Hayashi, *Appl. Phys. Lett.* **107**, 232408 (2015).
25. D. Qu, S. Y. Huang, G. Y. Guo, and C. L. Chien, *Phys. Rev. B* **97**, 024402 (2018).
26. T. Li, W. Jia, T. Gao, S. Haku, Z. Ye, M. Qiu, and H. An, *Appl. Phys. Lett.* **121**, 132403 (2022).
27. J. W. Lee, Y. –W. Oh, S. –Y. Park, A. I. Figueroa, G. van der Laan, G. Go, K. –Y. Lee, and B. –G. Park, *Phys. Rev. B* **96**, 064405 (2017).
28. L. Zhu, L. Zhu, M. Sui, D. C. Ralph, and R. A. Burhman, *Sci. Adv.* **5**, eeav8025 (2019).
29. Z. Chi, Y. –C. Lau, M. Kawaguchi, and M. Hayashi, *APL Mater.* **9** 061111 (2021).
30. M. Harder, Y. Gui, and C.-M. Hu, *Phys. Rep*. **661**, 1 (2016).
31. T. Skinner, Electrical control of spin dynamics in spin-orbit coupled ferromagnets, Ph.D. thesis, University of Cambridge, 2014.
32. J. Sklenar, W. Zhang, M. B. Jungfleisch, H. Saglam, S. Grudichak, W. Jiang, J. E. Pearson, J. B. Ketterson, and A. Hoffman, *Phys. Rev. B* **95**, 224431 (2017).
33. D. MacNeill, G. M. Steihl, M. H. D. Guimaraes, R. A. Burhman, J. Park, and D. C. Ralph, *Nat. Phys*. **13**, 300 (2017).
34. A. Okada, Y. Takeuchi, K. Furuya, C. Zhang, H. Sato, S. Fukami, and H. Ohno, *Phys. Rev. Appl.* **12**, 014040 (2019).
35. T. Nan, S. Emori, C. T. Boone, X. Wang, T. X. Oxholm, J. G. Jones, B. M. Howe, G. J. Brown, and N. X. Sun, *Phys. Rev. B* **91**, 214416 (2015).
36. T.-Y. Chen, C.-T. Wu, H.-W. Yen, and C.-F. Pai, *Phys. Rev. B* **96**, 104434 (2017).

Chapter 7

Beyond Ion-implanted Pt: Room temperature charge-to-spin conversion from q-2DEG-based interfaces

(This chapter is based on the results published in physica status solidi (RRL)-Rapid Research Letters (2022), Wiley [Ref. 39], and it appears here as a modified version with additional details and discussions)

In chapter 1, we discussed about the candidates for SOC material in SOT-MRAM, with one them being the quasi-two-dimensional electron gas (q-2DEG) created between two insulating oxides. In chapter 3-6, we explored the charge-to-spin conversion in Ion implanted Pt. Therefore, in this chapter, we extend our quest of SOC material beyond the implanted Pt, to a new, less explored and intriguing candidate- the q-2DEG.

7.1. Introduction

Ever since its discovery, the formation of 2-dimensional electron gas (2DEG) at oxide interfaces has attracted significant research interest owing to the presence of conduction electrons and its interesting phenomena, such as superconductivity and magnetism [1-3]. In addition to the observation of interfacial conductivity, the ability to achieve high carrier mobility > 10^5 cm $V^{-1}s^{-1}$ in 2DEG is particularly interesting in the development of all-oxide devices [4-5]. Theoretical reports [6-8] predicted that, due to the presence of an inversion asymmetry at the interface, a 2DEG electron with momentum $\boldsymbol{p}$ in the presence of an electric field $\boldsymbol{E}$ can experience a Rashba-like field $\propto \boldsymbol{p} \times \boldsymbol{E}$ in its rest frame because of spin-orbit coupling (SOC)[9]. The possibility of achieving a strong Rashba SOC at these 2DEG allows compatibility with spintronic devices, and, therefore, has given rise to a series of experiments to understand magneto transport in the 2DEG [10-20]. A large number of these investigations have been focused on spin-charge interconversion in 2DEG formed at interfaces of epitaxial $LaAlO_3$ (LAO) and $LaTiO_3$ (LTO) films grown on single-crystalline $SrTiO_3$ (STO) substrates [15-20]. Recently, reports on giant room temperature charge to spin conversion

efficiency, θ_{cs} as high as 6.3 in epitaxial LAO/STO-based 2DEG [15], implying that they are significantly more efficient than most heavy metals (HM) [21], topological insulators [22-23] and engineered HM [24-26] towards spin current generation. Such properties position the 2DEG as an interesting candidate for applications in future spintronic devices, such as power-efficient spin-charge current interconversion.

Recent reports on high mobility in these amorphous oxides/2DEG formed in systems like STO/Al_2O_3 interfaces have brought back attention towards 2DEG formed in such materials owing to their relative ease of deposition compared to their crystalline counterparts [4,27]. These 2DEG originate from oxygen vacancies in the STO side and are confined to a few nanometers (nm) inside the substrate surface. Broadly speaking, when a metal-based oxide/nitride, especially the Al-based materials, is deposited on an STO substrate, a layer of oxygen vacancies is created at the surface of STO due to the redox reactions between Al-based oxide/nitride and STO [28- 30]. Such oxygen vacancies lead to mobile electrons, producing interfacial quasi-2DEG (hereafter, q-2DEG) inside STO. This leads to the creation of a conductive channel inside the STO substrate. Such q-2DEG induced by oxygen vacancy have often been overlooked in earlier studies and therefore we focus on potential higher charge-spin interconversion in these systems. Furthermore, although spin-charge current interconversion in 2DEG was reported at cryogenic temperatures[27], a systematic analysis of such a phenomenon at room temperature is lacking. Previous studies have indicated that angular-dependent measurement of magnetization dynamics is crucial towards an accurate estimation of magnetic anisotropies and torques [26, 31-34]. Therefore, we use such an approach to systematically investigate the charge-to-spin conversion efficiency of q-2DEG.

7.2. Experimental details (Device fabrication)

First, a marker of Ti (10 nm) is created by lift-off patterning on TiO_2 terminated $SrTiO_3$ (STO) as shown in Fig. 7.1 (a) to use it for the alignment in the next pattern. Then, the hall bar and ST-FMR pattern is created (Fig. 7.1 (b)) and subsequently, AlN and Al_2O_3 is deposited inside the pattern using pulsed laser deposition (PLD) at room temperature at a pressure of 10^{-4} Pa. The sheet resistance, R_s of the STO/AlN and STO/Al_2O_3 samples are ~90 kΩ/□. and ~10^3 kΩ/□, respectively. The top half of the sample is covered with

a resist while the bottom half is used to deposit NiFe (5 nm) to create ST-FMR devices. From the top half, i.e., hall bars are used to measure sheet resistance, R_s and is found to be ~90 kΩ/□. and ~10^3 kΩ/□ for STO/AlN and STO/Al_2O_3, respectively. The optical image after deposition of AlN (hall bars) is shown in Fig. 7.1 (d), in top half (orange box). While the bottom half (red box) shows AlN/NiFe inside the same pattern in Fig. 7.1 (d). CPW is patterned for ST-FMR devices as shown in Fig. 7.1 (e) and finally, Ti (10 nm)/Al (200 nm) electrodes is deposited via DC sputtering as shown in Fig. 7.1 (f). A flowchart for the device fabrication is also shown to help in the better visualization of these devices using a side view as shown in Fig. 7.2.

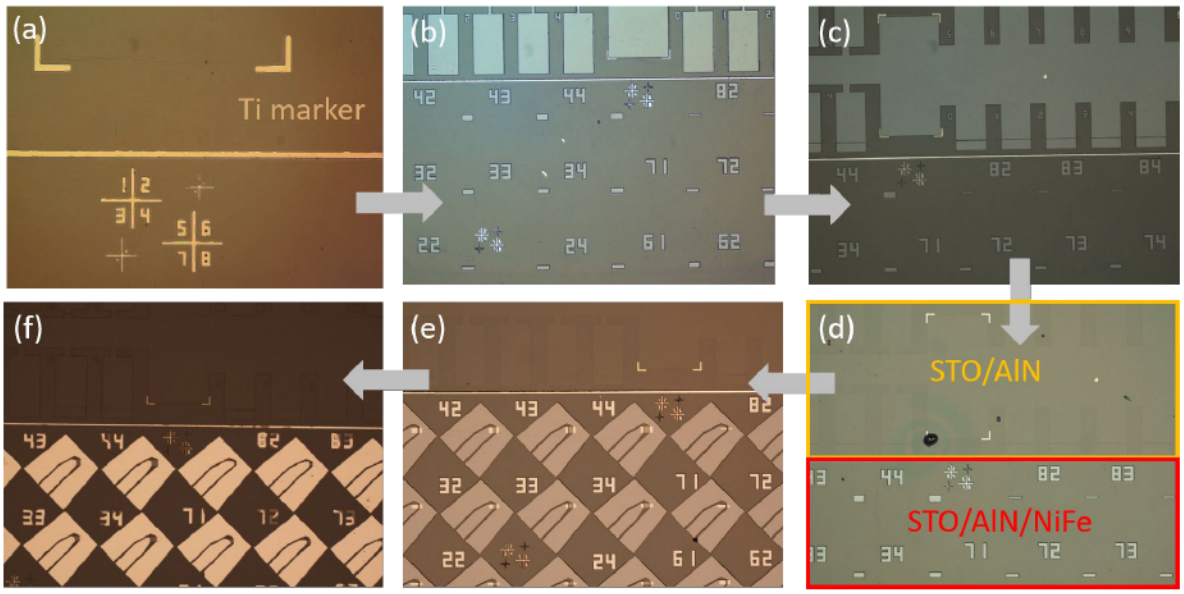

Figure 7.1. Optical microscope image of device fabrication.

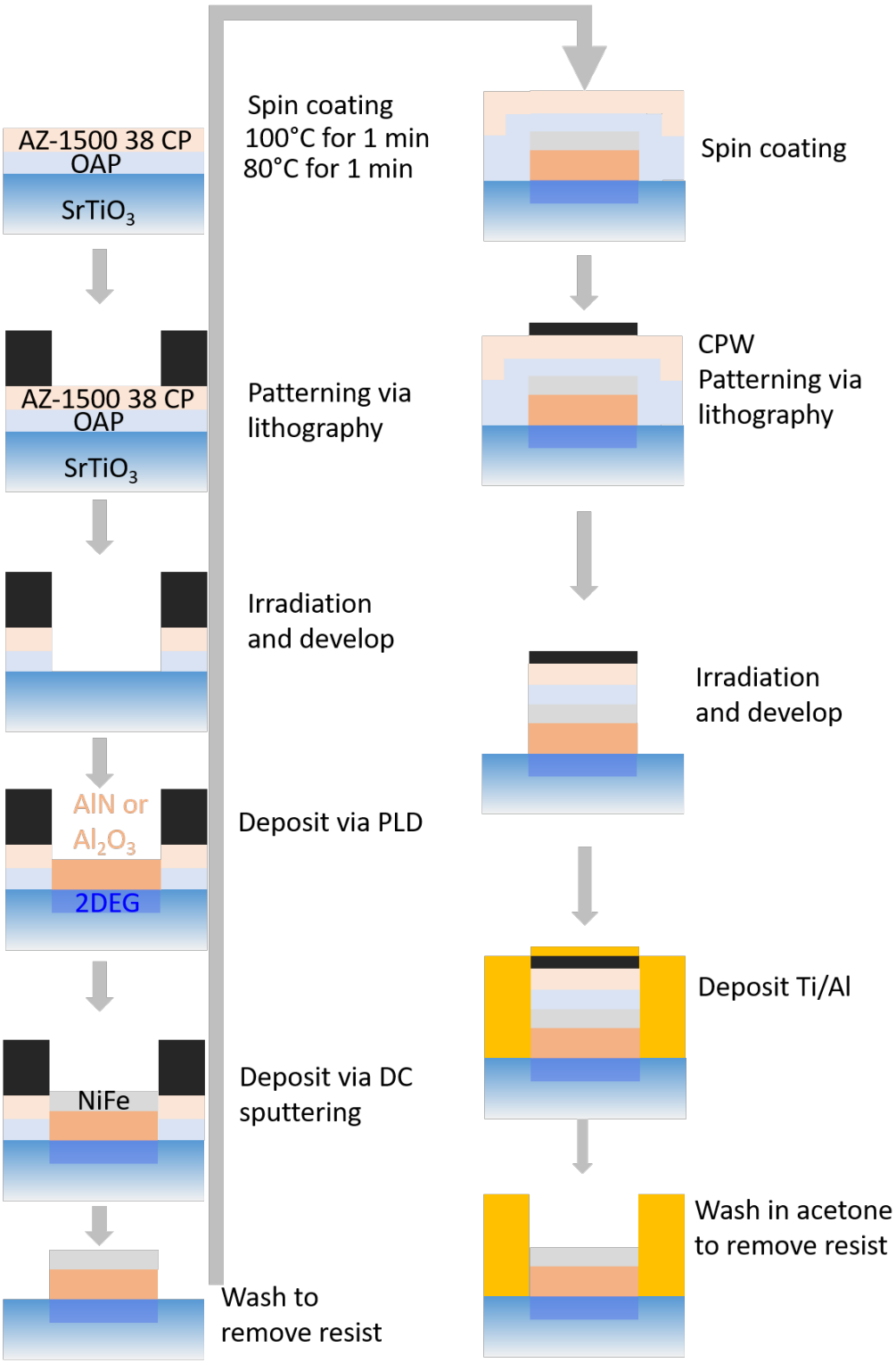

Figure 7.2. Flowchart of ST-FMR devices made for $SrTiO_3$/AlN/NiFe and $SrTiO_3$/Al_2O_3/NiFe using lithography.

7.3. Results and discussion

7.3.1. Creation of quasi-2DEG and Line shape analysis

Creation of quasi-2DEG

For the experimental confirmation of 2DEG, we chose *T*-dependent sheet resistance R_s measurement. Figure 7.3(a), (b) shows the normalized R_s of STO/AlN and STO/Al_2O_3 samples, respectively. The resistance of STO/AlN and $SrTiO_3$/Al_2O_3 decreases with *T*, affirming the metallic nature of both types of 2DEG. In agreement with previous literature [19], for both samples, a kink in the temperature dependence is observed at ~105 K which can be ascribed to the cubic-to tetragonal phase transition of $SrTiO_3$, indicating that the 2DEG exists inside the substrate.

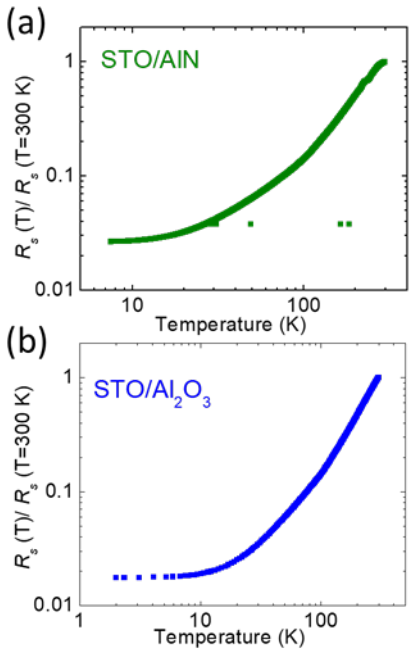

Figure 7.3. Temperature dependence of the R_s (*T*) /R_s (*T* = 300 K) of the (a) $SrTiO_3$ (STO)/AlN and (b) STO/Al_2O_3.

Line shape analysis

Due to the SOC at the q-2DEG, a spin current is generated in q-2DEG, which flows to the adjacent NiFe layer and exerts a torque on its magnetization. This can lead to FMR in the NiFe layer. A combined effect of an alternating anisotropic magnetoresistance (AMR) of NiFe and the microwave current I_{rf} (proportional to spin current), gives the rectified DC voltage V_{mix}, which is recorded using a lock-in amplifier (Fig. 7.4(b)). The input I_{rf} is amplitude modulated by a low frequency sinusoidal wave signal. Moreover, the low frequency modulating signal serves a trigger since it is provided as a reference signal into the reference port of lock-in amplifier. Here, in the ST-FMR device as shown in Fig. 7.4(b)), the modulated I_{rf} is applied that leads to typical ST-FMR spectrum (voltage). Finally, ST-FMR spectrum here is the low frequency voltage (instead of DC) due to the I_{rf} being amplitude modulated. The ST-FMR spectrum can be detected using the phase locking technique. A typical spectrum obtained from this measurement at a frequency of 4.0 GHz is shown in Fig. 7.4(c). This spectrum is then fitted with the sum of a symmetric Lorentzian and an antisymmetric component using the following equation [35].

$$V_{mix} = SF_{sym}(H_{ext}) + AF_{asym}(H_{ext}), \tag{7.1}$$

where $F_{sym}(H_{ext}) = \frac{(\Delta H)^2}{(H_{ext}-H_o)^2+(\Delta H)^2}$, is the symmetric component with weight S, $F_{asym}(H_{ext}) = \frac{\Delta H(H_{ext}-H_o)}{(H_{ext}-H_o)^2+(\Delta H)^2}$, is the antisymmetric component with weight A, and ΔH and H_0 are the half-width-at-half-maximum and resonance field of the FMR spectra [25,35]. From the fit, we obtain $\mu_o\Delta H$= 4.34 mT for STO/AlN/NiFe and $\mu_o\Delta H$= 1.71 mT for the STO/Al_2O_3/NiFe sample at f = 5 GHz, which indicates lower damping for the latter sample (also see section 7.3.3). Meanwhile, we obtain $\mu_o H_0$ = 38.54 mT for STO/AlN/NiFe and $\mu_o H_0$= 33.59 mT for the STO/Al_2O_3/NiFe sample at f= 5 GHz. Because the NiFe layers were deposited on both samples simultaneously, the difference in resonance field may be due to different effective demagnetizing fields, M_{eff}, in the two samples [33].

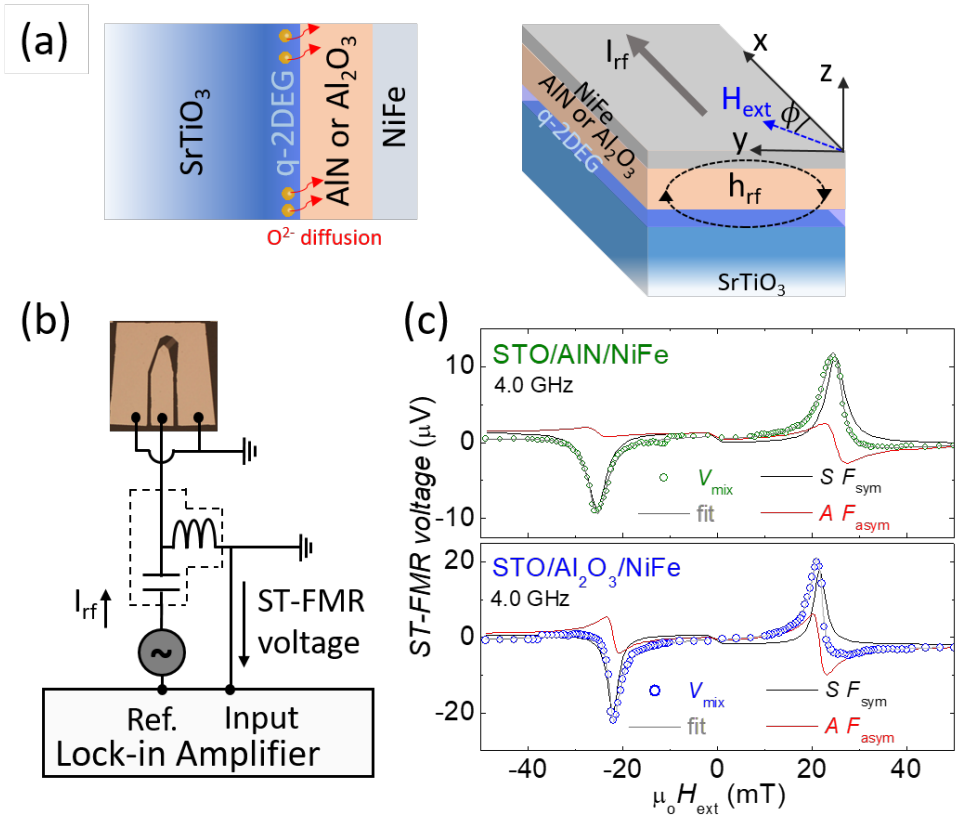

Figure 7.4. (a) Schematic of q-2DEG formed inside the STO substrate at the interface with AlN or Al_2O_3. Upon deposition of AlN or Al_2O_3, the O^{2-} diffuses outwards from the TiO_2-terminated STO, resulting in formation of an oxygen-vacancy induced quasi-2DEG (q-2DEG) near the surface of STO. The right panel additionally shows the multilayer structures and different parameters used in the measurement. (b) Schematic of ST-FMR set-up along with an optical image of the device. (c) ST-FMR spectra V_{mix}, together with fitted symmetric and antisymmetric components, which were obtained at f = 4 GHz for STO/AlN/NiFe and STO/Al_2O_3/NiFe.

In addition, we also observed that, while the symmetric component magnitude is almost similar with an opposite sign with the H_{ext} reversed, the antisymmetric component is different upon H_{ext} reversal (also see section 7.3.3). The odd parity of the symmetric component with respect to the direction of the magnetic field indicates that it originates from the spin-torque generated by the q-2DEG. Due to the SOC at the q-2DEG, a spin current is generated transverse to the flow of microwave current I_{rf}. This spin current

flows from the q-2DEG to the NiFe layer and exerts a torque on the magnetization of NiFe, resulting in the symmetric component of the ST-FMR spectra. Additionally, the I_{rf} also generates an Oersted field, h_{rf} which can exert a field-torque on the magnetization of NiFe layer and give rise to the antisymmetric component of the ST-FMR spectra [25].

7.3.2. Power dependent ST-FMR measurements

To understand if the applied power in our experiments (which is 10 dBm) is not large enough to induce a non-linear magnetization dynamics in NiFe, we perform the power-dependent ST-FMR measurements. We study ΔH and H_o as a function of the applied power in a wide range of 0-13 dBm (1-19.96 mW). At high powers, the cone angle of precession during FMR increases significantly. At such high cone angles of precession, the effective perpendicular demagnetizing field reduces because the demagnetization coefficients along the in-plane direction can no longer be ignored. This leads to a change in H_o at higher powers. ΔH may increase because of excitation of higher order magnon modes [33-34]. We observe an invariant ΔH and H_0 obtained as a function of power for STO/AlN/NiFe and STO/Al_2O_3/NiFe, as shown in Fig. 7.5. Therefore, we restrict all our measurements to 10 dBm (10 mW).

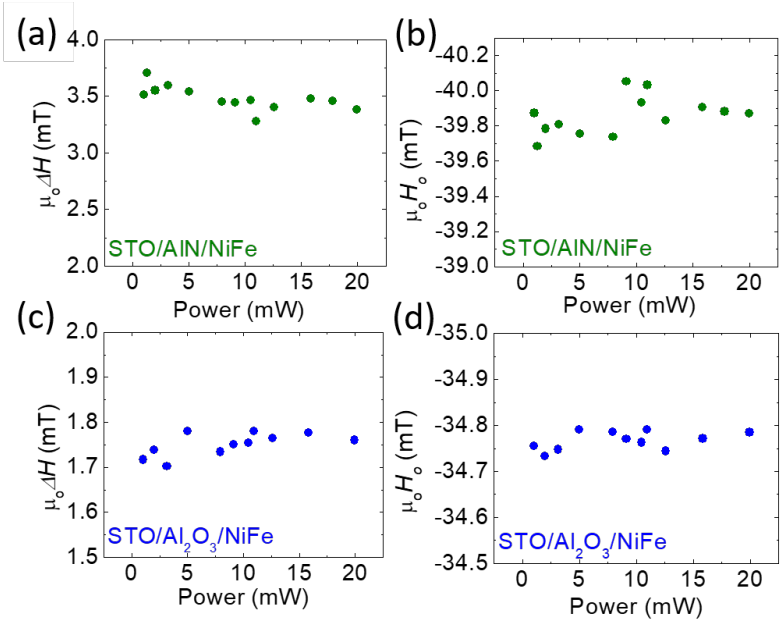

Figure 7.5. ΔH and H_0 obtained as a function of applied power for STO/AlN/NiFe and STO/Al_2O_3/NiFe.

7.3.3. Frequency dependent ST-FMR measurements

Frequency-dependent measurements of the ST-FMR spectra in the range of 3.5 - 5 GHz for the STO/AlN/NiFe and STO/Al_2O_3/NiFe samples were performed (see Fig. 7.6(a), (b)). Throughout the frequency range, we observed a similar behaviour of the symmetric and antisymmetric components of the ST-FMR spectra for both samples as described in the previous paragraph. The amplitude of the spectra decreases at a higher frequency. The resonance field, H_o increases increasing frequency, which in turn leads to a lower precession cone angle at higher H_{ext}. Additionally, the H_o increases with the frequency, which agrees well with the Kittel equation. Upon fitting to the Kittel equation [34], we obtained $\mu_o M_{eff}$ = 698 mT and 814 mT for the STO/AlN/NiFe and the STO/ Al_2O_3/NiFe samples, respectively ((see Fig. 7.6(c), (d)). This confirms that the difference in resonance fields in STO/AlN/NiFe and STO/Al_2O_3/NiFe samples arises from the different effective demagnetizing fields [34].

The gilbert damping parameter, αis also an important parameter to understand the transverse spin current created from the Onsager reciprocity of charge-to-spin conversion. We obtain a higher α for STO/AlN/NiFe as compared to STO/Al_2O_3. In concordance with the higher α, a lower effective demagnetizing fields is seen for STO/AlN/NiFe as seen in (see 7.6(e), (f)).

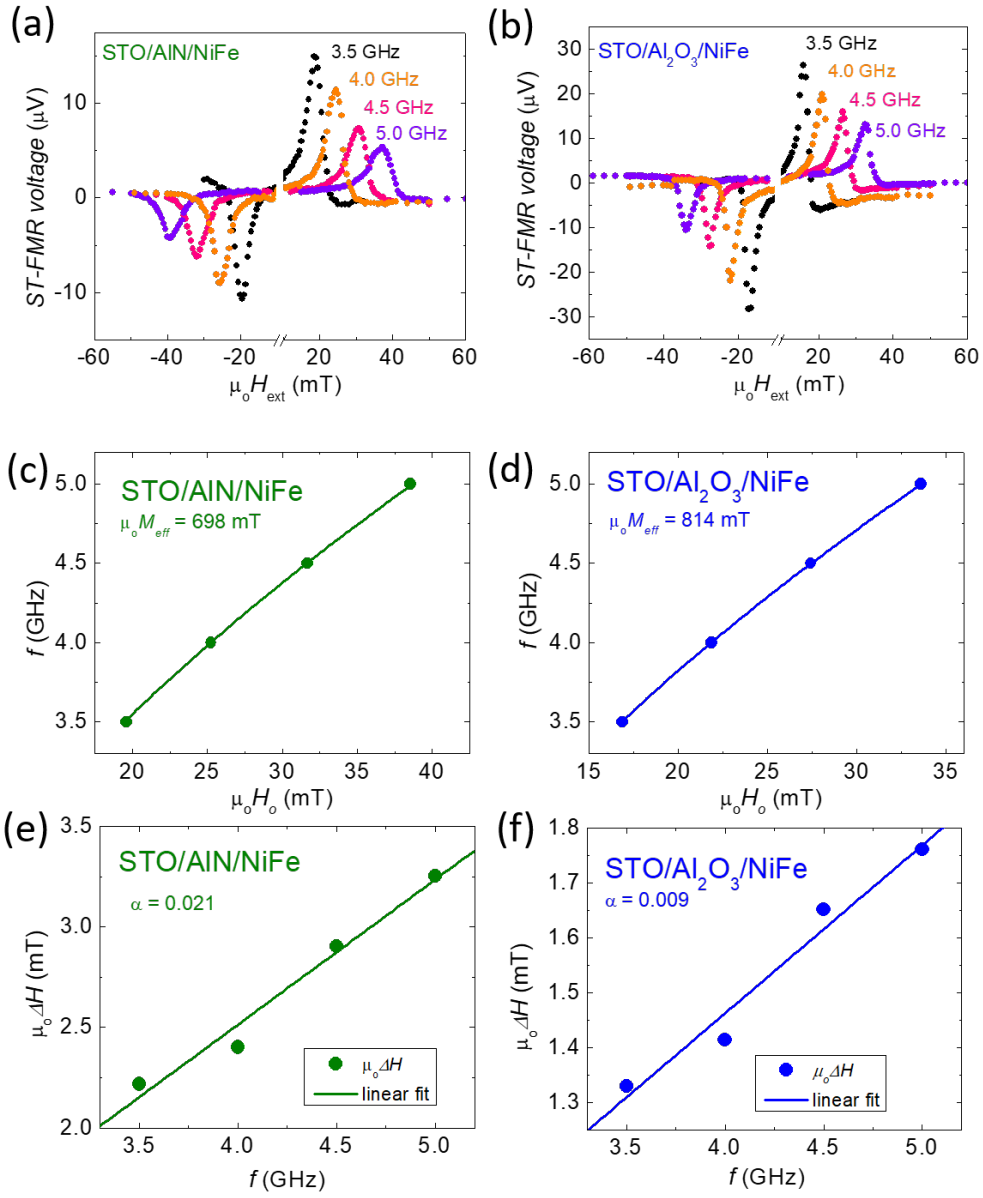

Figure 7.6. Frequency-dependent ST-FMR spectra, for f = 3.5-5 GHz, as a function of H_{ext}, for (a) STO/AlN/NiFe and (b) STO/Al_2O_3/NiFe, f vs H_o (with solid lines as Kittel equation fit) and ΔH vs f (with solid lines as linear fit), for ((c), (e)) STO/AlN/NiFe and ((d), (f)) STO/Al_2O_3/NiFe.

7.3.4. Angular dependence of symmetry of torques

The symmetric component can be fitted by using some other additional components if the two-fold and mirror symmetry of the torques is broken as:

$$V_S = a \sin2\phi\cos\phi + b \sin\phi\sin2\phi, \quad (7.2)$$

where a is the amplitude of the angular dependence of $\sin2\phi\cos\phi$ arising from the presence of an in-plane damping-like spin-orbit torque τ_{DL} due to y-polarized spin currents $\hat{\sigma}_y$ injected into NiFe. The τ_{DL} has a $\cos\phi$ symmetry, while the additional $\sin2\phi$ arises from the AMR of NiFe. There is also an additional term b $\sin\phi\sin2\phi$, where b is the amplitude of the angular dependence arising from the x-polarized spin currents $\hat{\sigma}_x$ injected into NiFe. So far, we do not know the exact origin of this additional b $\sin\phi\sin2\phi$ term, but it can be observed due to the presence of $\hat{\sigma}_x$. Additionally, to investigate the change in the antisymmetric spectra, the antisymmetric component can be fitted with additional components apart from $\sin2\phi\cos\phi$ as:

$$V_A = c \sin2\phi\cos\phi + d \sin\phi\sin2\phi + é \sin2\phi, \quad (7.3)$$

where c is the amplitude of angular dependence of $\sin2\phi\cos\phi$ arising from τ_{OFT} due to the Oersted field in the y-direction $h_{rf,y}$. Further, d is the amplitude of $\sin\phi\sin2\phi$ arising from the Oersted field in x-direction $h_{rf,x}$. Finally, é is the amplitude of $\sin2\phi$ arising from the Oersted field in the z-direction $h_{rf,z}$. The additional components arising from $h_{rf,x}$ and $h_{rf,z}$ are attributed to the non-uniform current flow that may arise from the q-2DEG and adjacent NiFe above the oxide layer.

The values for each of the components arising in the symmetric and antisymmetric part of ST-FMR spectra are summarized in Supporting Table 7-I and 7-II for STO/AlN/NiFe and STO/Al_2O_3/NiFe, respectively. Please see Fig. 7.7. for the Symmetric and Antisymmetric components.

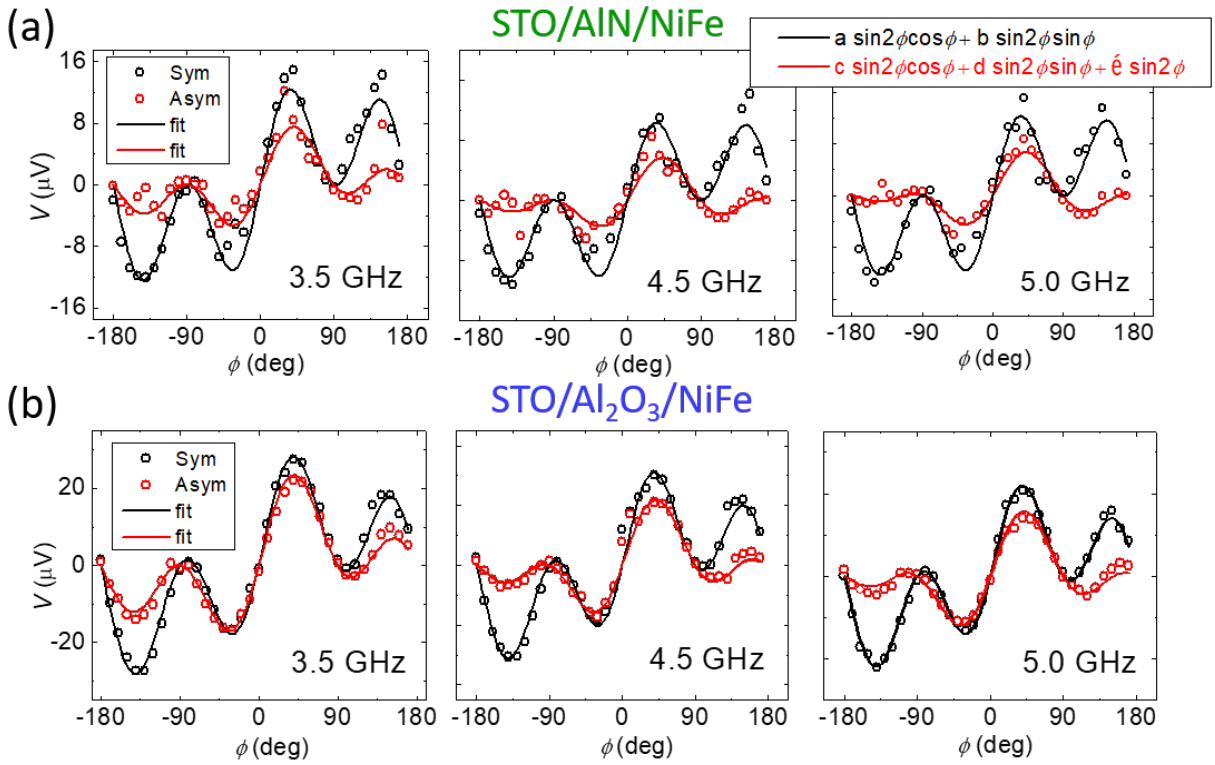

Figure 7.7. Angular-dependent ST-FMR measurements for (a) STO/AlN/NiFe and (b)STO/Al_2O_3/NiFe measured for f = 3.5, 4.5, 5.0 GHz with the fitting using Eq. (7.2) and Eq. (7.3) for symmetric (red) and antisymmetric (black) component, respectively.

Table 7-I. f, θ_{CS}/t (lineshape), θ_{CS}/t (angular), and Symmetric and Antisymmetric weightage for STO/AlN/NiFe.

f (GHz)	θ_{CS}/t Lineshape (nm^{-1})	θ_{CS}/t Angular (nm^{-1})	Symmetric		Antisymmetric		
			$\sin 2\phi \cos\phi$ (a)	$\sin\phi \sin 2\phi$ (b)	$\sin 2\phi \cos\phi$ (c)	$\sin\phi \sin 2\phi$ (d)	$\sin 2\phi$(é)
3.5	0.132	0.202	15.27 µV (92.6 %)	1.22 µV (7.4 %)	5.87 µV (60.7 %)	1.89 µV (19.5 %)	1.90 µV (19.8 %)
4	0.137	0.264	11.71 µV (94.2 %)	0.72 µV (5.8 %)	2.95 µV (48.8 %)	1.42 µV (23.5 %)	1.67 µV (27.7 %)
4.5	0.127	0.275	8.27 µV (98.4 %)	0.13 µV (1.6 %)	2.03 µV (45.5 %)	1.14 µV (25.5 %)	1.30 µV (29.0 %)
5	0.104	0.234	5.81 µV (95.8 %)	0.25 µV (4.2 %)	1.31 µV (42.8 %)	0.66 µV (21.5 %)	1.09 µV (35.7 %)

Table 7-II. f, θ_{CS}/t (lineshape), θ_{CS}/t (angular), and Symmetric and Antisymmetric weightage for STO/Al_2O_3/NiFe.

f (GHz)	θ_{CS}/t Lineshape (nm^{-1})	θ_{CS}/t Angular (nm^{-1})	Symmetric		Antisymmetric		
			$\sin2\phi \cos\phi$ (a)	$\sin\phi \sin2\phi$ (b)	$\sin2\phi \cos\phi$ (c)	$\sin\phi \sin2\phi$ (d)	$\sin2\phi$(é)
3.5	0.081	0.097	29.30 µV (75.3 %)	9.59 µV (24.7 %)	19.03 µV (63.1 %)	5.40 µV (17.9 %)	5.74 µV (19.0 %)
4	0.074	0.093	24.21 µV (75.1 %)	7.99 µV (24.9 %)	10.46 µV (60.1 %)	2.19 µV (12.7 %)	4.74 µV (27.2 %)
4.5	0.069	0.103	16.32 µV (76.1 %)	5.11 µV (23.9 %)	6.98 µV (51.1 %)	2.56 µV (18.8 %)	4.10 µV (30.1 %)
5	0.072	0.112	11.46 µV (75.5 %)	3.70 µV (24.5 %)	4.68 µV (48.6 %)	1.57 µV (16.4 %)	3.37 µV (35.0 %)

7.3.5. Angular dependent ST-FMR for Pt/NiFe

In an HM/FM bilayer system such as Pt/NiFe, the problem of impedance mismatch and unconventional spin polarization is less pronounced. Hence, it should lead to the anticipated $\sin2\phi\cos\phi$ arising in both S and A. The S and A arising from angular dependent ST-FMR can be fit using 100% $\sin2\phi\cos\phi$ implying the unbroken two-fold and mirror symmetry of torques in Pt/NiFe, as shown in Figure 7.8. This implies that the lineshape and angular methods give the same value of θ_{cs}, which is ~ 0.08 evaluated using Eq. (7.4) and Eq. (7.5) (See later section 7.3.6). Furthermore, from the DC-biased ST-FMR, (see later section 7.3.7). We find a similar θ_{cs} ~ 0.10, which is in agreement with the lineshape and angular methods.

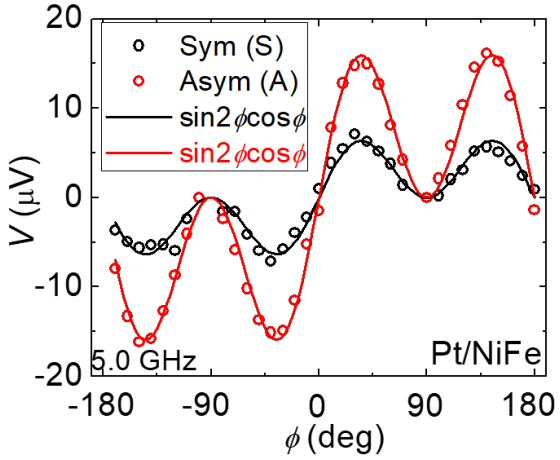

Figure 7.8. Angular-dependent ST-FMR measurements for Pt/NiFe device.

7.3.6. Estimation of charge-to-spin conversion

When the symmetric component of the ST-FMR spectra is attributed to a y-polarized spin current, $\hat{\sigma}_y$ travelling in the z-direction, the angular dependence of the symmetric amplitude follows a $\sin2\phi\cos\phi$ dependence. Simultaneously, due to the flow of an x-axial microwave current in the device, an antisymmetric component is also produced by the corresponding Oersted field, which follows a $\sin2\phi\cos\phi$ dependence. In this scenario, the θ_{cs} can be estimated using [35]:

$$\theta_{\mathrm{cs}} = \frac{S}{A}\frac{e\mu_o M_s dt}{\hbar}\sqrt{1+\frac{M_{eff}}{H_o}}, \tag{7.4}$$

where t is the q-2DEG thickness, e is the elementary charge, μ_o is the permeability of free space, M_S is the saturation magnetization of NiFe, d is NiFe thickness, ħ is the reduced Planck constant and M_{eff} is effective magnetization obtained from the Kittel fitting. The corresponding angular dependent components of voltages in the STO/AlN/NiFe and STO/Al_2O_3/NiFe samples are plotted in Fig. 7.8(a) and 7.8(c), respectively. The symmetric component is fitted to the Eq. 7.1 (see previous section 7.3.1 for details). Furthermore, the antisymmetric component is fitted to eqn. 7.1.

We note that, in our devices, the angular dependence of symmetric and antisymmetric components is not purely $\sin 2\phi\cos\phi$. Figures 7.9(b) and 7.9(d) show the weightage of the different symmetric and antisymmetric parts of the spectra for f = 3.5-5 GHz in the case of the STO/AlN/NiFe and STO/Al_2O_3/NiFe samples, respectively. For STO/AlN/NiFe, the symmetric component has a 95.3% $\sin 2\phi\cos\phi$ dependence, with the rest 4.7% arising from a $\sin 2\phi\sin\phi$ dependence when averaged over the entire frequency range. Meanwhile, its antisymmetric component has an average of 49.5%, 22.5% and 28.0% contributions from a $\sin 2\phi\cos\phi$, $\sin 2\phi\sin\phi$ and $\sin 2\phi$dependence, respectively. In the case of the STO/Al_2O_3/NiFe, we find that the symmetric component has 75.5% $\sin 2\phi\cos\phi$ dependence and 24.5% $\sin\sin\phi$ dependence averaged over the entire frequency range. On the other hand, its antisymmetric component has an average of 55.7%, 16.4% and 27.9% contributions from $\sin 2\phi\cos\phi$, $\sin 2\phi\sin\phi$ and $\sin 2\phi$ dependences, respectively. This indicates breaking of the twofold ($180^\circ+\phi$) and mirror ($180^\circ-\phi$) symmetries of torques for both the q-2DEG-NiFe samples. Therefore the lineshape analysis method, *i.e.*, Eq. (7.4), which uses a spectrum obtained at a single azimuthal angle ϕ, may not reveal the comprehensive picture of torques, leading to inaccurate quantification of SOTs [36].

Although an investigation into the exact origins of these additional components in the ST-FMR spectra is beyond the scope of this article, we would like to emphasize that we reproducibly observed this behaviour in multiple devices over a wide range of frequencies. This may be a consequence of non-uniform

microwave current flow in devices. In order to rule out the possibility that it is caused by our device design, we further verified the same experiments in a Pt/NiFe device fabricated under similar conditions and found 100% $\sin 2\phi\cos\phi$ dependence for both symmetric and antisymmetric components of the ST-FMR spectra (see section 7.3.5). NiFe has a much lower resistivity compared to the q-2DEG created at the STO/AlN interface. This may lead to non-uniform current flow in the q-2DEG-NiFe device, giving rise to the additional angular-dependent components in the ST-FMR spectra for the STO/AlN/NiFe sample. It is noteworthy that the $\sin 2\phi\cos\phi$ contribution reduces for both the symmetric and antisymmetric components in the case of STO/Al_2O_3/NiFe samples, whose 2DEG has ~10 times higher sheet resistance compared to that of STO/AlN/NiFe samples.

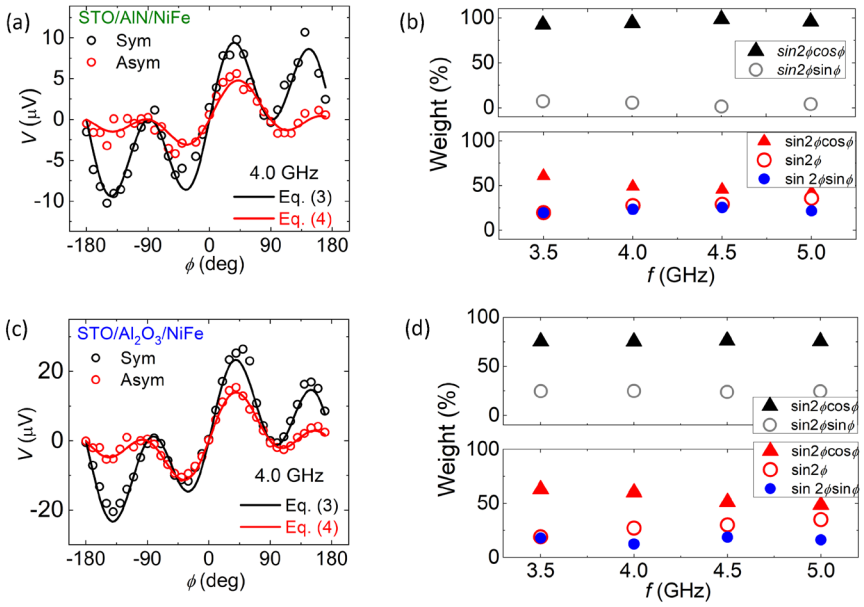

Figure 7.9. Angular dependence of symmetric (Sym) and antisymmetric (Asym) components in ST-FMR spectra obtained as a function of ϕ for (a) STO/AlN/NiFe, and (c) STO/Al_2O_3/NiFe for f = 4.0 GHz with solid lines (black and red) fit by Eq. (7.2) and Eq. (7.3), respectively. Weight (in %) of $\sin 2\phi\cos\phi$ and $\sin 2\phi\sin\phi$ for Symmetric (Sym) and $\sin 2\phi\cos\phi$, $\sin 2\phi\sin\phi$, $\sin 2\phi$ for Antisymmetric (Asym) components are obtained as a function of f for (b) STO/AlN/NiFe and (d) STO/Al_2O_3/NiFe.

Before we proceed to the estimation of θ_{cs}, it should be noted that θ_{cs} is directly proportional to the thickness of the q-2DEG. Therefore, without a direct measurement of the 2DEG thickness, we may end up with overestimated values of θ_{cs}. In order to avoid such a discrepancy in our study, we estimate the q-2DEG thickness normalized conversion efficiency as seen from Eq. (7.5) below. Additionally, to estimate the θ_{cs} corresponding to the dominant y-polarized spin current, $\hat{\sigma}_y$ in the samples, we introduce a ratio a/c, where a and c are weight percentages of the $\sin 2\phi \cos\phi$ component of the symmetric and antisymmetric parts at a specific frequency mentioned earlier. This allows us to rewrite Eq. (7.4) as follows:

$$\frac{\theta_{cs}}{t} = \left(\frac{a}{c}\right)\frac{S}{A}\frac{e\mu_o M_s d}{\hbar}\sqrt{1+\frac{M_{eff}}{H_o}} \quad . \tag{7.5}$$

Using Eq. (7.5), we estimated the median θ_{cs}/t to be 0.244 nm^{-1} for the STO/AlN sample and 0.101 nm^{-1} for the STO/Al_2O_3 sample. The frequency dependence of θ_{cs}/t is shown in Fig. 7.10. The values of θ_{cs}/t estimated using Eq. (7.4) are also plotted in the same figure to show the discrepancy between the two methods.

As mentioned earlier, the calculated values in our case are normalized by the 2DEG thickness. Typically, in previous reports, the 2DEG thickness is assumed to be 10 nm, and a θ_{cs} ~ 1.8 at room temperature has been reported for STO/$LaAlO_3$/NiFe [20], θ_{cs} ~ 2.4 for quasi-2DEG in an STO/$LaTiO_3$/NiFe system [18] and θ_{cs} ~ 6.3 for STO/$LaAlO_3$/CoFeB [15]. In our case, if we assume the 2DEG thickness, t = 10 nm, the θ_{cs} comes out to be 2.44 for the STO/AlN/NiFe and 1.01 for STO/Al_2O_3/NiFe samples. These values are comparable to previous reports on 2DEG formed in epitaxial oxides grown on STO substrates. Note that the AlN and Al_2O_3 layers are amorphous in our case. Hence, the θ_{cs} created at the q-2DEG in our STO/amorphous oxide interfaces are shown to be comparable in terms of charge-to-spin conversion efficiencies with the 2DEG reported for the epitaxial oxides on STO. Moreover, the θ_{cs} in our sample is 1 or 2 orders of magnitude higher than that of HM, such as Pt [37], Ta [21], W [38], and also than engineered HM [24-26]. As seen from the sheet resistance values, the q-2DEG in STO/AlN has 1 order smaller resistance values

compared to STO/Al_2O_3. This indicates that when AlN is deposited over STO substrates, higher number of O^{2-} diffuse outward from the substrate to oxidize AlN compared to when Al_2O_3 is deposited. This in turn creates a larger number of oxygen defects inside the STO substrate. As demonstrated by Chen et al., this difference in diffusion may have to do with the difference in chemical reactivity of AlN and Al_2O_3 with TiO_2-terminated STO[28]. Our observation of a higher charge-to-spin conversion in the STO/AlN samples indicates that the higher oxygen vacancies not only play a role in enhancing the electronic transport, but may also lead to a higher charge-to-spin conversion efficiency in the q-2DEG.

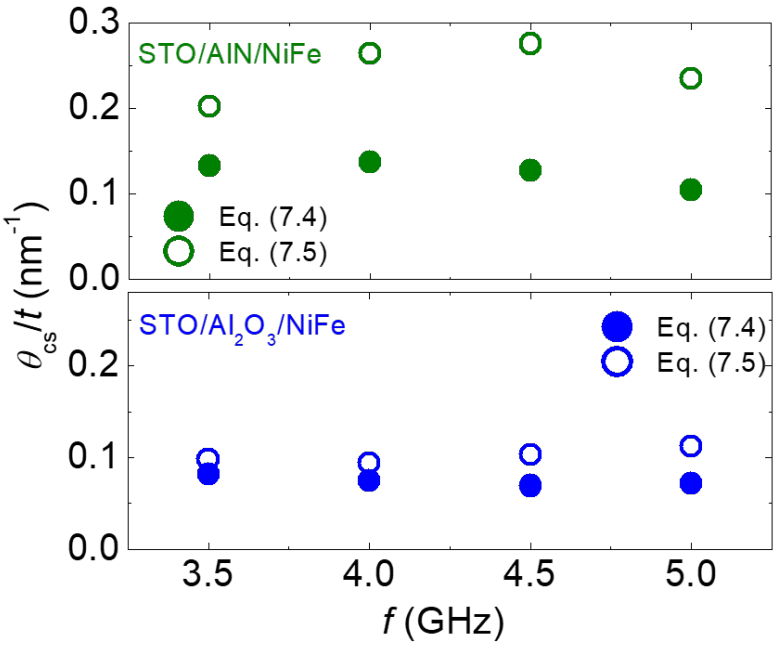

Figure 7.10. Thickness normalized charge to spin conversion efficiency θ_{cs}/t obtained from Eq. (7.4) and Eq. (7.5) as a function of f for STO/AlN/NiFe and STO/Al_2O_3/NiFe.

7.3.7. DC-biased ST-FMR: linewidth modulation

I. Linewidth modulation (modulation of damping) for f = 5GHz

The modulation of damping of FMR can also be an additional tool to overcome the issues with θ_{cs} estimation mentioned in this paper as it provides a direct insight into the strength of damping-like spin torques. This is free from problems arising from impedance mismatch, unconventional spin current polarized in different directions, and Nernst heating [35]. In this method, an additional direct current (DC) I_{dc} is applied along with I_{rf}. The spin current at the Rashba interface, which is proportional to I_{dc}, modulates the ferromagnetic resonance linewidth (or the Gilbert damping) [35] of NiFe via damping-like torque which has an odd polarity with I_{dc}. By measuring the change in linewidth as a function of I_{dc}, the θ_{cs} can be evaluated if the thickness of the q-2DEG is known. Therefore, we performed the I_{dc}-biased ST-FMR measurement on the STO/AlN/NiFe and STO/Al_2O_3/NiFe samples by applying an $I_{dc} \sim \pm$ 7mA along with I_{rf}. The data at f = 5 GHz is shown in Fig. 7.10(a) and 7.10(b). For the STO/AlN/NiFe, we observe a linear modulation of ΔH with I_{dc}. Upon changing the polarity of I_{dc}, we observe a reversed slope of ΔH vs I_{dc} (see Fig. 7.11(a) and section 7.3.7-II). This confirms the presence of dominant damping-like torque in STO/AlN/NiFe. The slope of linewidth modulation for STO/AlN/NiFe is ~3 times higher than the modulation seen for the Pt/NiFe samples as seen in Fig. 7.11(a) and 7.11(c). Due to a much lower resistivity of Pt, it implies that θ_{cs} for STO/AlN/NiFe will be ~1-2 orders higher compared to Pt/NiFe. However, we are unable to quantify θ_{cs} beyond its qualitative discussion since an accurate measure of q-2DEG resistivity is paramount for quantifying θ_{cs} from this measurement, and we do not know the exact thickness of q-2DEG. Furthermore, as seen in Fig. .7.11(b), we are unable to detect any linear modulation in linewidth for STO/Al_2O_3/NiFe. This is due to a significantly higher sheet resistance of the q-2DEG in STO/Al_2O_3, which results in very little current through its q-2DEG and difficulty in detecting any linear modulation of ΔH by I_{dc}. Instead, we obtain the dependence of ΔH vs I_{dc} shown in Fig. 7.11(b), which can be attributed to the dominance of the heating effect over modulation of damping in the sample. An increase of H_o with

increasing I_{dc} magnitude in STO/Al_2O_3/NiFe samples confirms the heating effect [22]. Notably, the H_o does not change with I_{dc} in either STO/AlN/NiFe or Pt/NiFe (see section 7.3.8). We will later explore the heating effect in section 7.3.8.

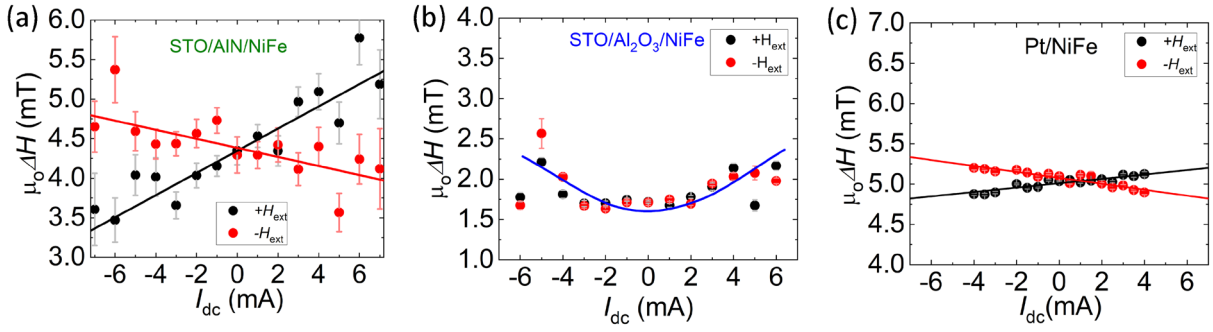

Figure 7.11. DC-biased ST-FMR measurements for (a) STO/AlN/NiFe (b) STO/Al_2O_3/NiFe, and (c) Pt/NiFe showing $\mu_o\Delta H$ as a function of I_{dc}. The red and black lines depict the linear fitting in (a), (c) and non-linear curve in (b).

II. Linewidth modulation (modulation of damping) for other f = 3.5, 4.0, 4.5GHz

We performed the DC-bias ST-FMR to observe the modulation of linewidth for STO/AlN/NiFe measured for f = 3.5, 4.0, and 4.5 GHz under an applied I_{dc} along with I_{rf}. A clear modulation in $\mu_o\Delta H$ of ~1.3-2.0 mT is seen for all the frequencies implying a dominant in-plane damping-like torque in the sample as shown in Fig. 7.12.

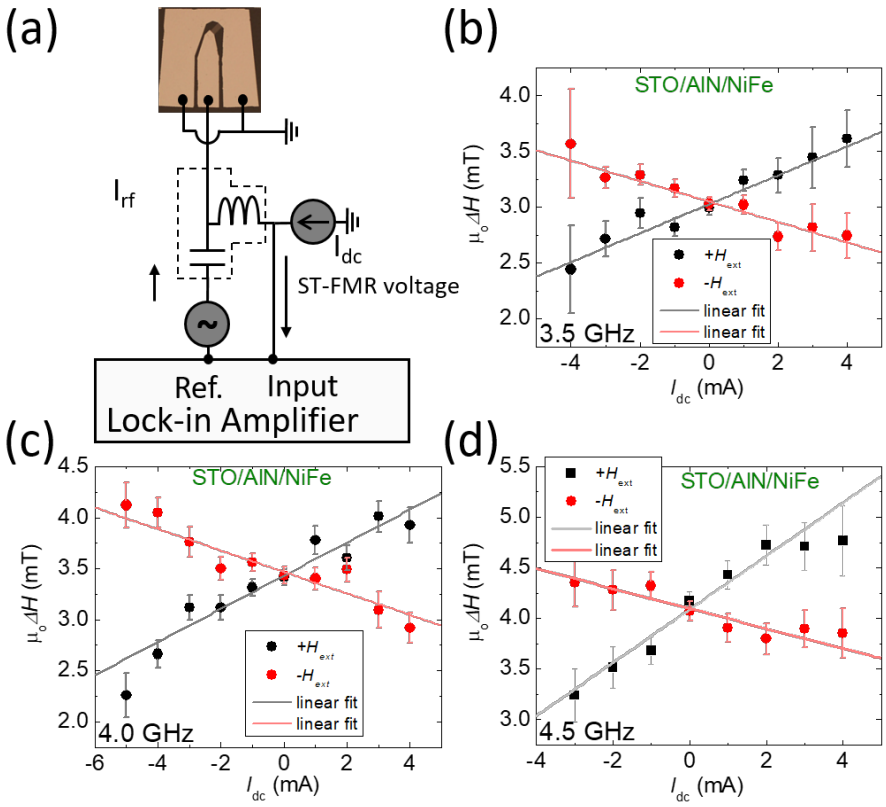

Figure 7.12. (a) DC-bias ST-FMR set-up and (b)-(d) ΔH obtained as a function of I_{dc} for STO/AlN/NiFe measured at f = 3.5, 4.0 and 4.5 GHz, respectively.

7.3.8. DC-biased ST-FMR: resonance field modulation

In addition to the linewidth modulation using DC-bias ST-FMR measurements, the same measurement can also be used to calculate the out-of-plane field-like torque, τ_{FL} if it exists. The lineshape analysis which uses the self-calibrated ratio of S/A (Eq. (7.4)) assumes that the A arises purely from the Oersted field. Though such an assumption seems valid for thick heavy metal (HM)/ferromagnet (FM) systems, a thorough investigation is required for a complex system such as 2DEG created between two insulating oxides. The presence of τ_{FL} may counterbalance the Oersted field torque τ_{OFT}, and eventually, lead to a false symmetric ST-FMR spectrum. To confirm that the large symmetric spectra in our q-2DEG are primarily from the high symmetric component arising from damping-like torque, we also checked the resonance field modulation. By measuring the change in resonance magnetic field H_o as a function of I_{dc}, the τ_{FL} can be estimated. For the STO/AlN/NiFe, we can observe no linear shift in $\mu_o H_o$ as a function of I_{dc} implying no presence of out-of-plane field-like torque as shown in figure 7.13 (a). On the contrary, we observed an increasing H_o with I_{dc} magnitude for STO/Al_2O_3 that might lead to heating in the sample and no τ_{FL} (Fig. 7.13(b)). For comparison, we show the data of H_o vs I_{dc} for Pt/NiFe and do not find τ_{FL} as expected for a thick HM/FM system (see Fig. 7.13(c)).

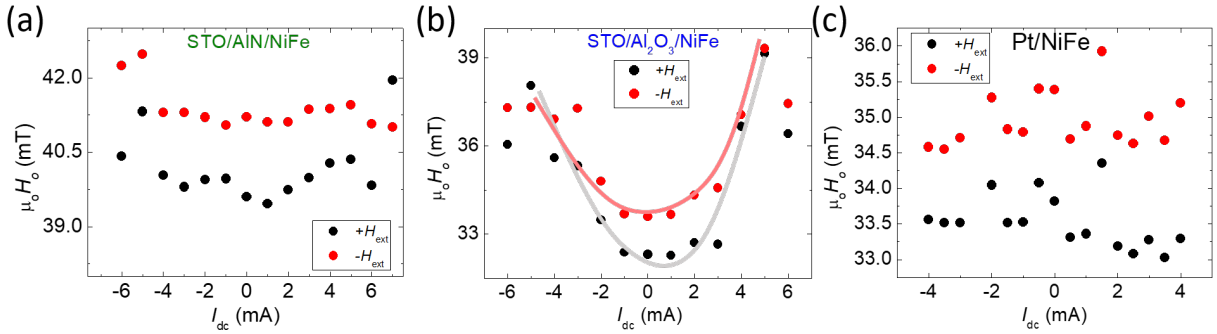

Figure 7.13. H_o obtained as a function of I_{dc} for (a) STO/AlN/NiFe, (b) STO/Al_2O_3/NiFe, and (c) Pt/NiFe.

7.4. Conclusion

In summary, we report a large charge to spin conversion efficiency θ_{cs} at room temperature in 2DEG formed at the interface of amorphous AlN and Al_2O_3 with $SrTiO_3$ substrate. Previous reports on spin-charge interconversion have been reported for 2DEG formed in epitaxial thin films at room temperature [15-20] and amorphous oxide/STO substrates in 2DEG at cryogenic temperatures [27], which arises from the spin-momentum locking at Rashba interfaces lacking inversion symmetry. From angular-dependent ST-FMR measurements in our q-2DEG-NiFe samples, we observe the breaking of two-fold and mirror symmetry of spin-torques which may be due to non-uniform microwave current flow in the high impedance q-2DEG. Our estimation of θ_{cs}/t ~ 0.244 nm^{-1} in STO/AlN and ~ 0.101 nm^{-1} in STO/Al_2O_3, comparable to that of epitaxial films is important because of the relative ease with which amorphous films can provide added functionalities in 2DEG applications [4,28-30]. Moreover, a large direct current modulation of linewidth for STO/AlN provides direct confirmation of high θ_{cs} in our q-2DEG. The similarity between our amorphous and crystalline oxide interfaces in terms of charge density and conductivity along with the charge-to-spin conversion may provide insight into the microscopic mechanisms and further optimization of the conversion efficiencies. An ability to efficiently generate spin current from q-2DEG, while simultaneously understanding their angular dependent properties that shed light on the directionality of spin torques, is crucial for their implementation in spintronic device applications. However, due to the challenges in estimating the correct thickness of 2DEGs and hence the amount of current flowing through it, there seems to be a long road ahead for its incorporation as a charge-to-spin material in SOT-MRAM for low power consumption. The results presented in this chapter have been based on the research article published in physica status solidi (RRL)-Rapid Research Letters [39].

References for chapter 7

1. A. Ohtomo and H. Y. Hwang, *Nature* **427**, 423 (2004).
2. K. Han, K. Hu, X. Li, K. Huang, Z. Huang, S. Zeng, D. Qi, C. Ye, J. Yang, H. Xu, A. Ariando, J. Yi, W. Lü, S. Yan. and X. R. Wang, *Sci. Adv.* **5**, eaaw7286 (2019).
3. H. Y. Hwang, Y. Iwasa, M. Kawasaki, B. Keimer, N. Nagaosa, and Y. Tokura, *Nat. Mater*. **11**, 103 (2012).
4. Y. Z. Chen, F. Trier, T. Wijnands, R. J. Green, N. Gauquelin, N. Egoavil, D. V. Christensen, G. Koster, M. Hujiben, N. Bovet, S. Macke, F. He, R. Sutarto, N. H. Andersen, J. A. Sulpizio, M. Honig, G. E. D. K. Prawiroatmodjo, T. S. Jespersen, S. Linderoth, S. Ilani, J. Verbeeck, G. Van Tendeloo, G. Rijnders, G. A. Sawatzky, and N. Pryds, *Nat. Mater.* **14**, 801 (2012).
5. W. Niu, Y. Gan, Y. Zhang, D. V. Christensen, M. V. Soosten, X. Wang, Y. Xu, R. Zhang, N. Pryds, and Y. Chen, *Appl. Phys. Lett.* **111**, 021602 (2017).
6. A. D. Caviglia, M. Gabay, S. Gariglio, N. Reyren, C. Cancellieri, and J. –M. Triscone, *Phys. Rev. Lett.* **104**, 126803 (2010).
7. A. Soumyanarayanan, N. Reyren, A. Fert, and C. Panagopoulos, *Nature* **539**, 509 (2016).
8. Z. Zhong, A. Toth, and K. Held, *Phys. Rev. B* **87**, 161102(R) (2013).
9. A. Manchon, H. C. Koo, J. Nitta, S. M. Frolov, and R. A. Duine, *Nat. Mater.* **14**, 871 (2015).
10. K. Narayanapillai, K. Gopinadhan, X. Qiu, A. Annadi, Ariando, T. Venkatesan, and H. Yang, *Appl. Phys. Lett.* **105**, 162405 (2014).
11. H. R. Zhang, Y. Zhang, H. Zhang, J. Zhang, X. Shen, X. X. Guan, Y. Z. Chen, R. C. Yu, N. Pryds, Y. S. Chen, B. G. Shen, and J. R. Sun, *Phys. Rev. B* **96**, 195167 (2017).
12. M. J. Jin, S. Y. Moon, J. Park, V. Modepalli, J. Jo, S. I. Kim, H. C. Koo, B. C. Min, H. W. Lee, S. H. Baek, and J. W. Yoo, *Nano Lett.* **17**, 36 (2017).
13. E. Lesne, Y. Fu, S. Oyarzun, J. C. Rojas Sánchez, D. C. Vaz, H. Naganuma, G. Sicoli, J. –P. Attané, M. Jamet, E. Jacquet, J. –M. George, A. Barthélémy, H. Jaffrès, A. Fert, M. Bibes, and L. Vila, *Nat. Mater.* **15**, 1261 (2016).
14. J. –Y. Chauleau, M. Boselli, S. Gariglio, R. Weil, G. de Loubens, J. –M. Triscone, and M. Viret, *Europhys. Lett.* **116**, 17006 (2016).
15. Y. Wang, R. Ramaswamy, M. Motapothula, K. Narayanapillai, D. Zhu, J. Yu, T. Venkatesan, and H. Yang, *Nano Lett.* **17**, 7659 (2017).
16. Q. Song, H. Zhang, T. Su, W. Yuan, Y. Chen, W. Xing, J. Shi, J. Sun, and W. Han, *Sci. Adv.* **3**, e1602312 (2017).
17. H. Nakayama, T. Yamamoto, H. An, K. Tsuda, Y. Einaga, and K. Ando, *Sci. Adv.* **4**, eaar3899 (2018).

18. J. Zhang, J. Zhang, X. Chi, R. Hao, W. Chen, H. Yang, D. Zhu, Q. Zhang. W. Zhao, H. Zhang, and J. Sun, *Phys. Rev B* **105**, 195110 (2022).
19. N. Soya, T. Katase, and K. Ando, *Adv. Elec. Mater.* **8**, 2200232 (2022).
20. H. Yang, B. Zhang, X. Zhang, X. Yan, W. Cai, Y. Zhao, J. Sun, K.L. Wang, D. Zhu, and W. Zhao, *Phys. Rev. Appl.* **12**, 034004 (2019).
21. L. Liu, C. –F. Pai, Y. Li, H. W. Tseng, D. C. Ralph, and R. A. Burhman, *Science* **336**, 555 (2012).
22. K. Kondou, R. Yoshimi, A. Tsukazaki, Y. Fukuma, J. Matsuno, K. S. Takahashi, M. Kawasaki, Y. Tokura, and Y. Otani, *Nat. Phys.* **12**, 1027 (2016).
23. A. R. Mellnik, J. S. Lee, A. Richardella, J. L. Grab, P. J. Mintun, M. H. Fischer, A. Vaezi, A. Manchon, E. –A. Kim, N. Samarth, and D. C. Ralph, *Nature* **511**, 449 (2014).
24. K. W. Demasius, T. Phung, W. Zhang, B.P. Hughes, S. -H. Yang, A. Kellock, W. Han, A. Pushp, S. S. P. Parkin, *Nat. Commun.* **7**, 10644 (2016).
25. U. Shashank, R. Medwal, T. Shibata, R. Nongjai, J. V. Vas, M. Duchamp, K. Asokan, R. S. Rawat, H. Asada, S. Gupta, and Y. Fukuma, *Adv. Quantum Technol.* **4**, 2000112 (2021).
26. U. Shashank, R. Medwal, Y. Nakamura, J. R. Mohan, R. Nongjai, A. Kandasami, R. S. Rawat, H. Asada, S. Gupta, and Y. Fukuma, *Appl. Phys. Lett.* **118**, 252406 (2021).
27. P. Noël, F. Trier, L. M. V. Arche, J. Bréhin, D. C. Vaz, V. Garcia, S. Fusil, A. Barthélémy, L. Vila, M. Bibes, and J. –P. Attané, Nature **580**, 483 (2020).
28. Y. Chen, N. Pryds, J. E. Kleibeuker, G. Koster, J. Sun, E. Stamate, B. Shen, G. Rijnders, and S. Linderoth, *Nano Lett.* **11**, 3774 (2011).
29. Z. Q. Liu, C. J. Li, W. M. Lü, X. H. Huang, Z. Huang, S.W. Zeng, X. P. Qiu, L. S. Huang, A. Annadi, J. S. Chen, J. M. D. Coey, T. Venkatesan, and Ariando, *Phys. Rev. X* **3**, 0210210 (2013).
30. A. Annadi, Q. Zhang, X. R. Wang, N. Tuzla, K. Gopinadhan, W. M. Lü, A. R. Barman, Z. Q. Liu, A. Srivastava, S. Saha, Y. L. Zhao, S. W. Zeng, S. Dhar, E. Olsson, B. Gu, S. Yunoki, S. Maekawa, H. Hilgenkamp, T. Venkatesan, and Ariando, *Nat. Commun.* **4,** 1838 (2013).
31. J. Sklenar, W. Zhang, M. B. Jungfleisch, H. Saglam, S. Grudichak, W. Jiang, J. E. Pearson, J. B. Ketterson, and A. Hoffman, *Phys. Rev. B* **95**, 224431 (2017).
32. M. Harder, Y. Gui, and C-M. Hu, *Phys. Rep.* **661**, 1 (2016).
33. R. Medwal, A. Deka, J.V. Vas, M. Duchamp, H. Asada, S. Gupta, Y. Fukuma, and R.S. Rawat, *Appl. Phys. Lett.* **119**, 162403 (2021).
34. A. Deka, B. Rana, R. Anami, K. Miura, H. Takahashi, Y. Otani, and Y. Fukuma. *Phys. Rev. Res.* **4**, 023139, (2022).
35. L. Liu, T. Moriyama, D. C. Ralph, and R. A. Burhman, *Phys. Rev. Lett.* **106**, 036601 (2011).

36. D. MacNeill, G. M. Stiehl, M. H. D. Guimaraes, R. A. Burhman, J. Park, and D. C. Ralph, *Nat. Phys.* **13**, 300 (2017).
37. S. Gupta, R. Medwal, D. Kodama, K. Kondou, Y. Otani, and Y. Fukuma, *Appl. Phys. Lett.* **110**, 022404 (2017).
38. R. Bansal, G. Nirala, A. Kumar, S. Chaudhary, and P. K. Muduli, *SPIN* **8,** 1850018 (2018).
39. U. Shashank, A. Deka, C. Ye, S. Gupta, R. Medwal, R. S. Rawat, H. Asada, X. R. Wang, and Y. Fukuma, *Phys. Status Solidi RRL* 2200377 (2022).

Conclusions and future outlook based on the results reported in this thesis

In this thesis, we perform a series of experiments to investigate the charge-to-spin conversion phenomena in non-metallic impurity (S, O, N, P) incorporated in Pt via ion implantation and a quasi-two dimensional electron gas (q-2DEG) created between insulating $SrTiO_3$/AlN and $SrTiO_3/Al_2O_3$. We study the charge-to-spin conversion efficiency, θ_{DL} by using spin-torque ferromagnetic resonance measurements. To study its Onsager reciprocity, i.e., spin-to-charge, we also employ the spin-pumping inverse spin Hall voltage (SP-ISHV) measurements. Therefore, to find a high θ_{DL} and low resistivity, ρ_{xx} material as well as to investigate the spin Hall effect (SHE) mechanism in non-metallic impurity in host Pt, we employ the less explored material engineering technique of ion implantation in the archetypal Pt.

First, we report a new spin Hall material, designed by implanting 12 keV S-ion implantation in Pt i.e., Pt(S) at a dose of 5×10^{16} ions/cm^2. We observe an 8 times (3 times) enhanced charge-to-spin conversion efficiency, θ_{DL} at 10 K (300 K) for Pt(S). We obtain a large spin Hall conductivity, σ_{SH}^{xy} = 8.32 $\times10^5$ $(\hbar/2e)$ Ω^{-1} m^{-1} at 10 K for Pt(S), highest amongst reported Pt and its derivative alloys suitable for spin-orbit torque (SOT) MRAM applications. Furthermore, we confirm the Onsager reciprocity of spin-to-charge via SP-ISHV measurements and observe an anticipated 3 times increase in ISHV from charge current generated via spin current. We also observe a double increase in spin mixing conductance, $g_{eff}^{\uparrow\downarrow}$ in Pt(S) as compared to pure Pt, but a 43 % reduction in spin diffusion length, λ_{sd} due to the increase in resistivity, ρ_{xx} of Pt(S). Finally, we observe no breaking of the two-fold and mirror symmetry of spin-orbit-torque. For the material characterization, we use the cross sectional TEM and unveil relatively no change in the interface quality and thickness of target Pt layer after S-implantation. We confirm the polycrystalline nature of both Pt and Pt(S) via high resolution TEM.

Second, we implant oxygen in Pt, i.e., Pt(O) at a low energy of 20 KeV. We report a 3.5 times increase in θ_{DL} with varying dose from 0×10^{16}-1×10^{17} ions/cm^2. We observe an increase in θ_{DL} from 0.064 to 0.230 with a smaller trade-off in ρ_{xx} from 55.4 to 159.5 μΩ-cm. We confirm a linear dependence of spin

Hall resistivity from impurities, ρ_{imp}^{SH} with the square of resistivity from impurities, ρ_{imp}^{2}, *i.e.,* $\rho_{imp}^{SH} \propto \rho_{imp}^{2}$, implying an extrinsic origin of side-jump scattering as the dominant origin of SHE. Furthermore, we observe no breaking of the mirror and two-fold symmetry of torques allowing the use of ST-FMR based lineshape analysis to quantify the damping-like torque. Simultaneously, we employ the sputtering method to incorporate O in Pt, *i.e.,* PtO_x by varying the Ar: O_2 gas ratio during deposition of Pt and enhance the SHE. We find that the higher concentration of oxygen impurity in Pt in influenced by the extrinsic side-jump scattering while the lower concentration is not-a-side-jump but an intrinsic SHE one.

Third, as an extension of our approach to study the non-metallic impurity in Pt, we implant nitrogen, N and study the dose/temperature dependent ST-FMR studies. We measure θ_{DL} as a function of temperature for different O, N dose from 2.5×10^{16}-1×10^{17} ions/cm^2. We find the θ_{DL} to be invariant for the lower dose i.e., 2.5×10^{16} and pure Pt, suggesting an intrinsic SHE. Whereas for the higher doses, i.e., 5×10^{16} and 5×10^{16}, we observe an increase of θ_{DL} with decrease in temperature (T). In analogy to anomalous Hall effect (AHE), by expressing the σ_{SH}^{xy} as a sum of intrinsic and extrinsic SHE, we disentangle the intrinsic and extrinsic side-jump contribution of SHE. We find a crossover of intrinsic to extrinsic side-jump SHE as we increase the dose of O and N ions in Pt from 0×10^{16} to 1×10^{17} ions/cm^2. We show that a sudden decrease in intrinsic spin Hall conductivity, σ_{SH}^{int} is counterbalanced by the increase in side-jump induced SHE, θ_{SH}^{sj} due to the increase in residual resistivity from impurities, $\rho_{xx,0}$. To confirm, our assumption of considering the contribution of extrinsic side-jump, we also employ an independent model, To confirm the influence of impurities on extrinsic side-jump induced SHE, we next focus on spin Hall resistivity from impurities, $\rho_{\mathrm{SH}}^{\mathrm{imp}} = \rho_{\mathrm{SH}}^{\mathrm{Pt(O)or\ Pt(N)}} - \rho_{\mathrm{SH}}^{\mathrm{Pt}}$ where $\rho_{\mathrm{SH}}^{\mathrm{Pt(O)or\ Pt(N)}}$ and $\rho_{\mathrm{SH}}^{\mathrm{Pt}}$ are the SH resistivity of Pt(O) and Pt(N), and pure Pt which are estimated from respective charge-spin interconversion efficiency, and the resistivity from impurities ρ_{imp}, i.e., $\rho_{\mathrm{imp}} = \rho_{\mathrm{Pt-Oxide\ or\ nitride}} - \rho_{\mathrm{Pt}}$. We observe a prominent signature of linear trend in $\rho_{\mathrm{SH}}^{\mathrm{imp}}$ vs ρ_{imp}^{2}, implying a dominant extrinsic side-jump scattering induced SHE for both Pt(O) and Pt(N).

Fourth, we investigate the influence of moderate implantation energy of 30 keV and a non-metallic phosphorus in Pt, *i.e.,* Pt(P) at a varying dose of 2.5-9×10^{17} ions/cm^2. By using X-ray diffraction, we observe a reduction in the intensity of Pt (111) peak with the increase in dose confirming the polycrystalline to amorphous transition of Pt(P). We see voids/bubbles in Pt(P), ascribing to the presence of lighter atoms, possibly phosphorus in Pt. Using electron diffraction from Pt, we observe clear rings in pure Pt and halo rings in Pt(P) supporting our observation of polycrystalline to amorphous transition of Pt. We obtain a giant θ_{DL} ≈0.75 in Pt(P), for amorphous Pt(P). In our first-four studies, including Pt(P), we observe no breaking of the two-fold and mirror symmetry of SOT. Finally, by expressing the σ_{SH}^{xy} as a sum of intrinsic and extrinsic SHE as $\left|\sigma_{SH}^{xy}\right| = \sigma_{SH}^{int} + \left|(\theta_{SH}^{sj}\,\rho_{xx,0})\sigma_{xx}^{2}\right|$, we find that the dominant contribution is extrinsic side-jump as shown Pt(S, O, N, P) samples, as the implantation dose increases. This brings us to the assertion that higher the $\rho_{\mathrm{xx},0}$, higher is the θ_{SH}^{sj} , and therefore lower is the σ_{SH}^{int}. This gives us a model that by simply increasing the ρ_{xx} and hence the $\rho_{xx,0}$, the SHE can be enhanced for all the ion implanted samples. Therefore, in terms of future outlook, these ion-implanted materials might be useful in being a desirable candidate for implementation of low power consumption in spin-orbit torque based MRAM applications. Out of all the candidates, the Pt(P) and Pt(S) seems to be a better candidate for SOT-MRAM due to their high θ_{DL} and moderate ρ_{xx}.

Finally, in our fifth study, we go beyond the ion-implanted Pt, and explore a new avenue, the quasi two dimensional electron gas created at the interface of $SrTiO_3$/amorphous oxides due to the creation of oxygen vacancy, namely the $SrTiO_3$/AlN and $SrTiO_3/Al_2O_3$. To confirm the q-2DEG, we measure the sheet resistance. R_s of STO/AlN and $SrTiO_3/Al_2O_3$. We observe that the normalized R_s decreases with T, affirming the metallic nature of both types of 2DEG. For both samples, we see a kink in the R_s at ~105 K which can be ascribed to the cubic-to tetragonal phase transition of $SrTiO_3$, indicating that the 2DEG exists inside the substrate. We observe a very high θ_{DL} due to oxygen vacancy enabled Rashba-Edelstein effect, an order higher than our ion implanted Pt but with the additional challenges of unknown thickness of q-2DEG, high sheet resistance, R_S and broken symmetry of SOT for SOT-MRAM applications.

Therefore, we report that θ_{DL} can be enhanced in host Pt by incorporating non-metallic impurity such as S, O, N, and P in Pt. We find a better SHE material for SOT-MRAM in Pt(S) and Pt(P) due to high θ_{DL} with a smaller trade-off in ρ_{xx}. We find an extrinsic side-jump scattering induced SHE to influence the θ_{DL} enhancement in Pt(O), Pt(N) and Pt(S). We observe an oxygen vacancy enabled Rashba-Edelstein effect, at the q-2DEG. Finally, the various SHE/Rashba materials *viz.,* the ion implanted Pt and q-2DEG may help us in unveiling the host-impurity combinations, and role of oxygen-vacancy, respectively to unlock the full potential of charge-to-spin conversion in future.

Acknowledgements

First, and foremost, I would to like to sincerely thank my PhD supervisor, Prof. Yasuhiro Fukuma from Kyushu Institute of Technology (KIT), Japan for agreeing to supervise me for my doctoral degree and shaping me into an independent, yet collaborative researcher. His persistent help and guidance for complete five years in my experiments, and the freedom in performing the research in laboratory based on my interest, is the reason why I learned a lot. While working with him, I realized the true value of work ethic and the importance of process more than the result, even when the experiment fails. His critical evaluation of my results and collaborative projects with brilliant researchers from different laboratories around the globe has broadened my approach to view scientific research in an inquisitive, responsible and diligent manner.

I thank Dr. Surbhi Gupta, especially during the first two years of my PhD during her tenure in the laboratory, for teaching me the basics with Prof. Fukuma during my initial stage and helping me understand and perform the microwave measurements on my own. In the same tone, I thank Dr. Rohit Medwal (now Assistant Prof. in IIT Kanpur, India) for helping me start my PhD in the Fukuma laboratory. His constant support, encouragement and discussion of my research at various stages of my PhD were really fruitful for me.

I am thankful to Prof. Hironori Asada, Yamaguchi University, for providing me with the high quality thin films and laboratory facilities from his laboratory. I will cherish his constant support and critical evaluation of my research work. I thank Prof. Rajdeep S. Rawat, National Institute of Education, Nanyang Technological University, Singapore his support and critical evaluation of my work. I am thankful to Prof. S. Annapoorni from University of Delhi, India, Prof. and Prof. T. Okamoto from KIT, Japan for reviewing my thesis. I also thank Edmund S. Otabe from KIT, Japan for his support during my stay in university and also agreeing to review my thesis.

I extend my acknowledgement to Prof. A. Kandasami, UPES Dehradun, India for the fruitful collaboration of the ion implantation project. I really thank him for the hospitality rendered to me during my stay in Inter University Accelerator Center, India to prepare the ion implantation samples. I would also like to thank Dr. Razia Nongjai for the persistent help in the preparation of ion implantation samples and her availability to discuss my experimental queries.

I am thankful to Prof. X. Renshaw Wang, Nanyang Technological University (NTU), Singapore for the collaborative project on $SrTiO_3$ based quasi-two dimensional electron gas (q-2DEG). His guidance, persistent help and discussion on improving my background in q-2DEG helped me in the completion of the project, despite all the hurdles. I thank Dr. Chen Ye (NTU), for the deposition of the q-2DEG.

I would also like to thank Prof. Yoichi Horibe and Prof. Manabu Ishimaru from Dept. of Materials and Engineering, Kyushu Institute of Technology, Japan for their help with the material characterization of moderate energy ion implantation project (Phosphorus). I thank Prof. Martial Duchamp (NTU), Dr. Joseph. V. Vas (previously in NTU), for their material characterization of the sulfur implanted Pt work. I thank Prof. A. Baba, and Mr. H. Sato from Center for microelectronics system, KIT for their constant help in availing the cleanroom facilities for device fabrication.

For the people in the Fukuma laboratory, I would like to thank Dr. Angshuman Deka, (now in Purdue University, USA) for his constant help during and after his departure from the laboratory. Since my arrival in Fukuma laboratory in 2018, his guidance, support and help in experiments, device fabrication, and understanding of spintronics as a senior PhD student at that time, was really important in building my knowledge and confidence. I thank John Rex Mohan, for not only being a helpful co-worker, but also being my cooperative flat mate for 5 long years. He always motivated and advised me on both research and life, and to keep going every day. I thank Shibata, Nakamura, Tomoda, and Kusaba for their continuous support and hard work in the completion of the research projects. Besides the co-authors of my research project, I would like to thank Arun Jacob Mathew and Dr. Garima Vashisht for proof-reading of my thesis and for their help inside and outside of lab. I also thank Tyagi, Matsushita, Iino, Matsui, Momota, Imai, Feng, Kou, Yamanaka, Wang for their help inside and outside the lab.

For people outside of laboratory, I am thankful to Dr. Osamu Nawata, Iizuka Friendship Network, for his constant support and help during my stay in the flat. I am thankful to Kobayashi-san for her continuous support since my arrival in Japan.

I would like to thank my family, especially my sister, and my elder uncle for encouraging me in taking the leap of faith, to come to Japan and do a PhD. I would like to thank my mother, my brother and my younger uncle for their support and help.

My father always encouraged me to be highly educated and do well in academics. Today, after 17 years, although he is no longer with me, I am happy to have contributed my bit to the scientific community. This thesis is dedicated to my father, in memory.

Shashank Utkarsh

Kyushu Institute of Technology, Japan

December 2022